The University Of Sheffield.

Access To Thesis.

- A bound copy of every thesis which is accepted as worthy for a higher degree, must be deposited in the University of Sheffield Library, where it will be made available for borrowing or consultation in accordance with University Regulations.
- All students registering from 2008–09 onwards are also required to submit an electronic copy of their final, approved thesis. Students who registered prior to 2008–09 may also submit electronically, but this is not required.

Author: ..... Dept: .....

Thesis Title: ..... Registration No: .....

For completion by all students:

Submit in print form only (for deposit in the University Library): ☐

Submit in print form and also upload to the *White Rose eTheses Online* server: In full ☐

Edited eThesis ☐

Please indicate if there are any embargo restrictions on this thesis. Please note that if no boxes are ticked, you will have consented to your thesis being made available without any restrictions.

Embargo details: (complete only if requesting an embargo to either your print and/or eThesis)	Embargo required?		Length of embargo (in years)
Print Thesis	Yes ☐	No ☐	_____
eThesis	Yes ☐	No ☐	_____

Supervisor: I, the supervisor, agree to the named thesis being made available under the conditions specified above.

Name: ..... Dept: .....

Signed: ..... Date: .....

Student: I, the author, agree to the named thesis being made available under the conditions specified above.

I give permission to the University of Sheffield to reproduce the print thesis in whole or in part in order to supply single copies for the purpose of research or private study for a non-commercial purpose.

I confirm that this thesis is my own work, and where materials owned by a third party have been used copyright clearance has been obtained. I am aware of the University's *Guidance on the Use of Unfair Means* (www.sheffield.ac.uk/lets/design/unfair)

I confirm that all copies of the thesis submitted to the University (including electronic copies on CD/DVD) are identical in content.

Name: ..... Dept: .....

Signed: ..... Date: .....

For completion by students also submitting an electronic thesis (eThesis):

I, the author, agree that the University of Sheffield's eThesis repository (currently WREO) will make my eThesis available over the internet via an entirely non-exclusive agreement and that, without changing content, WREO may convert my thesis to any medium or format for the purpose of future preservation and accessibility.

I, the author, agree that the metadata relating to the eThesis will normally appear on both the University's eThesis server and the British Library's EThOS service, even if the thesis is subject to an embargo. I agree that a copy of the eThesis may be supplied to the British Library.

I confirm that the upload is identical to the final, examined and awarded version of the thesis as submitted in print to the University for deposit in the Library (unless edited as indicated above).

Name: ..... Dept: .....

Signed: ..... Date: .....

THIS SHEET MUST BE BOUND IN THE FRONT OF THE PRINTED THESIS BEFORE IT IS SUBMITTED

The Preparation and Characterisation of Graphene and Its Analogues

By

Liangxu Lin

University of Sheffield

Submitted for the award of the

Degree of Doctor of Philosophy

(PhD)

from the

Department of Materials Science and Engineering

Supervised by Dr. Dan A. Allwood and Prof. Shaowei Zhang

October, 2013

Declaration

The thesis has been composed by myself and has not been submitted or accepted in any previous degree application. The work has been conducted by myself, except where due acknowledgement has been given.

Some works contained in this thesis are published and submitted:
1, Liangxu Lin and Shaowei Zhang, Effective Solvothermal Deoxidization of Graphene Oxide Using Solid Sulphur as a Reducing Agent. *J. Mater. Chem.* **2012**, *22*, 14385-14393.

2, Liangxu Lin and Shaowei Zhang, Creating High Yield Water Soluble Luminescent Graphene Quantum Dots *via* Exfoliating and Disintegrating Carbon Nanotubes and Graphene Flakes. *Chem. Commun.* **2012**, *48*, 10177-10179.

3, Liangxu Lin, Yaoxian Xu, Shaowei Zhang, Ian M. Ross, Albert C. M. Ong and Dan A. Allwood, Fabrication and Luminescence of Monolayered Boron Nitride Quantum Dot. *Small* **2014**, *10*, 60-65.

4, Liangxu Lin, Yaoxian Xu, Shaowei Zhang, Ian M. Ross, Albert C. M. Ong and Dan A. Allwood, Fabrication of Luminescent Monolayered Tungsten Dichalcogenides Quantum Dots with Giant Spin-Valley Coupling. *ACS Nano* **2013**, *7*, 8214-8223.

5, Liangxu Lin, Xuelin Zheng, Shaowei Zhang and Dan A. Allwood, Surface Energy Engineering in the Solvothermal Deoxidation of Graphene Oxide. Submitted to *Advanced Materials Interfaces* **2013**.

Acknowledgements

First of all, I would like to sincerely thank my supervisors, Dr. Dan A. Allwood and Prof. Shaowei Zhang for their constant support, valuable advice and guidance throughout my doctorate. Great thanks to Dr. Dan A. Allwood again for kind help and discussions.

I really appreciate The University of Sheffield for granting me the Faculty scholarship, also great thanks to Dr. Dan Allwood and Prof. Shaowei Zhang for the financial support on this study.

I would like to thank Prof. Albert C. M. Ong, Dr. Yaoxian Xu (Department of Infection and Immunity, University of Sheffield) for the assistance with confocal microscopy experiments, Dr. Weiping Wu (Engineering Department, University of Cambridge) for the assistance with four-points probe measurements, Dr. Jan. Pokorny (Department of Materials Science and Engineering, University of Sheffield) for the training of Raman tests, Prof. C. A Hunter, Miss H. Sun (Department of Chemistry, University of Sheffield) for the permission of using their fluorescence spectrophotometer, Mr. Y. Wen (College of Engineering, Mathematics and Physical Sciences, University of Exeter) and Dr. Ian Ross (Department of Electronic and Electrical Engineering, University of Sheffield) for the assistance with HRTEM characterisations, Dr. Claire R. Hurley (Sheffield Surface Analysis Centre, University of Sheffield) and Dr. Anders Barlow (NEXUS, University of Newcastle) for the assistance with XPS tests, Dr. En Ma (Fujian Institute of Research on The Structure of Matter, Chinese Academy of Sciences) for the assistance with time-resolved photoluminescence tests and Dr. Xuelin Zheng (College of Chemistry and Chemical Engineering, Fujian Normal University) for the assistance with surface tension measurements.

I would like to thank all the staffs at the Department of the Materials Science and Engineering (The University of Sheffield) who have been very kind and friendly during my stay. I also thank to the technical staff for the technical training.

Big love to my wife (Guoqian Chen) and daughter (Lin-Er Chen). Without your support and understanding I would not have made it this far.

Glossary of Acronyms

2D	*Two-Dimensional*
3D	*Three-Dimensional*
AFM	*Atomic Force Microscopy*
BF	*Bright Field*
BN	*Boron Nitride*
BGO	*Boiled Graphene Oxide*
BGO-DMF-H_2O	*Boiled Graphene Oxide in DMF/H_2O Solvent*
BGO-NMP-H_2O	*Boiled Graphene Oxide in NMP/H_2O Solvent*
CNTs	*Carbon Nanotubes*
CVD	*Chemical Vapor Deposition*
DAPI	*Diamidino-2-Phenylindole*
DF	*Dark Field*
DMA	*Dimethylacetamide*
DMAc	*N,N-Dimethylacetamide*
DMEM	*Dulbecco's Modified Eagle Medium*
DMEU	*1,3-Dimethyl-2-Imidazolidinone*
DMF	*Dimethylformamide*
EDS	*Energy Dispersive X-ray Spectrometers (Spectra)*
EDTA	*Ethylenediaminetetraacetic Acid*
EELS	*Electron Energy Loss Spectroscopy*
FBS	*Fetal Bovine Serum*
FITC	*Fluorescein Isothyocyanate*
Fe-rGO-H_2O	*Reduced GO in H_2O by Fe^{2+}*
Fe-rGO-DMF-H_2O	*Reduced GO in DMF-H_2O by Fe^{2+}*
Fe-rGO-NMP-H_2O	*Reduced GO in NMP-H_2O by Fe^{2+}*
FFT	*Fast Fourier Transform*
FT-IR	*Fourier Transform Infrared*
GBL	*g-Butyrolactone*
GFs	*Graphite Flakes*
GO	*Graphene Oxide*
GQD	*Graphene Quantum Dot*
hBN	*Hexagonal Boron Nitride*
HRTEM	*High-Resolution Transmission Electron Microscopy*
IPA	*Isopropyl Alcohol*
K-GICs	*Potassium Intercalated Graphite Compounds*
ITO	*Indium Tin Oxide*
LTMDs	*Layered Transition-Metal Dichalcogenides*
MDCKII	*Madin-Darby Canine Kidney Type II*
MWCNTs	*Multi-Layered Carbon Nanotubes*
NMP	*N-Methyl Pyrrolidone*
NMR	*Nuclear Magnetic Resonance*
PBS	*Phosphate Buffered Saline*
PL	*Photoluminescence*
PLE	*Photoluminescence Excitation*
P-rGO	*Partially Reduced Graphene Oxide*
QD	*Quantum Dot*
QY	*Quantum Yield*
rGO	*Reduced Graphene Oxide*
rGO-DMF-H_2O	*Reduced Graphene Oxide in DMF-H_2O*
rGO-NMP-H_2O	*Reduced Graphene Oxide in NMP-H_2O*
SAED	*Selected Area Electron Diffraction*
SEM	*Scanning Electron Microscopy*
S-rGO-H_2O	*Reduced Graphene Oxide in H_2O by Sulphur*
S-rGO-DMF-H_2O	*Reduced Graphene Oxide in DMF-H_2O by Sulphur*
S-rGO-NMP-H_2O	*Reduced Graphene Oxide in NMP-H_2O by Sulphur*
TEM	*Transmission Electron Microscopy*
TGA	*Thermogravimetric Analysis*
TMDs	*Transition-metal Dichalcogenides*
TRPL	*Time-Resolved Photoluminescence*
UV/Vis	*Ultraviolet/Visible*
XPS	*X-ray Photoelectron Spectroscopy*
XRD	*X-ray Diffraction*

Abstract

The studies in this thesis give deep insights on the large scale preparation of graphene and the fabrication and properties of novel monolayered quantum dots (QDs). Graphene has received remarkable attention due to its interesting physical and chemical properties. Among various preparations for graphene, the solvothermal deoxidation of graphene oxide (GO) is highly attractive as it potentially offers a relatively economical and scalable manufacturing route for use in industrial applications. Unfortunately, the deep deoxidation of GO and highly dispersable reduced GO (rGO) are difficult to achieve using this approach, although the reasons for this deoxidation remain unclear. This thesis shows that the agglomeration/self-assembly of partially reduced GO (p-rGO) sheets in the solvothermal deoxidation reaction suppresses the deep deoxidation of GO and led to low dispersibility/electrical conductivity of the product. By tuning the surface energy of the solvent to minimize the surface enthalpy of the dispersion, these technical problems can be ameliorated and full deoxidation of GO with high dispersibility and electrical conductivity achieved. In this thesis, an alternative novel and effective route to fabricating graphene QDs (GQDs, lateral size ~ 20 nm) is also described. This technique of delaminating layered structures has also been developed to produce monolayered QDs of boron nitride (BN, lateral size of ~ 10 nm), tungsten disulfide (WS_2, lateral size ~ 8-15 nm) and molybdenum disulfide (MoS_2, lateral size of ~ 8-20 nm). This has opened up many opportunities in studying these interesting materials with reduced dimensions, with new behaviours and properties emerging from the various QDs. The zigzag edges of GQDs led to the appearance of new band gaps and give strong blue-green luminescence centred at 420 nm wavelength (quantum yield of ~7.6%). In monolayered BN QDs, carbene-replaced zigzag edges, carbon-replaced N vacancy point and BO_x^- (x = 1 and 2) species added new luminescence at around 425 nm wavelength (quantum yield of ~2.5%). Strong luminescence was created by the reduced dimensions of WS_2 and MoS_2 monolayered QDs causing them to became direct semiconductors. The reduced lateral dimensions also caused marked quantum confinement effects to arise, such as large blue shifts in absorption features of BN, WS_2 and MoS_2 monolayered QDs. The formation of monolayered WS_2 and MoS_2 QDs also led to their valance bands being split by giant spin-orbit coupling effects to a far greater degree than is observed form monolayered sheets. The studies suggest strongly that these features are likely to be tunable with lateral dimensions, which makes the QDs potentially very interesting for

applications. Although these uses may include spintronics, optoelectronics and even quantum computing, their application in biology is demonstrated by all the monolayered QDs being used as non-toxic fluorescent labels in confocal microscopy of biological cells.

Contents

Chapter I. Introduction and Overview of the Thesis

1.1 Introduction

Carbon materials (*e.g.* C_{60}[1-2], carbon nanotubes[3]) have received extensive attention for use in electronic devices[4-11], green chemistry[12-14], medical treatment[15-17], clean energy[18-20] and structural materials[21-23]. The formation of its monolayered phase, graphene, gives new opportunities for practical application of carbon-based materials.[24] Further studies have highlighted the remarkable properties and potential applications of graphene.[25-35] However, the industrial application of graphene has not been developed so far, which is mainly due to the lack of an effective and scalable preparation method, and its zero band gap nature.[36-37] There is a clear imperative to develop new fabrication and spatial confinement methods for engineering a non-zero band gap in graphene.[37] With graphene preparation, the chemical reduction of graphene oxide (GO) offers a very interesting route. Although the quality of the graphene may not be comparable with that prepared using chemical vapor deposition (CVD) growth method, the large scale preparation of graphene following chemical reduction can satisfy the materials requirements in many industrial fields (*e.g.* catalysts, ceramics, solar-cells, electrochemistry). However, graphene prepared from this route normally suffers from a low extent of deoxidation, low dispersibility and low electrical conductivity. The technical difficulties behind this approach remain unclear.

Hexagonal boron nitride (hBN) and metal dichalcogenides (MX_2, M=Mo, W, and X=S, Se) are similar to graphite in being layered materials which consist of covalently bonded layers (BN and MX_2) that stack together by weak van der Waals forces.[38-42] Interesting changes of the electronic, magnetic and optical properties can be expected upon the formation of these monolayered materials.[42] For instance, unlike its bulk counterpart, monolayered MoS_2 is a direct gap semiconductor with strong luminescence.[39-41] Monolayered MoS_2 can also be ferromagnetic/nonmagnetic or metallic/semiconducting depending on its edge structure.[38-41] Further reduction of the lateral size of these monolayered sheets should, in principle, allow the edge and defect dependent properties much more dominant, providing a new route to controlling materials properties through quantum dot (QD) size and quality. It has been shown that some of

these layered materials (*e.g.* MoS_2, WS_2) can be chemically exfoliated into thin monolayer colloidal suspension.[42] Nevertheless, decreasing the lateral size of these monolayered sheet to that of two-dimensional quantum dots (2D-QDs) in an effective manner remains a significant challenge.

These insights led to the following aims for the PhD study: 1) To develop a feasible and scalable route for graphene preparation; 2) To further reduce the graphene lateral size and engineer a non-zero gap in graphene; 3) To create graphene analogues (including atomically thin BN, MoS_2/WS_2 QDs) with small lateral size and discover their new properties for future application. It is reasonable to believe that meeting these aims will provide much that is useful for industrial application of graphene and could pave the way for novel applications of the thin QDs of other materials.

1.2 Overview of the Thesis

This thesis is divided into ten chapters. The thesis chapters are organized as follows:

Chapter II presents an overview of the properties, preparations and applications of these interesting, layered materials (graphene and its analogues) based on published experimental and theoretical findings. This provides much of the underpinning information relevant to the thesis aims.

Chapter III describes the various analysis techniques used in this thesis.

Chapter IV is the first chapter to contain research results. It first discusses the difficulties of low deoxidation and poor dispersibility of reduced GO/rGO produced from the solvothermal deoxidation of GO. These features are attributed to π-π stacking and self-assembly between the rGO sheets during the reaction. The chapter demonstrates how these technical problems can be solved to produce high yields of fully deoxidized graphene using a scalable chemical approach. Using solid sulphur (S) as a reducing agent and by tuning the solvent surface tension, GO can be deeply reduced to form rGO with good dispersibility and high electronic conductivity.

Chapter V builds upon the previous chapter by studying in more detail how the tuning solvent surface energy assists in the solvothermal deoxidation of GO. The results of this are generalized in an empirical model that can be used for different solvents and temperatures. These studies confirm that incomplete deoxidation and poor

dispersibility of rGO in the solvothermal deoxidation of GO are indeed induced by π-π stacking and self-assembly between the partially reduced GO sheets.

Chapter VI describes the fabrication of high yield graphene QDs (GQDs) using a novel method. The formation mechanism of the GQDs from carbon nanotubes and graphite flakes is well studied in this chapter. The spatial confinement of electronic states is a potential route to tuning the properties of graphene and creating a useful band gap. This chapter confirms the existence of such a band gap and also describes the wider electronic structure, optical properties and bio-imaging application of the fabricated GQDs.

In ***Chapter VII***, the fabrication method used in ***Chapter VI*** for GQDs is further developed to fabricate monolayered BN QDs. Structural analysis confirms the monolayered thickness of the QDs, while their optical properties are shown to be dependent on the QD edge structure, chemical doping and quantum confinement effect. This chapter also describes the use of monolayered BN QDs as a fluorophore in bio-imaging.

Chapter VIII describes the fabrication of monolayered WS_2 QDs using the method described in ***Chapter VI***. The structural properties, electronic structure, optical property and bio-imaging application of the QDs are presented in this chapter.

Chapter IV presents a study of monolayered MoS_2 QD fabrication, again by adapting the method described in ***Chapter VI***. The MoS_2 QDs are investigated structurally and optically, which reveals their electronic structure, and bio-imaging using monolayered MoS_2 QD fluorophores is demonstrated.

Chapter X summarizes the key findings of the work contained in this thesis. The conclusions from ***Chapters IV-IX*** are also included in this chapter. On the basis of the result from this thesis, the directions for future work are also proposed.

References and Notes

[1] H. W. Kroto, J. R. Heath, S. C. O'Brien, R. F. Curl and R. E. Smalley, C_{60}: Buckminsterfullerene. *Nature* **1985**, *318*, 162-163.

[2] W. Krätschmer, L. D. Lamb, K. Fostiropoulos and D. R. Huffman, Solid C_{60}: a New Form of Carbon. *Nature* **1990**, *347*, 354-358.

[3] S. Iijima, Helical Microtubules of Graphitic Carbon. *Nature* **1991**, *354*, 56-58.

[4] X. Lu and Z. Chen, Curved Pi-Conjugation and the Related Chemistry of Small Fullerenes (smaller than C_{60}) and Single-Wall Carbon Nanotubes. *Chem. Rev.* **2005**, *105*, 3643-3696.

[5] S. Hong and S. Myung, Nanotube Electronics: a Flexible Approach to Mobility. *Nat. Nanotechnol.* **2007**, *2*, 207-208.

[6] I. Takesue, J. Haruyama, N. Kobayashi1, S. Chiashi, S. Maruyama, T. Sugai and H. Shinohara, Superconductivity in Entirely Dnd-bonded Multiwalled Carbon Nanotubes. *Phy. Rev. Lett.* **2006**, *96*, 057001.

[7] R. C. Haddon, A. F. Hebard, M. J. Rosseinsky, D. W. Murphy, S. J. Duclos, K. B. Lyons, B. Miller, J. M. Rosamilia, R. M. Fleming, A. R. Kortan, S. H. Glarum, A. V. Makhija, A. J. Muller, R. H. Eick, S. M. Zahurak, R. Tycko, G. Dabbagh and F. A. Thiel, Superconductivity at 18 K in Potassium-Doped C_{60}. *Nature* **1991**, *350*, 320-322.

[8] K. Tanigaki, T. W. Ebbesen, S. Saito, J. Mizuki, J. S. Tsai, Y. Kubo and S. Kuroshima, Superconductivity at 33 K in $Cs_xRb_yC_{60}$. *Nature* **1991**, *352*, 222-223.

[9] A. F. Hebard, M. J. Rosseinsky, R. C. Haddon, D. W. Murphy, S. H. Glarum, T. T. M. Palstra, A. P. Ramirez and A. R. Kortan, Superconductivity at 18 K in Potassium-Doped C_{60}. *Nature* **1991**, *350*, 600-601.

[10] C. C. CHEN, S. P. Kelty and C. M. Lieber, $(Rb_xK_{1-x})_3C_{60}$ Superconductors: Formation of a Continuous Series of Solid Solutions. *Science* **1991**, *253*, 886-888.

[11] O. Zhou, Q. Zhu, J. E. Fischer, N. Coustel, G. B. M. Vaughan, P. A. Heiney, J. P. Mccauley and JR. A. B. Smith, III, Compressibility of M_3C_{60} Fullerene Superconductors: Correlation Between Tc and Lattice Parameter. *Science* **1992**, *255*, 833-835.

[12] K. Shimizu, J. S. Wang and C. M. Wai, Application of Green Chemistry Techniques to Perpare Electrocatalysts for Direct Methanol Fuel Cells. *J. Phys. Chem. A* **2010**, *114*, 3956-3961.

[13] Z. Sun, Y. Zhao, Y. Xie, R. Tao, H. Zhang, C. Huang and Z. Liu, The Solvent-free Selective Hydrogenation of Nitrobenzene to Aniline: an Unexpected Catalytic Activity of Ultrafine Pt Nanoparticles Deposited on Carbon Nanotubes. *Green Chem.* **2010**, *12*, 1007-1011.

[14] K. Gong, F. Du, Z. Xia, M. Durstock and L. Dai, Nitrogen-Doped Carbon Nanotube Arrays with High Electrocatalytic Activity for Oxygen Reduction. *Science* **2009**, *323*, 760-764.

[15] R. H. Baughman, A. A. Zakhidov and W. A. de Heer, Carbon Nanotubes--the Route Toward Applications. *Science* **2002**, *297*, 787-792.

[16] M. F. Cesta, J. P. Ryman-Rasmussen, D. G. Wallace, T. Masinde, G. Hurlburt, A. J. Taylor and J. C. Bonner, Bacterial Lipopolysaccharide Enhances PDGF Signaling and Pulmonary Fibrosis in Rats Exposed to Carbon Nanotubes. *Am. J. Respir. Cell Mol. Bio.* **2010**, *43*, 142-151.

[17] S. Koyama, H. Haniu, K. Osaka1, H. Koyama1, N. Kuroiwa1, M. Endo, Y. A. Kim and T. Hayashi. Medical Application of Carbon-Nanotube-Filled Nanocomposites: The Microcatheter. *Small* **2006**, *2*, 1406-1411.

[18] C. Liu and H. Cheng, Carbon Nanotubes for Clean Energy Applications. *J. Phys, D: Appl. Phys.* **2005**, *38*, R231.

[19] J. Kong, M. G. Chapline and H. Dai, Functionalized Carbon Nanotubes for Molecular Hydrogen Sensors. *Adv. Mater.* **2001**, *13*, 1384-1386.

[20] D. M. Guldi, G. M. A. Rahman, M. Prato, N. Jux, S. Qin and W. Ford, Single-Wall Carbon Nanotubes as Integrative Building Blocks for Solar-Energy Conversion. *Angew. Chem.* **2005**, *117*, 2051-2054.

[21] B. Ashrafi, P. Hubert and S. Vengallatore, Carbon Nanotube-reinforced Composites as Structural Materials for Microactuators in Microelectromechanical Systems. *Nanotechnology* **2006**, *17*, 4895-4903

[22] G. Zhan, J. D. Kuntz, J. Wan and A. K. Mukherjee, Single-Wall Carbon Nanotubes as Attractive Toughening Agents in Alumina-Based Nanocomposites. *Nat. Mat.* **2003**, *2*, 38-42.

[23] J. Zhu, J. D. Kim, H. Peng, J. L. Margrave, V. N. Khabashesku and E. V. Barrera, Improving the Dispersion and Integration of Single-Walled Carbon Nanotubes in Epoxy Composites through Functionalization. *Nano Lett.* **2003**, *3*, 1107-1113.

[24] K. S. Novoselov, A. K. Geim, S. V. Morozov, D. Jiang, Y. Zhang, S. V. Dubonos, I. V. Grigorieva and A. A. Firsov, Electric Field Effect in Atomically Thin Carbon Films. *Science* **2004**, *306*, 666-669.

[25] S.V. Morozov, K. S. Novoselov, M. I. Katsnelson, F. Schedin, L. A. Ponomarenko, D. Jiang and A. K. Geim, Strong Suppression of Weak Localization in Graphene. *Phys. Rev. Lett.* **2006**, *97*, 016801.

[26] K. S. Novoselov, E. Mccann, S. V. Morozov, V. I. Fal' Ko, M. I. Katsnelson, U. Zeitler, D. Jiang, F. Schedin and A. K. Geim, Unconventional Quantum Hall Effect and Berry's Phase of 2π in Bilayer Graphene. *Nat. Phys.* **2002**, *2*, 177-180

[27] M. I. Katsnelson, K. S. Novoselov and A. K. Geim, Chiral Tunnelling and the Klein Paradox in Graphene. *Nat. Phys.* **2006**, *2*, 620-625.

[28] E. V. Castro, K. S. Novoselov, S.V. Morozov, N. M. R. Peres, J. M. B. L. dos Santos, J. Nilsson, F. Guinea, A. K. Geim and A. H. C. Neto, Biased Bilayer Graphene: Semiconductor with a Gap Tunable by the Electric Field Effect. *Phys. Rev. Lett.* **2007**, *99*, 216802.

[29] K. S. Novoselov, Z. Jiang, Y. Zhang, S. V. Morozov, H. L. Stormer, U. Zeitler, J. C. Maan, G. S. Boebinger, P. Kim and A. K. Geim, Room-Temperature Quantum Hall Effect in Graphene. *Science* **2007**, *315*, 1379.

[30] D. A. Abanin, K. S. Novoselov, U. Zeitler, P. A. Lee, A. K. Geim and L. S. Levitov, Dissipative Quantum Hall Effect in Graphene near the Dirac Point. *Phys. Rev. Lett*. **2007**, *98*, 196806.

[31] S. Pisana, M. Lazzeri, C. Casiraghi, K. S. Novoselov, A. K. Geim, A. C. Ferrari and F. Mauri, Breakdown of the Adiabatic Born–Oppenheimer Approximation in Graphene. *Nat. Mat.* **2007**, *6*, 198-201

[32] S.V. Morozov, K. S. Novoselov, M. I. Katsnelson, F. Schedin, D. C. Elias, J. A. Jaszczak and A. K. Geim, Giant Intrinsic Carrier Mobilities in Graphene and Its Bilayer. *Phys. Rev. Lett.* **2008**, *100*, 016602.

[33] L. A. Ponomarenko, F. Schedin, M. I. Katsnelson, R. Yang, E. W. Hill, K. S. Novoselov and A. K. Geim, Chaotic Dirac Billiard in Graphene Quantum Dots. *Science* **2008**, *320*, 356-358.

[34] L. A. Ponomarenko, R. Yang, T. M. Mohiuddin, M. I. Katsnelson, K. S. Novoselov, S.V. Morozov, A. A. Zhukov, F. Schedin, E.W. Hill and A. K. Geim, Effect of a High-Environment on Charge Carrier. *Phys. Rev. Lett.* **2009**, *102*, 206603.

[35] K. I. Bolotin, F. Ghahari, M. D. Shulman, H. L. Stormer and P. Kim, Observation of the Fractional Quantum Hall Effect in Graphene. *Nature* **2009**, *462*, 196-199.

[36] X. Yang, C. Cheng, Y. Wang, L. Qiu and D. Li, Liquid-Mediated Dense Integration of Graphene Materials for Compact Capacitive Energy Storage. *Science* **2013**, 341, 534-537.

[37] A. K. Geim and K. S. Novoselov, The Rise of Graphene. *Nat. Mat.* **2007**, *6*, 183-191.

[38] A. R. Botello-Méndez, F. López-Urías, M. Terrones and H. Terrones, Metallic and Ferromagnetic Edges in Molybdenum Disulfide Nanoribbons. *Nanotechnology* **2009**, *20*, 325703.

[39] A. Splendiani, L. Sun, Y. Zhang, T. Li, J. Kim, C.-Y. Chim, G. Galli, and F. Wang, Emerging Photoluminescence in Monolayer MoS_2. *Nano Lett.* **2010**, *10*, 1271-1275.

[40] K. F. Mak, C. Lee, J. Hone, J. Shan and T. F. Heinz, Atomically Thin MoS_2: a New Direct-Gap Semiconductor. *Phys. Rev. Lett.* **2010**, *105*, 136805.

[41] G. Eda, H. Yamaguchi, D. Voiry, T. Fujita, M. Chen and M. Chhowalla, Photoluminescence from Chemically Exfoliated MoS_2. *Nano Lett.* **2011**, *11*, 5111-5116.

[42] J. N. Coleman, M. Lotya1, A. O'Neill1, S. D. Bergin, P. J. King, U. Khan, K. Young, A. Gaucher, S. De, R. J. Smith, I. V. Shvets, S. K. Arora, G. Stanton, H.-Y. Kim, K. Lee, G. T. Kim, G. S. Duesberg, T. Hallam, J. J. Boland, J. Wang, J. F. Donegan, J. C. Grunlan, G. Moriarty, A. Shmeliov, R. J. Nicholls, J. M. Perkins, E. M. Grieveson, K, Theuwissen, D. W. McComb, P. D. Nellist and V. Nicolosi, Two-Dimensional Nanosheets Produced by Liquid Exfoliation of Layered Materials. *Science* **2011**, *331*, 568-571.

Chapter II. Literature Review

2.1 Structure and Property of Graphene and Its Analogues (Monolayered BN, MoS_2 and WS_2 Sheets)

2.1.1 Molecular Orbitals Theory[1]

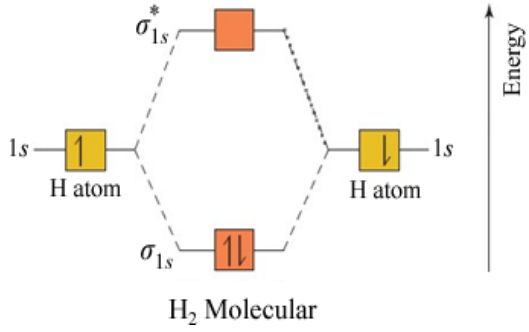

Figure 2-1. Molecular orbital diagrams for H_2. The asterisk denotes that the molecular orbital is an antibonding orbital.

This section describes molecular orbital (MO) theory relevant to graphene and its inorganic analogues. MO theory describes electrons in molecules by using specific wave functions. In a molecule, atoms can share one, two or three electrons to form single, double and triple bonds, respectively.

Consider the simplest molecule, H_2. The lowest energy MO concentrates electron density between the two hydrogen nuclei and this is termed the bonding MO (***Figure 2-1***). This MO results from summing the two hydrogen atomic orbitals (AO). The electrons in this MO are more stable (*i.e.* lower energy) than in the 1s atomic orbital of an isolated hydrogen atom because this MO is attracted to both nuclei. The MO concentrates electron density between the nuclei and therefore holds the atoms together in a covalent bond. The higher energy MO has very little electron density between the nuclei, which is named as antibonding MO. Unlike bonding MO, the AO wave functions in antibonding MO cancel each other, leaving the greatest electron density on opposite sides of the nuclei. Therefore, this MO excludes electrons from the region where a bond must be formed, leading to a higher energy and less stable MO than for the 1s AO of a hydrogen atom.

The electron density in both the bonding MO and the antibonding MO of H_2 is centered about the internuclear axis. These are both referred to as sigma MOs (σ). In contrast, π-MOs describe cases where the electron density is not centred about the internuclear axis.

In H_2, the interaction between two 1s AO and the MO can be described by ***Figure 2.1***. In this diagram, each H atom brings one electron to the molecule. These two electrons occupy the lower-energy bonding MO with opposite spins. In a more complex system, such as in quantum dots (QDs), different energy levels can also be described using MO theory.

2.1.2 Structure and Property of Graphene

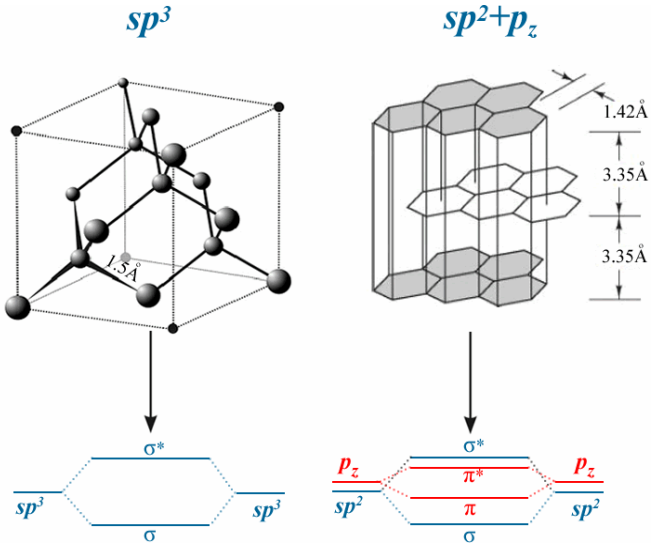

Figure 2-2. Molecular structures of sp^3 diamond and sp^2 graphite.

Carbon is a group IV element ($^6C=1s^22s^22p^2$). The tendency for the 2s, $2p_x$, $2p_y$ and $2p_z$ orbitals in carbon to mix with each other is responsible for creating a wide range of different properties in carbon-based molecules and materials. For example, sp^3 hybridized carbon (diamond, ***Figure 2-2***) is an insulator while sp^2 hybridized carbon (graphite, ***Figure 2-2***) is a conductor. The crystal structure of sp^2 hybridized graphite is clearly different to that of diamond. As shown in ***Figure 2-2***, in graphite, the stable hexagonal form is obtained by stacking planar layers in an ABAB arrangement. Each layer is composed of sp^2 hybridized hexagonal carbon rings. The sp^2 hybridization between one *s* and two *p* orbitals gives a trigonal planar structure with the formation of a σ bond between carbon atoms (bond distance of 1.42 Å) and lends considerable robustness to the lattice structure. The p_z orbitals perpendicular to the sheets overlap

to form a filled valence band (bonding π orbitals) and an empty conduction band (antibonding) π orbital, giving graphite its character of good electrical conduction.

Unlike graphite, graphene is a single layer of carbon atoms, densely packed into a semi-continuous sp^2 benzene-ring structure.[2,3] The energy bands of graphene at low energies can be described by a two-dimensional (2D) Dirac-like equation:

$$\hat{H}=\hbar v_F \begin{pmatrix} 0 & k_x - ik_y \\ k_x + ik_y & 0 \end{pmatrix} = \hbar v_F \sigma.\mathrm{K} \qquad (eq.\ 2\text{-}1)$$

with linear dispersion near K/K′ in k space, where k, σ and V_F represent the quasiparticle momentum, the 2D Pauli matrix and the k-independent Fermi velocity respectively.[4,5] One main result from this equation is the zero-gap nature of graphene.[5] In addition, the low-energy excitations of graphene are massless chiral, Dirac fermions. These characters make interesting physical phenomena and properties to graphene, such as the measured anomalous integer quantum Hall effect, and unusual mechanical and electronic properties.[6-8]

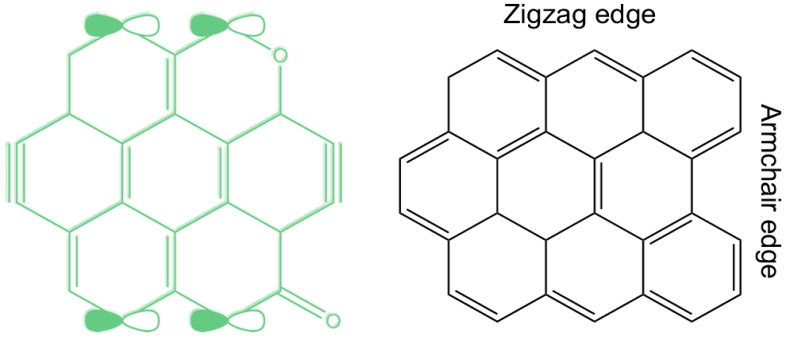

Figure 2-3. Chemical and edge structures of GQDs.

Although the formation of graphene can give many new interesting properties, its application has been limited due to its zero-gap nature.[9] Therefore, many techniques have been developed to induce a useful non-zero gap to graphene, including the formation of bilayered graphene, the formation of graphene nanoribbons and the reduction of the lateral size for spatial confinement.[9] Among these, the formation of graphene QDs (GQDs) is believed to be the most feasible approach to engender a useful band gap to graphene. As generally recognised, QDs are nanoparticles having small sizes comparable to the exciton Bohr radius of their bulk counterpart.[10-12] Unlike many semiconductors, graphene has an infinite exciton Bohr radius.[13] Substantially enhanced quantum confinement and edge (such as zigzag and armchair edges; ***Figure 2-3***) effects are achievable as the lateral sizes of GQDs are reduced.[13] New

properties/applications (*e.g.* luminescence for bio-imaging[14] and photoelectronic devices[15,16]) could be expected for GQDs even though they may have some surface defects.

Unlike in large graphene sheets, the edge structure of GQDs plays a key role in determining their physical properties. However, there remains a lack of understanding on the non-zero band gap origins. For example, GQDs (lateral size: 5 and 10 nm) created from C_{60} molecules show band gap variation from 0.25 to 0.8 eV.[17] By contrast, GQDs cut from graphene oxide (GO) sheets (GQDs lateral size: 5-13 nm)[18] and graphene sheet (GQDs lateral size: 3-5 nm)[19] show a similar band gap of ~4 eV. A useful model from graphene nanoribbons suggests that both the armchair and zigzag edges influence the gap value of graphene.[20] These edges have different mechanisms of the gap opening, as the gap of an armchair edge originates from quantum confinement effect and that of zigzag shaped edge (shown in ***Figure 2-3***) originates from a staggered sublattice potential (due to spin ordered states at the edges). As for the wide gap (up to 4 eV) discovered in GQDs, Pan *et al.* suggested that the gap originates from the HOMO-LUMO structure in carbene-like free zigzag sites (***Figure 2-3*** and ***Figure 2-4***). No matter which mechanism is mainly responsible for the creation of a finite band gap in GQDs, the formation of GQDs can broaden the properties and applications of graphene (*e.g.* photoelectronic device applications and demonstration of Coulomb blockade effects for quantum information applications[21]).

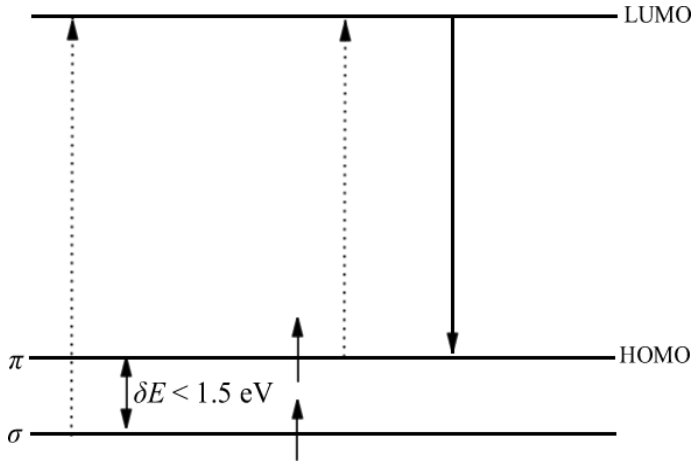

Figure 2-4. Typical electronic transitions of triple carbene at zigzag sites.

2.1.3 Structure and Property of Monolayered hBN

Like graphite, hBN has a layered structure, consisting of covalently sp^2-bonded boron and nitride layers which are stacked together by weak van der Waals forces.[22] As a

result, hBN shows remarkable chemical resistance and physical properties, which can be used in catalyst, ceramics and lubricants.[23-25] As shown in ***Figure 2-5,*** the stacking of monolayered BN in hBN is different with that of graphene in graphite. Normally, BN exhibits AA' stacking where each B atom eclipses a N atom on the adjacent layer, leading to stronger layer interactions than that of graphene in graphite.[26] It follows that exfoliation of monolayered BN sheets from bulk hBN crystals is harder than that of graphene from graphite. Although the formation of monolayered BN has been achieved very recently, some property differences between bulk hBN crystal and monolayered BN have been discovered and expected (for example, unlike bulk hBN, monolayered BN has no optical absorption in the visible region).[27] In bulk hBN, the layers can stack in many ways, as one layer can slide/rotate respect to the other layers.[28,29] It is unclear how the stacking influences the band structure of bulk hBN. There is also disagreement between the various measurements of hBN band gap values and whether it is a direct or indirect gap.[30-31] However, upon formation of a monolayered structure, the band structure of BN is much clearer than that of bulk hBN due to the disappearance of the layer stacking. Theoretical calculations show that monolayered BN sheet is an insulator with a bandgap of ~6.0 eV.[32] Due to the absence of layer-layer interactions, the observed optical band gap of monolayered BN is bigger than that of their bulk hBN.[32] Quantum confinement effect in monolayered BN QDs might also induce a larger gap. The proposed large direct band gap for deep UV emission from highly crystallized hBN[33] suggests that the formation of monolayered BN QDs might also be an effective route to achieving similar deep UV emission. This would give BN more significance as a potential material for optoelectronic applications.

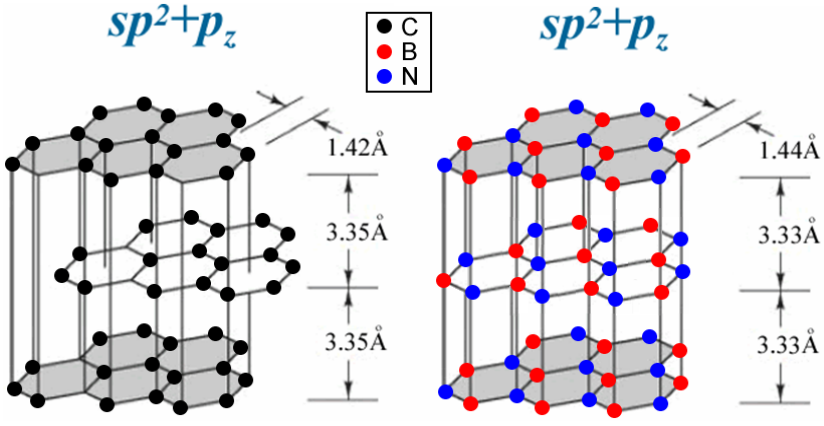

Figure 2-5. Molecular structures of sp^2 graphite (left) and hBN (right).

As with graphene, the edge structure of monolayered BN is also important for understanding various physical properties. As show in ***Figure 2-6***, the edge of

monolayered BN sheet can be either zigzag (B- or N terminated edges) or armchair (BN pair edged). Theoretical calculations predict that BN nanoribbion with zigzag edges can be metallic.[34] The edge dependent properties also vary in different chemical environments. For example, armchair BN nanoribbons with C dopants (BN domains are expected to grow outside of C domains) can reproduce the otherwise unique electronic properties of armchair graphene nanoribbons, while in the zigzag edged BN nanoribbons with C dopant and a particular C/BN ratio, the materials may exhibit intrinsic half-metallicity without any external constraints.[35] Additionally, introduction of O dopants into the armchair edges can lead to the formation of a new bandgap at around 2.65 eV.[36] This introduction of BO^- and BO^{2-} are believed to be strong luminescence centres.[37] The formation of monolayered BN QDs may also make these edge and defect dependent properties much more evident.

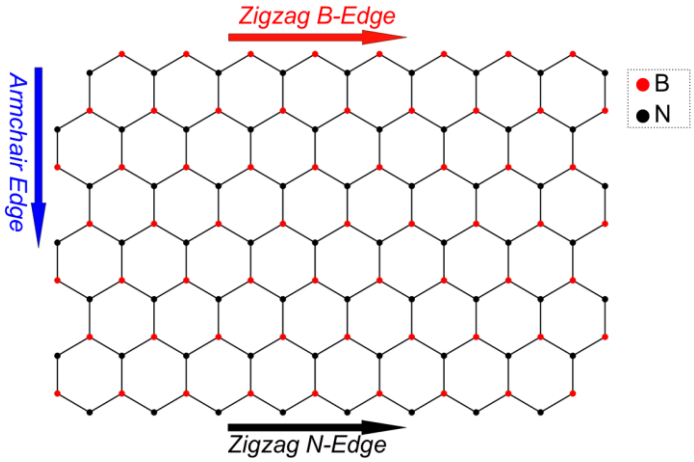

Figure 2-6. Edge structure of monolayered BN.

2.1.4 Structure and Property of Monolayered Transition-Metal Dichalcogenides (TMDs, MX_2, M=W, Mo; X=S)

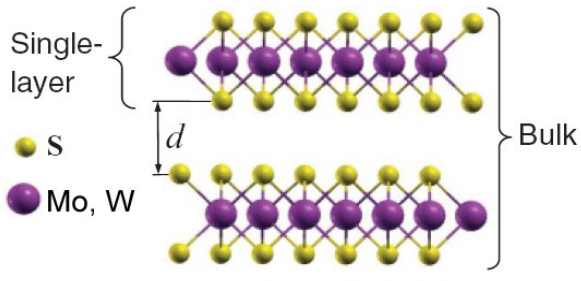

Figure 2-7. Structure of bulk and monolayered MX_2 (M=W, Mo; X=S).[38]

WS_2 and MoS_2 are typical layered transition-metal dichalcogenides (LTMDs) with fundamental two-dimensional building blocks (strongly bonded S-M-S layers) that are

weakly bonded to each other by van der Waals forces (***Figure 2-7***).[38] This highly anisotropic bonding of LTMDs leads to strongly anisotropic electrical and mechanical properties[38] and is responsible for the wide range of applications, including solid state lubricants, catalytic reactions, and solar cells.[38]

Although bulk WS_2 and MoS_2 have been studied for many years, the recent successful preparation of monolayered sheets of these materials[39] has led to resurgence in interest. Certain properties can be achieved from these thin materials which are absent from the bulk phase. A typical example is the MoS_2 which is widely known as a solid lubricant and catalyst.[40] Bulk MoS_2 is an indirect band gap semiconductor with an energy gap of ~1.2 eV and negligible luminescence. The formation of monolayered MoS_2 creates strong quantum confinement effects leading to the MoS_2 becoming a direct band gap semiconductor with strong luminescence. These changes have also been found in other LTMDs (*e.g.* WS_2).[41] As with graphene and monolayered BN, the physical properties of monolayered WS_2/MoS_2 are also highly dependent on their edge structures. For instance, monolayered MoS_2 can be ferromagnetic/metallic or nonmagnetic/semiconducting depending on the details of its edge structure.[42] These changes become more evident with decreasing lateral sizes of the structures, because of the increased influence of edge atoms. Nevertheless, these effects are not understood well due to the difficulties in preparing small monolayers reliably. The formation of monolayered MoS_2/WS_2 QDs could give new properties to the material which have potential applications in the fields of optoelectronics and energy harvesting.[43-45]

2.2 Preparation Methods

2.2.1 Preparation of Graphene

There are various reported preparation methods of graphene, including micro-mechanical exfoliation,[46] chemical vapor deposition (CVD) method,[47-54] epitaxial growth,[55-58] liquid exfoliation,[39, 59,60] GO reduction,[61-69] unzipping of carbon nanotubes,[70-72] alkali intercalation method[73-75] and direct chemical synthesis.[76-79]

Micro-Mechanical Exfoliation: Micro-mechanical exfoliation was one of the early reported preparation methods for "free state" graphene.[46] In this preparation,[46] mesas on top of the platelets were firstly prepared by using dry etching in oxygen plasma. The structured surface was pressed against a thin layer of a fresh wet photoresist spun over a glass substrate. Then the mesas were baked onto the photoresist layer. As reported, graphene can be obtained by repeatedly peeling highly

oriented pyrolytic graphite from the mesas. Acetone is then used to release the graphene from the photoresist to leave a graphene solution. Although only low volumes of graphene can be prepared this way, the discovery of this method was important as most early discoveries of graphene's properties were based on materials fabricated this way.

CVD Method: Many methods were developed after the discovery of graphene.[24] Among these, CVD has been shown to be an effective method to prepare high quality graphene.[47-54] Unlike the growth of carbon nanotubes, CVD of graphene does not need metal particle catalysts. In a typical CVD route, a carbon-containing precursor (*e.g.* CH_4, CH_2=CH_2) is decomposed and deposited on a substrate at high temperature. Graphene can be obtained by controlling the reaction condition. Published reports indicate that different types of graphene structure can grow on the substrates. For example, mono-, bi- and tri-layered graphene can grow on SiC substrates,[47] while monolayer graphene can grow on the hot Ir surfaces by low-pressure CVD of ethylene.[48] The advantage of this method is that high quality, large size graphene can be produced. For instance, high quality graphene with square centimeter size has been prepared successfully by A. N. Obraztsov *et al.*[49] However, there are technical problems for transferring the graphene from the growth substrate and in the scale-up of the technique. For example, transfer graphene from metal substrate using wet etching method is likely to lead to doped graphene and lower quality.[51] As a result, CVD is still a high cost and low volume production method.

Molecular Epitaxial Growth Method: High quality graphene can also be grown using molecular epitaxial growth methods.[51-58] For example, with a substrate of 6H-SiC, oxidation of the surface and subsequent removal of the oxidized species under high vacuum conditions can lead to a carbon film. Graphene can be prepared by crystallization of the carbon film using controlled heating procedures. High quality monolayered and multi-layered graphene can be obtained using this method.[51-52] However, it is difficult to prepare graphene with large size, uniform surface and layers, suggesting the molecular epitaxial growth method still needs to be improved.

Liquid Exfoliation: Liquid exfoliation of graphite can be a useful method for creating high quality graphene.[39,59,60] Based on the reports by Coleman *et al.* [39,59] N-methylpyrrolidone (NMP), N,N-dimethylacetamide (DMA), g-butyrolactone (GBL) and 1,3-dimethyl-2-imidazolidinone (DMEU) can be used for the exfoliation solvents. By

optimizing the exfoliation parameters, the yield of graphene can reach 7-12 wt%. The solvents for this exfoliation have been further expanded to hexafluorobenzene (C_6F_6), octafluorotoluene ($C_6F_5CF_3$), pentafluorobenzonitrile (C_6F_5CN), and pentafluoropyridine (C_5F_5N).[60] The key parameters of this method are use of a suitable solvent and ultrasonic processing. Once the surface energy of the solvent is controlled to be close to that of graphite, the graphene can be readily exfoliated using ultrasonication. Nevertheless, the applications of this method are also limited due to the residual organic solvent on the graphene and high energy cost during the preparation.

Chemical Reduction Method: For practical applications in some industrial fields (*e.g.* catalyst, ceramics, solar-cell, electrochemistry), the highest quality of graphene is often not required. Therefore, the chemical reduction route from GO is one of the most interesting and scalable preparation methods for these applications.[61-69] In this method, the interlayer space of graphite is generally initially expanded by oxidization. The GO sheets can be exfoliated from the oxidized graphite (graphite oxide) in a subsequent sonication treatment. The sheets can then be chemically reduced to form graphene. Graphite oxide has been the subject of studies since the 19th century.[80] In 1958, Hummers *et al.* reported an improved route to prepare graphite oxide which is still often used in graphene preparation today.[81] For achieving high quality graphene, it is imperative to control the extent of graphite oxidation. Full exfoliation of graphite requires a particular degree of oxidization beforehand.[62] Insufficient oxidation of graphite may suppress the GO exfoliation. By contrast, over-oxidation results in excess C=O, C-O, C-O-C and breaks the aromatic structure. This will suppress the electrical conductivity of the reduced product, especially when the aromatic structure of graphene is severely destroyed. In addition, for preparing high quality graphene, the GO should be highly reduced and dispersable for further processing. Many reducing methods have been developed to achieve this, including the direct using of reducing agents (*e.g.* $NaBH_4$, $N_2H_4.H_2O$),[61-63] electrochemistry reduction methods,[64] heating reduction methods,[65,66] and photocatalyst reduction methods.[67] Among these, the directly chemical reduction of GO using strong reducing agents (*e.g.* $N_2H_4.H_2O$) was established as the most effective way to reduce free-standing GO.[61] However, technical efforts have been made to improve the deoxidation efficiency by addressing low reducing ability, agglomeration and poor dispersion of graphene. A previous study indicated that most oxygen on GO can be removed by hydrazine,[61] though the mechanism of the epoxide removal is not yet completely clear. Nevertheless, the existence of lactones, anhydrides, and quinines in GO also led to the incorporation of

nitrogen into the reduced GO[61] and suppressed the electrical mobility of the graphene. Besides, hydrazine is a highly toxic agent, which limited the application of this preparation. Therefore, other reducing agents were further studied for the GO reduction. For example, Chen *et al.* reported on the efficacy of $NaHSO_3$, $Na_2S.9H_2O$, $Na_2S_2O_3$, $SOCl_2$, and SO_2 for GO reduction.[68] All of these can reduce GO to a certain extent but $NaHSO_3$ and $SOCl_2$ in particular exhibited similar or higher reducing ability to that of hydrazine. However, as illustrated in a study by Li *et al.* GO reduction is usually inhibited by the agglomeration of GO sheets, which leads to poor deoxidation and dispersion of the graphene product, making further fabrication difficult.[63]

Longitudinal Unzipping of Carbon Nanotubes: There has been much interest in creating nanoribbons of graphene, usually unzipping carbon nanotubes through oxidation reactions, for example, by using H_2SO_4 and $KMnO_4$.[70] The oxidized graphene nanoribbons are water soluble, as GO above, and need to be reduced appropriately before further use.[71] Carbon nanotubes can also be unzipped into nanoribbons by etching and sonication.[72] However, the defects in the nanoribbons are difficult to control. In these reported routes, the carbon nanotubes were all fully oxidized. This would be expected to lead to the irregular disintegration of the nanotubes and result in a low yield of nanoribbon with regular edge structures, especially as the oxidization method reported is the same as that for preparing graphite oxide.[70,81] It is therefore mysterious why instead the oxidation results reliably in a uniform unzipping of the nanotubes along a straight line to creates nanoribbons. However, controlling the oxidation of nanotubes and reduction of the unzipped nanoribbons remains a technical challenge.

Intercalation of Graphite: Viculis *et al.* reported a novel method to exfoliate graphite.[73] First, potassium was intercalated into the graphite interlayers. The violent reaction of the intercalated graphite and EtOH generated H_2 which drove the exfoliation of graphene sheets with the assistance of sonication. However, the exfoliation does not give high yields of monolayered graphene as the products often become scrolled to form a tubular phase.[73] This may due to the surface energy imbalance between solvent and exfoliated sheets. There is an opportunity here to develop techniques to improve this preparation route. The mechanism of this exfoliation has also been used in an attempt to prepare graphene nanoribbons from carbon nanotubes.[74,75] Although the claimed yield of the nanoribbons was quite high (100%),[75] atomic force microscopy

(AFM) showed a large proportion of small fragments, which is consistent with the intercalation-driven expansion causing disintegration of the carbon nanotubes.

Chemical Synthesis and Other Methods: Direct chemical synthesis can be an effective way to prepare graphene with controlled size and edge structure. However, as reported by Qian *et al.*[76] chemically synthesized graphene has functionalized edge groups. It remains unclear what the precise effects of these groups are on the properties of the graphene. Although this method is suitable for synthesizing small GQDs, the product yield is quite low. For example, Li's group recently reported the chemical synthesis of functionalized GQDs.[76-79] The size of the obtained GQDs can be controlled well. However, the operation and purification involved in the preparation are quite complex and the final yield of the GQDs is still low (overall yield: *ca.* 1.29%).

Other methods of preparing GQDs include transformation of C_{60} molecules (low yield and un-scalable)[17] and cutting of graphene sheets using electron-beam lithography,[82,83] hydrothermal (including some modified hydrothermal cutting approaches, which will be discussed later)[18,84,85] and electrochemical routes.[19] The transformation of C_{60} and electron-beam lithography cutting are not suitable for the scalable preparation of GQDs. The various other methods suffer from low yield (1-1.6%) while the majority of GQDs created using these methods are multi-layered. Among these methods, the hydrothermal and electrochemical cutting routes are potentially scalable to allow economic preparation of GQDs, although the production yield would have to be improved substantially. Hydrothermal cutting[18,84,85] normally involves three steps to provide GQD product: 1) preparation of GO base on graphite starting material; 2) hydrothermal cutting of the prepared GO; 3) dialysis to separate GQDs from large GO sheets. The electrochemical cutting route[19] follows a similar approach.

As described before, preparation of graphite oxide has been known since the 19th century.[80] The modern interest in graphene has led to much recent interest in the chemical reduction of GO (exfoliated graphite oxide) to obtain large graphene sheets with big size.[61-69] Although strong ultrasonication treatment was used to exfoliate GO sheets before chemical reduction, all these studies showed that the majority product of reduced hydrothermally cut GO were large sheets rather than small GQDs.[61-69] Some GO sheets were found to break down due to over-oxidization and ultrasonication treatment. However, the small dots cut from GO sheets made up a small proportion of

the starting materials, which is the reason for the low yield (ca.1-1.6%)[18,84,85] mentioned above, even after many attempts to modify GO cutting methods.

Recently, Peng[85] and Dong *et al.*[86] reported the preparation of high yield GQDs from carbon fibers and carbon blacks respectively. The claimed yields (*e.g.* 44.5% multi-layered GQDs and 9.0% monolayered GQDs from carbon blacks[86]) of the GQDs are much improved in contrast with that prepared from hydrothermal cutting route. However, Xia *et al.*[87] comment that the collected products are a mixture of GQDs and amorphous carbon QDs. The exact chemical identities of the thin dots prepared using this route should be clarified (*e.g.* further separation of the product for C^{13} NMR analysis/nuclear magnetic resonance analysis). Considering the preparation mechanism makes it is easy to understand the potential difficulties of this route. Both of these preparations are based on the existence of small crystallized carbon domains in the raw material (carbon fibers and carbon blacks). Using strong oxidization and sonication treatment, the small crystallized carbon domains can, in principle, be exfoliated to from thin QDs. Nevertheless, the question here is what happens to the amorphous carbon phase that inevitably exists in large quantities in the raw materials once it is fragmented from the precursor material and dissolved in the collected solution (see Ref. 87 for more comment). Greater clarity would be achieved by experiments to separate the GQDs and amorphous carbon dots.

2.2.2 Preparation of Monolayered BN, WS_2 and MoS_2

Unlike graphene, the preparation of monolayered BN, WS_2 and MoS_2 have not received much attention. Monolayered BN, WS_2 and MoS_2 were prepared recently using a liquid exfoliation.[39] Other methods such as promoted liquid exfoliation method,[88] high-energy electron beam irradiation[89] and CVD[90,91] were also investigated for the preparation of monolayered BN sheets (these methods are also limited in the preparation of monolayered WS_2 and MoS_2 sheets due to uneconomic and unscalable features). Although separation of graphite layers by oxidation can be seen as a scalable preparation route, analogous methods are inapplicable in the case of BN, WS_2 and MoS_2. An alternative route to exfoliate these monolayered materials is the intercalation and exfoliation method,[92] which is similar with that reported by Viculis *et al.*[73] However, as for the QDs of these monolayered BN, WS_2 and MoS_2, the preparation is great undeveloped.

2.3 Potential Applications of the Monolayered Graphene, BN, WS_2 and

MoS_2

Carbon materials such as CNTs, carbon fibers and carbon nanocrystals have been used in electrochemistry because of the good electrical conductivity, high activity of electro-catalyst etc.[93-95] Graphene has a much higher electrical conductivity and surface-to-volume ratio than other materials and, therefore, is potentially well suited to use as an electro-catalyst.[96-97] Due to the good biological compatibility, graphene has also used as biological sensor (DNA).[98] Graphene is an excellent candidate for use in supercapacitors (for energy storage) due to its high surface area-to-volume ratio and high electrical conductivity. In this respect, it is similar to CNTs, which have been used as supercapacitors for many years.[99,100] For example, metal oxide-graphene hybrid nanostructures can be good electrode materials in Li-ion battery.[101] Paek *et al*. studied the use of graphene as the negative electrode in supercapacitors and achieved 810 mAh/g capacity.[102] The high electrical conductivity and transparent character of graphene suggest that many applications of graphene can be expected in other fields. For instance, Xu *et al.* prepared metal (Au, Pt, Pd)/graphene composites for fuel cells (methanol) and found that the graphene resulted in improved cell performance.[103] The effective use of graphene in fuel cells was further confirmed by other studies.[104,105] Graphene is also attractive as a highly transparent and robust alternative to indium tin oxide (ITO), which is suffering from indium resource limitation, in order to improve the efficiency of solar cells.[106,107] Other recent studies suggest other potential applications of graphene, including as a structural material, as a catalyst, in drug delivery and as a gas sensor.[108-113]

The potential applications of monolayered BN, WS_2 and MoS_2 sheets are also interesting. BN has a wide range of applications such as a deep ultraviolet emitter, a transparent membrane, dielectric layers or for protective coatings.[33,114] Theoretically, monolayered BN sheets can reproduce the unusual electronic properties of 'armchair'-edged graphene (***Figure 2-2***), have new electronic band gaps introduced and be manipulated into a half-metal electronic configuration by controlling the edge structure and defect centres.[34-37] Further reduction of the lateral size of monolayered BN sheets should allow these defect dependent properties become much more evident, providing a new route to broad the properties and applications.[32-37] Monolayered WS_2 and MoS_2 find potential application in the fields of optoelectronics and energy harvesting.[43-45] Similar to the monolayered BN QDs, edge dependent properties in small monolayered WS_2 and MoS_2 sheets may also pave the way for many new interesting properties and applications (*e.g.* optoelectronics and bio-imaging), which need further development.

However, all of these potential applications first require the preparation of monolayered materials with small size to be addressed.

References and Notes

[1] T. E. Brown, H. E. LeMay, B. E. Bursten, C. Murphy and P. Woodward, Chemistry: The Central Science (11th Ed.). **2009**, Prentice Hall.

[2] M. S. Dresselhaus and G. Dresselhaus, Intercalation Compounds of Graphite. *Adv. Phys.* **2002**, *51*, 1-186.

[3] O. A. Shenderova, V. V. Zhirnov and D. W. Brenner, Carbon Nanostructures. *Crit. Rev. Solid State Mater. Sci.* **2002**, *27*, 227-356.

[4] A. H. Castro Neto, F. Guinea, N. M. R. Peres, K. S. Novoselov and A. K. Geim, The Electronic Properties of Graphene. *Rev. Mod. Phys.* **2009**, *81*, 109-162.

[5] A. K. Geim and K. S. Novoselov, The Rise of Graphene. *Nat. Mat.* **2007**, *6*, 183-191.

[6] K. S. Novoselov, A. K. Geim, S. V. Morozov, D. Jiang, M. I. Katsnelson, I. V. Grigorieva, S. V. Dubonos and A. A. Firsov, Two-Dimensional Gas of Massless Dirac Fermions in Graphene. *Nature* **2005**, *438*, 197-200.

[7] Y. Zhang, Y.-W. Tan, H. L. Stormer and P. Kim, Experimental Observation of the Quantum Hall Effect and Berry's Phase in Graphene. *Nature* **2005**, *438*, 201-204.

[8] D. Nelson, D. R. Piran and S. Weinberg, *Statistical Mechanics of Membranes and Surfaces* **2004**, (World Scientific, Singapore).

[9] A. K. Geim and K. S. Novoselov, The Rise of Graphene. *Nat. Mat.* **2007**, *6*, 183-191.

[10] L. E. Brus, Quantum Crystallites and Nonlinear Optics. Appl. Phys. A **1991**, 53, 465-474.

[11] A. L. Efros and M. Rosen, The Electronic Structure of Semiconductor Nanocrystals. *Annu. Rev. Mater. Sci.* **2000**, *30*, 475-521.

[12] L. Li, G. Wu, G. Yang, J. Peng, J. Zhao and J. Zhu, Focusing on Luminescent Graphene Quantum Dots: Current Status and Future Prespectives. *Nanoscale* **2013**, *5*, 4015-4039.

[13] L. Li and X. Yan, Colloidal Graphene Quantum Dots. *J. Phys. Chem. Lett.* **2010**, *1*, 12572-12576.

[14] J. Shen, Y. Hua, X. Yang and C. Li, Graphene Quantum Dots: Emergent Nanolights for Bioimaging, Sensors, Catalysis and Photovoltaic Devices. *Chem. Commun.* **2012**, *48*, 3686-2699.

[15] G. Konstantatos, M. Badioli, L. Gaudreau, J. Osmond, M. Bernechea, F. P. G. de Arquer, F. Gatti, and F. H. L. Koppens, Hybrid Graphene–Quantum Dot Phototransistors with Ultrahigh Gain. *Nat. Nanotechnol.* **2012**, *7*, 363-368.

[16] D. I. Son, B. W. Kwon, D. H. Park, W.-S. Seo, Y. Yi, B. Angadi, C.-L. Lee and W. K. Choi, Emissive ZnO–graphene Quantum Dots for White-Light-Emitting Diodes. *Nat. Nanotechnol.* **2012**, *7*, 465-471.

[17] J. Lu, P. S. E. Yeo, C. K. Gan, P. Wu and K. P. Loh, Transforming C_{60} Molecules into Graphene Quantum Dots. *Nat. Nanotechnol.* **2011**, *6*, 247-252.

[18] D. Pan, J. Zhang, Z. Li and M. Wu, Hydrothermal Route for Cutting Graphene Sheets into Blue-luminescent Graphene Guantum Dots. *Adv. Mater.* **2010**, *22*, 734-738.

[19] Y. Li, Y. Hu, Y. Zhao, G. Shi, L. Deng, Y. Hou and L. Qu, An Electrochemical Avenue to Green-luminescent Graphene Quantum Dots as Potential Electron-acceptors for Photovoltaics. *Adv. Mater.* **2011**, *23*, 776-780.

[20] Y.-W. Son, M. L. Cohen and S. G. Louie, Energy Gaps in Graphene Nanoribbons. *Phys. Rev. Lett.* **2006**, *97*, 216803.

[21] L. A. Ponomarenko, F. Schedin, M. I. Katsnelson, R. Yang, E. W. Hill, K. S. Novoselov and A. K. Geim, Chaotic Dirac Billiard in Graphene Quantum Dots. *Science* **2008**, *320*, 356-358.

[22] R. T. Paine and C. K. Narula, Synthetic Routes to Boron Nitride. *Chem. Rev.* **1990**, *90*, 73-91.

[23] L. Lin, Z. Li, Y. Zheng and K. Wei, Synthesis and Application in the CO Oxidation Conversion Reaction of Hexagonal Boron Nitride with High Surface Area. *J. Am. Ceram. Soc.* **2009**, *92*, 1347-1349.

[24] J. M. Carrapichano, J. R. Gomes and R. F. Silva, Tribological Behaviour of Si_3N_4-BN Ceramic Materials for Dry Sliding Applications. *Wear* **2002**, *253*, 1070-1076.

[25] T. Saito, T. Hosoe and F. Honda, Chemical Wear of Sintered Si_3N_4, hBN and Si_3N_4-hBN Composites by Water Lubrication. *Wear* **2001**, *247*, 223-230.

[26] Y. Lin and W. Connell, Advances in 2D Boron Nitride Nanostructures: Nanosheets, Nanoribbons, Nanomeshes, and Hybrids with Graphene. *Nanoscale* **2012**, *4*, 6908-6939.

[27] W. Han, L. Wu, Y. Zhu, K. Watanabe and T. Taniguchi, Structure of Chemically Derived Mono- and Few-Atomic-Layer Boron Nitride Sheets. *App. Phys. Lett.* **2008**, *93*, 223103.

[28] W. Paszkowicz, J. B. Pelka, M. Knapp, T. Szyszko and S. Podsiadlo, Lattice Parameters and Anisotropic Thermal Expansion of Hexagonal Boron Nitride in the 10-297.5 K Temperature Range. *Appl. Phys. A: Mater. Sci. Process.* **2002**, *75*, 431-435.

[29] R S. Pease, An X-ray Study of Boron Nitride. *Acta Crystallogr.* **1952**, *6*, 356–361.

[30] K. Watanabe, T. Taniguchi and H. Kanda, Direct-Bandgap Properties and Evidence for Ultraviolet Lasing of Hexagonal Boron Nitride Single Crystal. *Nat. Mat.* **2004**, *3*, 404–409.

[31] V. L. Solozhenko, A. G. Lazarenko, J. P. Petitet and A. V. Kanaev, Bandgap Energy of Graphite-Like Hexagonal Boron Nitride. *J. Phys. Chem. Solids* **2001**, *62*, 1331-1334.

[32] M. Terrones, J. M. Romo-Herrera, E. Cruz-Silva, F. López-Urías, E. Muñoz-Sandoval, J. J. Velázquez-Salazar, H. Terrones, Y. Bando and D. Golberg, Pure and Doped Boron Nitride Nanotubes. *Mater. Today* **2007**, *10*, 30-38.

[33] Y. Kubota, K. Watanabe, O. Tsuda and T. Taniguchi, Deep Ultraviolet Light-Emitting Hexagonal Boron Nitride Synthesized at Atmospheric Pressure. *Science* **2007**, *317*, 932-934.

[34] M. Terrones, J.-C. Charlier, A. Gloter, E. Cruz-Silva, E. Terrés, Y. B. Li, A. Vinu, Z. Zanolli, J. M. Dominguez, H. Terrones, Y. Bando, and D. Golberg, Experimental and Theoretical Studies Suggesting the Possibility of Metallic Boron Nitride Edges in Porous Nanourchins. *Nano Lett.* **2008**, *8*, 1026-1032.

[35] B. Huang, H. Lee, B.-L. Gu, F. Liu and W. Duan, Edge Stability of BN Sheets and Its Application for Designing Hybrid BNC Structures. *Nano Research* **2012**, *5*, 62-72.

[36] A. Lopez-Bezanilla, J. Huang, H. Terrones and B. G. Sumpter, Boron Nitride Nanoribbons Become Metallic. *Nano Lett.* **2011**, *11*, 3267-3273.

[37] C. Tang, Y. Bando, C. Zhi and D. Golberg, Boron-Oxygen Luminescence Centres in Boron-nitrogen Systems. *Chem. Commun.* **2007**, 4599-4601

[38] A. Molina-Sánchez and L. Wirtz, Phonos in Single-Layer and Few-Layer MoS_2 and WS_2. *Phys. Rev. B* **2011**, *84*, 155413.

[39] J. N. Coleman, M. Lotya1, A. O'Neill1, S. D. Bergin, P. J. King, U. Khan, K. Young, A. Gaucher, S. De, R. J. Smith, I. V. Shvets, S. K. Arora, G. Stanton, H.-Y. Kim, K. Lee, G. T. Kim, G. S. Duesberg, T. Hallam, J. J. Boland, J. Wang, J. F. Donegan, J. C. Grunlan, G. Moriarty, A. Shmeliov, R. J. Nicholls, J. M. Perkins, E. M.

Grieveson, K, Theuwissen, D. W. McComb, P. D. Nellist and V. Nicolosi, Two-Dimensional Nanosheets Produced by Liquid Exfoliation of Layered Materials. *Science* **2011**, *331*, 568-571.

[40] K. F. Mak, C. Lee, J. Hone, J. Shan and T. F. Heinz, Atomically Thin MoS_2: a New Direct-Gap Semiconductor. *Phys. Rev. Lett.* **2010**, *105*, 136805.

[41] H. R. Gutiérrez, N. Perea-López, A. L. Elías, A. Berkdemir, B. Wang, R. Lv, F. López-Urías, V. H. Crespi, H. Terrones and M. Terrones, Extraordinary Room-Temperature Photoluminescence in Triangular WS_2 Monolayers. *Nano Lett.* **2012**, *13*, 3447-3454.

[42] A. R. Botello-Méndez, F. López-Urías, M. Terrones and H. Terrones, Metallic and Ferromagnetic Edges in Molybdenum Disulfide Nanoribbons. *Nanotechnology* **2009**, *20*, 325703.

[43] B. Radisavljevic, A. Radenovic, J. Brivio, V. Giacometti and A. Kis, Single-Layer MoS_2 Transistors. *Nat. Nanotechnol.* **2011**, *6*, 147-150.

[44] W. Choi, M. Y. Cho, A. Konar, J. H. Lee, G.-B. Cha, S. C. Hong, S. Kim, J. Kim, D. Jena, J. Joo and S. Kim, High-Detectivity Multilayer MoS_2 Phototransistors with Spectral Response from Ultraviolet to Infrared. *Adv. Mater.* **2012**, *24*, 5832-5836.

[45] W. S. Hwang, M. Remskar, R. Yan, V. Protasenko, K. Tahy, S. D. Chae, P. Zhao, A. Konar, H. Xing, A. Seabaugh, and D. Jena, Transistors with Chemically Synthesized Layered Semiconductor WS_2 Exhibiting 10^5 Room Temperature Modulation and Ambipolar Behavior. *Appl. Phys. Lett.* **2012**, *101*, 013107.

[46] K. S. Novoselov, A. K. Geim, S. V. Morozov, D. Jiang, Y. Zhang, S. V. Dubonos, I. V. Grigorieva and A. A. Firsov, Electric Field Effect in Atomically Thin Carbon Films. *Science* **2004**, *306*, 666-669.

[47] I. Forbeaux, J. M. Themlin and J. M. Debever, Heteroepitaxial Graphite on 6H-SiC(0001). *Phys. Rev. B* **1998**, *58*, 16396.

[48] J. Coraux, A. T. N'Diaye, C. Busse and T. Michely, Structural Coherency of Graphene on Ir(111). *Nano Lett.* **2008**, *8*, 565-570.

[49] A. N. Obraztsov, Chemical Vapour Deposition: Making Graphene on a Large Scale. *Nat. Nanotechnol.* **2009**, *4*, 212-213.

[50] A. L. V. de Parga, F. Calleja, B. Borca, M. C. G. Passeggi Jr., J. J. Hinarejos, F.Guinea and R. Miranda, Periodically Rippled Graphene: Growth and Spatially Resolved Electronic Structure. *Phys. Rev. Lett.* **2008**, *100*, 056807.

[51] C. Mattevi, H. Kim, M. Chhowalla, A Review of Chemical Vapour Deposition of Graphene on Copper. *J. Mater. Chem.* **2011**, *21*, 3324-3334.

[52] K. S. Kim, Y. Zhao, H. Jang, S. Y. Lee, J. M. Kim, K. S. Kim, J. H. Ahn, P. Kim, J. Y. Choi and B. H. Hong, Large-Scale Pattern Growth of Graphene Films for Stretchable Transparent Electrodes. *Nature* **2009**, *457*, 706-710.

[53] X. S. Li, W.W. Cai, J. H. An, S. Y. Kim, J. Nah, D. X. Yang, R. Piner, A. Velamakanni, I. Jung, E. Tutuc, S. K. Banerjee, L. Colombo and R. S. Ruoff, Large-Area Synthesis of High-Quality and Uniform Graphene Films on Copper Foils. *Science* **2009**, *324*, 1312-1314.

[54] Y. Lee, S. Bae, H. Jang, S. Jang, S. Zhu, S. H. Sim, Y. I. Song, B. H. Hong and J. H.Ahn, Wafer-Scale Synthesis and Transfer of Graphene Films. *Nano Lett.* **2010**, *10*, 490-493.

[55] C. Berger, Z. Song, T. Li, X. Li, A. Y. Ogbazghi, R. Feng, Z. Dai, A. N. Marchenkov, E. H. Conrad, P. N. First and W. A. de Heer, Ultrathin Epitaxial Graphite: 2D Electron Gas Properties and a Route toward Graphene-based Nanoelectronics. *J. Phys. Chem. C* **2004**, *108*, 19912-19916.

[56] C. Berger, Z. Song, X. Li, X. Wu, N. Brown, C. Naud, D. Mayou, T. Li, J. Hass, A. N. Marchenkov, E. H. Conrad, P. N. First and W. A. deHeer, Electronic Confinement and Coherence in Patterned Epitaxial Graphene. *Science* **2006**, *312*, 1191-1196.

[57] V. Borovikov and A. Zangwill, Step-Edge Instability During Epitaxial Growth of Graphene. *Phys. Rev. B* **2009**, *80*, 121406.

[58] A. Charrier, A. Coati, T. Argunova, F. Thibaudau, Y. Garreau, R. Pinchaux, I. Forbeaux, J. M. Debever, M. Sauvage-Simkin and J. M. Themlin, Solid-State Decomposition of Silicon Carbide for Growing Ultra-Thin Heteroepitaxial Graphite Films. *J. Appl. Phys.* **2002**, *92*, 2479.

[59] Y, Hernandez, V. Nicolos, M. Lotya, F. M. Blighe, Z. Sun, S. De, I. T. McGovern, B. Holland, M. Byrne, Y. K. Gun'Ko, J. J. Boland, P. Niraj, G. Duesberg, S. Krishanmurthy, R. Goodhue, H. Hutchison, V. Scardaci, A. C. Ferrari and J. N. Coleman, High-Yield Production of Graphene by Liquid-Phase Exfoliation of Graphite. *Nat. Nanotechnol.* **2008**, *3*, 563-568.

[60] B. B. Athanasios, G. Vasilios, Z. Radek, A. S. Theodore and K. S. Athanasios, Liquid-Phase Exfoliation of Graphite Towards Solubilized Graphenes. *Small* **2009**, *5*, 1841-1845.

[61] S. Stankovich, D. A. Dikin, R. D. Piner, K. A. Kohlhaas, A. Kleinhammes, Y. Jia, Y. Wu, S. T. Nguyen and R. S. Ruoff, Synthesis of Graphene-Based Nanosheets *via* Chemical Reduction of Exfoliated Graphite Oxide. *Carbon* **2007**, *45*, 1558-1565.

[62] L. Zhang, J. Liang, Y. Huang, Y. Ma, Y. Wang and Y. Chen, Size-Controlled Synthesis of Graphene Oxide Sheets on a Large Scale Using Chemical Exfoliation. *Carbon* **2009**, *47*, 3365-3368.

[63] D. Li, M. B. Müller, S. Gilje, R. B. Kaner and G. G. Wallace, Processable Aqueous Dispersions of Graphene Nanosheets. *Nat. Nanotechnol.* **2008**, *3*, 101-105.

[64] M. Zhou, Y. Wang, Y. Zhai, J. Zhai, W. Ren, F. Wang and S. Dong, Controlled Synthesis of Large-Area and Patterned Electrochemically Reduced Graphene Oxide Films. *Chem. Eur. J.* **2009**, *15*, 6116-6120.

[65] J. M. Michael, J. Li, D. H. Adamson, H. C. Schniepp, A. A. Abdala, J. Liu, H. A. Margarita, L. M. David, C. Roberto, K. P. Robert and A. A. Ilhan, Single Sheet Functionalized Graphene by Oxidation and Thermal Expansion of Graphite. *Chem. Mater.* **2007**, *19*, 4396-4404.

[66] P. Steurer, R. Wissert, R. Thomann and R. Mulhaupt, Functionalized Graphenes and Thermoplastic Nanocomposites Based upon Expanded Graphite Oxide. *Macromol. Rapid Commun.* **2009**, *30*, 316-327.

[67] Y. Hu, J. Jin, H. Zhang, P. Wu and C. Cai, Graphene: Synthesis, Functionalization and Applications in Chemistry. *Acta. Phys. Chim. Sin.* **2010**, *26*, 2073-2086.

[68] W. Chen, L. Yan and P. R. Bangal, Chemical Reduction of Graphene Oxide to Graphene by Sulfur-Containing Compounds. *J. Phys. Chem. C* **2010**, *114*, 19885-19890.

[69] S. Dubin, S. Gilje, K. Wang, V. C. Tung, K. Cha, A. S. Hall, J. Farrar, R. Varshneya, Y. Yang and R. B. Kaner, A One-Step, Solvothermal Reduction Method for Producing Reduced Graphene Oxide Dispersions in Organic Solvents. *ACS Nano* **2010**, *4*, 3845-3852.

[70] D. V. Kosynkin, A. L. Higginbotham, A. Sinitskii, J. R. Lomeda, A. Dimiev, B. K. Price and J. M. Tour, Longitudinal Unzipping of Carbon Nanotubes to Form Graphene Nanoribbons. *Nature* **2009**, *458*, 872-876.

[71] D. B. Shinde, J. Debgupta, A. Kushwaha, M. Aslam and V. K. Pillai, Electrochemical Unzipping of Multi-Walled Carbon Nanotubes for Facile Synthesis of High-Quality Graphene Nanoribbons. *J. Am. Chem. Soc.* **2011**, *133*, 4168-4171.

[72] L. Jiao, X. Wang, G. Diankov, H. Wang and H. Dai, Facile Synthesis of High-Quality Graphene Nanoribbons. *Nat. Nanotechnol.* **2010**, *5*, 321-325.

[73] L. M. Viculis, J. J. Mack and R. B. Kaner, A Chemical Route to Carbon Nanoscrolls. *Science* **2003**, *299*, 1361.

[74] A. G. Cano-Márquez, F. J. Rodríguez-MacÍas, J. Campos-Delgado, C. G. Espinosa-González, F. Tristán-López, D. Ramírez-González, D. A. Cullen, D. J. Smith, M. Terrones and Y. I. Vega-Cantú, Ex-MWNTs:

Graphene Sheets and Ribbons Produced by Lithium Intercalation and Exfoliation of Carbon Nanotubes. *Nano Lett.* **2009**, *9*, 1527-1533.

[75] D. V. Kosynkin, W. Lu, A. Sinitskii, G. Pera, Z. Sun and J. M. Tour, Highly Conductive Graphene Nanoribbons by Longitudinal Splitting of Carbon Nanotubes using Potassium Vapor. *ACS Nano* **2011**, *5*, 968-974.

[76] H. L. Qian, F.Negri, C. R. Wang and Z. H. Wang, Fully Conjugated Tri(perylene bisimides): an Approach to the Construction of n-type Graphene Nanoribbons. *J. Am. Chem. Soc.* **2008**, *130*, 17970-17976.

[77] X. Yan, X. Cui and L. Li, Synthesis of Large, Stable Colloidal Graphene Quantum Dots with Tunable Size. *J. Am. Chem. Soc.* **2010**, *132*, 59445945.

[78] X. Yan, X. Cui, B. Li and L. Li, Large, Solution-Processable Graphene Quantum Dots as Light Absorbers for Photovoltaics. *Nano Lett.* **2010**, 1*0*, 1869-1873.

[79] I. P. Hamilton, B. Li, X. Yan and L. Li, Alignment of Colloidal Graphene Quantum Dots on Polar Surfaces. *Nano Lett.* **2011**, *11*, 1524-1529.

[80] B. Brodie, On the Atomic Weight of Graphite. *Phil. Trans.* **1859**, *149*, 249-259.

[81] W. S Hummers, Jr., and R. E. Offeman, Preparation of Graphitic Oxide. *J. Am. Chem. Soc.* 1958, *80*, 1339.

[82] A. K. Geim and K. S. Novoselov, The Rise of Graphene. *Nat. Mat.* **2007**, *6*, 183-191.

[83] C. Stampfer, J. Güttinger, F. Molitor, D. Graf, T. Ihn and K. Ensslin, Tunable Coulomb Blockade in Nanostructured Graphene. *Appl. Phys. Lett.* **2008**, *92*, 012102.

[84] S. Zhu, J. Zhang, C. Qiao, S. Tang, Y. Li, W. Yuan, B. Li, L. Tian, F. Liu, R. Hu, H. Gao, H. Wei, H. Zhang, H. Sun and B. Yang, Strongly Green-Photoluminescent Graphene Quantum Dots for Bioimaging Applications. *Chem. Commun.* **2011**, *47*, 6858-6860.

[85] J. Peng, W. Gao, B. K. Gupta, Z. Liu, R. Romero-Aburto, L. Ge, L. Song, L. B. Alemany, X. Zhan, G. Gao, S. A. Vithayathil, B. A. Kaipparettu, A. A. Marti, T. Hayashi, J. Zhu and P. M. Ajayan, Graphene Quantum Dots Derived from Carbon Fibers. *Nano Lett.* **2012**, *12*, 844-849.

[86] Y. Dong, C. Chen, X. Zheng, L. Gao, Z. Cui, H. yang, C. Guo and Y. Chi, C. Li, One-Step and High Yield Simultaneous Preparation of Single- and Multi-Layer Graphene Quantum Dots from CX-72 Carbon Black. *J. Mater. Chem.* **2012**, *22*, 8764-8766.

[87] X. Xia and Y. Zheng, Comment on "One-Step and High Yield Simultaneous Preparation of Single- and Multi-Layer Graphene Quantum Dots from CX-72 Carbon Black". *J. Mater. Chem.* **2012**, *22*, 21776.

[88] Y. Lin, T. V. Williams, T.-B. Xu, W. Cao, H. E. Elsayed-Ali and J. W. Connell, Aqueous Dispersions of Few-Layered and Monolayered Hexagonal Boron Nitride Nanosheets from Sonication-Assisted Hydrolysis: Critical Role of Water. *J. Phys. Chem. C* **2011**, *115*, 2679-2685.

[89] C. Jin, F. Lin, K. Suenaga and S. Iijima, Fabrication of a Freestanding Boron Nitride Single Layer and Its Defect Assignments. *Phys. Rev. Lett.* **2009**, *102*, 195505.

[90] L. Song, L. Ci, H. Lu, P. B. Sorokin, C. Jin, J. Ni, A. G. Kvashnin, D. G. Kvashnin, J. Lou, B. I. Yakobson, and P. M. Ajayan, Large Scale Growth and Characterization of Atomic Hexagonal Boron Nitride Layers. *Nano Lett.* **2010**, *10*, 3209-3215.

[91] Y. Shi, C. Hamsen, X. Jia, K. K. Kim, A. Reina, M. Hofmann, A. L. Hsu, K. Zhang, H. Li, Z.-Y. Juang, M. S. Dresselhaus, L.-J. Li and J. Kong, Synthesis of Few-Layer Hexagonal Boron Nitride Thin Film by Chemical Vapor Deposition. *Nano Lett.* **2010**, *10*, 4134-4139.

[92] H. S. S. R. Matte, A. Gomathi, A. K. Manna, D. J. Late, R. Datta, S. K. Pati and C. N. R. Rao, MoS_2 and WS_2 Analogues of Graphene. *Angew. Chem. Int. Ed.* **2010**, *49*, 4059-4062.

[93] M. Musameh, J. Wang, A. Merkoci and Y. Lin, Low-Potential Stable NADH Detection at Carbon-Nanotube-Modified Glassy Carbon Electrodes. *Electrochem. Commun.* **2002**, *4*, 743-746.

[94] L. N. Wu, X. J. Zhang and H. X. Ju, Detection of NADH and Ethanol Based on Catalytic Activity of Soluble Carbon Nanofiber with Low Overpotential. *Anal. Chem.* **2007**, *79*, 453-458.

[95] M. Zhou, J. Ding, L. P. Guo and Q. K. Shang, Electrochemical Behavior of L-cysteine and Its Detection at Ordered Mesoporous Carbon-Modified Glassy Carbon Electrode. *Anal. Chem.* **2007**, *79*, 5328.

[96] N. G. Shang, P. Papakonstantinou, M. McMullan, M. Chu, A. Stamboulis, A. Potenza, S. S. Dhesi and H. Marchetto, Graphene Nanoflake Films with Sharp Edge Planes. *Adv. Funct. Mater.* **2008**, *18*, 3506-3514.

[97] L. H.Tang, Y. Wang, Y. M. Li, H. B. Feng, J. Lu and J. H. Li, Preparation, Structure, and Electrochemical Properties of Reduced Graphene Sheet Films. *Adv. Funct. Mater.* **2009**, *19*, 2782-2789.

[98] M. Zhou, Y. M. Zhai and S. Dong, Electrochemical Sensing and Biosensing Platform Based on Chemically Reduced Graphene Oxide. *J. Anal. Chem.* **2009**, *81*, 5603-5613.

[99] E. Frackowiak and F. Beguin, Electrochemical Storage of Energy in Carbon Nanotubes and Nanostructured Carbons. *Carbon* **2002**, *40*, 1775-1787.

[100] E. Frackowiak, S. Gautier, H. Gaucher, S. Bonnamy and F. Beguin, Electrochemical Storage of Lithium in Multiwalled Carbon Nanotubes. *Carbon* **1999**, *37*, 61-69.

[101] D.Wang, D. Choi, J. Li, Z. Yang, Z. Nie, R. Kou, D. Hu, C. Wang, L. V. Saraf, J. Zhang, I. A. Aksay and J. Liu, Self-Assembled TiO_2–Graphene Hybrid Nanostructures for Enhanced Li-Ion Insertion. *ACS Nano* **2009**, *3*, 907-914.

[102] S. M. Paek, E. J. Yoo and I. Honma, Enhanced Cyclic Performance and Lithium Storage Capacity of SnO_2/Graphene Nanoporous Electrodes with Three-Dimensionally Delaminated Flexible Structure. *Nano Lett.* **2009**, *9*, 72-75.

[103] C. Xu, X. Wang and J. W. Zhu, Graphene-Metal Particle Nanocomposites. *J. Phys. Chem. C* **2008**, *112*, 19841-19845.

[104] R. Kou, Y. Y. Shao, D. H. Wang, M. H. Engelhard, J. H. Kwak, J. Wang, V. V. Viswanathan, C. M. Wang, Y. H. Lin, Y. Wang, I. A. Aksay and J. Liu, Enhanced Activity and Stability of Pt Catalysts on Functionalized Graphene Sheets for Electrocatalytic Oxygen Reduction. *Electrochem. Commun.* **2009**, *11*, 954-957.

[105] B. Seger and P. V. Kamat, Electrocatalytically Active Graphene-Platinum Nanocomposites. Role of 2-D Carbon Support in PEM Fuel Cells. *J. Phys. Chem. C* **2009**, *113*, 7990-7995.

[106] J. C. Scott, J. H. Kaufman, P. J. Brock, R. Dipietro, J. Salem and J. A. Goitia, Degradation and Failure of MEH-PPV Light-Emitting Diodes. *J. Appl. Phys.* **1996**, *79*, 2745.

[107] H. A. Becerril, J. Mao, Z. F. Liu, R. M. Stoltenberg, Z. N. Bao and Y. S. Chen, Evaluation of Solution-Processed Reduced Graphene Oxide Films as Transparent Conductors. *ACS Nano* **2008**, *2*, 463-470.

[148] T. O. Wehling, K. S. Novoselov, S. V. Morozov, E. E. Vdovin, M. I. Katsnelson, A. K. Geim and A. I. Lichtenstein, Molecular Doping of Graphene. *Nano Lett.* **2008**, *8*, 173-177.

[109] X. Y. Yang, X. Y. Zhang, Z. F. Liu, Y. F. Ma, Y. Huang and Y. S. Chen, High-Efficiency Loading and Controlled Release of Doxorubicin Hydrochloride on Graphene Oxide. *J. Phys. Chem. C* **2008**, *112*, 17554-17558.

[110] X. L. Pan, Z. L. Fan, W. Chen, Y. J. Ding, H. Y. Luo and X. H. Bao, Enhanced Ethanol Production Inside Carbon-Nanotube Reactors Containing Catalytic Particles. *Nat. Mat.* **2007**, *6*, 507-511.

[111] W. Chen, Z. L. Fan, X. L. Pan and X. H. Bao, Effect of Confinement in Carbon Nanotubes on the Activity of Fischer-Tropsch iron Catalyst. *J. Am. Chem. Soc.* **2008**, *130*, 9414-9419.

[112] A. Mastalir, Z. Kiraly, M. Benko and I. Dekany, Graphite Oxide as a Novel Host Material of Catalytically Active Pd Nanoparticles. *Catal. Lett.* **2008**, *124*, 34-38.

[113] Z. Liu, J. T. Robinson, X. M. Sun, H and J. Dai, PEGylated Nanographene Oxide for Delivery of Water-Insoluble Cancer Drugs. *J. Am. Chem. Soc.* **2008**, *130*, 10876-10877.

[114] T. Sugino and T. Tai, Dielectric Constant of Boron Nitride Films Synthesized by Plasma-Assisted Chemical Vapor Deposition. *Jpn. J. Appl. Phys.* Part 2 **2000**, *39* (11A), L1101–L1104.

Chapter III. Analysis Techniques and Raw Materials

3.1 Fourier Transform Infrared (FT-IR) Spectroscopy[1,2]

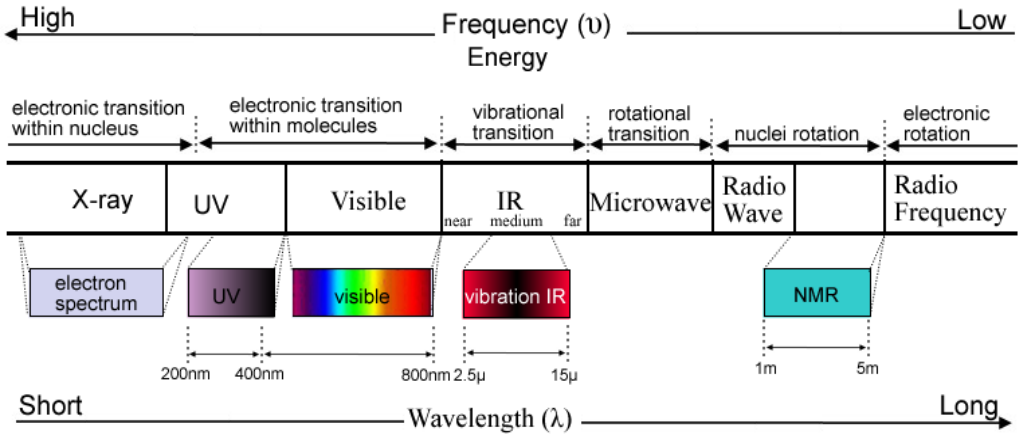

Figure 3-1. Different transitions and corresponding wavelength distribution of the material.

Fourier transform infrared (FT-IR) spectroscopy is an approach used to obtain infrared spectra of absorption, emission, photoconductivity of a solid, liquid or gas. ***Figure 3-1*** shows the various possible transitions in atoms and molecules as well as their associated characteristic wavelength distributions. Molecular vibrational transitions occur due to a molecule interacting with a photon of wavelength, λ, usually in the mid-IR range, *i.e.* 2.5<λ<15.4 μm (4000>wave numbers>650 cm^{-1}). The vibration modes include stretch vibration (bond length changes) and flexible vibration (bending deformation). This molecular vibrational energy can be calculated using*:*

$$\upsilon = \frac{1}{2\pi c}\sqrt{\frac{k}{\mu}} \qquad (eq.\ 3\text{-}1)$$

where *k, μ* and *c* represent the bond spring constant, reduced mass and *in vacuo* light speed, respectively. The vibrational energy can be further transformed to wavenumbers (normally used in FT-IR spectra) using:

$$\upsilon = h \times f = h \times \frac{c}{\lambda} = 100h \times c \times n \qquad (eq.\ 3\text{-}2)$$

where h, f, λ, and n represtnts the Planck constant, frequency, wavelength and wavenumber, respectively. Therefore, the wavenumber (n) in FT-IR can be calculated using:

$$n = \frac{1}{200h\pi c^2}\sqrt{\frac{k}{\mu}} \qquad (eq.\ 3\text{-}3)$$

The reduced mass μ can be further calculated in a simplified A-B molecular system as:

$$\mu = m_A \times m_B /(m_A + m_B) \qquad (eq.\ 3\text{-}4)$$

where m_i is the mass of atom i. The difference in characteristic molecular vibrational energy between materials offers a simple way to distinguish them. Unfortunately, the application of FT-IR techniques is limited because not all the molecular structures are IR active (have IR vibrations). An IR active structure must have an asymmetric dipole moment and thus can absorb or emit photons of energy characteristic to the vibrational transitions. Therefore, some molecules (*e.g.* H_2, O_2, N_2) are IR inactive because no dipole moment exists. In this case, other analysis techniques should be further introduced to determine the chemical structure (*e.g.* Raman spectroscopy).

For IR active materials, FT-IR analysis allows the basic structure (*e.g.* C=C and –C-C in graphene) of a material to be analyzed, particularly if the chemical composition is already known. Besides, vibrational spectra and their changes can also be used to determine special information of the material. To understand changes in vibrational energies, we need to know that every structure (chemical bond) has characteristic vibrational frequencies that are affected by inductive effects, conjugate effects, Fermi resonance, hydrogen bond effect and vibrational coupling.[1,2] Recognising these effects is imperative for understanding the effect of changes in molecular structure. For example, the FT-IR vibrations of aromatic C=C/C-C of graphene and graphite was found at around 1640 cm^{-1}. However, in graphene oxide (GO), this vibration is shifted to 1624 cm^{-1}.[3] As we know, during the oxidization of graphite and graphene, the oxygen-containing groups are introduced into the edge and plane of the graphene layer. This is accompanied by the chemical hybridization of carbon changing from sp^2 C-C=C-C to sp^3 C-C. The bond spring constant (k) therefore weakens after oxidization, which reduces the quantum of vibrational energy (and the wavenumber). Similarly, due to the small size of the graphene quantum dots (GQDs), even with oxygen-containing groups mainly attached to the edge of the dot, this kind of shift is also evident. As for the monolayered boron nitride (BN) QDs, the oxygen doping (*e.g.* formation of N=B-O-) may also lead to vibrational shift. However, in this case, only energy (or wavenumber) increases are

found as the inductive effects (electron shifted from O to B=N as the electronegativity of O higher than that of B) make the bond spring constant slight higher than that of pure BN (see ***Section 7.3.2*** in ***Chapter VII***). Clearly, based on the vibration changes, we can qualitatively know the material's structure. This will be very useful for the following analysis and study.

Not all the apparent vibrational changes or features can always be explained precisely by the effects described above. Other external effects caused by, for example, diluents or instrument resolution, can be significant and must be taken into account. Furthermore, the chemical structure of a material should also be further confirmed with other techniques.

In this thesis, the FT-IR tests of all the samples were performed on a commercial PerkinElmer Spectrum 2000 spectrometer by using pressed mixture (KBr and resultant product disks). Except the BN and graphene QDs, all the other samples were prepared by mixturing solid samples (or dried suspensions) and appropriate amounts of KBr (~ 99 wt% ratio of the mixture), which were pressed in a die to form a thin pellet sample for the FT-IR test. As for BN and graphene QDs, one drop of the concentrated QDs solutions were mixed with appropriate amounts of KBr (~ 99 wt% ratio of the mixture) and then oven dried. The resultant dry mixture was pressed in a die to form a thin pellet sample for the FT-IR test.

3.2 Raman Spectroscopy[4]

Raman spectroscopy is a technique used to measure the characteristic Stokes Raman shift (see ***Figure 3-2***) of the material. When a photon interacts with a material, the resulting scattering can be either elastic and inelastic. Elastic scattering (or 'Rayleigh' scattering) doesn't involve energy exchange between the photon and specimen (only the photon direction is changed). This is in contrast to inelastic scattering (or 'Raman' scattering) which describes photon-matter interactions in which energy is exchanged; *i.e.* the wavelength of the scattered photon is changed and the material becomes either excited or relaxed. This energy change can be described as, first, the optical excitation of the material (see ***Figure 3-2***) from a low lying state A to a higher lying virtual state and then, second, from the virtual state to a (real) low lying state B again, accompanied by re-emission (scattering) of the photon. When state A and state B are different in energy, then the energy (and wavelength) of the scattered photon will also have changed. When the final state B has a greater energy than initial state A, the energy of the scattered

photon will be reduced and the difference transferred to molecular vibration (Stokes Raman in ***Figure 3-2***). The specific energy differences allow different materials to be distinguished. In ***Figure 3-2***, the anti-Stokes Raman show an opposite energy shift with that of Stokes Raman and generally not used in the Raman analysis. ***Figure 3-2*** also gives the transition process of the luminescence (fluorescent transition) which will be further described in ***Section 3.4.***

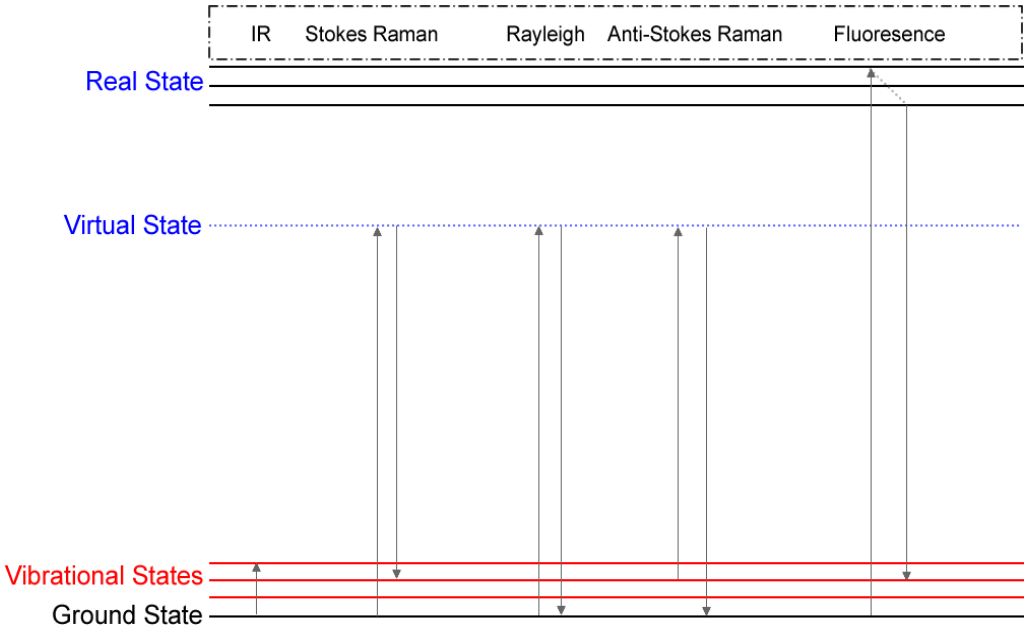

Figure 3-2. Scheme of different energy transitions.

Unlike FT-IR vibrations (using IR vibrations in ***Figure 3-2***), Raman vibrations have no direct relation with molecular dipole moments. In this thesis, because the FT-IR spectra of WS_2 and MoS_2 are not clear, their basic structures are analyzed using Raman spectroscopy. As with FT-IR, shifts in the location of Raman spectra features can be used to determine particular aspects relevant to a material.[4] For example, the Raman spectra of GO and chemically reduced GO are different to each other.[3] The G mode of chemically reduced GO was found at around 1588 cm^{-1}, while the G mode of GO was found at around 1602 cm^{-1}.[3] These Raman shifts are mainly due to the structure changes (oxidization) of the material and thus can be used to determine the oxidization extent of the material. In other words, to check whether the GO has been deoxidized effectively, Raman spectroscopy can be a useful technique.

In this thesis, Raman spectra of all the samples (solid or dried suspension samples) were recorded on a Renishaw in plus laser Raman spectrometer with an excitation wavelength of 785 nm.

3.3 Ultraviolet/Visible (UV/Vis) Spectroscopy[5]

UV/Vis spectroscopy is usually used in analytical chemistry for quantitative or qualitative analysis of specimens, such as biological macromolecules, conjugated organic compounds and transition metal ions. The sample for UV/Vis analysis can be solid, liquid or vapour. The typical wavelength applied for UV/Vis analysis ranges from 200-800 nm (see ***Figure 3-1***, wavelengths at 200-400 nm and 400-800 nm are UV and visible regions, respectively). UV/Vis absorptions below 200 nm cannot be resolved well because the absorption from the air molecules(*e.g.* N_2, O_2, CO_2 and H_2O) are mostly located in this vacuum UV region (100 nm - 200 nm).

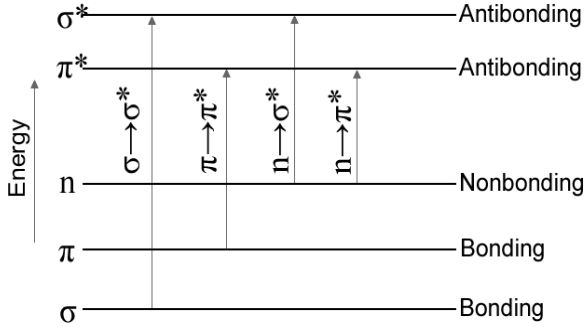

Figure 3-3. Electronic states and transitions of molecular.

During the analysis (wavelength from 200-800 nm), the outer electron of the specimen absorbs an incident photon and is excited from the ground state to a higher lying state. The different structures of different molecules and materials are reflected in the different UV/Vis absorption spectra characteristics. In other words, the UV/Vis absorption of the sample creates an energy level transition of valence electron of the molecule. There are three types valence electrons in chemical structures (***Figure 3-3***), comprising σ bonding electrons, π bonding electrons and non-bonding (n) electrons.[5] Therefore, based on molecular orbital theory,[6] the electronic transition of the chemical structure might be the $\sigma \rightarrow \sigma^*$, $n \rightarrow \sigma^*$, $\pi \rightarrow \pi^*$ and $n \rightarrow \pi^*$ (where * denotes an electronically excited state). The transition energy of $\sigma \rightarrow \sigma^*$ is much bigger than that of others, which normally have a corresponding absorption wavelength within 150 nm (in vacuum UV region). This is usually beyond the low wavelength limit of UV/Vis analysis due to available excitation sources and optical absorption in even fused silica optics. Similarly, most $n \rightarrow \sigma^*$ transitions cannot be easily analyzed using UV/Vis spectroscopy because of their short wavelength and weak absorption.[5] However, unlike the above transitions, the transitions of $\pi \rightarrow \pi^*$ and $n \rightarrow \pi^*$ are routinely observed in the UV/Vis spectra with suitable intensity and wavelength (near UV region to visible region, 200-800 nm). Besides, the d→d transition in a metal complex and charge transfer transitions between

different species (ions, ion and molecules, internal conversion in molecules can also be analyzed using UV/Vis spectroscopy.[5]

In addition, measurement of optical absorption coefficients at certain wavelengths allows UV/Vis spectroscopy to be used to determine the concentration of dispersed/dissolved samples. To understand this application, we need to use the Lambert-Beer law:

$$A=\varepsilon.c.I \qquad (eq.\ 3\text{-}5)$$

where A is the absorbance, ε is the absorption coefficient, c is sample concentration and I represents the cell length. The absorption coefficient can be calculated from a measured UV/Vis spectra once we know the material's mass (measured from mass of dried solution). The concentration of an uncertain solution/dispersion therefore can be simply estimated from *eq.* 3-5. However, for this estimation, plots of A/I versus the concentration should provide a straight line fit, satisfying the Lambert-Beer law.

In this thesis, UV/Vis spectra of all the samples were recorded by a PerkinElmer Lambda 900 Spectrometer at room temperature. For the test, all the samples were prepared as liquid phase solutions or dispersions in quartz cuvette with a standard optical length of 10 mm.

3.4 Photoluminescence (PL), PL Excitation (PLE) and Time-Resolved PL (TRPL) Spectroscopy

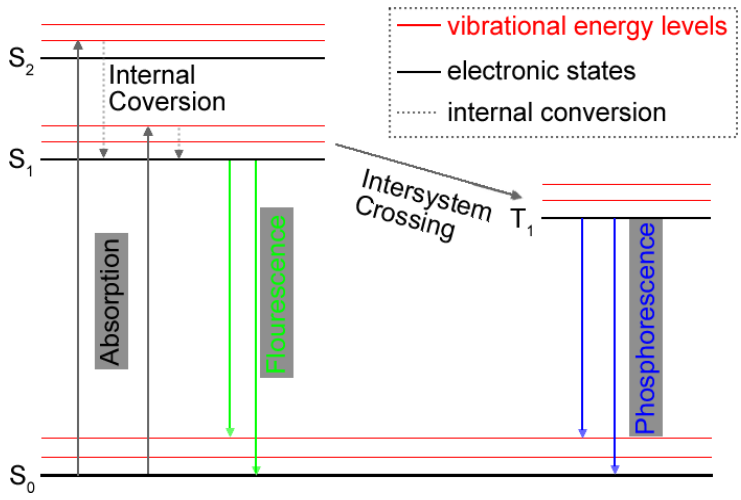

Figure 3-4. Simplified form of Jablonski diagram of molecular energy structure. The red lines represent vibrational energy levels.

PL spectroscopy is a non-destructive and contactless method to probe the electronic structure of materials.[7] During the analysis, light is directed onto the sample and imparts excess energy into the materials, which causes electron within a material to move into permissible excited states. This process is the same as that described in the UV/Vis spectroscopy (***Section 3.3***). When these electrons return to their equilibrium states, the excess energy is released either as emitted light (radiative process) or thermal energy (nonradiative process).[7] In these processes, light emission (includes fluorescent and phosphorescent emissions) is called PL.[7] The energy of the PL relates to the difference in energy levels between the two electron states (excited states and equilibrium state). This absorption and emission processes can be understood using a simplified form of a Jablonski diagram (***Figure 3-4***).[7] In this diagram, the singlet ground, first and second electronic states are presented by S_0, S_1 and S_2, respectively. Following light absorption, several processes usually occur (***Figure 3-4***). The fluorophores (electrons whose transition produce PL) are usually excited to some higher vibrational levels of either S_1 and S_2. Thermalization of the excess vibrational energy usually relaxes the molecule to the lowest vibrational level of S_1, generally with lifetimes within 10^{-12} s.[7] However, the lifetimes of fluorescence emissions are typically near 10^{-8} s. The fluorescence emission generally results from a thermally equilibrated excited state (the lowest energy vibrational state of S_1).[7] The return of fluorophores to the ground state typically occurs to a higher excited vibrational ground state level firstly, then quickly (10^{-12} s) reaches thermal equilibrium. That is the reason why a typical PL position is lower in energy than that of the corresponding excitation energy. The energy gap between the PL and a corresponding excitation energy is called as Stokes Shift.[7] When a fluorophore is in the first excited singlet state S_1, it can also undergo a spin conversion to the first excited triplet state T_1 via 'intersystem crossing'. Radiative emission from T_1 to S_0 is called phosphorescence, which is generally shifted to lower energies than fluorescent transitions.[7] The $T_1 - S_0$ transition is forbidden but this condition can be broken, resulting in phosphorescent decay rates typically several orders of magnitude smaller than for fluorescence.[7]

Based on these considerations, the electronic structure of semiconductors can be probed well using PL spectroscopy. PL excitation (PLE) spectroscopy generally maintains constant emission wavelength while the excitation wavelength is scanned. This is a powerful technique that allows various absorption and emission features to be related and, thus, a picture of the electronic structure of the fluorophore built.

PL efficiency is usually expressed in terms of a quantum yield (Φ) of the number of emitted photons divided by the number of absorbed photons. Appropriate standards can be used to help determine Φ in another sample. For example, Φ for anthracene in ethanol is 30% at an excitation wavelength of 360 nm.[8-10] The specimen Φ at the same excitation wavelength can then be determined according to:[7]

$$\Phi_x=\Phi_{st}(I_x/I_{st})(\eta_x^2/\eta_{st}^2)(A_{st}/A_x) \qquad (eq.\ 3\text{-}6)$$

where the subscripts *x* and *st* denote the specimen and standard values, respectively, for *Φ,* measured integrated emission intensity *I,* refractive index of the solvent *η* and optical density *A*.

To understand the precise processes of PL, time-resolved photoluminescence (TRPL) measurements can be used. For this measurement, the sample is excited with a pulse of light. The width of the pulse is made as short as possible and shorter than the decay time (also called as lifetime, *τ*) of the sample. Then the time-dependent intensity is measured following the excitation pulse, and the decay time *τ* is calculated from the slop of a plot of log *I(t)* versus t. The decay time *τ* is the time for decreasing the luminescent intensity to 1/e of the initial intensity (after pulse), which can be derived from:[7]

$$I(t)=I_0\times e^{(-t/\tau)} \qquad (eq.\ 3\text{-}7)$$

where *I(t)* and I_0 are the intensity at time t and 0, respectively. On the basis of *eq.* 3-7, different decays of the emission can be calculated from one measurement. For example, a single exponential decay curve means only one decay process is causing photoemission and the calculated lifetime is the decay time of this process. In a more complex process, multi-exponential decay must be considered and the various lifetimes correspond to different decay processes. TRPL can thus allows emission from the conduction band minimum to different energy levels and defect traps to be resolved.

In this thesis, PL and PLE spectra of all the samples were recorded by a Hitachi F-4500 Fluorescence Spectrophotometer at room temperature. For calculating Φ of samples, the UV/Vis absorptions of the samples (H_2O solvent) and standard materials (anthracene and Rhodamine B in absolute ethanol) were recorded by a PerkinElmer Lambda 900 Spectrometer at room temperature. Φ of anthracene (absolute ethanol solvent) was assumed to be 30% with excitation wavelengths 310-360 nm.[8-10] Φ of Rhodamine B (absolute ethanol solvent) is ~70% with a 400 nm excitation wavelength.[8,11,12] Φ of monolayered graphene, BN and WS_2 QDs (evaporate ethanol in

oven to leave H_2O solvent alone) were calculated from *eq. 3-6* with the standard material of anthracene (in absolute ethanol). Φ of monolayered MoS_2 QDs (evaporate ethanol in oven to leave H_2O solvent alone) were calculated from *eq. 3-6* with the standard material of Rhodamine B (in absolute ethanol). TRPL of all samples were recorded using a time-correlated single photon counting technique with an Edinburgh Analytical Instruments F920 using picosecond pulse width laser diodes as the source of excitation, at room temperature.

3.5 Scanning Electron Microscopy (SEM), Transmission Electron Microscopy (TEM), Selected Area Electron Diffraction (SAED) and Atomic Force Microscopy (AFM)[13-15]

SEM, TEM and AFM techniques can be used to determine sample information, such as particle size, morphology and surface structure. However, the operating principles of these three techniques are quite different from each other.

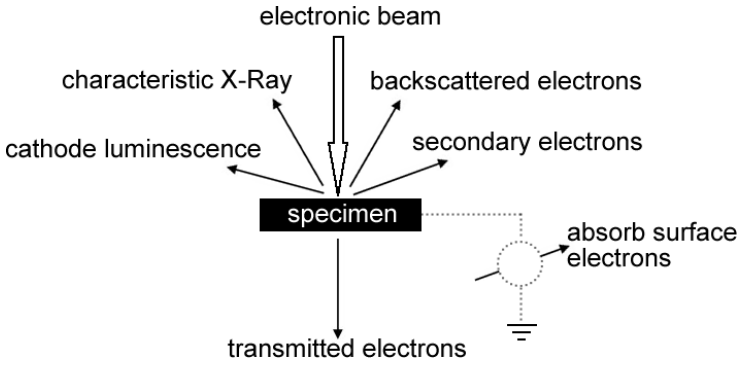

Figure 3-5.Electrons produced during SEM analysis.

During SEM analysis, many kinds of electrons (*e.g.* secondary electrons, backscattered electrons, Auger electrons) are generated when a focused electron beam scans a sample's surface (***Figure 3-5***).[13] The backscattered electrons are the electrons reflected by the specimen after several collisions, including elastic and inelastic backscattered electrons. Secondary electrons are released from the sample by the action of the incident electrons. X-rays can also be emitted due to transitions between inner energy levels in the sample's atoms. During this transition process, the energy produced may also excite other electrons, leading to the release of secondary electrons called Auger electrons. Among these electrons, the secondary electrons and backscattered electrons are generally used to produce SEM images.[13] The number of secondary electrons depends on the incident angle of the electron beam as well as the surface structure of the sample. Then the secondary electrons are collected by a

detector and synchronized with the electronic beam positional information to construct an image.[13] Images obtained with backscattered electrons show three-dimensional structure and reflect the surface structure of the sample. Secondary electrons are more commonly used in SEM imaging for this reason.[13] By contrast, the backscattered electrons are less sensitive to surface topography but can be used to map surface chemistry variations in the sample.

In a typical SEM experiment, the negative charge may accumulate on the surface of sample, which leads to difficulty in obtaining SEM images with high quality. Therefore, a thin conductive material (carbon or Au) is generally deposited on the surface of a sample to transport the generated negative charge, if the electrical conductivity of sample is low.[13] Using SEM technique, the relative composition of the sample's surface can also be determined by energy dispersive X-ray spectrometers (EDS/EDX) attached to the microscopes.[13] Every element emits a characteristic spectrum of X-rays, which allows the composition of a surface to be probed by analyzing the X-ray emissions using EDS. However, there is a drawback of EDS test as not all the elements can be detected accurately. For light elements (atomic number smaller than 6), other methods should be introduced (*e.g.* EELS, electron energy loss spectroscopy).

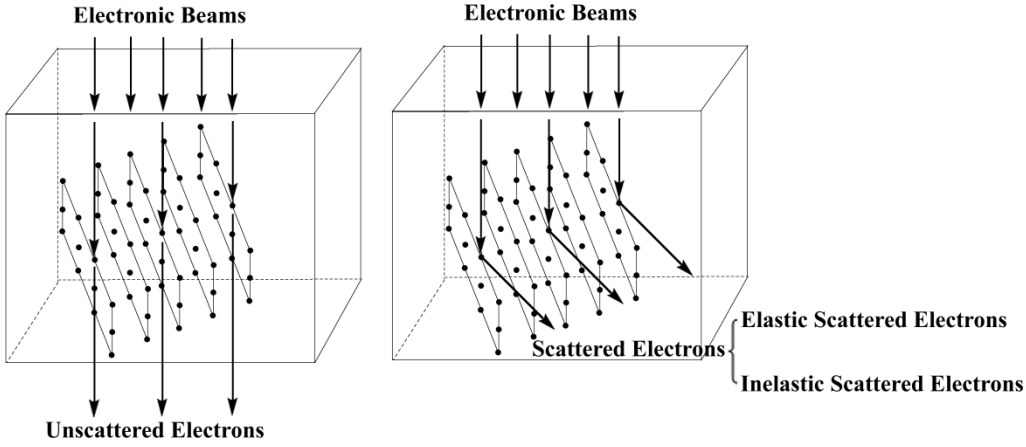

Figure 3-6.Transmitted electrons.

TEM differs somewhat from SEM in that electrons transmitted through thin samples are collected. TEM is a technique used to obtain the morphology, fine structure (*e.g.* crystal lattice and defects) as well as diffraction patterns of the crystal.[14] During TEM analysis, there are three kinds of transmitted electrons produced when the primary electronic beam transmitted the thin specimen, including unscattered electrons, elastic scattered electrons and inelastic scattered electrons (***Figure 3-6***).[14] TEM images may be obtained using bright field (BF) or dark field (DF) imaging using unscattered and

scattered electrons, respectively. ***Figure 3-7*** (left image) shows a simplified model for BF TEM imaging. By using electron optics, the unscattered electron beam is magnified to form an image at the image plane.

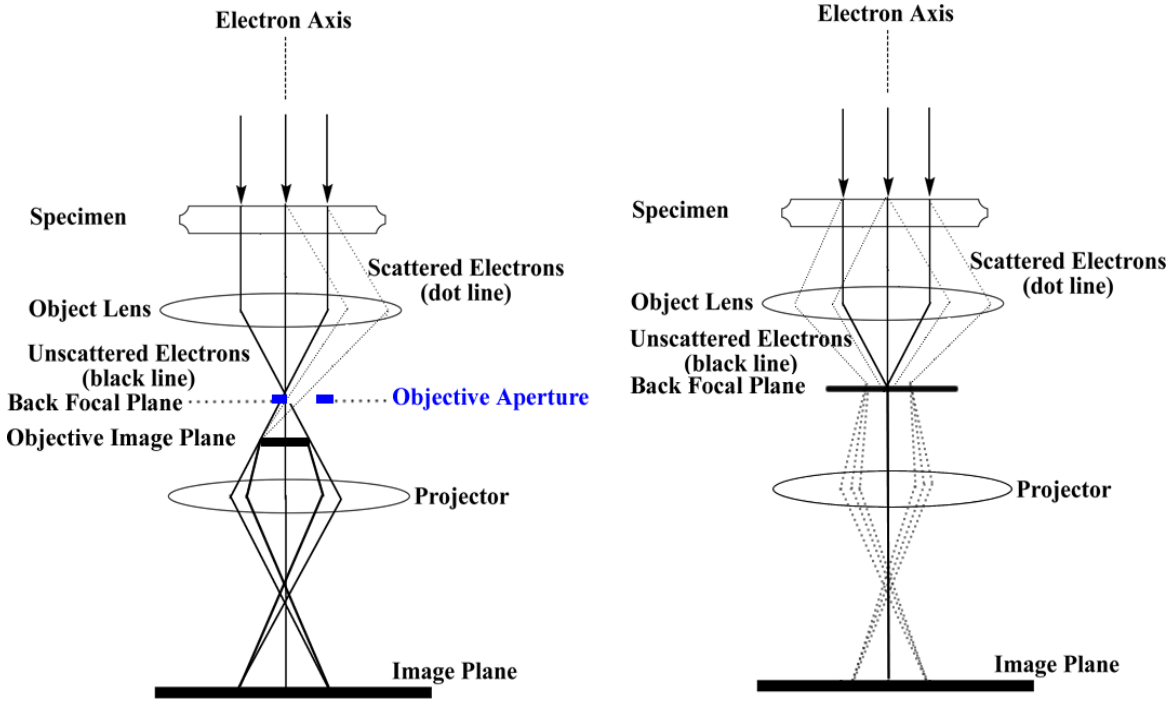

Figure 3-7.The formation of TEM image(left) and diffraction pattern (right).

The unscattered electron image has different contrast regions that are a direct image of the specimen's structure. For example, regions of a specimen that have higher density or thickness than other regions will have strong inelastic scattering (see ***Figure 3-8a***, the electron in Pt has more inelastic scattering than that in Co). The increase of inelastic scattering will decrease the intensity of unscattered electrons and thus appear dark contrast in a BF image (see ***Figures 3-8c&d***). Besides, the crystal orientation can also influence the image contrast. Diffraction will occur when a crystal is at specific orientations with respect to the incident beam, depending on the electron beam energy. Diffraction can significantly change the amount of elastic electron scattering. For example, consider ***Figures 3-8b&e*** of a polycrystalline material. In the region between 3 and 4 (***Figure 3-8e***), the number of unscattered electrons was decreased by the influence of diffraction. By contrast, there is no obvious change of electronic intensity in the region between 1 and 3 as well as between 2 and 4 (***Figure 3-8e***). This influence results in different contrasts as show in ***Figure 3-8e***. Unlike BF imaging, DF imaging is performed by using scattered electrons. This can be achieved by inserting an objective aperture between the objective lens and objective image plane (blue aperture in ***Figure 3-7***).[14]

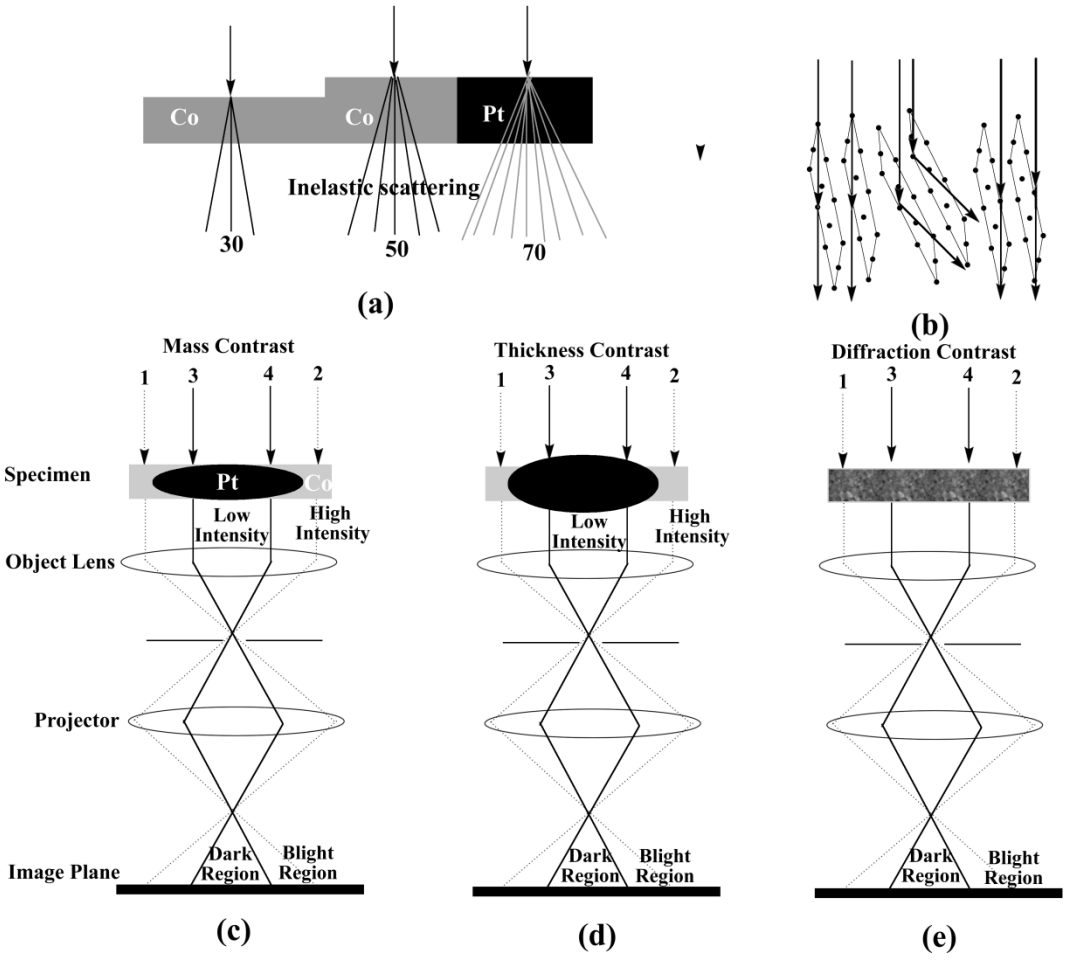

Figure 3-8. The formation of different contrast in BF image.

In TEM measurements, the objective lens (see ***Figure 3-7***) also focuses the scattered electrons (see the middle case in ***Figure 3-8b***) which come out from the bottom side of the diffracted electrons of the specimen.[14] If a back focal plane is inserted between the specimen and objective lens (the right image of ***Figure 3-7***), the electrons which have not been scattered though any net angle are focused to a spot in the centre of this plane. The electrons whose direction has been changed are focused at increasing distance from the centre with increased scattering angle to form the diffraction patterns of the specimen at the image plane. This analysis is also called as SAED analysis, which can be used to probe the molecular and atomic structure of the crystal by measuring the diffraction patterns of the crystal.[13] From the SAED pattern, atomic and molecular structures of the crystal can also be probed well.

Besides SEM and TEM, AFM is also a useful technique in probing the morphology (size and thickness) of the specimen by scanning the specimen's surface using a cantilever with a sharp tip at its end.[15] When the tip is brought closing a sample surface, forces

between the specimen and tip lead to a deflection of the cantilever according to Hooke's law.[15] The deflection of the cantilever is further measured using a laser spot reflected from the top surface of the cantilever into an array of photodiodes. These forces include mechanical contact force, van der Waals forces, electrostatic forces and magnetic forces which depend on the situation. Scan modes of AFM include static and dynamic modes.[15] In static mode, the cantilever is moved across specimen's surface and the surface' contours are directly measured using the deflection of the cantilever. By contrast, in the dynamic mode, the cantilever is externally oscillated, and the oscillation amplitude, phase and resonance frequency are modified by the interaction force between the tip and the specimen's surface. On the base on these changes, surface contours can be probed.

In this thesis, all the SEM images were taken by a commercial Inspect-F scanning electron microscope. The samples were placed on a conductive silica gel film for the scan. In some experiments, samples were coated by Au to improve the surface conductivity (WS_2 and MoS_2 samples), and some have not any surface coating treatments (reduced GO, graphite). For the TEM tests, samples (include solid samples and samples in solution) were diluted and dispersed (ultrasonication for around 10 minutes) in the EtOH solvent. Around 0.1 mL solution was dropped onto (use 1 mL disposable transfer pipet) the lacy carbon film (400 meshes) for air drying. TEM images were taken by a Phillips 420 transmission electron microscope at 120 kV (for reduced GO, BN flakes, carbon nanotubes and their sediments), and by a JEOL 2010F transmission electron microscope operated at 200 kV with field emission gun (for monolayered QDs). EDS of the samples were recorded during the SEM (Inspect-F) and TEM (JEOL 2010F) characterisations. As for the SAED, characterisations were performed on Phillips 420 transmission electron microscope. AFM images were taken by using a VEECO Dimension 3100 Atomic Force Microscope in a tapping mode (one dynamic mode) with a scan rate of 1 Hz. All the AFM samples were prepared on a fresh peeled mica substrate.

3.6 Powder X-ray Diffraction (XRD)[16]

XRD is a method used for determining the atomic and molecular structures of the crystal, in which the crystalline atoms cause a X-rays beam to diffract (elastic scattering) into many specific directions.[16]

A crystal is a regular array of atoms. When the X-rays (Kα produced by electron beaming on a metal source) are incident on a crystal, the beam spreads into many particular directions that depend on the crystal structure. The atoms scatter (diffract) part of the beam, to form secondary spherical waves (emanating from the electron, this phenomenon is also called elastic scattering). A three-dimensional picture of the density of electrons within the crystal can be determined (also the position of the atoms in the crystal) by measuring angles and intensities of the diffracted beams. During this diffraction, a regular atom array can produces a regular array of spherical waves. Although these waves cancel one another out in most directions through destructive interference, they add constructively in a few specific directions, determined by Bragg's law:[16]

$$2d\sin\theta = n\lambda \qquad (eq.\ 3\text{-}8)$$

where d, θ, λ and n are the spacing between diffracting planes, incident angle (typically within 5-45^{o} in this thesis), wavelength of the beam and any interger (n is 1 when calculating lattice space d using Bragg's law). These specific directions appear as spots on the diffraction pattern. Therefore, XRD results from an electromagnetic wave (the X-ray) impinging on the repeating arrangement of atoms within the crystal, and which can be used to probe crystal structure.

In this thesis, XRD patterns were obtained using a Philips PW1830 powder diffractometer (Cu Kα, wavelength ~ 0.154 nm) and Siemens D5000 X-ray diffractometer (Co Kα, wavelength ~ 0.179 nm). Except the XRD patterns of carbon nanotubes (includes sediment), GQDs created from MWCNTs, WS_2 (includes sediment), MoS_2 (includes sediment) and WS_2/MoS_2 QDs, all the XRD patterns of the other samples were performed on Philips PW1830 powder diffractometer. All the XRD data were collected with a scanning step of 2 ^{o}/min. For normalized data analysis, the data (XRD from Co Kα) were calibrated to the standard data which corresponds to the XRD from Cu Kα.

3.7 X-ray Photoelectron Spectroscopy (XPS)[17]

XPS is a sensitive quantitative spectroscopic technique for measuring the elemental composition, chemical state and electronic state of the elements within the material. During analysis, a specimen is irradiated by X-rays, which excite the inner electron/valence electrons of the specimen's atoms.[17] Some electrons gain sufficient energy to be emitted and become photoelectrons. These show characteristic binding

energies that correspond to the electron configuration of the electrons within the atoms and can be discriminated for analysis. The number of detected electrons in each of the characteristic peaks is directly related to the amount of a particular element within the area (volume) irradiated. Therefore, by normalizing the XPS intensities of different elements using a "relative sensitivity factor" (RSF),[17] detailed elemental composition of the specimen can be determined.

In this thesis, XPS analysis of GO, reduced GO, GQDs and purified monolayered MoS_2 QDs were performed on a Kratos AXIS Ultra ''DLD'' X-ray photoelectron spectrometer with an exciting source of Al *Ka* (wavelength ~0.155 nm). XPS analysis of the other samples were performed on Kratos AXIS Nova X-ray photoelectron spectrometer with an exciting source of Al *Ka*. Before data collecting, the surface of the specimen were cleaned with argon etching for a few minutes. Data were analyzed using Casa XPS. A binding energy of C1s at 284.6 eV was used to calibrate all the XPS results.

3.8 Thermogravimetric Analysis (TGA)[18]

TGA is a method of thermal analysis that is designed to measure physical and chemical property changes of the material as a function of increasing temperature. Characteristic temperatures can be used to assign particular chemical groups to a material or to measure their relative proportion. TGA makes use of various processes, such as vaporization, sublimation, absorption, desorption, solid-gas reaction and decomposition, and measures mass loss or gain during the heating process.[18]

In this thesis, TGA of all the samples (all around 20 mg) was carried out in argon at a heating rate of 5 ^{o}/min using a Pyris 1 TGA Thermogravimetric Analyzer (PerkinElmer Inc.).

3.9 Four Point Probe Resistivity Measurements[19]

A four point probe resistivity measurement is a simple method for measuring the electrical conductivity of samples. This method can be used to measure the resistivity of thin film, as well as diffusion layers. As indicated in ***Figure 3-9***, passing a current through two outer probes (probes 1 and 4) and measuring the voltage through the inner probes (probes 2 and 3) allow the measurement of the substrate resistivity. At a constant temperature, the relationship of the voltage (V) and current values (I) is dependent on the resistivity (Rs) of the material under test, and the geometrical characteristics (ρ) of the probe as follows:[19]

$$Rs = \rho \times \frac{V}{I} \qquad (eq.\ 3\text{-}9)$$

where sheet resistance Rs is in Ω per square; V (in mV) is the voltage between the inner two probes (probes 2 and 3); I (in mA) is the current flow between the outer two probes (probes 1 and 4); ρ is the geometric factor for thin film measured on four-point probe (ρ equals to 4.5324, if the size of the sample is 40 times larger than the spacing between the probes (is the case in this thesis)). If the W/S (W is the thickness of the film, μm; S is the spacing between the probes) smaller than 0.5 (is the case in this thesis), the real sheet resistance (R) is further dependent on the thickness factor (F_T) as follows:[19]

$$R = Rs \times F_T = \frac{W}{S} \times \frac{1}{2\ln^2} \times \rho \times \frac{V}{I} \qquad (eq.\ 3\text{-}10)$$

where R is the real sheet resistance of the thin film; F_T is the thickness factor for the thin film measured on four-point probe. Therefore, on the basis of the measured voltage (V) and current values (I), the real sheet resistance of the thin film can be calculated. In this thesis, a four-point probe measurement station (Keithley 2100 Digital Multimeter with Jandel Four Point Probe Heads) was used for the electrical measurement of rGO film. During the measurement, five data points for each sample were recorded and the average was taken. The average thickness of a rGO film was calculated based on five different cross-sectional SEM images (several samples were cut from the rGO film and were vertically pasted on the carbon film. In case any changes of the sample positions under SEM observations, the thickness measurements were performed on the samples which perpendicular to (close to 90°) the carbon film).

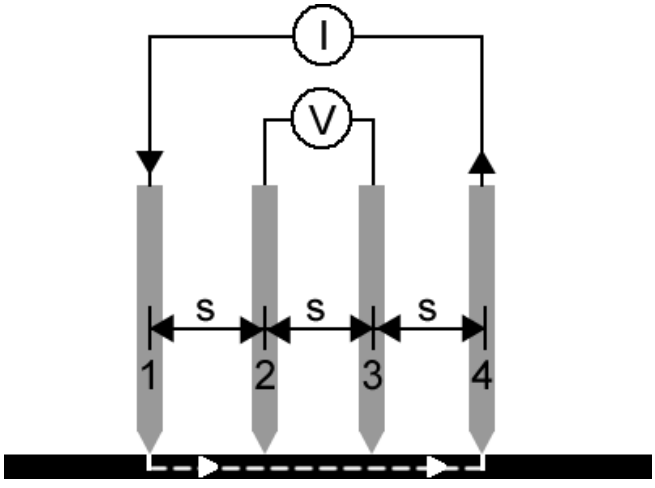

Figure 3-9. Diagram of four point probe resistence measurement.

3.10 Bio-Imaging and Cytotoxicity Evaluation

In this thesis, an inverted microscope was used for bio-imaging estimation of the QDs. Inverted microscope is a microscope with its light source and condenser on the top (above the stage pointing down). The objectives and turret of the microscope are below the stage. Usually, the stage of the inverted microscope is fixed. The focus is adjusted by moving the objective lens along a vertical axis to bring it closer to or further from the specimen. The focus mechanism typically has a dual concentric knob for coarse and fine adjustment. During the experiment, the light source of the inverted microscope is controlled (with different wavelengths) to illuminate the cell. If a suitable luminescent material can be taken up by the cells and excited by the light source, emissions (visible wavelength range) of the luminescent materials then can be captured by the microscope. This technique is useful for observing living cells or organisms.

In this thesis, for the bio-imaging, two pieces of round cover glass (13 mm diameter, VWR International) were placed in a 12-well plate with 1 cover glass and 1 mL DMEM culture medium per well. 2×10^4 cells were plated in each well of that 12-well plate. The cells were incubated at 37 ^{o}C overnight to adhere on cover glass. QDs were added in culture medium to final concentration of 25 μg/ml and then the cells were incubated at 37 ^{o}C for 24 hours. After incubation, the cells on two cover glasses were washed with 1 mL 1× PBS separately. Cells were fixed using 4% paraformaldehyde at room temperature for 5 min. Then cells on cover glasses were washed by 1 mL 1 × PBS and mounted with Vectashield antifade mounting media with and without DAPI (Vector Laboratories, Inc., CA) respectively. Cellular images were taken using the Olympus IX71 inverted research microscope equipped with the Olympus DP70 Color/Black and White camera (Olympus, America), using fluorescein isothyocyanate (FITC) mode. Olympus U-RFL-T power supply unit was used as the fluorescence light source.

As the materials for bio-imaging, the inherent toxicity of the materials should be minimized. In a typical procedure of cytotoxicity evaluation of the QDs, the cells were cultured and maintained in DMEM (Dulbecco's Modified Eagle Medium) media gibco containing 4.5g/L D-glucose, 4 mM L-Glutamine, and 110 mg/mL sodium pyruvate, with 10% fetal bovine serum (FBS), 100 IU/mL penicillin and 100 μg/mL streptomycin. MDCKII cells were plated at 1.85×10^4 cells per well on 12-well plates, and were left to adhere overnight. Different concentrations of QDs (0-125 μg/mL) in culture media (50% distilled water and 50% culture media, in volume) were added to each well in triplicate. The cells were then incubated at 37 ^{o}C for 24 and 48 hours respectively. At the end of each incubation, cells were gently washed with 1 mL of warm, sterile 1×PBS

(phosphate buffered saline) per well. Then 1mL per well of 0.05% Trypsin-EDTA (Gibco) was added to each well which were then incubated at 37 degree for 2 hours. The cells in each well were re-suspended in 0.05% Trypsin-EDTA. The number of cells in each well was counted by using Hemocytometer (Hawksley UK).

3.11 Raw Materials

$NaNO_3$ (Product No. S5506), H_2SO_4 (95.0-98.0%, Product No. 320501), $KMnO_4$ (Product No. 223468), H_2O_2 (30 wt%, Product No. 216763), NMP (product No. 242799), DMF (product No. 319937), S (product No. 84683), hydrazine (35 wt%, product No. 309400), Fe (product No.: 12310-500G-R), multi-walled carbon nanotubes (MWCNTs) (Product No. 694185-5G), potassium (K) chunks (Product No. 244864), cation exchange resin (Product No. 06423-250G), hBN flakes (Product No: 255475), tungsten disulphide (WS_2) flakes (Product No: 24639), molybdenum (IV) sulfide (MoS_2) flakes (Product No: 234842-100G) and potassium (K) chunks (Product No: 244864) were purchased from Sigma-Aldrich. The dialysis tubing (product No: 88242), isopropyl alcohol (IPA, >99.5%), graphite flake (GFs, product No.17346-25) and HCl (36 wt%, product No.: 7647-01-0) used in this thesis were purchased from Thermo Scientific, Fisher Scientific, Acros, Nacalai Tesque and Alfa Aesar, respectively.

References and Notes

[1] P. R. Griffiths and J. A. de Hasseth, *Fourier Transform Infrared Spectrometry* (2nd Ed.). **2007**, Wiley-Blackwell, New Jersey pp1-509.

[2] D. A. Skoog, F. J. Holler and S. R. Crouch, *Principles of Instrumental Analysis* (6th Ed.). **2007**, Thomson Brooks Cole. pp 430-477.

[3] W. Chen, L. Yan and P. R. Bangal, Chemical Reduction of Graphene Oxide to GRAPHENE BY Sulfur-Containing Compounds. *J. Phys. Chem. C* **2010**, *114*, 19885-19890.

[5] D. A. Skoog, F. J. Holler and S. R. Crouch, *Principles of Instrumental Analysis* (6th Ed.). **2007**, Thomson Brooks Cole. pp 481-492.

[5] D. A. Skoog, F. J. Holler and S. R. Crouch, *Principles of Instrumental Analysis* (6th Ed.). **2007**, Thomson Brooks Cole. pp 335-390.

[6] C. Ballhausen and H. Gray, *Molecular Orbital Theory*. **1965**, W. A. Benjamin, Inc.

[7] J. R. Lakowica, *Principle of Fluorescence Specstroscopy* (3rd Ed.). **2006**, Springer.

[8] J. N. Demas and G. A. Grosby, The Measurement of Photoluminescence Quantum Yield. A Review. *J. Phys. Chem.* **1971**, *75*, 991-1024.

[9] W. R. Dawson and M. W. Windsor, Fluorescence Yield of Aromatic Compounds. *J. Phys. Chem.* **1968**, *72*, 3251-3260.

[10] G. Weber and F. W. J. Teale, Determination of the Absolute Quantum Yield of Fluorescent Solutions. *Trans. Faraday. Soc.* **1957**, *53*, 646-655.

[11] C. A. Parker and W. T. Rees, Correction of Fluorescence Spectra and Measurement of Fluorescence Quantum Efficiency. *Analyst* **1960**, *85*, 587-600.

[12] A. N. Fletcher, Quinine Sulfate as a Fulorescence Quantum Yield Standard. *Photochem. Photobio.* **1969**, *9*, 439-444.

[13] J. Goldstein, D. Newbury, D. Joy, C. Lyman, P. Echlin, E. Lifshin, L. Sawyer and J. Michael, *Scanning Electron Microscopy and X-ray Microanalysis*. (3rd. Ed.). **2003**, Spring, New York,.

[14] B. Fultz (Brent), *Transmission Electron Microscopy and Diffractometry of Materials*. (3rd. Ed.). **2008,** Springer, Berlin.

[15] P. Eaton and Paul West, *Atomic Force Microscopy*. **2010**, Oxford University Press, Oxford.

[16] D. Hukins, *X Ray Diffraction by Disordered and Ordered Systems.* **1982**, Pergamon Press. pp 1-164.

[17] D. Griggs and M. P. Seah, *Partical Surface Analysis*. (2nd. Ed.). **1990**, Wiley, Chichester.

[18] A. W. Coats and J. P. Redfern, *Thermogravimetric Analysis: A Review*. *Analyst* **1963**, *88*, 906-924.

[19] P. Tipler, *Physics for Scientists and Engineers: Electricity, Magnetism, Light, and Elementary Modern Physics* (5th. Ed.). 2004, W. H. Freeman.

Chapter IV. Effective Solvothermal Deoxidation of Graphene Oxide Using Solid Sulphur as a Reducing Agent

4.1 Introduction

There are several techniques developed for the preparation of graphene, including mechanical peeling,[1] chemical vapor deposition,[2] epitaxial growth,[3] liquid-phase exfoliation,[4] chemical exfoliation-reduction,[5] electrochemical expansion-reduction[6]. Among these methods, the chemical exfoliation-reduction has been most intensively investigated as a relatively economical and a plausible route to prepare graphene-like materials on a large scale. This technique normally involves the preparation of graphite oxide, the exfoliation of graphite oxide to form graphene oxide (GO) and the chemical reduction of the exfoliated GO.[5]

GO is a nonconductive, hydrophilic and thermally unstable material. These features of GO can be attributed to the plentiful decorated oxygen-containing groups.[7,8] Many of these oxygen-containing groups can be removed using hydrothermal process.[9] However, The π-π stacking and self-assembly between the reduced GO (rGO) sheets negatively affect the deoxygenation extent and prevent the formation of highly dispersed monolayered graphene products.[9] Chemical reducing agent and/or other techniques should be appropriately introduced to further reduce the exfoliated GO sheets. For this reason, many reducing agents were studied to reduce GO. For example, The most commonly used hydrazine and its derivates (*e.g.* its hydrates) were found to be the most effective in reducing GO.[5,10] Nevertheless, hydrazine and its derivates are highly toxic and explosive and so should not be used, in particular for large scale production. In addition, the nitrogen incorporation (from hydrazine or hydrazine based reducing agents) into the structure of rGO during the reaction process leads to a high electrical resistance/low electrical conductivity.[11] Apart from hydrazine and its derivates, some other alternative reducing agents such as $NaBH_4$,[11] strong alkalis (KOH and NaOH),[12] phenylenediamine,[13] and hydroquinone[14] were also attempted. Unfortunately, compared with the former, they showed much weaker deoxidation capacities.

Recently, Yan *et al.* have investigated the effect of sulfur containing compounds on the deoxidation of GO in its aqueous solution and found that $NaHSO_3$ showed a deoxidation capacity comparable to that of hydrazine, as a result of in situ formation of SO_2/HSO_3^- during the solvothermal reduction process.[15] However, the resultant rGO showed a low electrical conductivity, caused probably by the π-π stacking and self-assembly between GO/rGO sheets in the heated aqueous system and remaining oxygen containing groups in the deep regions (on the surface of GO, covered by the curly GO sheet) which are difficult to be removed.[9] This also leads to poor dispersibility undesired for many practical applications such as in the preparations of conductive films, coatings and homogeneous composite materials. Although the dispersibility can be improved by introducing some functional groups,[16-18] they adversely affect the electrical conductivity.

Clearly, it is necessary to develop a more feasible chemical reduction system for large scale (*e.g.* can be scaled up to prepare rGO with kilograms) productions of rGO, which should ideally meet the following criteria: (1) it should be able to effectively remove oxygen-containing groups from GO so as to restore the electronic structure of graphene, (2) the π-π stacking and self-assembly between rGO sheets should be avoided so as to well disperse rGO in a suitable solvent and accelerate the deoxidation, and (3) it should be inter-convertible between different forms of rGO: agglomerates, simply air dried powder and dispersed suspension, which would be beneficial to many future applications. According to these, a simple but novel process to prepare highly electrically conductive solid rGO and its dispersions was developed. The study in this chapter aims to discover and solve the real difficulties in reducing GO (using solvothermal reaction) to form high performance rGO. For this, solid sulphur (S) was selected as a model of gentle reducing agent to reduce GO. It is well known that the solid S can generate in situ H_2S and H_2SO_3 on reacting with boiling water.[19,20] The reducing effects of SO_2 and its hydrates H_2SO_3/ HSO_3^- upon GO have been confirmed by a previous study.[15] Theoretically, S^{2-} has a much stronger reductive effect than S^{4+}, so the solid S in aqueous GO might be able to provide comparable reducing capacity/efficiency to that of hydrazine, and to produce highly electrically conductive rGO. Nevertheless, in an aqueous system, the study in this chapter indicates that in the deep region of GO, the electronic structure of graphene cannot be fully restored by using only S. A similar difficulty in the deep deoxidation of GO was also commonly found with other solvothermal reaction processes previously studied (*e.g.* solvothermal deoxidation by using hydrazine).[10] This difficulty is considered to be related to the π-π stacking and

self-assembly between GO/rGO sheets. To address this, two water soluble organic surfactants (N-methyl pyrrolidone (NMP) and dimethylformamide (DMF)) were used to reduce the surface tension of the solvent, so as to improve the dispersion of a single rGO sheet. As a result, GO could be well deoxidized and rGO with high electrical conductivity and good dispersibility obtained. The experimental result gives an insight on the solvothermal deoxidation of GO: a wide range of other water soluble organic solvents and surfactants which have suitable surface tensions, along with a safe and moderate reducing agent, all might be combined appropriately to produce high quality graphene products (this will be further confirmed in ***Chapter V***).

4.2 Experimental Methods

4.2.1 Preparation of Graphite Oxide

Graphite oxide was prepared based on the Hummers method.[21] Typically, the preparation involves several steps described as following: 1) Add 2 g graphite flake (GFs) and 1.5 g $NaNO_3$ into 800 mL wide neck flask. Then add 150 mL H_2SO_4 (95.0-98.0%) into the flask and stir the mixture. 2) Keep the flask at around 35 ^oC using a water bath. Then add 9 g $KMnO_4$ into the flask within 1 h. Keep stirring the mixture for 24 h at around 35 ^oC. 3) Slowly add 280 mL 5% H_2SO_4 into the mixture. Meanwhile, heat and keep the temperature of mixture at around 85-95 ^oC using oil bath. Once all the 5% H_2SO_4 was added into the flask, stir the mixture for another 2 h. 4) Cool down the mixture in the flask to around 60 ^oC and then add 15 mL H_2O_2 (30 wt%) into the mixture. 5) Keep stirring for another 2 h and collect the mixture. Wash the product with diluted HCl (3 wt% and distilled water respectively for many times to remove any residual Mn^{4+} and acid. For this purpose, GO was gently diluted and stirred (avoid violent stirring which can exfoliate GO sheets and affect the following separation) in 500 mL H_2O solution to form homogenous suspension. Then, the GO suspension was separated using a Hettich Zentrifugen EBA 21 centrifuge for many times (each time for 30 minutes, 50 mL centrifuge tube, 30-35 mL suspensions in each tubes) at 6000 RPM until the pH value of suspension up to 6-7 (room temperature). During this process, the GO suspension was cooled to room temperature each time before separation (temperature will increase during separation process using centrifuge).

4.2.2 Preparation of rGO

Before the deoxidation reaction, the as-prepared graphite oxide was fully stirred and dispersed in water to form 500 mL homogeneous aqueous solution which was further diluted with water to the concentration of 0.5 mg mL^{-1} (the concentration here is

defined as the ‘‘net’’ carbon weight (excluding the weight of oxygen containing groups) divided by volume). This solution was further homogenized and exfoliated for 2 h using a Bandelin Sonorex RK-100H ultrasonic vibrator to form GO, and then used to prepare various samples for the deoxidation. These exfoliated GO was further diluted in different solvents (to form the solvent contains 1 : 1 H_2O-NMP in volume, 1 : 1 H_2O-DMF in volume respectively). Sigma-Aldrich NMP and DMF were used as surfactants to tune the surface tension of the reaction solvent. A typical deoxidation operation using S in H_2O-NMP or H_2O-DMF is described as follows. Initially, 0.4 g solid S and 200 mL GO solution were put into a 250 mL three neck round bottle which was then placed in an oil bath controlled at 110 ^oC (solvothermal temperature of around 100 ^oC) on a magnetic stirring hot plate. The solution was stirred to accelerate the refluxing reaction. After 10 h of refluxing reaction, the resultant black mixture was allowed to settle for 30 minutes followed by simple filtering to remove the solvent. Then an agglomerated raw product was obtained. To remove the superfluous solid S (part of S was sublimated and re-condensed later onto the inner surface of the condensation tube), the raw product was dispersed in 50 mL isopropyl alcohol (IPA) and allowed to settle for 10 minutes. After removing the cream-coloured sediment by using a separation funnel, the residual sample was ultra-sonicated for 10 minutes and then allowed to settle again. This process was repeated 3-5 times to fully remove the residual S. In the following purification process, most of the IPA was evaporated and the obtained solid sample was filtered and washed with NMP until the supernatant became clear, which was followed by washing with distilled water. Different samples, including solid agglomerates, filter supported paper, free-standing film and suspension in a solvent, were prepared using the product after washing. For collecting the solid sample from the homogeneous suspension, H_2O (>3 times volume of NMP, DMF or IPA) was added to the suspension and then aged in an oven at 50-70 ^oC for 30-60 min. After this, the rGO product would agglomerate together and thus readily be collected. For comparison, similar deoxidation reactions were also conducted in different solvents with S (0.4 g) and hydrazine (1.5 mL, 35 wt%) or without additions of a reducing agent (just boiling the aqueous suspensions). Samples were collected at different reaction stages for the ultraviolet/visible (UV/Vis) tests. For S-rGO-NMP-H_2O, S-rGO-DMF-H_2O, BGO-NMP-H_2O and BGO-DMF-H_2O (see ***Table 4-1*** for clarify), samples needed to be centrifuged and washed prior to the UV/Vis spectroscopy as otherwise absorptions from the NMP/DMF might cover the characteristic absorption peak of rGO.

4.2.3 Characterisation

Characterisation details are summarized in ***Chapter III***. For the test of the dispersibility in different solvents, the solid rGO product was dried in an oven at 120 °C for 5 h before weighing. Then it was mixed with appropriate amounts of NMP, DMF, IPA, or H_2O solvent in an amber glass and ultra-sonicated for at least 10 minutes, to form a stable homogeneous suspension (to check whether any sediment still exists at the bottom of amber glass after setting for over 10 minutes, a 1 mL disposable transfer pipet was used to gently remove black suspension). In any cases when the rGO cannot be dispersed well, more solvent (*e.g.* 1 mL, 2 mL) was added into the amber glass and the above procedure (ultra-sonicate the sample for at least 10 minutes and check whether sediments still exist at the bottom of the amber glass) was repeated until all the solid rGO (sediment) was dispersed well. The dispersibility was calculated by dividing the weight of the sample with the solvent volume.

4.3 Result and Discussion

4.3.1 Optimization of GO Concentration for Deoxidation

Various samples were prepared using different solvents and reducing agents and deoxidized for various times (*x*) at 110 °C (***Table 4-1***).

Table 4-1. List of the main test samples. The GO concentrations for all the reactions are controlled as 0.125 mg/mL (see ***Section 4.2.2*** for the definition of GO concentration).

rGO Sample	Solvent	Reducing Agent
BGO-H_2O-*x*	H_2O	--
S-rGO-H_2O-*x*	H_2O	S
H-rGO-H_2O-*x*	H_2O	Hydrazine
BGO-NMP-H_2O-*x*	H_2O/NMP (1:1 in volume)	--
BGO-DMF-H_2O-*x*	H_2O/DMF (1:1 in volume)	--
S-rGO-NMP-H_2O-*x*	H_2O/NMP (1:1 in volume)	S
S-rGO-DMF-H_2O-*x*	H_2O/DMF (1:1 in volume)	S

As GO and graphene have different electronic structures, UV/Vis spectroscopy can be used to effectively monitor the deoxidation extent. With increasing the deoxidation extent, the UV/Vis absorption peak (arising from the $\pi \rightarrow \pi^*$ transition of C=C) of reduced sample shifts towards the graphene's absorption peak at around 270 nm.[10] To find out the optimal GO concentration for deoxidation, 0.4 g S was added respectively to 200 mL aqueous GO suspensions with different concentrations. ***Figure 4-1a*** shows (summarized from ***Figures 4-1b-e***) the UV/Vis absorption peak positions of the resultant samples as a function of reaction time and GO concentration. As shown, the absorption peak position (*e.g.* the deoxidation extent of GO) highly depends on the

reaction time and the GO concentration. On reducing the GO concentration from 0.5 to 0.125 mg/mL, the deoxidation extent of GO increases owing to probably reduced π-π stacking and self-assembly between rGO sheets. On further reducing the GO concentration to 0.0625 mg/mL, however, the deoxidation extent adversely decreases. Therefore, 0.125 mg/mL is considered as the optimal GO concentration, and thus used to prepare all other samples for testing.

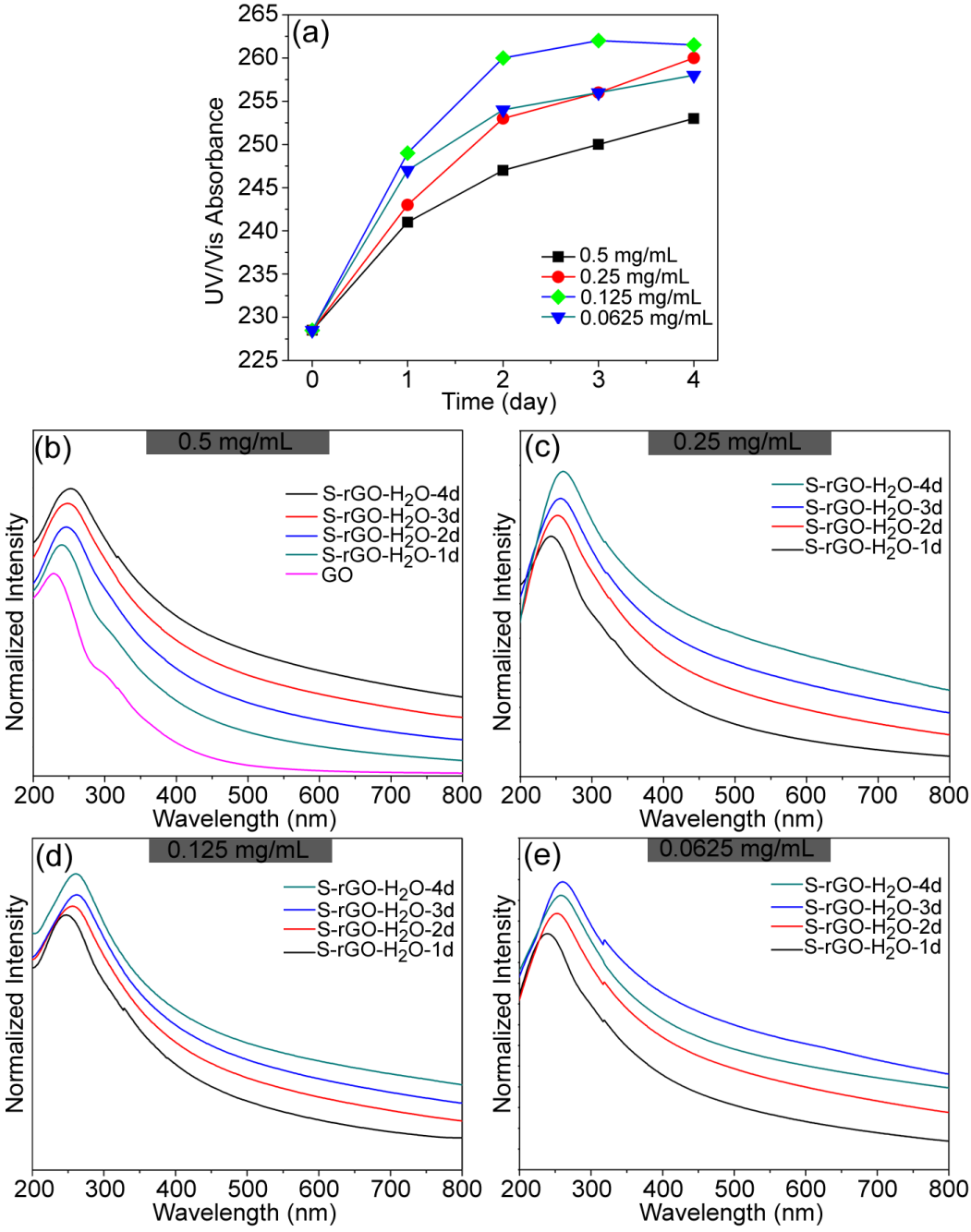

Figure 4-1. (a) UV/Vis absorption peak position (indicating the π→π* transition of C=C) as a function of reaction time and GO concentration; (b-e) UV/Vis spectra of GO and S-rGO-

H_2O-x (x= 1, 2, 3, 4 days) with different concentrations (For clarify, the absorption intensity was shifted for better comparison).

4.3.2 Reducing Effect of S upon Aqueous GO

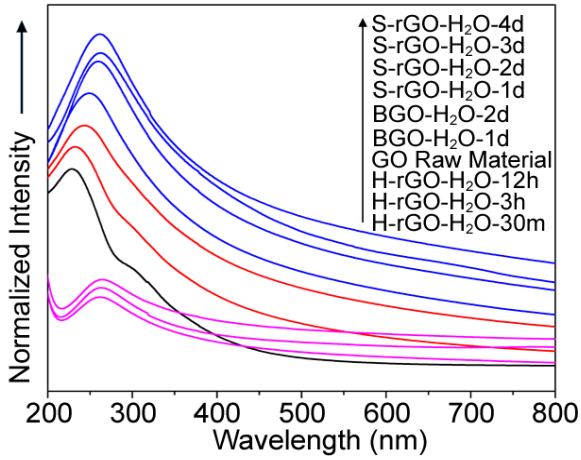

Figure 4-2. UV/Vis absorption spectra of GO, BGO-H_2O-*x*, S-rGO-H_2O-*x* and H-rGO-H_2O-*x*. The absorbance intensities of the spectrums were shifted for better comparison.

The UV/Vis results presented in ***Figure 4-2*** indicated that the refluxing reaction between GO and S deoxidized GO to a certain extent. However, it was not clear whether this deoxidation was caused by the presence of S, thermal deoxygenation, or both. To differentiate these and understand the reducing effect of S upon aqueous GO, a series of refluxing tests were conducted. ***Figure 4-2*** compares UV/Vis spectra of as-prepared GO solution, BGO-H_2O-*x*, H-rGO-H_2O-*x* and S-rGO-H_2O-*x*. The UV/Vis spectrum of the GO solution gives two main absorption peaks at around 229 and 300 nm, arising respectively from the π→π* transition of C=C in oxidized aromatic structure (GO)[10,22] and the n→π* transition of C=O bond.[23] When the GO solution was boiled at 110 °C for 1 day (BGO-H_2O-1d), the π→π* transition of C=C red-shifted to 232 nm whereas the n→π* transition of C=O became weaker, indicating that the electronic conjugation of graphene had been slightly restored. The former further red-shifted to 243.5 nm (π→π* of C=C) whereas the latter disappeared after 2 days refluxing reaction. These results indicated that, boiling GO solution only partially deoxidized the GO, *i.e.,* only to some extent restored the electronic conjugation of graphene. The deoxidation could be further enhanced by using S. As shown in ***Figure 4-2***, the π→π* transition of C=C in the UV/Vis absorption spectra of S-rGO-H_2O red-shifted to 249 and to 260 nm respectively after 1 and 2 days refluxing. Much greater shifts are seen in this case than in the case of BGO, verifying that S in a boiling water solution did additionally accelerate the deoxidation of GO.

The deoxidizing effect of S is mainly attributed to the reactive reducing agents H_2S and SO_2/H_2SO_3 generated by its reaction with boiling water.[19,20] The deoxidizing effect of H_2SO_3 has been confirmed by a previous study.[15] In addition to H_2SO_3, H_2S generated in the present case would contribute more to the deoxidation, as it theoretically has much stronger reducing ability than H_2SO_3. Nevertheless, experimental results showed that the electronic structure of graphene cannot be fully restored by using only S in the boiling aqueous GO, even when the refluxing time was greatly extended. For example, after 3-4 days refluxing reaction, the yellow GO solution changed to black agglomerates, but the UV/Vis peak indicating the π→π* transition of C=C in the sample (S-rGO-H_2O) still appeared at 262-261.5 nm (***Figure 4-2***) which is not much different from that in the case of 2 day refluxing (S-rGO-H_2O-2d), indicating that oxygen containing groups could not be further removed by only extending the reaction time. These results might be related to the π-π stacking and self-assembly between partially reduced GO sheets and their agglomeration in the boiled system,[9] where the residual oxygenated groups are more difficult to be removed than those on well dispersed monolayer GO sheets. A similar phenomenon was also observed in the case of hydrazine reduced aqueous GO (H-rGO-H_2O, see ***Table 4-1*** for clarify). As seen from UV/Vis spectra (***Figure 4-2***), on using hydrazine, the π→π* transition of C=C was rapidly restored to 261.5 nm within 30 min refluxing time. However, after extending the refluxing time to 3 and 12 h, the absorption peak only slightly red-shifted further, to 263 and 264 nm, respectively (*Note: base on the reported studies,[5,10] the addition amount of hydrazine is sufficient. The pH of the solvent all in a high value, further suggesting the addition amount of hydrazine is sufficient*).

Therefore, it can be deduced that the deoxidation of GO by using S will be further accelerated if the strong π-π stacking and self-assembly (agglomeration) of partially reduced GO are avoided or alleviated during the reaction. To achieve these, a solvent with suitable surface tension (~35-50 $mN.m^{-1}$)[4] can be used in the refluxing reaction system. To illustrate this, two water soluble organic surfactants, NMP (with a surface tension of 40.7 $mN.m^{-1}$ at 25 ^oC) and DMF (with a surface tension of 37.1 $mN.m^{-1}$ at 25 ^oC) were used respectively in the refluxing reaction systems.

4.3.3 Deep Deoxidation of GO by S in NMP/H_2O or DMF/H_2O Solvent

To verify the above deduction, 0.125 mg/mL GO solutions with different solvents (NMP/H_2O, DMF/H_2O, all in 1:1 volume ratio), were prepared, followed by adding S (see ***Section 4.2.2***). For comparison, samples without S (BGO-NMP-H_2O-1d and BGO-DMF-H_2O-1d) were also prepared and tested similarly. Their UV/Vis spectra (in ***Figure 4-3***

and ***Figure 4-4*** respectively) exhibit two absorption peaks at around 253.5 and 253 nm respectively. Comparison of these peaks with the corresponding peak of BGO-H_2O-1d (at 232 nm in ***Figure 4-2***) reveals that use of NMP or DMF does accelerate the deoxidation of GO. The surface tension changes with additions of these surfactants are believed to be responsible for such accelerating effect. Similar effect was also found in the case of addition of N,N-dimethylacetamide (DMAc, with low surface tension) to a boiling GO solution.[15,24]

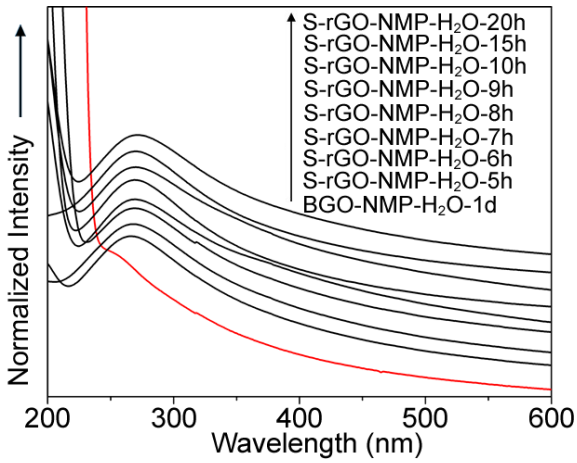

Figure 4-3. UV/Vis absorption spectra of BGO-NMP-H_2O-1d and S-rGO-NMP-H_2O-*x* (*x*=5, 6, 7, 8, 9, 10, 15, 20 h). The absorbance intensities of the spectrums were shifted for better comparison.

Figures 4-3 & 4-4 also present UV/Vis absorption spectra of S-rGO-NMP-H_2O-*x* and S-rGO-DMF-H_2O-*x* (*x*=5, 6, 7, 8, 9, 10, 15, 20 h). Interestingly, after 5 h refluxing reaction, the π→π* transition of C=C in the samples S-rGO-NMP-H_2O-5h and S-rGO-DMF-H_2O-5h already red-shifted (from 229 nm of GO) to 266 and 267 nm respectively. On further increasing the reaction time to 10 h, the characteristic absorption peaks of both S-rGO-NMP-H_2O-*x* and S-rGO-DMF-H_2O-*x* gradually red-shifted to 270 nm (the intrinsic π→π* transition absorption of C=C in graphene),[10] thus no obvious shifts were found on further prolonging the refluxing time, indicating that the electronic structure of graphene had been completely restored within 10 h. Comparison this result with that in the case of BGO-NMP-H_2O and BGO-DMF-H_2O further reveals that additions of S into NMP/H_2O and DMF/H_2O resulted in much better deoxidation effect. Complete conversion from GO to graphene can only be achieved when combined S and NMP (or DMF) are used. These results could be attributed to the improved dispersibility of rGO by the use of NMP or DMF. The oxygen containing groups on the dispersed monolayer GO and partially reduced GO sheet get exposed more to H_2S and H_2SO_3 and thus could be readily removed, facilitating the deep deoxidation. To further evaluate this newly

developed route to large scale preparations of graphene, S-rGO-NMP-H_2O-10h and S-rGO-DMF-H_2O-10h products were characterized in detail.

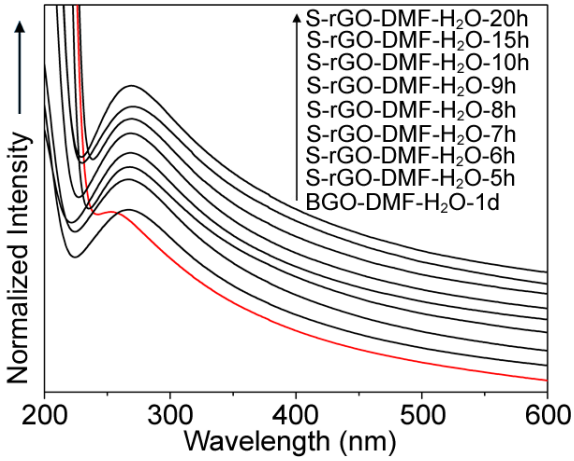

Figure 4-4. UV/Vis absorption spectra of BGO-DMF-H_2O-1d and S-rGO-DMF-H_2O-*x* (*x*=5, 6, 7, 8, 9, 10, 15, 20 h). The absorbance intensities of the spectrums were shifted for better comparison.

4.3.4 Characterisation of S-rGO-NMP-H_2O-10h and S-rGO-DMF-H_2O-10h

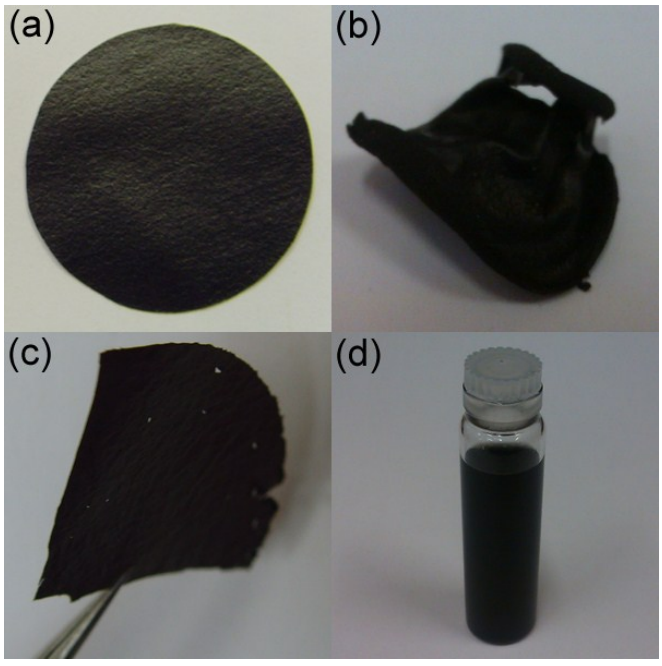

Figure 4-5. (a) Filter supported rGO paper; (b) Bulk solid rGO; (c) Free-standing rGO film; (d) Well-dispersed rGO-NMP suspension.

Both S-rGO-NMP-H_2O-10h and S-rGO-DMF-H_2O-10h can be readily made into different forms, including filter supported paper, bulk solid, free-standing film and well-dispersed suspension. ***Figure 4-5***, as an example, illustrates these forms prepared with S-rGO-NMP-H_2O-10h. A filter supported paper was obtained after filtering the rGO-NMP suspension and followed by washing and drying (***Figure 4-5a***). After peeling a free-standing film was then

obtained (***Figure 4-5c***). In addition, by diluting the rGO-NMP suspension with water (to increase the surface tension of the solvent) followed by aging in an oven at 50-70 °C for 30-60 min, rGO sheets would loosely agglomerate together, thus could be readily collected by filtering and washing. Subsequently, by simply air drying the collected agglomerations, bulk solid rGO (***Figure 4-5b***) could be obtained. This bulk solid rGO could be re-dispersed well in a solvent like NMP or DMF (***Figure 4-5d***).

Table 4-2. Dispersibility (mg/mL at 25 °C) of S-rGO-NMP-H_2O-10h and S-rGO-DMF-H_2O-10h in different solvents, with different surface tensions.

Description	NMP	DMF	IPA	H_2O
Surface Tension (at 25 °C, mN.m-1)	40.7	37.1	22.6	72
S-rGO-NMP-H_2O-10h	~1.3	~0.8	~0.5	~0.1
S-rGO-DMF-H_2O-10h	~1.3	~0.8	~0.5	~0.1

Table 4-2 lists the dispersibility data of S-rGO-NMP-H_2O-10h and S-rGO-DMF-H_2O-10h in NMP, DMF, IPA and H_2O, respectively. Considering the errors arising from the uncertainties in weighing operation, both S-rGO-NMP-H_2O-10h and S-rGO-DMF-H_2O-10h essentially showed similar dispersibility in a same solvent. Furthermore, the dispersibility of the samples in a solvent highly depends on the surface tension of the solvent. The highest dispersibility (1.3 mg/mL) was found in NMP whereas the lowest (0.1 mg/mL) found in H_2O. DMF shows moderate ability to disperse rGO (0.8 mg/mL). Although IPA has much lower surface tension than NMP and DMF (see ***Table 4-2***), it still showed a reasonably good dispersion ability (0.5 mg/mL). These data are comparable with those of functionalized graphene prepared using other routes.[25]

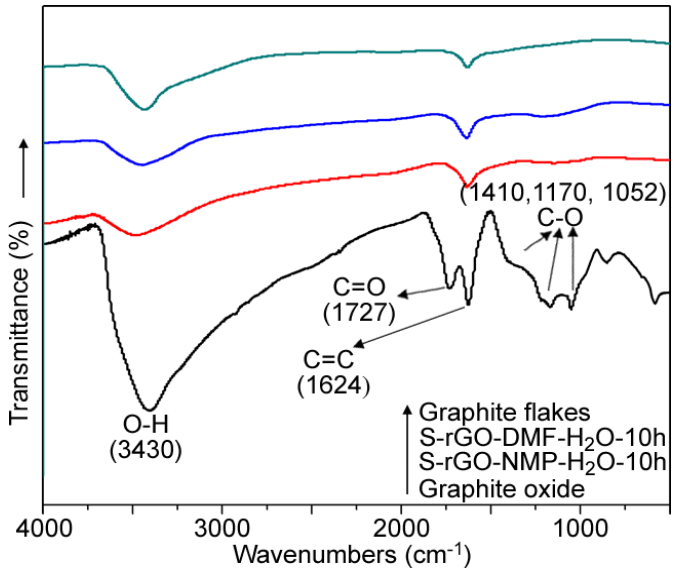

Figure 4-6. FT-IR spectra of graphite flakes, GO, S-rGO-NMP-H_2O-10h and S-rGO-DMF-H_2O-10h.

Shown in ***Figure 4-6*** are FT-IR spectra of graphite raw material, as-prepared GO and rGO products from S-rGO-NMP-H_2O-10h and S-rGO-DMF-H_2O-10h, respectively. The characteristic peaks of GO appear at around 1727 cm^{-1} (carbonyl C=O), 1624 cm^{-1} (aromatic C=C), 1410 cm^{-1} (shoulder peak, carboxyl C-O), 1170 cm^{-1} (epoxy C-O) and 1052 cm^{-1} (alkoxy C-O), which are consistent with those documented in the literature.[15,24] After 10 h reduction by S in NMP/H_2O or DMF/H_2O solvent, the carbonyl C=O vibration at about 1727 cm^{-1} disappears (the FT-IR is similar with that of graphite raw material), indicating the complete removal of the carbonyl group. Moreover, the vibrations at 1410, 1052 and 1170 cm^{-1} become much weaker than those of GO, indicating that other oxygen-containing groups such as carboxyl C-O, alkoxy and epoxy have been largely removed. In addition, compared to those on the FT-IR spectrum of GO, the intensities of the vibration peaks at around 1640 and 3430 cm^{-1} from both S-rGO-NMP-H_2O-10h and S-rGO-DMF-H_2O-10h decrease evidently, further verifying that the majority of O-H groups have been removed and the IR transmittance lowered. Furthermore, the aromatic C=C peaks in S-rGO-NMP-H_2O-10h and S-rGO-DMF-H_2O-10h are slighted shifted to a higher wavenumbers, suggesting the change of the chemical hybridization environment from sp^3 to sp^2. It is worth to note that no other functional groups from NMP and DMF (i.e. characteristics vibration of C-N at 1708 cm^{-1})[25] are found in the FT-IR spectra of S-rGO-NMP-H_2O-10h and S-rGO-DMF-H_2O-10h, possibly due to the low reaction temperature used in this work. As reported in Ref. 25, NMP may be grafted onto a graphene sheet at 180-240 ^oC. Full XPS of S-rGO-NMP-H_2O-10h and S-rGO-DMF-H_2O-10h further confirm that no functional groups remain in the as-prepared rGO. As shown in ***Figure 4-7***, apart from carbon and minor oxygen contamination, only trace amounts of residual N was detected, but the binding energy (398.5-399.5 eV) was smaller than that corresponding to the grafted N (401 eV).[25]

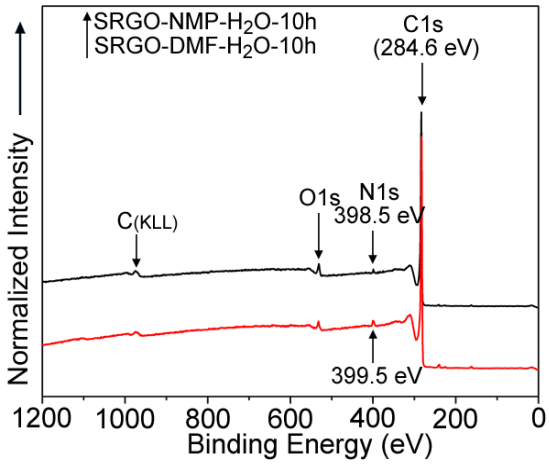

Figure 4-7. XPS survey of S-rGO-NMP-H_2O-10h and S-rGO-DMF-H_2O-10h.

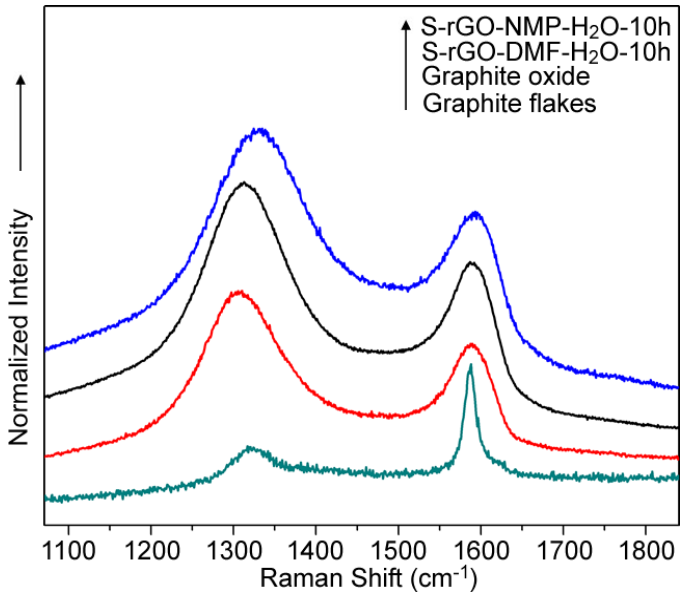

Figure 4-8. Raman spectra of graphite flakes, graphite oxide, S-rGO-NMP-H_2O-10h and S-rGO-DMF-H_2O-10h.

The structural changes from GO to rGO are also verified by their Raman spectra (λ_{exc} = 785 nm). As shown in ***Figure 4-8***, the Raman spectrum of GO gives two intense peaks at around 1325 and 1594 cm^{-1}, corresponding to the D and G bands respectively. The G bands of S-rGO-DMF-H_2O-10h and S-rGO-NMP-H_2O-10h both shift to 1588 cm^{-1} which is close to that from graphite (also see Raman spectrum of graphite in ***Figure 4-8***),[15] suggesting that GO was reduced and most of the oxygen containing groups were removed. In addition, the D bands of S-rGO-DMF-H_2O-10h and S-rGO-NMP-H_2O-10h both shift to about 1313 cm^{-1}. The D bands in all the samples may arise from some defects in the structures. Although the ratio between the intensities of D and G bands (I_D/I_G) in all samples varies, the average ratios (I_D/I_G) of S-rGO-NMP-H_2O-10h and S-rGO-DMF-H_2O-10h increase to 1.37 and 1.34 respectively from 1.24 (of GO). Similar results were also found with other chemical reduced graphene, indicating the decreased average size of the sp^2 domains after the chemical deoxidation.[5,15,25,26]

The effective removal of oxygen containing groups is further confirmed by TGA. As shown in ***Figure 4-9***, GO experienced 8.7 wt% weight loss at below 150 ^oC due to the loss of absorbed water, and lost much more (23.6 wt%) at 180-250 ^oC as a result of decomposition of thermally labile oxygen containing groups. Compared to GO, S-rGO-NMP-H_2O-10h and S-rGO-DMF-H_2O-10h showed greater thermal stabilities because of the absence of labile oxygen containing groups. Much less weight losses (2.9 wt%) were found in the same temperature range (180-250^oC). C1s XPS provide more direct evidence for the deoxidation in these two samples. As shown in ***Figure 4-10a***, the C1s

spectrum of GO includes four main components, arising from C=C/C-C (284.6 eV, peak 1,2), C-O (286.6 eV, hydroxyl and epoxy, peak 3), C=O (287.4 eV, carbonyl, peak 4) and small amount of C-OH (288.8 eV, carboxyl, peak 5).[15] However, the C-O, C=O and O=C-OH in S-rGO-NMP-H_2O-10h and S-rGO-DMF-H_2O-10h are reduced significantly (***Figures 4-10b & c***), and the main residual components become C=C (284.6 eV, peak 1 in ***Figures 4-10b & c***) and C-C (285.6 eV, peak 2 in ***Figures 4-10b & c***).[15]

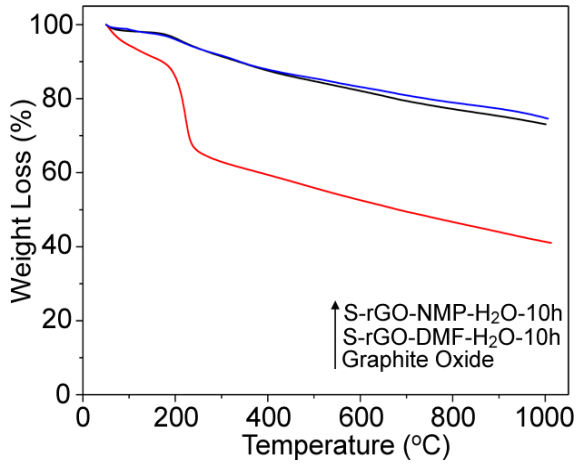

Figure 4-9. TGA curves for GO, S-rGO-NMP-H_2O-10h and S-rGO-DMF-H_2O-10h (in Ar).

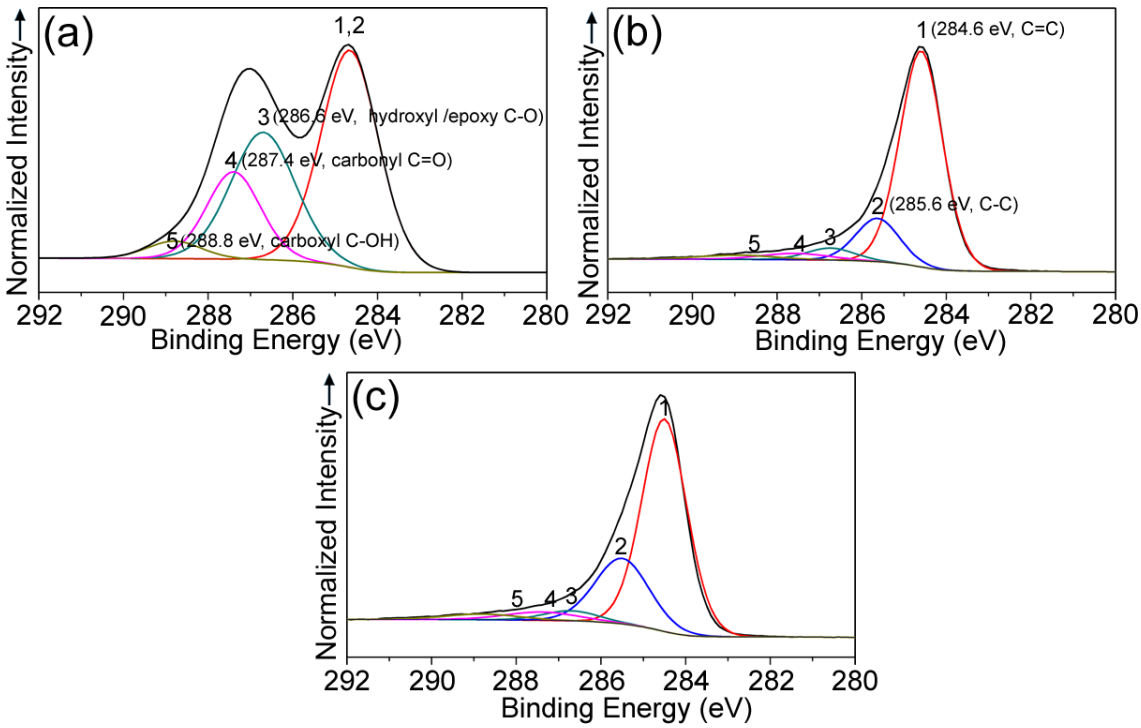

Figure 4-10. C1s XPS: (a) GO; (b) S-rGO-NMP-H_2O-10h; (c) S-rGO-DMF-H_2O-10h.

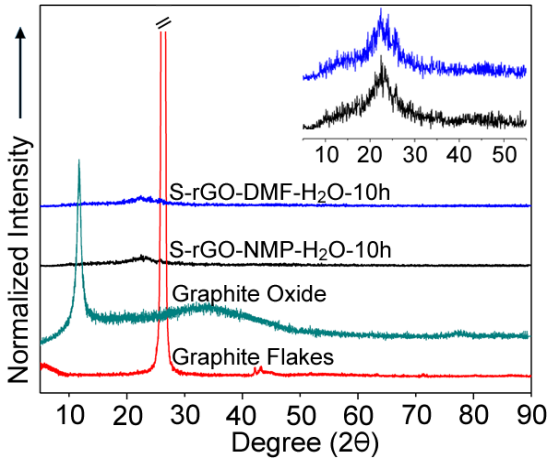

Figure 4-11. XRD patterns of graphite flake, graphite oxide, S-rGO-NMP-H_2O-10h and S-rGO-DMF-H_2O-10h.

As presented and discussed above, GO could be deeply deoxidized by using the method developed with this work. Nevertheless, it was still not clear whether the 3 D structure of graphite had been fully converted to the 2D structure of graphene. To clarify this, the collected solid rGO were further characterized by using XRD, SEM, TEM and AFM. ***Figure 4-11*** shows XRD of raw material graphite, graphitic oxide and solid rGO obtained from S-rGO-NMP-H_2O-10h and S-rGO-DMF-H_2O-10h samples. Graphitic oxide gives a low angle-shifted (002) diffraction peak at around 11.8° (d space = 7.49 Å), indicating an increased interlayer distance compared to that (3.34 Å) (2 theta = 26.7°) in graphite structure. During the oxidation process of graphite, the graphitic structure would be destroyed to a great extent, so only a weak (002) diffraction peak with intensity of 1.2 kcps is seen (whereas the (002) diffraction intensity of the original graphite material was > 40 kcps). The graphitic structure could be completely disintegrated to form GO under the ultra-sonication vibration and could not be restored back after removal of the oxidized groups. As indicated by XRD of rGO powders from S-rGO-NMP-H_2O-10h and S-rGO-DMF-H_2O-10h, only very weak broad diffraction peaks at around 21° were detected (see insets in ***Figure 4-11***). These peaks must arise from the loose stacking between some rGO sheets on drying, as discussed below.

Figures 4-12a-d show together cross-section and top surface SEM images of free standing films from S-rGO-NMP-H_2O-10h and S-rGO-DMF-H_2O-10h, respectively. Differently from the graphene sheets in graphite and un-dispersed GO, the rGO sheets in the films only loosely stacked together, as evidenced by the obvious gap between the sheets. So essentially there is no van der Waals's bond forming between the sheets. For this reason, the prepared simply air dried free standing film and bulk solid rGO can be

readily re-dispersed well in a solvent like NMP, DMF or IPA. In addition, due to the absence of strong van der Waals's force between the sheets, many exfoliated edges of very thin sheets are seen on top surface of the film (***Figures 4-12c-d***), indirectly indicating that the films were mainly composed of very thin graphene sheets.

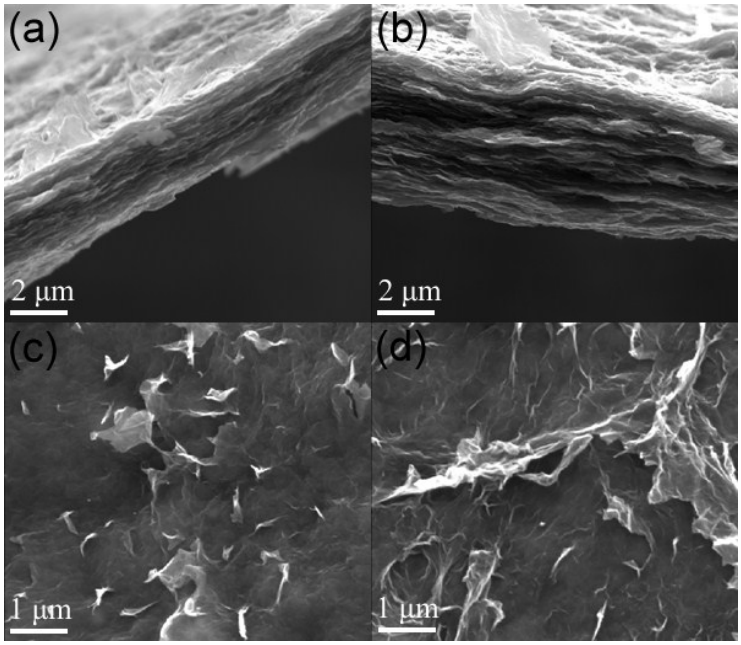

Figure 4-12. (a, c) SEM images of cross-section and top surface of a simply air-dried free-standing film from S-rGO-NMP-H_2O-10h; (b, d) SEM images of cross-section and top surface of a simply air-dried free-standing film from S-rGO-DMF-H_2O-10h.

For TEM and AFM observations, the collected solid rGO powders were re-dispersed and diluted in IPA. ***Figures 4-13a-d*** present TEM images and the selected electronic diffraction patterns (SAED) of the rGO products from S-rGO-NMP-H_2O-10h and S-rGO-DMF-H_2O-10h, revealing well dispersed sheets with some wrinkles. Higher magnification TEM images (images b and d) further reveal nearly transparent thin sheets. In addition, a dotted circle diffraction pattern was obtained, without obvious splitting between the spots, indicating that these sheets are single layered. The thickness measurements using AFM provided further evidence. Large scale AFM images of S-rGO-NMP-H_2O-10h and S-rGO-DMF-H_2O-10h (***Figures 4-14a,d and b,e***; 10 and 5 μm scan scale respectively) clearly cover many graphene sheets which have similar thickness as reflected by their similar contrasts. On the small scale (magnified) AFM (***Figures 4-14c & f***, 2 μm scale), most of the sheets look flat. The thicknesses of these sheets vary between 0.8-1 nm, as indicated by the white line and curves in ***Figures 4-14 b-c & e-f***. The measured thickness matches well with that of single layered graphene sheet.[27] By combining the XRD, SEM and TEM results presented and discussed above,

it can be concluded that monolayered graphene sheets were produced with the present technique.

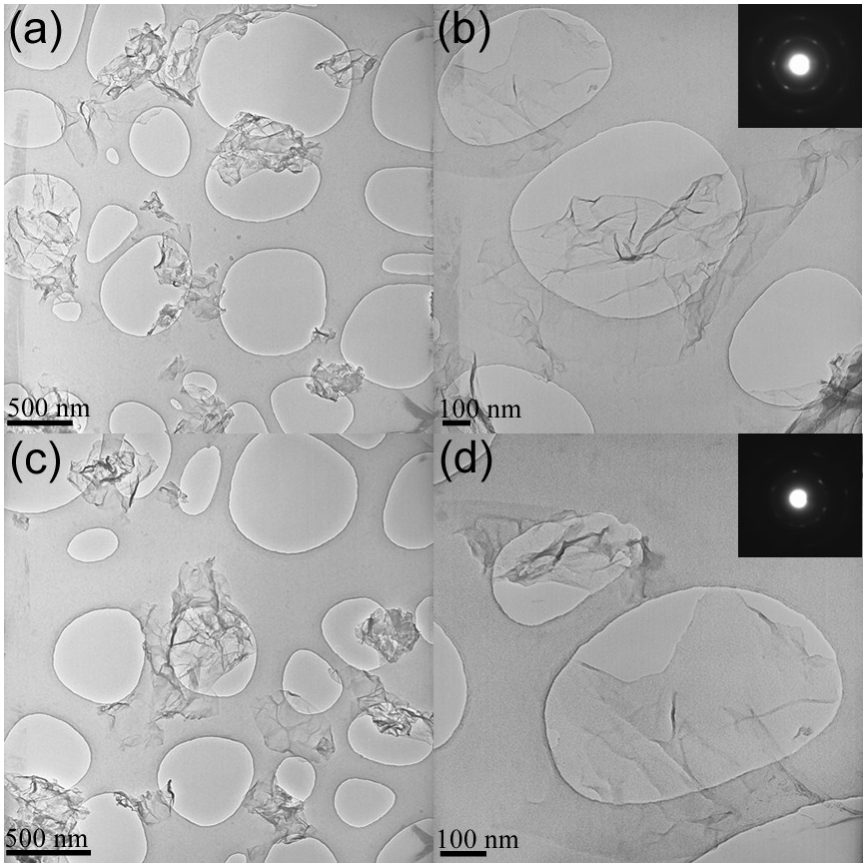

Figure 4-13. TEM images of S-rGO-NMP-H_2O-10h (a-b) and S-rGO-DMF-H_2O-10h (c-d). Insets are the SAED patterns of the rGO sheets.

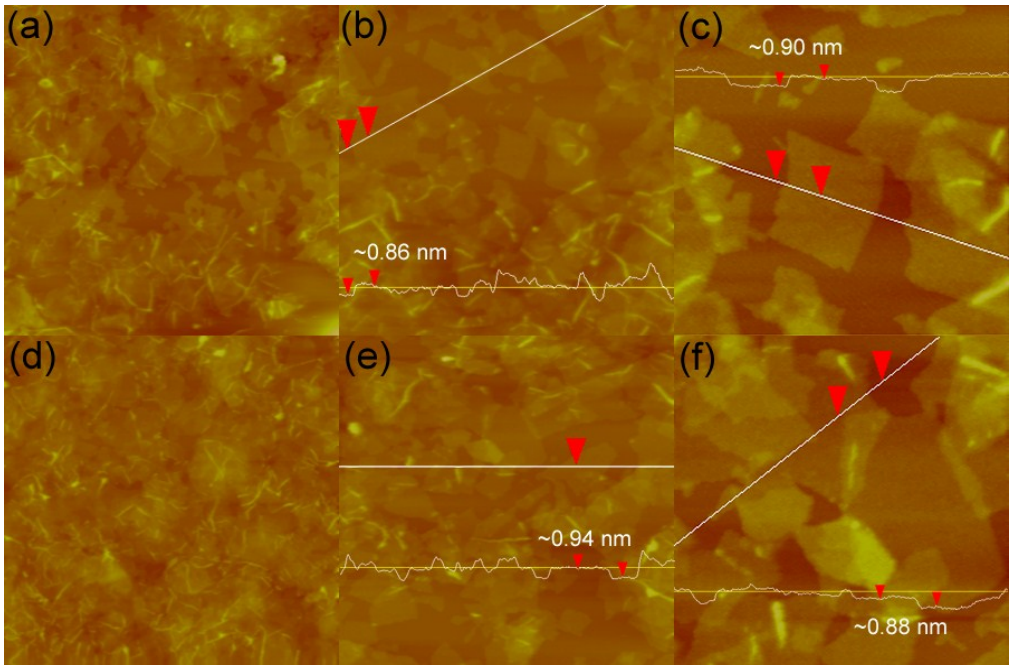

Figure 4-14. (a-c) AFM images of S-rGO-NMP-H_2O-10h on different scales: 10, 5 and 2 μm (from left to right); (d-f) AFM images of S-rGO-DMF-H_2O-10h on different scales: 10, 5 and 2 μm (from left to right).

The electrical conductivity of the prepared free standing films after drying in an oven at 150 ^oC for 3 h was also examined at room temperature by using the four-point probe method. As shown in ***Table 4-3***, the electrical conductivities of the films from S-rGO-NMP-H_2O-10h and S-rGO-DMF-H_2O-10h are about 16700 and 15200 S/m respectively, comparable to those of hydrazine reduced GO and much greater than those of BGO and rGO solvothermally reduced in an organic solvent.[18,28-30] BGO shows the lowest electrical conductivity. When the organic solvents such as NMP, DMAc and propylene carbonate (PC) were introduced into the solvothermal reaction system as surfactants, rGO products showed higher electrical conductivities. The reason was not clearly discussed in the relevant reference papers, but could be explained well based on one of the findings here, *i.e.*, the decrease of the surface tension of H_2O can promote the thermal deoxidation of GO. Another important finding from the data listed in ***Table 4-3*** is that samples produced by using a reducing agent[15] showed greater electrical conductivities than those of samples produced by the solvothermal reaction (with/without addition of a surfactant, except in one case reported in Ref. 25). In this exceptional case, a slightly greater electrical conductivity value (21600 $S.m^{-1}$)[25] was obtained. This is understandable, considering that the rGO was prepared in an NMP solvent at a relatively high temperature, so both the sheet size and the functionalization with NMP could have affected the electrical conductivity. Clearly, to prepare targeted

deeply deoxidized GO with a high electrical conductivity, a reducing agent and a surfactant should be used together. The products presented here showed higher electrical conductivity than $NaHSO_3$ reduced graphene,[15] which is attributable to the use of a surfactant and the better reducing effect of S.

Table 4-3. Electrical Conductivities of S-rGO-NMP-H_2O-10h, S-rGO-DMF-H_2O-10h and rGO prepared by other methods.

Description	Drying Temperature	Electrical Conductivity / $S.m^{-1}$
S-rGO-NMP-H_2O-10h	150 ^oC	1.67×10^4 (1 ± 9 %)
S-rGO-DMF-H_2O-10h	150 ^oC	1.52×10^4 (1 ± 8 %)
BGO[18]	air-dried	1×10^1
NMP Solvothermal rGO[18,25]	air-dried[18]	3.74×10^2
	250 ^oC[18]	1.38×10^3
	150 ^oC[25]	2.16×10^4
PC Solvothermal RGO[28]	150 ^oC	1.8×10^3
DMAc Solvothermal rGO with Microwaves[29]	--	2×10^2
Solvothermal rGO with $NaHSO_3$[15]	--	6.5×10^3
Hydrazine rGO[40]	150 ^oC	1.6×10^4

4.4 Conclusion

Base on experimental results presented above, it is reasonable to believe that an effective solvothermal deoxidation technique has been developed to prepare monolayered rGO, using solid S as a reducing agent and NMP or DMF as a surfactant. No obvious graphitic structure remained in as-prepared highly deoxidized solid rGO products which showed a high electrical conductivity (15200~16700 S/m). Although they were free from functional groups, they showed comparable dispersibility to that of functionalized rGO/graphene. In addition, it is inter-convertible between different rGO forms, such as agglomerates, dried powders, free-standing films and suspensions in a solvent, which is a great merit for a range of future applications. Reducing effects of H_2S and H_2SO_3 generated from the reaction between S and H_2O, combined with the thermal deoxygenation of GO at 110 ^oC, are believed to be responsible for the full deoxidation of GO. Complete chemical conversion from GO to graphene cannot be achieved by using only S in the boiling aqueous GO, due to probably π-π stacking and agglomeration (self-assembly) between rGO sheets. The introduction of suitable water soluble surfactants such as NMP and DMF, could avoid or alleviate such problems, thus favoring the deoxidation of GO. Based on this, it can be expected that other water soluble surfactants with suitable surface tension together with other moderate reducing agents (this will be

further confirmed in the next chapter) also can be used to prepare high quality chemically converted graphene for a wide range of applications.

References and Notes

[1] K. S. Novoselov, A. K. Geim, S. V. Morozov, D. Jiang, Y. Zhang, S. V. Dubonos, I. V. Grigorieva and A. A. Firsov, Electric Field Effect in Atomically Thin Carbon Films. *Science* **2004**, *306*, 666-669.

[2] A. N. Obraztsov, Chemical Vapour Deposition: Making Graphene on a Large Scale. *Nat. Nanotechnol.* **2009**, *4*, 212-213.

[3] C. Berger, Z. Song, T. Li, X. Li, A. Y. Ogbazghi, R. Feng, Z. Dai, A. N. Marchenkov, E. H. Conrad, P. N. First and W. A. De Heer, Ultrathin Epitaxial Graphite: 2D Electron Gas Properties and a Route toward Graphene-based Nanoelectronics. *J. Phys. Chem. B* **2004**, *108*, 19912-19916.

[4] Y. Hernandez, V. Nicolosi, M. Lotya, F. M. Blighe, Z. Sun, S. De, I. T. McGovern, B. Holland, M. Byrne, Y. K. Gun'Ko, J. J. Boland, P. Niraj, G. Duesberg, S. Krishanmurthy, R. Goodhue, J. Hutchison, V. Scardaci, A. C. Ferrari and J. N. Coleman, High-yield Production of Graphene by Liquid-phase Exfoliation of Graphite. *Nat. Nanotechnol.* **2008**, *3*, 563-568.

[5] S. Stankovich, D. A. Dikin, R. D. Piner, K. A. Kohlhaas, A. Kleinhammes, Y. Jia, Y. Wu, S. T. Nguyen and R. S. Ruoff, Synthesis of Graphene-based Nanosheets *via* Chemical Reduction of Exfoliated Graphite Oxide. *Carbon* **2007**, *45*, 1558-1565.

[6] J. Wang, K. K. Manga, Q. Bao and K. P. Loh, High-Yield Synthesis of Few-layer Graphene Flakes through Electrochemical Expansion of Graphite in Propylene Carbonate Electrolyte. *J. Am. Chem. Soc.* **2011**, *133*, 8888-8891.

[7] H. P. Boehm, A. Clauss, G. O. Fischer and U. Hofmann, Das Adsorptionsverhalten sehr dünner Kohlenstoff-Folien. *Z. Anorg. Allg. Chem.* **1962**, *316*, 119-127.

[8] D. R. Dreyer, S. Park, C. W. Bielawski and R. S. Ruoff, The Chemistry of Graphene Oxide. *Chem. Soc. Rev.* **2010**, *39*, 228-240.

[9] Y. Xu, K. Sheng, C. Li and G. Shi, Self-Assembled Graphene Hydrogel *via* a one-step Hydrothermal Process. *ACS Nano* **2010**, *7*, 4324-4330.

[10] D. Li, M. B. Müller, S. Gilje, R. B. Kaner and G. G. Wallace, Processable Aqueous Dispersions of Graphene Nanosheets. *Nat. Nanotechnol.* **2008**, *3*, 101-105.

[11] H.-J. Shin, K. K. Kim, A. Benayad, S.-M. Yoon, H. K. Park, I.-S. Jung, M. H. Jin, H.-K. Jeong, J. M. Kim, J.-Y. Choi and Y. H. Lee, Efficient Reduction of Graphite Oxide by Sodium Borohydride and Its Effect on Electrical Conductance. *Adv. Funct. Mater.* **2009**, *19*, 1987-1992.

[12] X. Fan, W. Peng, Y. Li, X. Li, S. Wang, G. Zhang and F. Zhang, Deoxygenation of Exfoliated Graphite Oxide under Alkaline Conditions: A Green Route to Graphene Preparation. *Adv. Mater.* **2008**, *20*, 4490-4493.

[13] Y. Chen, X. Zhang, P. Yu and Y. Ma, Stable Dispersions of Graphene and Highly Conducting Graphene Films: A New Approach to Creating Colloids of Graphene Monolayers. *Chem. Commun*. **2009**, 4527-4529.

[14] G. Wang, J. Yang, J. Park, X. Gou, B. Wang, H. Liu and J. Yao, Facile Synthesis and Characterization of Graphene Nanosheets. *J. Phys. Chem. C* **2008**, *112*, 8192-8195.

[15] W. Chen, L. Yan and P. R. Bangal, Chemical Reduction of Graphene Oxide to Graphene by Sulfur-containing Compounds. *J. Phys. Chem. C* **2010**, *114*, 19885-19890.

[16] G. Wang, X. Shen, B. Wang, J. Yao and J. Park, Synthesis and Characterisation of Hydrophilic and Organophilic Graphene Nanosheets. *Carbon* **2009**, *47*, 1359-1364.

[17] S. Stankovich, R. D. Piner, S. T. Nguyen and R. S. Ruoff, Synthesis and Exfoliation of Isocyanate-Treated Graphene Oxide Nanoplatelets. *Carbon* **2006**, *44*, 3342-3347.

[18] S. Dubin, S. Gilje, K. Wang, V. C. Tung, K. Cha, A. S. Hall, J. Farrar, R. Varshneya, Y. Yang and R. B. Kaner, A one-step, Solvothermal Reduction Method for Producing Reduced Graphene Oxide Dispersions in Organic Solvents. *ACS Nano* **2010**, *4*, 3845-3852.

[19] Handbook of Chemical Reactions of Elements. ed. S. Yao, Y. Zhu, S. He and Y. Nie, *Henan Jiaoyu Chu Ban She* **1998**, 498 pp.

[20] H. Lin, Z. Li, K. Tohji, N. Tsuchiya and N. Yamasaki, in Water, Steam and Aqueous Solutions for Electric Power: Advances in Science and Technology, *Proceedings of the 14th International Conference on the Properties of Water and Steam*, ed. M. Nakahara, N. Matubayasi, M. Ueno, K. Yasuoka and K. Watanabe, Maruzen Co., Ltd., **2005**, pp. 365-368.

[21] W. S. Hummers and R. E. Offeman, Preparation of Graphitic Oxide. *J. Am. Chem. Soc.* **1958**, 80, 1339.

[22] Z. Luo, Y. Lu, L. A. Somers and A. T. C. Johnson, High Yield Preparation of Macroscopic Graphene Oxide Membranes. *J. Am. Chem. Soc.* **2009**, *131*, 898-899.

[23] J. Luo, L. J. Cote, V. C. Tung, A. T. L. Tan, P. E. Goins, J. Wu and J. Huang, Graphene Oxide Nanocolloids. *J. Am. Chem. Soc.* **2010**, *132*, 17667-17669.

[24] J. Li, H. Lin, Z. Yang and J. Li, A Method for the Catalytic Reduction of Graphene Oxide at Temperatures Below 150 ^{o}C. *Carbon* **2011**, *49*, 3024-3030.

[25] V. H. Pham, T. V. Cuong, S. H. Hur, E. Oh, E. J. Kim, E. W. Shin and J. S. Chung, Chemical Functionalization of Graphene Sheets by Solvothermal Reduction of a Graphene Oxide Suspension in N-methyl-2-pyrrolidone. *J. Mater. Chem.* **2011**, *21*, 3371-3377.

[26] F. Tuinstra and J. L. Koenig, Raman Spectrum of Graphite. *J. Chem. Phys*. **1970**, *53*, 1126-1130.

[27] X. Li, X. Wang, L. Zhang, S. Lee and H. Dai, Chemically Derived, Ultrasmooth Graphene Nanoribbon Semiconductors. *Science* **2008**, *319*, 1229-1232.

[28] Y. Zhu, M. D. Stoller, W. Cai, A. Velamakanni, R. D. Piner, D. Chen and R. S. Ruoff, Exfoliation of Graphite Oxide in Propylene Carbonate and Thermal Reduction of the Resulting Graphene Oxide Platelets. *ACS Nano* **2010**, *4*, 1227-1233.

[29] W. Chen, L. Yan and P. R. Bangal, Preparation of Graphene by the Rapid and Mild Thermal Reduction of Graphene Oxide Induced by Microwaves. *Carbon* **2010**, *48*, 1146-1152.

[30] S. Park, J. An, I. Jung, R. D. Piner, S. J. An, X. Li, A. Velamakanni and R. S. Ruoff, Colloidal Suspensions of Highly Reduced Graphene Oxide in a Wide Variety of Organic Solvents. *Nano Lett.* **2009**, *9*, 1593-1597.

Chapter V. Surface Energy Engineering in Solvothermal Deoxidation of Graphene Oxide

5.1 Introduction

As a monolayered carbon material with an aromatic substructure, graphene has attracted remarkable attention due to its interesting physical and chemical properties.[1] Graphene could find application in many areas, such as supercapacitors,[2] sensors,[3] liquid crystal devices,[4] electrodes[5] and clean energy technologies.[6] Many techniques have been developed to prepare graphene, including chemical vapor deposition,[7] epitaxial growth,[8] liquid-phase exfoliation,[9] electrochemical expansion[10] and chemical reduction.[11] Among these, the solvothermal chemical reduction of graphene oxide (GO) has been investigated intensively. It is highly attractive as it potentially offers a relatively economical and scalable route to producing graphene, which is highly desired for industrial applications.

In a general solvothermal deoxidation route, graphite should be initially oxidized to form graphite oxide (with weak interlayer van der Waals' force), which can be exfoliated easily and chemically reduced to form graphene sheets. For this purpose, many reducing agents (*e.g.* hydrazine,[11] $NaBH_4$,[12] and strong alkalis[13]) have been investigated. Unfortunately, deep deoxidation of GO and highly dispersable reduced GO (rGO) are difficult to achieve using this approach. It is unlikely that this will be solved with more powerful reducing agents, given the strength of many that have been used already, but may be due to the tendency for the GO/rGO sheets to agglomerate *via* π-π stacking. Self-assembled rGO sheets are strongly adhered and cannot be easily exfoliated subsequently, leading to poor dispersibility and making further processing difficult. These problems appear to arise from the highly negatively charged nature of GO and the probable existence of carboxyl groups on rGO surfaces (when not deeply deoxidized). D. Li *et al.* suggested controlling the electrostatic repulsion of the rGO sheets by tuning the solvothermal system to have a pH ~ 10.[14] However, this procedure is not appropriate for the preparation of deeply deoxidized GO with few or no surface groups. The study in ***Chapter IV*** (also published as Ref. 15) confirmed that

GO cannot be reduced well with this approach, possibly due to the high degree of oxidization of the GO raw materials here and agglomeration/self-assembly of rGO sheets (also see ***Figure S5-1a***). Overcoming these difficulties to prepare deeply deoxidized GO with high dispersibility has became a significant technical challenge.

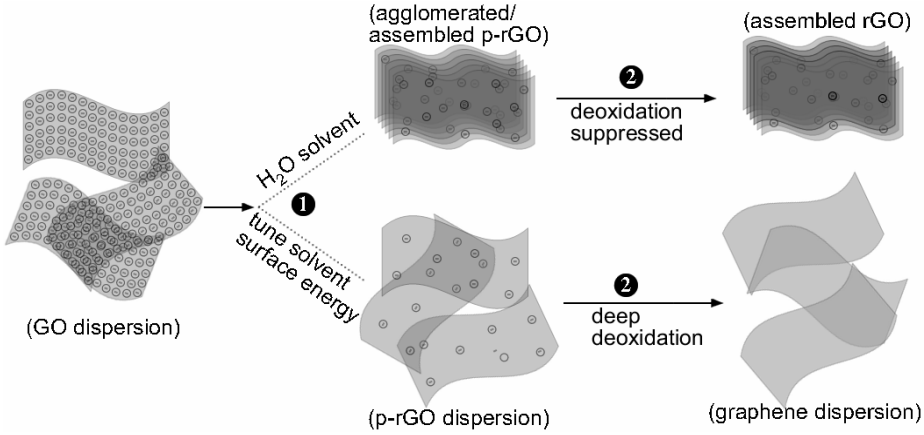

Scheme 5-1. GO deoxidation stages. p-rGO is the product of stage 1 reaction. With the H_2O alone, p-rGO agglomerated and assembled together which highly suppressed the further deoxidation. By contrast, by tuning solvent surface energy, the p-rGO can be readily dispersed and favour deep deoxidation and good dispersibility of the graphene product.

Here, the agglomeration/self-assembly of GO/rGO sheets is suggested should be considered the primary reason for suppression of GO deoxidation and low dispersibility of the rGO. In ***Chapter IV***, the addition of NMP (N-methyl-2-pyrrolidone) and DMF (dimethylformamide) to a solvothermal system containing S as the reducing agent allowed GO deoxidation to be promoted effectively and highly dispersible rGO with high electrical conductivity to be formed. Although the precise mechanism is unclear, it is believed that the lower surface tension of NMP/DMF compared to H_2O was responsible for the improved behaviour. As generally recognised, GO is hydrophilic while rGO (or re-stacked rGO) is insoluble with a surface energy close to that of graphene (or graphite). The dispersion of rGO sheets should, therefore, be strongly dependent on the surface energy of the solvent (minimal surface enthalpy of the dispersion is required).[9] Therefore, assuming reasonable GO concentrations (heated GO with high concentration tends to self-assemble[16]), tuning the solvent surface energy might be an effective way to avoid the agglomeration/self-assembly of rGO and promote the deoxidation reaction. In this chapter, a method of surface energy engineering was proposed for solvothermal deoxidation of GO (see ***Scheme 5-1***). By tuning surface energy of the solvent to minimize the surface enthalpy of the dispersion, the π-π stacked agglomeration and self-assembly between partially reduced GO (p-rGO) can be effectively alleviated and thus allow further deoxidation. The resultant deeply reduced GO sheets also show good

dispersibility without any surface functionalization. The experimental results and empirical calculations provide a good description of the relevant mechanisms and allow the solvent surface energy (at 100 °C) for the solvothermal deoxidation reaction to be optimized at around 85.6 mJ/m^2 (between 84.7-87.6 mJ/m^2). The insight gained here into the solvothermal deoxidation of GO is imperative to future larger scale industrial fabrication.

5.2 Experimental Methods

5.2.1 Preparation of Graphite Oxide and GO

Graphite oxide was prepared following the Hummers method (also described in ***Section 4.2.1***). The as-prepared graphite oxide was fully stirred and dispersed in water to form 500 mL homogeneous aqueous solution with the concentration of 4 mg/mL (the concentration here is defined as the ''net'' carbon weight (excluding the weight of oxygen containing groups) divided by volume). Before the deoxidation reaction, the graphitic oxide solution was further homogenized and exfoliated for 2 h using a Bandelin Sonorex RK-100H ultrasonic vibrator to form monolayered GO.

5.2.2 Preparation of Fresh $FeCl_2$

For deoxidation reaction, a fresh $FeCl_2$ solution was prepared as following procedures: 1) 20 g Fe was mixed with 59.1 mL 36 wt% HCl in a three-neck-flask; 2) the mixing was stirred for 10 h until no visible bubble was observed. At this moment, the pH value of the solution is near neutral (< 7); 3) the green $FeCl_2$ solution was collected after the removal of residual solid Fe using filtering. Then the $FeCl_2$ solution was diluted to 200 mL and threated for 10 mins in ultrasonic vibrator to remove soluble oxygen; 4) N_2 was bubbled into the solution (in a glass bottle) for 10 minutes. Then the bottle was carefully sealed for the next GO deoxidation reaction.

5.2.3 Preparation of rGO

Different solutions were used in the preparation. Sigma-Aldrich NMP and DMF were used as surfactants. Typically (preparing Fe-rGO-NMP-H_2O, NMP-H_2O equals 1:1 in volume), 25 mL prepared GO solution with concentration of 0.5 mg/mL, 20 mL prepared fresh $FeCl_2$ and 55 mL solution (the mixture of 50 mL NMP/DMF and 5 mL H_2O) were mixed and sonicated for 5 mins to form homogenous solution. The mixture was transferred into a 150 mL three neck round flask (connected with a condensing tube) with stirring at 100 °C (solvent temperature) on a magnetic stirring hot plate. Correspondingly, the final concentration of GO in the reaction was controlled as 0.125 mg/mL. The deoxidation procedures of GO in other solvents are the same except the

tuning of solvent to keep 0.125 mg/mL concentration of GO and the addition of 20 mL $FeCl_2$. Samples were collected at different reaction stages for the time-dependent UV/Vis tests (collected rGO was basically washed using HCl solution before tests). For further characterisations, samples were deeply washed using HCl/HNO_3 to remove any Fe impurities. For the deoxidation reaction of GO with long reaction time (15 h), after 10 h refluxing, another 20 mL $FeCl_2$ was further added into the reaction system. Besides, different rGO samples were also prepared using solid S reducing agent in different solvents (H_2O, different NMP-H_2O and DMF-H_2O solvents, GO concentration was also controlled as 0.125 mg/mL). The preparation is same as it described in ***Chapter IV***. As for preparation of rGO using hydrazine, 75 mL GO (0.125 mg/mL) was mixed with 1.5 mL hydrazine (35 wt%) and reacted at 100 °C (solvent temperature). The pH value of the solvent was measured as 9-11. After 12 h reaction, add another 1.5 mL hydrazine into the solvent and react for another 2 h to verify whether the reaction is completed.

Table 5-1. List of the main test samples. The GO concentrations for all the reactions are controlled as 0.125 mg/mL (see ***Section 4.2.2*** for the definition of GO concentration).

rGO samples	Solvent (volume ratio)	Reducing agents
BGO-H_2O-*x*	H_2O	--
Fe-rGO-H_2O-*x*	H_2O	$FeCl_2$
Fe-rGO-NMP-H_2O-*x*	NMP-H_2O (1:1)	$FeCl_2$
Fe-rGO-DMF-H_2O-*x*	DMF-H_2O (1:1)	$FeCl_2$
S-rGO-NMP-H_2O-*x*	NMP-H_2O (1:1)	S
S-rGO-NMP-H_2O-*x*	NMP-H_2O (3:2)	S
S-rGO-NMP-H_2O-*x*	NMP-H_2O (2:1)	S
S-rGO-DMF-H_2O-*x*	DMF-H_2O (1:1)	S
S-rGO-DMF-H_2O-*x*	DMF-H_2O (2:1)	S
S-rGO-DMF-H_2O-*x*	DMF-H_2O (3:1)	S
S-rGO-H_2O-*x*	H_2O	S
H-rGO-H_2O-*x*	H_2O	Hydrazine

5.3 Results and Discussion

The various rGO samples and solvents used in this study with various solvothermal reaction times (*x*) at 100 °C solvent temperature are summarized in ***Table 5-1***.

5.3.1. Promotion of GO Deoxidation by Adding NMP and DMF

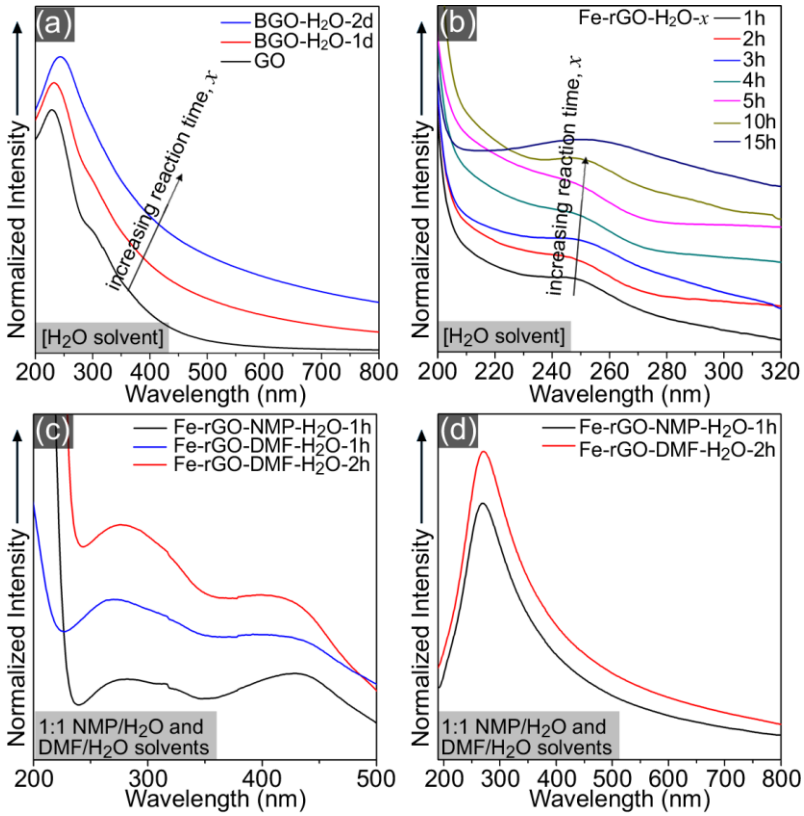

Figure 5-1. UV/Vis absorption spectra: (a) GO and BGO-H_2O-*x*; (b) Fe-rGO-H_2O-*x*; (c) Fe-rGO-NMP-H_2O-1h (1:1 NMP/H_2O) and Fe-rGO-DMF-H_2O-*x* (*x* = 1, 2 h, 1:1 DMF/H_2O) (samples were lightly washed using HCl to show absorption peak of rGO); (d) Fe-rGO-NMP-H_2O-1h and Fe-rGO-DMF-H_2O-2h (samples were washed until Fe absorption at above 400 nm disappear). For clarity, the zero intensities of the backgrounds in all images were shifted.

The reduction of GO using Fe^{2+} in an aqueous environment is first presented as a control. The different electronic structures of GO and graphene means that time-dependent ultraviolet-visible (UV/Vis) spectrophotometry can be used to monitor the extent of GO deoxidation during the reaction. ***Figure 5-1a*** gives the UV/Vis spectra of GO and BGO-H_2O-*x* (boiled GO, *x* = 1, 2 days). GO solutions exhibit two main UV/Vis absorption peaks at around 229 and 300 nm, corresponding the π→π* (C=C) and the n→π* (C=O) transitions of GO, respectively.[15] Upon 1 day boiling, this n→π* (C=O) transition weakened and the π→π* (C=C) transition shifted to 232 nm. The π→π* (C=C) transition shifted further to 243.5 nm after 2 days boiling, indicating that the electronic conjugation of graphene had been slightly restored. $FeCl_2$ is unstable in the heated aqueous system and its addition can promote GO deoxidation. As shown in ***Figure 5-1b***, in contrast to GO, the π→π* transition (C=C) of Fe-rGO-H_2O-1h in UV/Vis absorption spectra is already red-shifted to 248 nm, much higher than that for BGO-H_2O-1d (232 nm) and BGO-H_2O-2d (243.5 nm) (***Figure 5-1a***). A further shift of this absorption peak

to 252 nm was found after 10 h reaction time (***Figure 5-1b***). These features suggest that the $FeCl_2$ is able to deoxidize GO to certain extent in this reaction scheme (without inert atmosphere protection). However, with the addition of $FeCl_2$ (20 mL) alone, GO cannot be deeply deoxidized. Further addition of 20 mL $FeCl_2$ and reacting for another 5 h does not further promote the deoxidation reaction. As indicated by the UV/Vis spectra of Fe-rGO-H_2O-15h (with another 20 mL $FeCl_2$ added), the π→π* transition (C=C) was found at around 254 nm, which is only a slightly longer wavelength than that of Fe-rGO-H_2O-10h (252 nm). The suppression on the GO deoxidation here is possibly due to the agglomeration and self-assembly of GO and p-rGO (see ***Scheme 5-1***) in the H_2O solvent. It is noted that the deoxidation ability of Fe^{2+} was probably also suppressed by the oxygen in H_2O (to form Fe^{3+}) and the use of inert gas may be useful to promote the deoxidation reaction. Nevertheless, the following study (addition of NMP and DMF) indicates that the introduction of inert atmosphere is unnecessary for the deep deoxidation of GO.

It is reasonable to hypothesize that reduction of the solvent surface tension from that of H_2O will prevent the agglomeration and self-assembly between the p-rGO sheets (see ***Scheme 5-1***). To verify this prediction, NMP and DMF were further introduced into the solvent, forming 1:1 NMP-H_2O (volume ratio, see ***Table 5-1***, the following specified binary solvents are all mixed with volume ratio) and 1:1 DMF-H_2O, respectively, for GO deoxidation. ***Figure 5-1c*** gives the UV/Vis absorption spectra of these rGO samples (Fe-rGO-NMP-H_2O-1h, Fe-rGO-DMF-H_2O-1h and Fe-rGO-DMF-H_2O-2h). Two absorption bands at around 269-276 nm and 440 nm were found in these spectra, which correspond to the π→π* transition (C=C) of rGO and Fe absorption respectively. Interestingly, after undergoing only 1 h refluxing reaction, the π→π* transition (C=C) of Fe-rGO-DMF-H_2O-1h was already red-shifted to 269 nm, and shifted further to 276 nm with 2 h reaction time (Fe-rGO-DMF-H_2O-2h). The π→π* transition (C=C) of Fe-rGO-NMP-H_2O-1h was red-shifted just as much and found at around 276 nm. Extending the reaction time further in either case (Fe-rGO-NMP-H_2O and Fe-rGO-DMF-H_2O) did not produce any further peak shift, suggesting that the deoxidation reaction had reached a limit. Here, the π→π* transitions of C=C (Fe-rGO-NMP-H_2O-1h and Fe-rGO-DMF-H_2O-2h) were at higher wavelengths than the generally recognised value of graphene (270 nm),[14] which could be due to the interaction of Fe and rGO.[17] Once the Fe was removed from rGO surfaces (***Figure 5-1d***), the π→π* transition (C=C) of rGO was restored to at around 270 nm, corresponding well with that of graphene.[14] Evidently,

unlike Fe-rGO-H_2O-*x* (*x*= 1, 2, 3, 4, 5, 10, 15 h), the simple addition of NMP and DMF promotes GO deoxidation highly effectively.

Further FT-IR (***Figure S5-2a***), Raman (***Figure S5-2b***), XRD (***Figure S5-3***) and AFM (***Figures S5-4 & 5-5***) analyses of the product collected from the Fe-rGO-NMP-H_2O-1h and Fe-rGO-DMF-H_2O-2h reactions confirmed that the GO was reduced well and retained a thin structure. As shown in ***Table 5-2***, both rGO samples (Fe-rGO-NMP-H_2O-1h and Fe-rGO-DMF-H_2O-2h) had good dispersibilities that were highly dependent on the solvent surface tension. The highest dispersibility of the rGO (1.34-1.35 mg/mL) was found in NMP with a surface tension of ~40.79 mN/m (20 °C)[18], whereas the lowest (0.14-0.15 mg/mL) was found in H_2O with surface tension of ~72.74 mN/m (20 °C)[18]. DMF has a surface tension of around 37.1 mN/m[18] at 20 °C, which resulted in moderate dispersion of rGO (0.76-0.78 mg/mL). Although IPA (isopropyl alcohol) has much lower surface tension than NMP and DMF (see ***Table 5-2***), it still showed a reasonably good dispersion ability (0.52-0.53 mg/mL). These data are comparable with those of graphene prepared using routes with surface functionalization.[19]

Table 5-2. Dispersibility (mg/mL at 20 °C) of Fe-rGO-NMP-H_2O-1h and Fe-rGO-DMF-H_2O-2h in NMP, DMF, IPA and H_2O.

Description	NMP	DMF	IPA	H_2O
Surface Tension (at 20 °C, $mN.m^{-1}$)[18]	~40.79	~37.1	~21.7	~72.74
Fe-rGO-NMP-H2O-1h dispersibility	1.5	0.8	0.5	0.1
Fe-rGO-DMF-H2O-2h dispersibility	1.4	0.8	0.5	0.2

5.3.2. Surface Energy in the Solvolthermal Deoxidation Reaction of GO

The above study confirms that the addition of NMP and DMF can improve the deoxidation of GO. This is consistent with the addition of the surfactant solvent of lower surface tension (*e.g.* NMP and DMF) alleviating the aggregation of p-rGO sheets, leading to promotion of GO deoxidation and creation of thin rGO with good dispersibility (see ***Scheme 5-1***). However, this analysis provokes further questions: 1) why is the surface tension imperative for the promotion of GO reduction; 2) can a single solvent of H_2O, NMP and DMF be used to prepare highly exfoliated rGO at 100 °C (boiling point of H_2O at 1 atmos) or other temperatures; and 3) is surface tension the only solvent property that determines the promotion of GO reduction? To answer these questions, further studies on the surface energy engineering in the solvothermal deoxidation of GO were conducted.

Ideally, in solvothermal reaction systems, the GO and p-rGO should be highly exfoliated and dispersed to satisfy high contact surface area with the reducing agents. For estimating the solvent surface tension to disperse graphene, a model[9] could be considered, which was used to exfoliate non-oxidized graphene from graphite by calculating the energy balance of the exfoliation process. This can be expressed as the enthalpy of the mixing (ΔH_{mix}) per unit volume:

$$\frac{\Delta H_{mix}}{V_{mix}} \approx \frac{2}{T_{graphite}}(\delta_G - \delta_{Sol})^2 \phi \qquad \textit{(eq. 5-1)}$$

where δ_G and δ_{Sol} are the square root of the surface energy of graphene (E_{Sur}^{G}) and the solvent (E_{Sur}^{Sol}), respectively, and $T_{graphite}$ and ϕ are the thickness of the re-stacked p-rGO (graphite) and p-rGO (graphene) volume fractions, respectively. E_{Sur}^{G} is defined as the energy per unit area required to overcome the van der Waals force between the re-stacked p-rGO (graphite) layers. Therefore, ΔH_{mix} is dependent on the balance of the surface energies of p-rGO and the solvent (E_{Sur}^{G} and E_{Sur}^{Sol}), and the minimal enthalpy to stabilize the exfoliated p-rGO sheets (and suppress their re-stacking) can only be achieved when E_{Sur}^{G} matches E_{Sur}^{Sol}. On this basis, the suitable solvent surface tension (γ) for stabilizing exfoliated p-rGO can be found using:

$$\gamma = E_{Sur}^{Sol} - TS_{Sur}^{Sol} \qquad \textit{(eq. 5-2)}[20]$$

where T is temperature and S_{Sur}^{Sol} is the solvent surface entropy ($-\partial\gamma/\partial T$). Values of E_{Sur}^{Sol} are close to the surface energies of p-rGO. Although reported graphite surface energies vary from 55-85 mJ/m^2,[20-26] Colmen *et al.*[9] use *eq*. 5-1 & 5-2 and their experimental results to estimate a value lying between 70-80 mJ/m^2. The existence of oxygen on the surface of p-rGO also increases the surface energy.[27] Therefore, for calculating the matched solvent surface tension to avoid p-rGO agglomeration, the relevant surface energy of the p-rGO should be considered higher (*e.g.* 80-90 mJ/m^2) than that of the pure graphite/graphene that has been used previously. Although it is difficult to calculate the p-rGO surface energy directly, values can be estimated from the optimized reaction solvent surface energy (discussed below).

Using this approach, it is feasible to predict whether the single solvent of H_2O, NMP and DMF can be used to prepare highly exfoliated rGO. For example, at room temperature, Colmen *et al.* predicted that solvents with surface tension in the range of 40.7-50.7 mN/m (with defined surface entropy, S_{Sur}^{Sol}, as 0.1 mJ.m^{-2}.K^{-1}) could be used to disperse graphene.[9] For higher temperatures, it is necessary to calculate temperature-dependent solvent entropy. Solvent (NMP, DMF and H_2O) surface tensions as a function

of temperature have been studied previously and can be represented by interpolating data[31] and by the Guggenheim-Katayama surface tension equation[32,33] (*eq.* 5-3 for H_2O, *eq.* 5-4 for NMP and DMF):

$$\gamma = B\left(\frac{T_c - T}{T_c}\right)^{\mu}\left[1 + b\left(\frac{T_c - T}{T_c}\right)\right](1 + b) \qquad \textit{(eq. 5-3)}$$

$$\gamma = \gamma_0\left(1 - \frac{T}{T_c}\right)^{n} \qquad \textit{(eq. 5-4)}$$

where B = 235.8×10^{-3} N/m, b = -0.625, μ = 1.256, T is the solvent temperature, T_c is the critical temperature, γ_0 is a constant for each liquid and n is an empirical factor, whose value is 11/9 for organic liquids. With the generally accepted surface tensions of H_2O, NMP and DMF at different temperatures,[31,34] the surface tension (γ) of H_2O, NMP, DMP at different temperatures can be calculated (***Figure 5-2a***, the parameters of the solvents are listed in ***Table 5-3***). These calculations agree well with previously tested surface tensions at different temperatures.[31,34] Below the critical temperature, the surface tension of all these solvents decreases approximately linearly with temperature, further suggested the accuracy of the plots. Therefore, the solvent surface entropy ($S_{Sur}^{Sol} = -\partial\gamma/\partial T$) versus temperature can be obtained by differentiation (***Figure 5-2b***). From ***Figure 5-2b*** it is seen that S_{Sur}^{Sol} for all solvents varies gradually below 550 K but very dramatically close to T_c. This suggests that the surface entropy of NMP and DMF cannot be treated simply as 0.1 mN.m^{-1}.K^{-1}, as previously used for liquid exfoliation (using sonication) of graphite,[9,35-36] when calculating the system balance (solvent were heated during sonication).

Table 5-3. Properties (at 1 atmos) of H_2O, NMP and DMF

Description	H_2O	NMP	DMF
Boiling point (K)	373.15	477.5	426
Melting point (K)	273.15	249.15	212.15
$\gamma_{293.15K}$ (mN.m^{-1})[18]	72.74	40.79	37.1
T_c (K)[28-30]	647.15	724.15	647.15

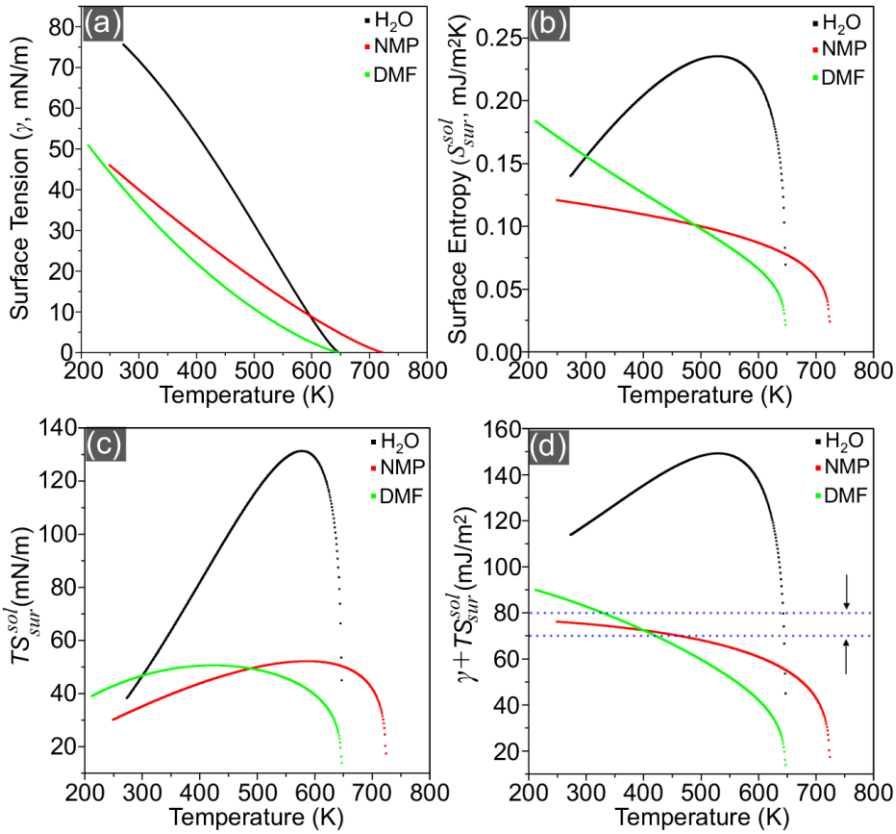

Figure 5-2. Solvent parameters as a function of temperature of H_2O, DMF and NMP: (a) surface tension (γ); (b) surface entropy (S_{Sur}^{Sol}) and (c) $T.S_{Sur}^{Sol}$ and d) the solvent surface energy ($\gamma + T.S_{Sur}^{Sol}$).

Figures 5-2c & d gives temperature-dependence of $T.S_{Sur}^{Sol}$ and $\gamma + T.S_{Sur}^{Sol}$ (solvent surface energy) for the three solvents, respectively. The suitable temperature range for efficient dispersal of p-rGO can be found by using *eq.* 5-2 and assuming that the p-rGO surface energy (E_{Sur}^{Sol}, close to the solvent surface energy $\gamma + T.S_{Sur}^{Sol}$) should be in the range 70-80 mN/m (mJ/m^2). The usable temperature region for H_2O is quite narrow at around 634 - 644 K, which is close to H_2O's T_c (647 K). The dispersal temperature of NMP should below 461 K (188 °C) while that for DMF should be between 328 and 420 K (55-147 °C). These calculations suggest, therefore, that p-rGO can be dispersed well in NMP and DMF with various temperatures, although the actual effective temperature regions of these solvents should be reduced slightly as the p-rGO surface energy is higher than that of pure graphene, as discussed above. Nevertheless, dispersing p-rGO in H_2O is unpractical due to the narrow temperature region (634 to 644 K) close to the critical temperature and far above the boiling point. The calculated result also explains why GO can be deoxidized in NMP at 180 °C to form rGO with high dispersibility.[19]

Table 5-4. Surface tension (mN.m^{-1}), surface entropy (S_{Sur}^{Sol}, mN.m^{-1}.K^{-1} at 100 °C) and the properties of different solvents. In this table, *x* and *y* represent the mole ratio of the organic solvent (NMP, DMF) and H_2O in the binary solvents of NMP-H_2O and DMF-H_2O respectively.

Solvent (volume ratio)	$\gamma_{293.15\ k}$	*x*	*y*	$\gamma_{373.15\ k}$	S_{Sur}^{Sol}
NMP-H_2O (1:1)	49.67	0.158	0.842	34.972	0.154
NMP-H_2O (3:2)	47.62	0.220	0.780	34.928	0.154
NMP-H_2O (2:1)	46.12	0.273	0.727	34.649	0.153
DMF-H_2O (1:1)	49.23	0.190	0.810	36.109	0.159
DMF-H_2O (2:1)	44.98	0.319	0.681	32.992	0.146
DMF-H_2O (3:1)	43.11	0.413	0.587	31.620	0.140

However, once binary solvents are introduced into the solvothermal system, the changes of solvent surface tension and surface entropy are much more complex but afford a high degree of tunability. ***To discover the most suitable solvent ratios of NMP-H_2O and DMF-H_2O at 100 ℃***, the surface tensions of different solvent were measured using a Krüss K100 tensiometer (***Table 5-4***). This was performed at room temperature (20°C) as it is difficult to measure surface tension at 100 °C directly due to H_2O boiling. As noted above, γ should be a simple linear function of temperature when well below T_c. All of the γ values of the binary solvents were much closer to NMP or DMF, ranging from 43-50 mN/m. Many equations have been proposed for predicting the surface tension of binary solvents. For an ideal solution of an organic compound and water, the surface tension can be described by:[37-40]

$$\gamma_{\text{mixing}} = x.\gamma_{NMP/DMF} + y.\gamma_{H_2O} \qquad \textit{(eq. 5-5)}$$

where *x* and *y* represent the mole fractions of the organic solvent (NMP, DMF) and H_2O, respectively. Unfortunately, the surface tensions of the various binary solvents at 20 °C (shown in ***Table 5-4***) are not described well by *eq.* 5-5 (see ***Table 5-4*** for *x*, *y* values and ***Figure 5-2a*** for surface tension of H_2O, DMF and NMP). It appears that NMP and DMF contribute disproportionately to surface tension compared with H_2O in binary solvents. This suggests that *eq.* 5-5 should be modified to:

$$\gamma_{\text{mixing}} = a.\gamma_{NMP/DMF} + b.\gamma_{H_2O} \quad \textit{(eq. 5-6)}$$

where *a* and *b* represent the contributions of NMP/DMF and H_2O to surface tension in a binary solvent, and *a*+*b*=1. The surface tensions of the binary solvents at different temperatures (*e.g.* 42, 60 and 82 °C, see ***Figure 5-3***) was further tested, which all agreed well with *eq.* 5-6, suggesting the feasibility of this approach.

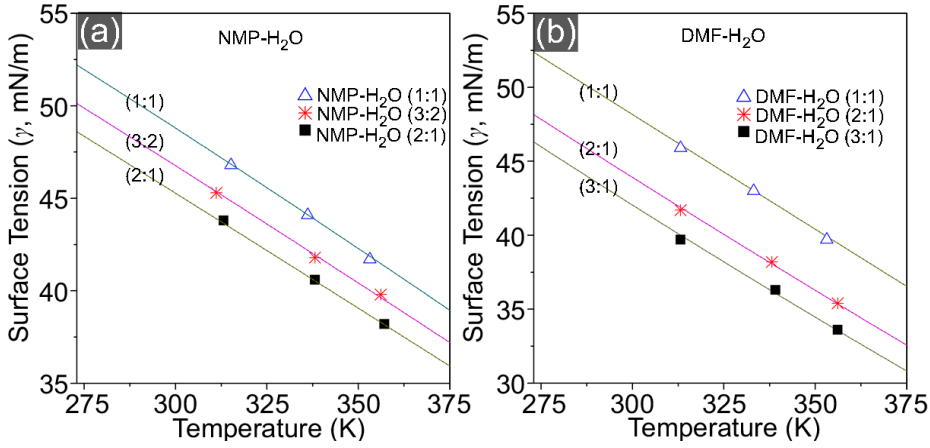

Figure 5-3. (a) The surface tension (γ) of the NMP-H_2O (volume ratio of 1:1, 3:2 and 2:1) as a function of temperature; (b) The surface tension (γ) of the DMF-H_2O (volume ratio of 1:1, 2:1 and 3:1) as a function of temperature. The symbol dots are the measured surface tensions at different temperatures. The lines are the predicted surface tension of binary solvent using *eq.* 5-6.

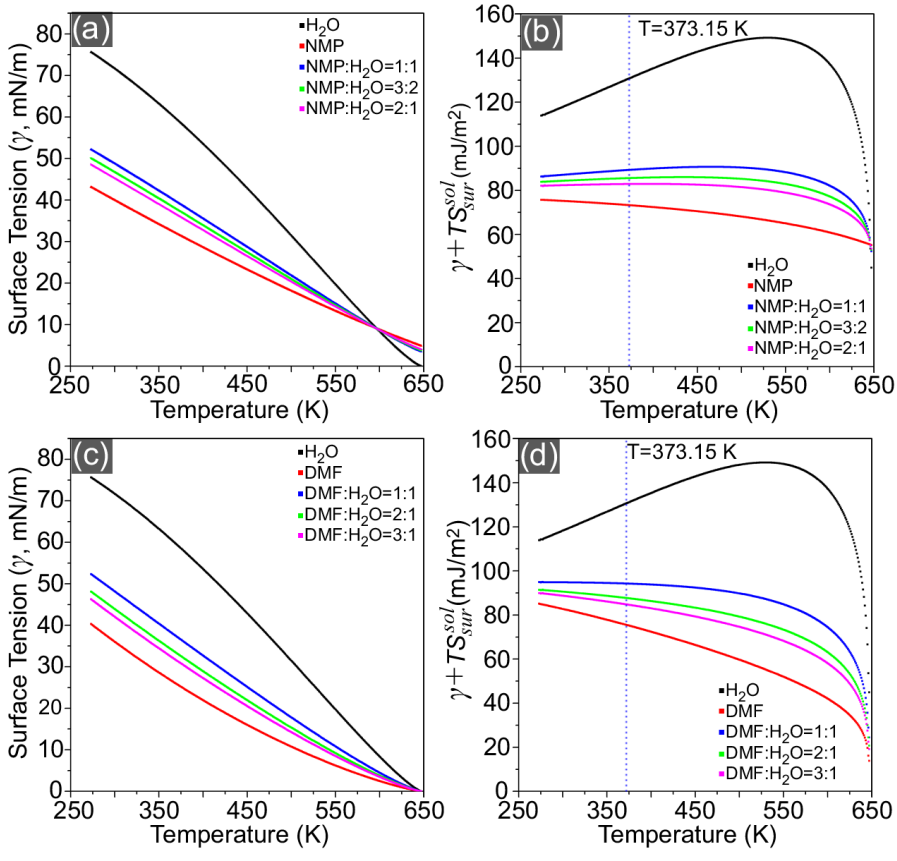

Figure 5-4. Solvent parameters as a function of temperature of NMP, H_2O and NMP-H_2O: (a) surface tension (γ); (b) surface energy ($\gamma + T.S_{Sur}^{Sol}$); (c) surface tension (γ); (d) surface energy ($\gamma + T.S_{Sur}^{Sol}$). Single solvent data (H_2O, NMP, DMF) from *eq.* 5-3 & 5-*4*, binary solvent data derived from *eq. 5-6*.

The continuous temperature-dependent surface tension of the binary solvents was calculated (***Figures 5-4a & c***) using *eq.* 5-6, the measured 20 °C surface tension (***Table 5-4***) and the separate temperature-dependent surface tensions of H_2O, NMP and DMF (***Figure 5-2a***, also plotted in ***Figures 5-4a & c***). Although the binary solvents have similar surface tensions, the calculated solvent surface energies ($\gamma + T.S_{Sur}^{Sol}$) at 100 °C differ more markedly (***Figures 5-4b & d***). The solvent surface energies ($\gamma + T.S_{Sur}^{Sol}$) of NMP-H_2O at 100 °C were calculated as 89.3, 85.6 and 82.9 mJ/m^2 for NMP/H_2O volume ratios of 1.0, 1.5 and 2.0, respectively, all of which lie between the surface energies of H_2O (130.8 mJ/m^2) and NMP (73.27 mJ/m^2) alone. The surface energy ($\gamma + T.S_{Sur}^{Sol}$) of DMF-H_2O at 100 °C (***Figure 5-4d***) has values of 94.3, 87.6 and 84.7 mJ/m^2 for DMF/H_2O volume ratios of 1.0, 2.0 and 3.0, respectively, representing a wider range than with NMP.

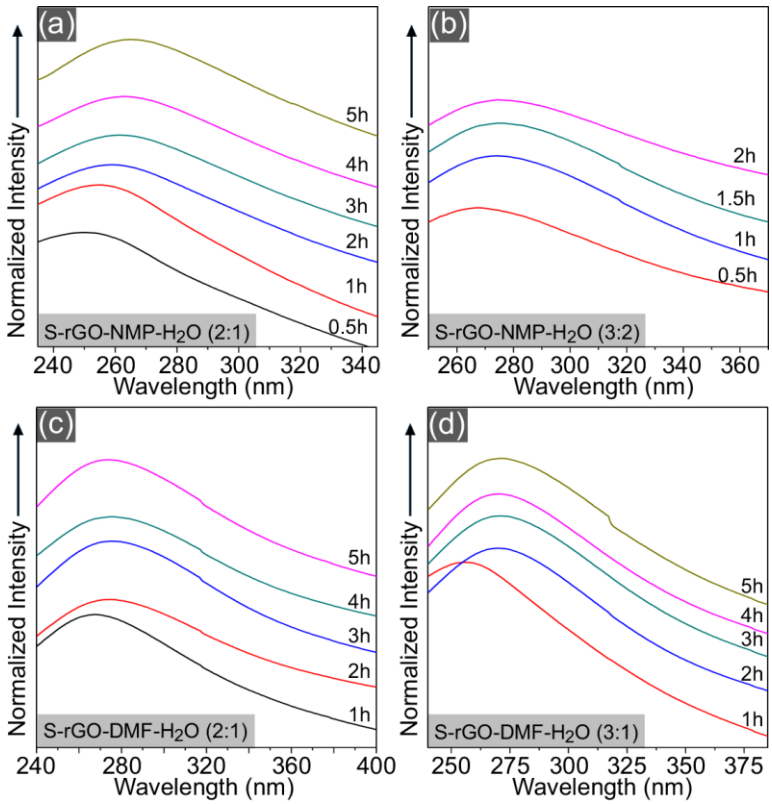

Figure 5-5. UV/Vis absorption spectra of S-rGO-NMP-H_2O-*x* and S-rGO-DMF-H_2O-*x* with different binary solvents: (a) 2:1 NMP/H_2O; (b) 3:2 NMP/H_2O; (c) 2:1 DMF/H_2O; (d) 3:1 DMF/H_2O. For clarity, the zero intensities in all images were shifted.

As already noted, the required solvent surface energy for the GO deoxidation reaction should be slight larger than that of pure graphite/rGO (>70-80 mN/m). To investigate this, the deoxidation experiments with different binary solvents were further conducted. Solid S was chose as the reducing agent since the necessary reaction time for deep

deoxidation of GO (10 h in 1:1 NMP-H_2O and 1:1 DMF-H_2O solvents, see ***Chapter IV***) is much longer than with Fe^{2+}, so this provides greater resolution to the necessary deoxidation times. Different S-rGO (sulphur reduced GO) samples (***Tables 5-1 & 5-5***) were prepared by changing the solvents and deoxidation times (*x*). The GO deoxidation in 2:1 NMP-H_2O was studied first. As shown in the UV/Vis spectra (***Figure 5-5a***), the π→π* absorption of the S-rGO-NMP-H_2O (2:1) shifted to 250, 255, 262, 262, 263, 265 nm upon 1, 2, 3, 4 and 5 h refluxing, respectively. This is not obviously different with that of S-rGO-NMP-H_2O-*x* (1:1 NMP-H_2O) as it was described in ***Chapter IV***. However, when tuning the solvent further to 3:2 NMP-H_2O (volume ratio), the mixture became black within 30 minutes. UV/Vis analysis (***Figure 5-5b***) suggested that the π→π* transition had already shifted to 267 nm and shifted further to 270 nm after 1 h refluxing. No further shift was found for more extended reactions, suggesting that the deoxidation reaction was complete. This represents a significant reduction in GO deoxidation time compared with using 1:1 NMP-H_2O solvent (10 h in ***Chapter IV***).

Similar promotion of GO deoxidation was also observed in the DMF-H_2O system once the solvent was tuned. ***Figures 5-5c & d*** show the UV/Vis spectra of S-rGO-DMF-H_2O-*x* (2:1 and 3:1 volume ratios respectively, *x*=1, 2, 3, 4 and 5 h). After 1 h refluxing reaction, the characteristic UV/Vis absorption peak of the rGO was found at around 267 nm (2:1 DMF-H_2O) and 256 nm (3:1 DMF-H_2O). The π→π* transition was restored fully after 2 h refluxing reaction with either 2:1 or 3:1 DMF-H_2O solvents, with the absorption peak shifted to 270 nm. By contrast, deep deoxidation of GO in 1:1 DMF-H_2O requires 10 h (see ***Chapter IV***).

Table 5-5. List of the main test samples of S-rGO and H-rGO (specified in the ***Table 5-1***, GO reduced by hydrazine), deoxidized at 100 °C (solvent temperature).

Solvent (volume ratio)	$T.S_{Sur}^{Sol}+\gamma$ at 100 °C (mJ/m^2)	Time-dependent π→π* (C=C) positions			
		1 h	2 h	5 h	Complete deoxidation time
H_2O	130.8	Only achieved peak position of 262 nm with 2-4 days reaction			
H_2O	130.8	Reduced by hydrazine, only achieved peak position of 263-264 nm with 3-12 h reaction.			
NMP-H_2O (1:1)	89.3	Ref. 25		266 nm	> 5 h
NMP-H_2O (3:2)	85.6	Complete deoxidation time ~ 1h			
NMP-H_2O (2:1)	82.9	250 nm	255 nm	265 nm	> 5 h
DMF-H_2O (1:1)	94.3	Ref. 25		267 nm	> 5h
DMF-H_2O (2:1)	87.6	267 nm	270 nm	Complete reaction ~ 2h	
DMF-H_2O (3:1)	84.7	256 nm	270 nm	Complete reaction ~ 2h	

*Note: see **Chapter IV**, the GO cannot be well deoxidized in pure H_2O, NMP and DMF solvent at 100 °C.*

The shifts of the UV/Vis absorption peak of various S-rGO samples are summarized in ***Table 5-5***. As described above, it was proposed that the deoxidation proceeds in two reaction stages of, first, initial solvent-polarity-dependent GO deoxidation and, second, continued deoxidation and further removal of functional groups that depend upon the solvent surface tension to avoid sheet agglomeration. The UV/Vis absorption peaks of the S-rGO deoxidized in H_2O (S-rGO-H_2O) is stable at around 262 nm with 2-4 days reaction time (***Table 5-5***, also see ***Figure S5-1b*** in ***Supporting Information*** of this chapter). The only increase in absorption (possibly caused by π-π stacking of p-rGO) was found at long (visible) wavelengths after long reaction time (> 2 days). This is similar to rGO deoxidized by hydrazine (H-rGO-H_2O, ***Figure S5-1a*** in ***Supporting Information***), suggesting that the first reaction stage occurs before sp^2 graphene structure is restored to give the π→π* (C=C) transition at around 262-264 nm. With H_2O as a solvent, the second stage of deoxidation appears to be suppressed due to the high surface energy (130.8 mJ/m^2, see ***Table 5-5***) of H_2O, which leads to the π-π stacking and self-assembly of p-rGO. The lower surface energies of the binary solvents NMP-H_2O and DMF-H_2O favour the general dispersion of p-rGO and promote its further deoxidation. Although the surface energies of different binary solvents (***Table 5-5***) are not greatly different to each other, all within the range of 82.9-94.3 mJ/m^2, the deoxidation progress of GO is remarkably sensitive to the solvent ratio. This highlights the extent to which the second stage of p-rGO deoxidation is dependent on the solvent surface energy. The optimized surface energy of NMP-H_2O that most effectively prevents agglomeration of p-rGO should to be around 85.6 mJ/m^2 at a 3:2 volume solvent ratio. With the DMF-H_2O solvent, the 2:1-3:1 optimized volume ratios give a solvent surface energy between 84.7-87.6 mJ/m^2. The remarkably agreement between the two surface energies provides strong evidence for the primacy of this parameter in facilitating the complete deoxidation of p-rGO. The slight difference in deoxidation extent between 2:1 and 3:1 DMF-H_2O volume ratios for short (1 h) reactions (absorption peak at 267 nm and 256 nm, respectively; ***Figures 5-5c & d*** and ***Table 5-5***) is explained by the difference in solvent polarity in driving the first part of the deoxidation. That full deoxidation is then achieved in both cases after 2 h again supports the hypothesis of the second stage of GO deoxidation being limited by solvent surface energy rather than polarity.

5.4 Conclusion

In this chapter, it is shown that the solvothermal deoxidation of graphene oxide (GO) proceeds in two stages: 1) partial deoxidation that depends on the solvent polarity and 2) further deoxidation to fully restore sp^2 structure of graphene. The second stage is

strongly dependent upon solvent surface energy, which is consistent with controlling (and preventing) the agglomeration of partially reduced GO agglomeration. Experimental results indicate that GO cannot be fully deoxidized in a hydrothermal reaction simply by adding strong reducing agents (*e.g.* Fe^{2+}, S and hydrazine) since this doesn't overcome the p-rGO sheet amalgamation due to their high surface enthalpy. In any solvothermal reaction of GO, the solvent surface energy should be considered a primary factor in maintaining a good dispersal of p-rGO, which can then go on to be fully deoxidized. The dispersal was achieved with heated NMP (<188 °C) and DMF (55-147 °C) solvents alone. Binary solvents such as NMP-H_2O and DMF-H_2O also achieved this at 100 °C by tuning of the solvent ratios in the presence of suitable reducing agents. The ideal solvent surface energy of around 85.6 mJ/m^2 (between 84.7-87.6 mJ/m^2) for alleviating p-rGO agglomeration and assembly can be further calculated. In a solvothermal reaction, the polarity of the solvent remains important as it allows dissolution of the GO and reducing agent. However, it is not as influential as the solvent surface energy on achieving deeply deoxidation of GO. With the approach developed here, deeply deoxidized GO with high dispersibility can now be expected and achieved in various solvothermal systems with suitable reducing agents by tuning the solvent surface energy to around 85.6 mJ/m^2 for 100°C reactions. It will also be possible to achieve this at other temperatures by following the same method but using a different target surface energy. The findings here are relevant to the large-scale preparation of highly reduced GO for various industrial and technical applications.

5.5 Supporting Information

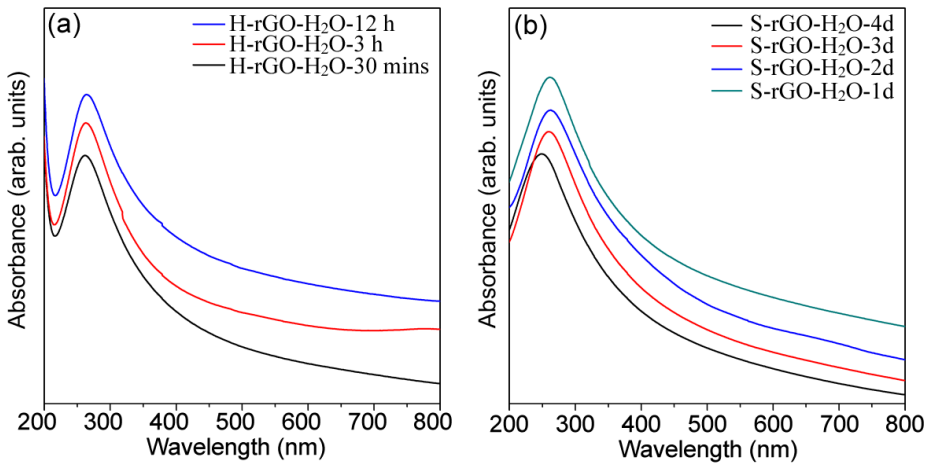

Figure S5-1. (a) Time-dependent UV/Vis spectra of H-rGO. The π→π* transition of C=C was rapidly restored to 261.5 nm within 30 min refluxing time. However, after extending the refluxing time to 3 and 12 h, the absorption peak only slightly red-shifted further, to 263 and 264 nm, respectively. No further shift was observed with additional hydrazine and

reaction, suggesting the GO deoxidation was highly suppressed; (b) Time-dependent UV/Vis spectra of S-rGO. The π→π* transition of C=C appeared at around 249, 260 nm upon 1 and 2 days reaction. This transition stabilized at around 262 nm with 3 and 4 days reaction.

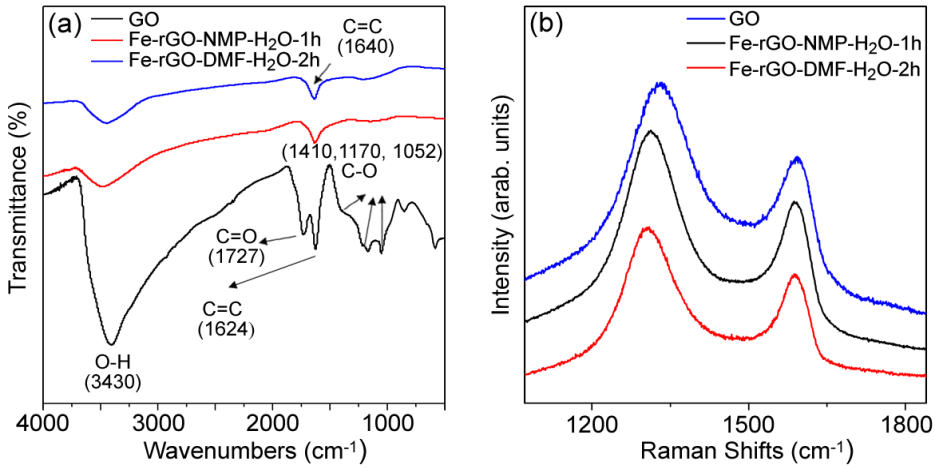

Figure S5-2. FT-IR (a) and Raman spectra (b) of purified Fe-rGO-NMP-H_2O-1h (1:1 NMP/H_2O), Fe-rGO-DMF-H_2O-2h (1:1 DMF/H_2O) and GO raw material. the FT-IR spectra of GO give the characteristic peaks at around 1727, 1624, 1410, 1170, 1052 cm^{-1}, corresponding the vibrations from carbonyl C=O, aromatic C=C, carboxyl C-O, epoxy C-O and alkoxy C-O respectively.[19] By contrast, the FT-IR spectra of Fe-rGO-NMP-H_2O-1h and Fe-rGO-DMF-H_2O-2h only show the vibrations of C=C (1640 cm^{-1}) and absorbed H_2O (3400 cm^{-1}), indicating the oxygen-containing groups have been greatly removed. Besides, the blue-shift of the C-C/C=C vibration (from 1624 to 1640 cm^{-1}) also confirmed that the sp^3 C-C structure in GO was restored to sp^2 aromatic C-C/C=C structure (the bond spring constant was enhanced). This structure restoration was further confirmed by Raman analysis as the G bands of Fe-rGO-NMP-H_2O-1h, Fe-rGO-DMF-H_2O-2h both shifted from 1594 cm^{-1} (GO) to around 1588 cm^{-}, closing to that of graphite.[19] In the Raman spectra, the other band at around 1330 can be attributed to the D band of graphene.[19]

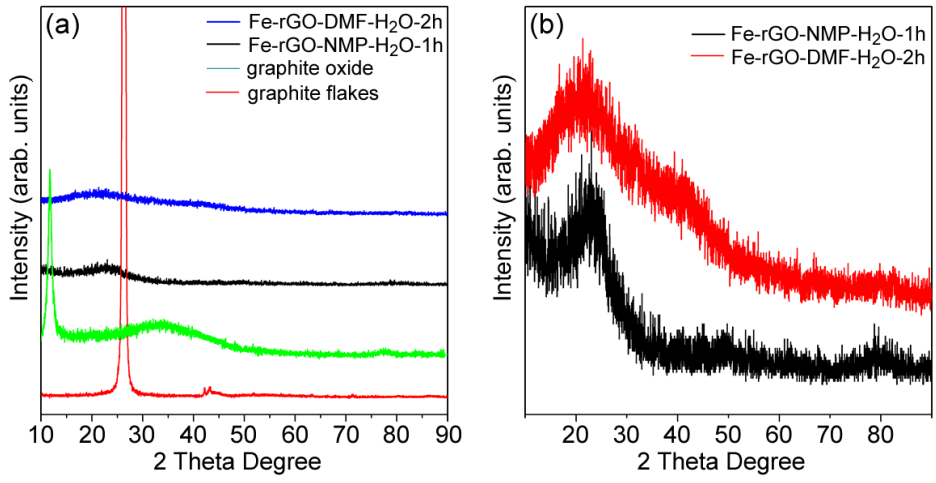

Figure S5-3. (a) XRD patterns of Fe-rGO-DMF-H_2O-2h, Fe-rGO-NMP-H_2O-1h, graphite raw material and GO (prior exfoliation); (b) Enlarged XRD patterns of Fe-rGO-DMF-H_2O-2h and Fe-rGO-NMP-H_2O-1h. In the XRD patterns, the GO has a low angle-shifted (002) diffraction peak at around 11.8° (d space = 7.49 Å) with peak intensity of 1.2 kcps, while graphite flakes (raw material) has a (002) diffraction peak at 26.7° (d space =3.34 Å) with the intensity > 40 kcps. By contrast, the (002) diffraction of rGO nearly disappeared at around 20° (loosely stacked together with distance of around 4.4 Å), suggesting that the purified Fe-rGO-NMP-H_2O-1h and Fe-rGO-DMF-H_2O-2h all contain thin structured sheets.

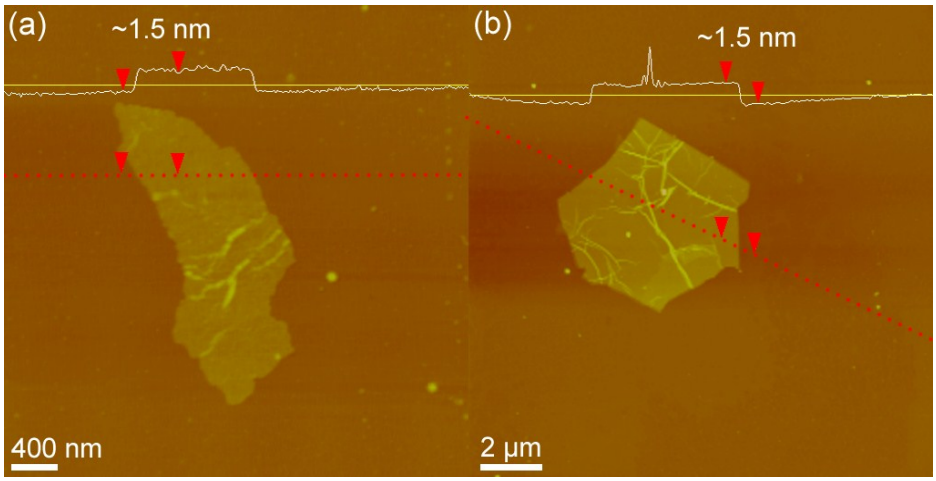

Figure S5-4. AFM images of GO sheets.

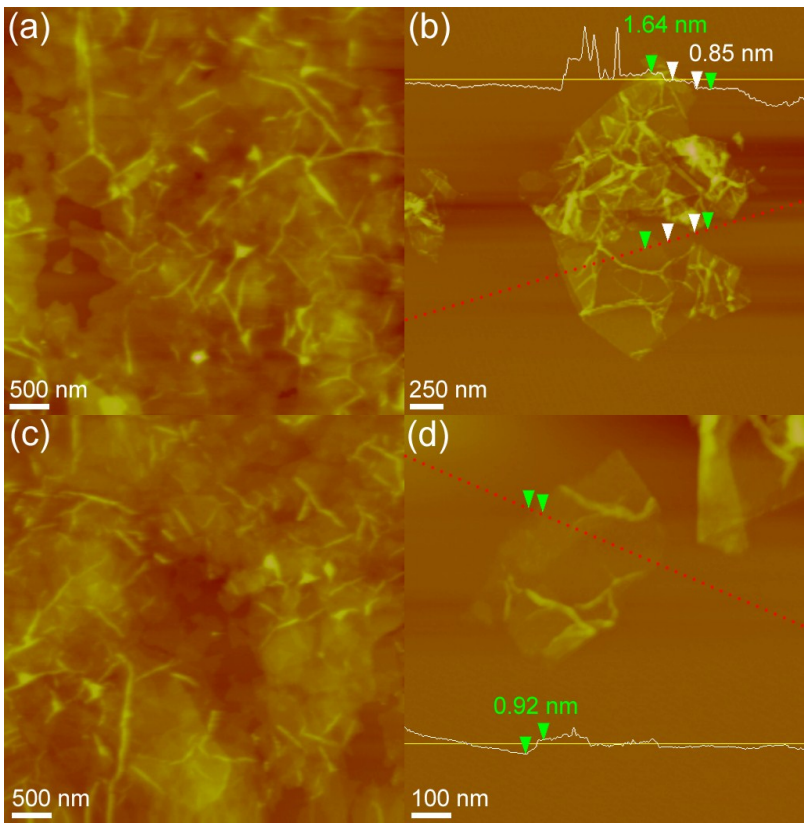

Figure S5-5. AFM images: (a, b) Fe-rGO-NMP-H_2O-1h; (c, d) Fe-rGO-DMF-H_2O-2h. AFM analysis show the thickness of around 0.9 nm of Fe-rGO-NMP-H_2O-1h and Fe-rGO-DMF-H_2O-2h, which is much lower than that of GO (around 1.5 nm in ***Figure S5-4***) and corresponding well with the thickness of monolayered graphene.[14] The AFM images (a and c) covered by high concentration rGO sheets which should have similar thickness as revealed by their similar contrast. The AFM result also suggested that the agglomeration (π-π stacking between graphene) and self-assembly between rGO sheets were avoided upon the addition of NMP and DMF.

References and Notes

[1] A. K.Geim, K. S. Novoselov, The Rise of Graphene. *Nat. Mat.* **2007**, *6*, 183-191.

[2] S. M. Paek, E. J. Yoo and I. Honma, Enhanced Cyclic Performance and Lithium Storage Capacity of SnO_2/Graphene Nanoporous Electrodes with Three-Dimensionally Delaminated Flexible Structure. *Nano Lett.* **2009**, *9*, 72-75.

[3] F. Schedin, A. K. Geim, S. V. Morozov, E. W. Hill, P. Blake, M. I. Katsnelson and K. S. Novoselov, Nature Materials. *Nat. Mat.* **2007**, *6*, 652-655.

[4] P. Blake, P. D. Brimicombe, R. R. Nair, T. J. Booth, D. Jiang, F. Schedin, L. A. Ponomarenko, S. V. Morozov, H. F. Gleeson, E. W. Hill, A. K. Geim and K. S. Novoselov, Graphene-Based Liquid Crystal Device. *Nano Lett.* **2008**, *8*, 1704-1708.

[5] S. Bae, H. Kim, Y. Lee, X. Xu, J. S. Park, Y. Zheng, J. Balakrishnan, T. Lei, H. R. Kim, Y. I. Song, Y. J. Kim, K. S. Kim, B. Özyilmaz, J. H. Ahn, B. H. Hong and S. Iijima, Roll-to-Roll Production of 30-inch Graphene Films for Transparent Electrodes. *Nat. Nanotechnol.* **2010**, *5*, 574-578.

[6] B. Seger and P. V. Kamat, Electrocatalytically Active Graphene-Platinum Nanocomposites. Role of 2-D Carbon Support in PEM Fuel Cells. *J. Phys. Chem. C* **2009**, *113*, 7990-7995.

[7] A. N. Obraztsov, Chemical Vapour Deposition: Making Graphene on a Large Scale. *Nat. Nanotechnol.* **2009**, *4*, 212-213.

[8] C. Berger, Z. Song, X. Li, X. Wu, N. Brown, C. Naud, D. Mayou, T. Li, J. Hass, A. N. Marchenkov, E. H. Conrad, P. N. First and W. A. de Heer, Electronic Confinement and Coherence in Patterned Epitaxial Graphene. *Science* 2006, *312*, 1191-1196.

[9] Y. Hernandez, V. Nicolosi, M. Lotya, F. M. Blighe, Z. Sun, S. De, I. T. McGovern, B. Holland, M. Byrne, Y. K. Gun'Ko, J. J. Boland, P. Niraj, G. Duesberg, S. Krishanmurthy, R. Goodhue, J. Hutchison, V. Scardaci, A. C. Ferrari and J. N. Coleman, High-yield Production of Graphene by Liquid-phase Exfoliation of Graphite. *Nat. Nanotechnol.* **2008**, *3*, 563-568.

[10] J. Wang, K. K. Manga, Q. Bao and K. P. Loh, High-Yield Synthesis of Few-Layer Graphene Flakes through Electrochemical Expansion of Graphite in Propylene Carbonate Electrolyte. *J. Am. Chem. Soc.* **2011**, *133*, 8888-8891.

[11] S. Stankovich, D. A. Dikin, R. D. Piner, K. A. Kohlhaas, A. Kleinhammes, Y. Jia, Y. Wu, S. T. Nguyen and R. S. Ruoff, Synthesis of Graphene-based Nanosheets *via* Chemical Reduction of Exfoliated Graphite Oxide. *Carbon* **2007**, *45*, 1558-1565.

[12] H. -J. Shin, K. K. Kim, A. Benayad, S. -M. Yoon, H. K. Park, I. -S. Jung, M. H. Jin, H. -K. Jeong, J. M. Kim, J. -Y. Choi and Y. H. Lee, Efficient Reduction of Graphite Oxide by Sodium Borohydried and Its Effect on Electrical Conductance. *Adv. Funct. Mater.* **2009**, *19*, 1987-1992.

[13] X. Fan, W. Peng, Y. Li, X. Li, S. Wang, G. Zhang and F. Zhang, Deoxygenation of Exfoliated Graphite Oxide under Alkaline Conditions: A Green Route to Graphene Preparation. *Adv. Mater.* **2008**, *20*, 4490-4493.

[14] D. Li, M. B. Müller, S. Gilje, R. B. Kaner and G. G. Wallace, Processable Aqueous Dispersions of Graphene Nanosheets. *Nat. Nanotechnol.* **2008**, *3*, 101-105.

[15] L. Lin and S. Zhang, Effective Solvothermal Deoxidization of Graphene Oxide using Solid Sulphur as a Reducing Agent. *J. Mater. Chem.* **2012**, *22*, 14385-14393.

[16] Y. Xu, K. Sheng, C. Li and G. Shi, Self-Assembled Graphene Hydrogel *via* a One-step Hydrothermal Process. *ACS Nano* **2010**, *7*, 4324-4330.

[17] S. Liu, J. Xie, Q. Pan, C. Wu, G. Cao, T. Zhu and X. Zhao, Graphene Anchored with Nanocrystal Fe2O3 with Improved Electrochemical Li-Storage Properties. *Int. J. Electrochem. Sci.* **2012**, *7*, 354-362.

[18] Given by IAPWS (The International Association for the Properties of Water and Steam) and dataphysics.

[19] V. H. Pham, T. V. Cuong, S. H. Hur, E. Oh, E. J. Kim, E. W. Shin and J. S. Chung, Chemical Functionalization of Graphene Sheets by Solvothermalreduction of a Graphene Oxide Suspension in N-methyl-2-pyrrolidone. *J. Mater. Chem.* **2011**, *21*, 3371-3377..

[20] J. Lyklema, *Colloids and Surfaces A: Physicochem. Eng. Aspects* **1999**, *156*, 1-3.

[21] L. X. Benedict, N. G. Chopra, M. L. Cohen, A. Zettl, S. G. Louie and V. H. Crespi, Microscopic Determination of the Interlayer Binding Energy in Graphite. *Chem. Phys. Lett.* **1998**, *286*, 490-496.

[23] M. Hodak and L. A. Girifalco, Fullerenes Inside Carbon Nanotubes and Multi-Walled Carbon Nanotubes: Optimum and Maximum Sizes. *Chem. Phys. Lett.* **2001**, *350*, 405-411.

[24] R. Zacharia, H. Ulbricht and T. Hertel, The Interlayer Cohesive Energy of Graphite from Thermal Desorption of Polyaromatic Hydrocarbons. *Phys. Rev. B* **2004**, *69*, 155406.

[25] S. Wang, Y. Zhang, N. Abidi and L. Carbrales, Wettability and Surface Free Energy of Graphene Films. *Langmuire* **2009**, *25*, 11078-11081.

[26] N. Ooi, A. Rairkar and J. B. Adams, Density Functional Study of Graphite Bulk and Surface Properties. *Carbon* **2006**, *44*, 231-242.

[27] D. Chan, M. A. Hozbor and E. Bayramli, Surface Characterization of Intermediate Modulus Graphite Fibers *via* Surface Free Energy Measurement and Esca. *Carbon* **1991**, *29*, 1091-1098.

[28] J. M. H. Levelt Sengers, J. Straub, K. Watanabe and P. G. Hill, Assessment of Critical Parameter Values for H_2O and D_2O. *J. Phys. Chem. Ref. Data* **1985**, *14*, 193-207.

[29] W. Gerhartz, (exec ed.). *Ullmann's Encyclopedia of Industrial Chemistry* (5th Ed.), **1993**, Deerfield Beach, FL: VCH Publishers, *VA22*, pp. 458.

[30] Kirk-Othmer, *Encyclopedia of Chemical Technology* (4th Ed.). **1994**, John Wiley and Sons, New York, *V11*, pp. 968.

[31] N. B. Vargaftik, B. N. Volkov and L. D. Voljak, International Tables of the Surface Tension of Water. *J. Phys. Chem. Ref. Data* **1983**, *12*, 817-820.

[32] N. K. Adam, *The Physics and Chemistry of Surfaces* (3rd Ed.) **1941**, Oxford University Press.

[33] P. W. Atkins, *Physical Chemistry* (2nd Ed.), **1982**, Oxford University Press,.

[34] H. Kahl, T. Wadewitz and H. Winkelmann, Surface Tension of Pure Liquids and Binary Liquid Mixtures. *J. Chem. Eng. Data* **2003**, *48*, 580-586.

[35] N. G. Tsierkezos and A. C. Filippou, Thermodynamic Investigation of N,N-dimethylformamide/toluene Binary Mixtures in the Temperature Range from 278.15 to 293.15K. *J. Chem. Thermodyn*. **2006**, 3*8*, 952-961.

[36] T. Hasan, F. Torrisi, Z. Sun, D. Popa, V. Nicolosi, G. Privitera, F. Bonaccorso and A. F. Ferrari, Solution-Phase Exfoliation of Graphite for Ultrafast Photonics. *Phys. Status Solidi B* **2010**, *247*, 2953-2957.

[37] K. A. Connors and J. L. Wright, Dependence of Surface Tension on Composition of Binary Aqueous-Organic Solutions. *Anal. Chem.* **1989**, *61*, 194-198.

[38] D. Khossravi and K. A. Connors, Solvent Effects on Chemical Processes. 3. Surface Tension of Binary Aqueous Organic Solvents. *J. Solution Chem*. **1993**, *22*, 321-330.

[39] J. Ecsobedo and G. A. Mansoori, Surface Tension Prediction for Liquid Mixtures. *AIChE J.* **1998**, *44*, 2324-2332.

[40] R. Tahery and H. Modarress, A New And a Simple Model for Surface Tension Prediction of Water and Organic Liquid Mixtures. *Iran J. Sci. Technol. B* **2005**, *29*, 501-509.

Chapter VI. Graphene Quantum Dots: Exfoliated and Disintegrated from Carbon Nanotubes and Graphite Flakes

6.1 Introduction

The rise of graphene offers an exceptional choice for the material in the electronics application. However, graphene has not semiconductor gap which is a major problem for mainstream logic application.[1] One solution using the spatial confinement of the graphene (the formation of graphene quantum dots, GQDs) can be considered for introducing the non-zero gap to the graphene. Quantum dots (QDs) are nanoparticles having small sizes comparable to the exciton Bohr radius of their bulk counterpart. The three spatial dimension confinements of the exciton render interesting quantum confinement effect.[2,3] Unlike many semiconductive materials, graphene is single atom thick nanomaterial with an infinite exciton Bohr radius.[4] Substantially-enhanced quantum confinement and edge (such as zigzag and armchair edges) effects are achievable in them with a certain size. New and unique properties (*e.g.* luminescence) could be expected for GQDs even though they may have some surface defects. This could make them highly valuable in many potential applications, including in solar cell, photocatalysis, bioimaging, and quantum electronic device.[1,4]

So far, various methods and techniques, including transformation of C_{60} molecules,[5] electron-beam lithography,[1,6] organic synthesis,[7] hydrothermal cutting,[8,9] and electrochemical processing,[10] have been used in attempts to prepare GQDs (here, few-layered graphite is referred to as multi-layered graphene). With these techniques, small amounts of tiny GQDs,[1,5,6] 3D covalently caged GQDs[7] (overall yield: ca. 1.29% through a complex organic synthesis route) and 1-2.5 nm thick multi-layered oxidized GQDs (overall yield: ca. 1.1% from GO/graphite oxide sheets,[8] ca. 1.6% from GO sheets,[9] or ca. 1.28% from graphene film[10-11]) have been produced. Other routes based on the hydrothermal cutting mechanism also suffer from the technical difficulty of quite low yield production.[11] The majority formed graphene (or graphene oxide) using these hydrothermal cutting routes are still in big size.[8-10] It's still a technical challenge to effectively cut down the graphene (or graphene oxide) as QDs. For this reason,

alternative raw materials (such as low crystallized carbon blacks and fibers) were also tried to prepare GQDs using promoted hydrothermal cutting method.[12-13] Unfortunately, their study suggested that the final products were actually majority oxidized graphite nanoparticles rather than the so-claimed GQDs (see Ref. 12b for further comment).[12] Starting from these raw materials, there is also one immediate question that should be addressed: condensed amorphous carbon phase (instead of crystallized GQDs, which normally exists in the low crystallized carbon blacks and fibers with large proportion) also exists in the created soluble product, which cannot be easily removed. Base on these reasons, to pave the way for the useful application of GQDs, effective avenues should be immediately introduced for the preparation.

This chapter describes a novel effective approach to the preparation of water-soluble GQDs based on exfoliating and disintegrating multi-walled carbon nanotubes (MWCNTs) and graphite flakes (GFs). By using this approach, high yields (~23 wt% and 10 wt%) GQDs can be effectively cut from the MWCNTs and GFs respectively. These GQDs show a size around 20 nm, and majority of them are monolayered. Further analysis indicates that the dots exhibit strong luminescence with high quantum yield, which is highly desired for the practical application of the GQDs. This chapter also demonstrates that created GQDs can be used as a non-toxic fluorescent label in confocal microscopy of biological cells.

6.2 Experimental Methods

6.2.1 Intercalation Reaction and Addition Amount of the Raw Materials

The preparation involved an intercalation reaction of graphite to form C_8K. As reported, C_8K has characteristic bronze-colour, which is different with that of graphite.[14] During the preparation, a Pyrex tube with a diameter of ~3 cm (~25 cm length) was used to perform the intercalation reaction. The suitable addition amount of K was initially estimated. Addition of ~0.6 g K into the Pyrex tube was safe to react with $EtOH/H_2O$. More addition of K into the tube induced violent reaction which should be avoided (less addition of K was not suggested for an effective intercalation reaction). On the basis of the addition of ~0.6 g K, the addition of solid powder (graphite and other powder materials involved in other chapters: hBN, WS_2 and MoS_2) can be estimated and easily weighed. As for the intercalation reaction, theoretically, 1.44 g graphite and 0.6 g K can be used to form C_8K. However, a high yield product requires a high ratio of K/C (to improve the interaction efficiency). The preparation efficiency can be determined by the colour of the collected suspension (GQDs suspension showed yellow colour, which

changed to dark with the increasement of concentration). After several preparations, results base on the observations showed that 0.08-0.1 g MWCNTs (K was kept as 0.6 g) was the best addition amount for creating a high yield product (the MWCNTs can mixed well with K). However, the interaction reaction between K and GFs are more difficult than that of K and MWCNTs. More GFs should be introduced into the Pyrex tube to improve the production, which was essential for obtaining a suitable amount of the product (for further characterisations and applications). Therefore, 0.25 g GFs was used for the intercalation reaction, which have a similar volume to that of 0.08-0.1 g MWCNTs (can mix well with 0.6 g K and favour the reaction; more addition of GFs led to poor intercalation and yield).

6.2.2 Preparation of GQDs from MWCNTs

0.082 g (more raw materials can be used, *e.g.* 0.1 g) MWCNTs were put into a Pyrex tube with a stop and a side vacuum connection, followed by adding ~0.6 g K. The two materials were mixed by gently shaking the Pyrex tube. The tube was initially heated in an oil bath to ~110 ^{o}C (the temperature of the oil bath) under vacuum condition (0.05 Torr) and held for 10 min to remove any evaporable phases and then further heated to 190-200 ^{o}C and held for >3 h until the mixture in the tube changed to bronze colour (a few silver grey segments were seen on the surface of the mixture), after which the mixture was held for another 1 h. After cooling down the tube to room temperature (direct reaction between hot intercalated MWCNTs and EtOH/H_2O was too violent), the vacuum pump was turned off. *The following process needs to be carefully carried out since the intercalated MWCNTs are highly reactive in air, ethanol and water.* After all the security measures had been taken, the bottom of the Pyrex tube was placed in a room temperature water bath in an ultrasonic vibrator (Bandelin Sonorex RK-100H). Then air was introduced slowly into the Pyrex tube by carefully controlling the valve *(Caution: the rapid introduction of air into the tube through the side valve or by opening the stop cover will make violent burning of the mixture).* After light and burning in the Pyrex tube were not visible, the ultrasonic vibrator was turned on. Then the stop cover of the tube was removed and 50 mL ethanol was added into the tube followed by addition of 50 mL deionized water (do not add water until the residual silver K suspension on the surface of EtOH was disappear). The tube was kept in the ultrasonic bath for 2 h. A deep yellow solution containing GQD was separated from the residual solid carbon by using a Hettich Zentrifugen EBA 21 centrifuge and filter paper. The remaining K ions in the solution were absorbed/removed with the cation exchange resin. The resultant faint yellow solution was centrifuged at least 3 times (each time for 15 minutes) at 6000 RPM to further remove any residual solid carbon, before it was concentrated to a higher

concentration (deep yellow/brown) solution *via* distillation at 120 °C for requisite times. During the concentration/distillation process, the residual ethanol was evaporated, resulting in an aqueous solution of GQDs.

6.2.3 Preparation of GQDs from GFs

The preparation of GQDs from GFs was similar to the procedure described above (0.25 g graphite flakes and ~0.6 g K were used). However, the process was much more gentle and easier as no burning of potassium intercalated graphite was found during the exposure. The mixture of K and GFs changed to bronze colour after 1 h heating reaction. Nevertheless, a longer intercalation time (> 4 h) was required to achieve a high yield (base on the colour changes of the mixed raw materials). In addition, it was necessary to add ethanol into the tube after the side valve and stop cover were quickly removed, which was different from that in the case of using MWCNTs. In contrast with the preparation of GQDs from MWCNTs, for quick removal of the stop cover here was safe as no violent burning of the mixture was observed. Because K intercalated GFs also de-intercalate under air condition, the quick removal of the stop cover and quick adding of the EtOH are essentials to improve the yield of the GQDs. To remove K ions, the same purification procedure was followed (see preparation of GQDs from MWCNTs in **Section 6.2.2**).

6.2.4 Calculation of Production Yields

As-prepared GQDs from MWCNTs were oven-dried overnight at 120 °C. After cooling in a sealed amber glass, their weights ("gross" weights) were weighed. The yield described here (23 wt%, see ***Section 6.3.2***) was calculated by dividing the weight of dried GQD product by the weight of the starting MWCNTs. By using the same method, the yield of GQD prepared from graphite flakes was calculated as ~10 wt% (see ***Section 6.3.2***). However, since the GQDs contained some oxygen-containing groups, their "net" weights excluding oxygen are also calculated based on the "gross" weight of as-prepared GQDs and the C1s XPS results (***Figure 6-6d*** and ***Figure 6-11a***). The corresponding "net" yields of GQDs created from MWCNTs and graphite flakes were calculated as 17.2 wt% and 8.8% wt%.

6.2.5 Calculation of the Quantum Yield

See ***Section 3.4*** in ***Chapter III*** for the calculation method of quantum yield.

Table 6-1. Quantum yield of GQDs (in water, pH~8-9, created from MWCNTs) using anthracene as a reference.

Sample	Integrated Emission Intensity (*I*)	Absorptance at 310 nm (*A*)	Refractive Index of Solvent (η)	Quantum Yield (Φ)

Anthracene	76899	0.0226	1.36	30% (Known)[14-16]
GQDs	14017	0.0181	1.33	6.5%

Table 6-2. Quantum yield of GQDs (in water, pH~8-9, created from GFs) using anthracene as a reference.

Sample	**Integrated Emission Intensity (*I*)**	**Absorptance at 310 nm (*A*)**	**Refractive Index of Solvent (*η*)**	**Quantum Yield (*Φ*)**
Anthracene	76899	0.0226	1.36	30% (Known)[14-16]
GQDs	26345	0.0312	1.33	7.1%

6.3 Result and Discussion

6.3.1 Intercalation and De-intercalation Reactions of MWCNTs and GFs

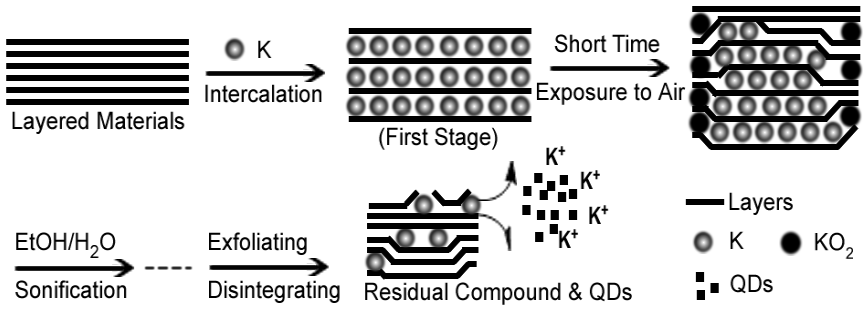

Scheme 6-1. A simple intercalation and de-intercalation of the MWCNTs and GFs was used to describe the formation mechanism of GQDs.

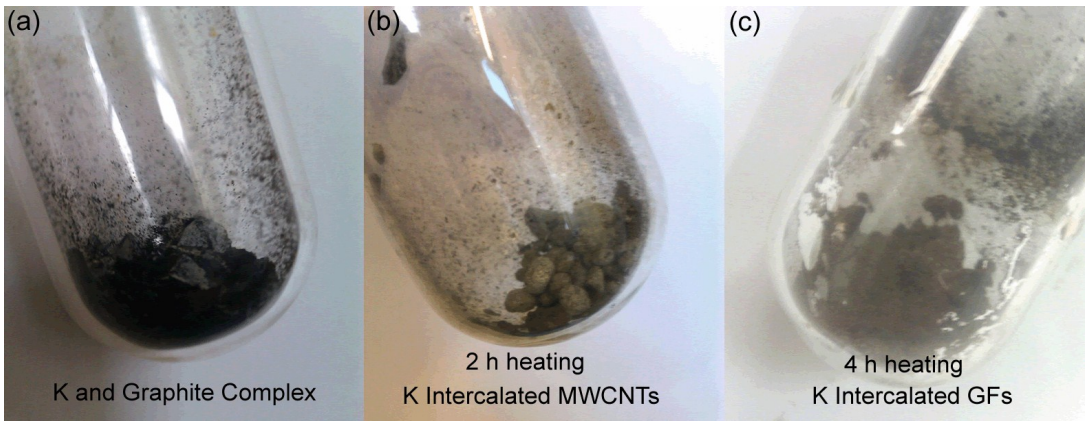

Figure 6-1. (a) Complex of MWCNTs and K show black colour (same as the complex of GFs and K); (b) The K intercalated MWCNTs shows bronze-colour, which is sallow than that of K intercalated GFs. The intercalation reaction of GFs is longer than that of MWCNTs due to large size of the GFs. Tube diameter: ~3 cm.

For better understanding of the preparation, a formation mechanism of the GQDs is proposed as ***Scheme 6-1***. To illustrate the fundamental principle and mechanism of the preparation, the work on the preparation of high yield gently oxidized GQDs from MWCNTs is initially described. This is followed by presenting more results on exfoliation and disintegration of GFs to create GQDs.

The preparations of GQDs from MWCNTs and GFs are based on the high reactivity of potassium-graphite intercalation compounds (K-GICs, ***Scheme 6-1***). K-GICs were formed by intercalating K atoms between the covalently-bonded graphene sheets in MWCNTs, taking advantage of the weak interlayer Van der Waals force. As desired K-GIC (C_8K) has characteristic bronze-colour,[14] its formation as a major phase can be visually evaluated in terms of the colour changes (see ***Figure 6-1***). Its reaction with EtOH in an inert atmosphere while generating hydrogen gas can simultaneously exfoliate the thin graphite sheets.[18] Upon short exposure of the K-GICs (MWCNTs and GFs) to air, violent combustion was observed on K intercalated MWCNTs (while no combustion found on K intercalated GFs, this difference will be discussed in ***Section 6.3.3***), which resulted in many defects on the graphene layers. In addition, as found by Oh *et al.* during the deintercalation stage (with the formation of KO_2), more defects could be generated on the graphene walls owing to the partial overlapping between them (***Scheme 6-1***).[19] Afterwards, with the assistance of ultrasonication, K-GICs continued to react violently with $EtOH/H_2O$, further exfoliating and disintegrating the graphene layers of MWCNTs and GFs to yield monolayered GQDs. The proposed formation mechanism base on MWCNTs was supported by two main findings: 1) pores and defects are seen on the residual MWCNT sediment (***Figures 6-2 & 6-3***) and 2) the final products are predominantly (>90%) monolayered oxidized GQDs with high crystallinity (will be discussed late). As shown in ***Figure 6-2***, the TEM images of MWCNTs raw materials and residual MWCNTs sediment, the tubular structure of MWCNTs was highly destroyed to form flat sheet segment during the reaction. Meanwhile, many defects and pores were found on the residual MWCNTs sediment. All these information suggested that the MWCNTs were successfully exfoliated and disintegrated during the reaction.

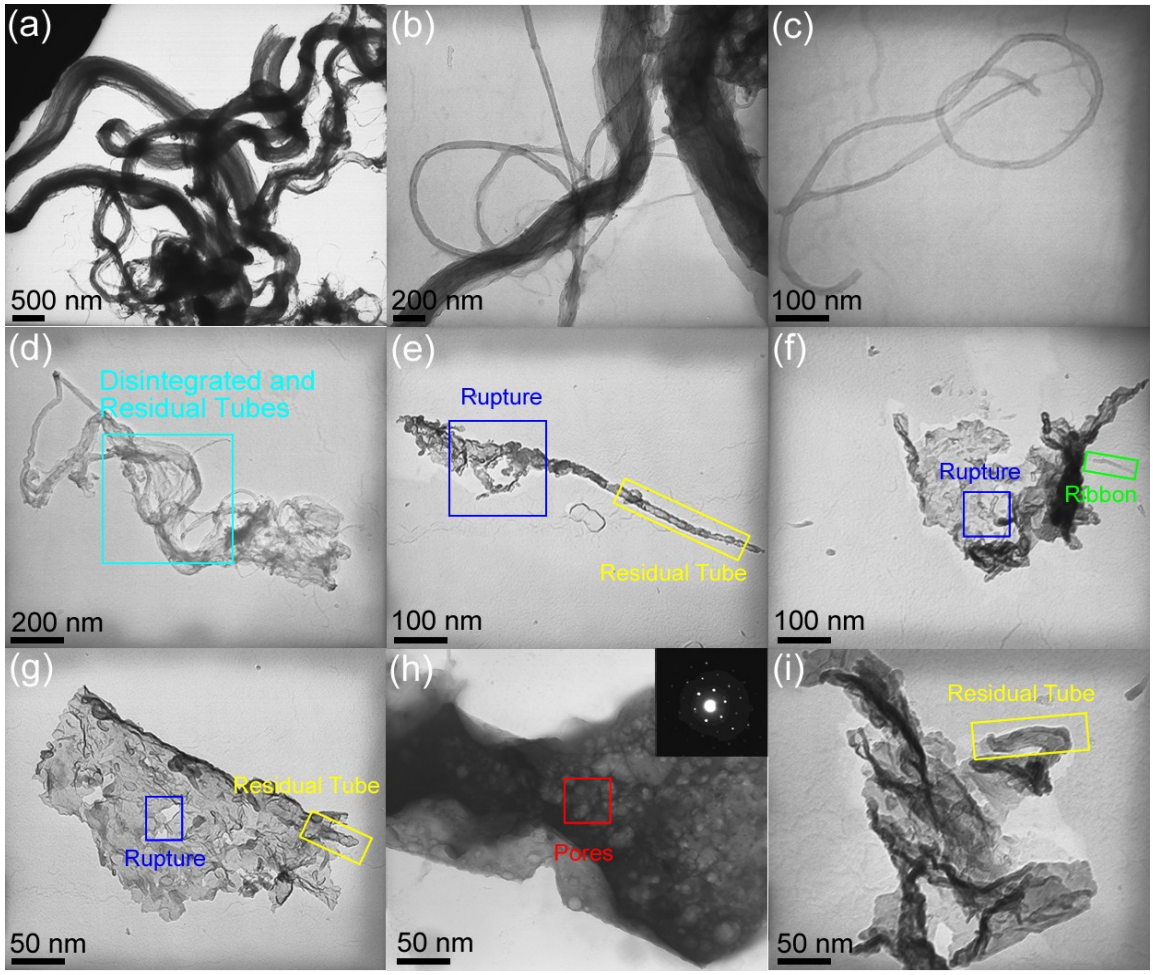

Figure 6-2. (a-c) MWCNTs raw materials; (d-i) residual MWCNTs sediment. Inset in image h is the corresponding SAED pattern which shows hexagonal structure of exfoliated graphene sheets.

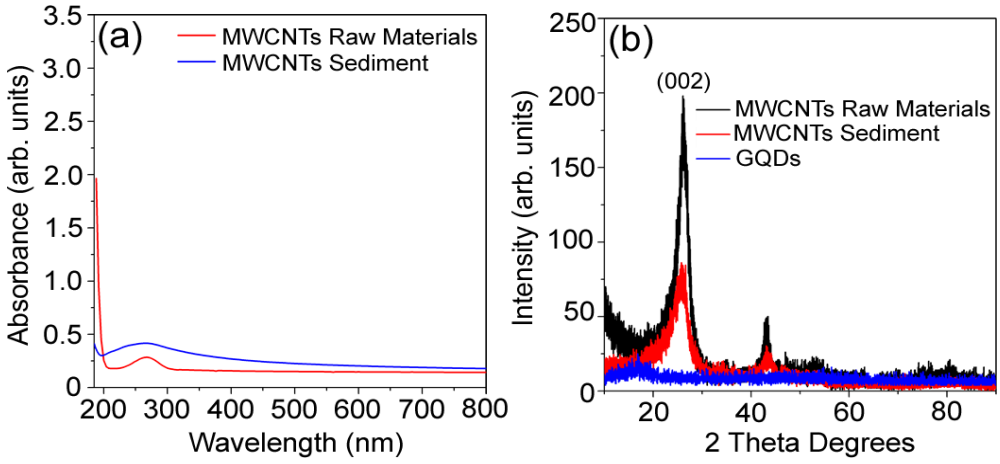

Figure 6-3. (a) UV/Vis spectra of MWCNTs raw material and residual MWCNTs sediment; (b) XRD patterns of MWCNTs raw material, residual MWCNTs sediment and the corresponding GQDs.

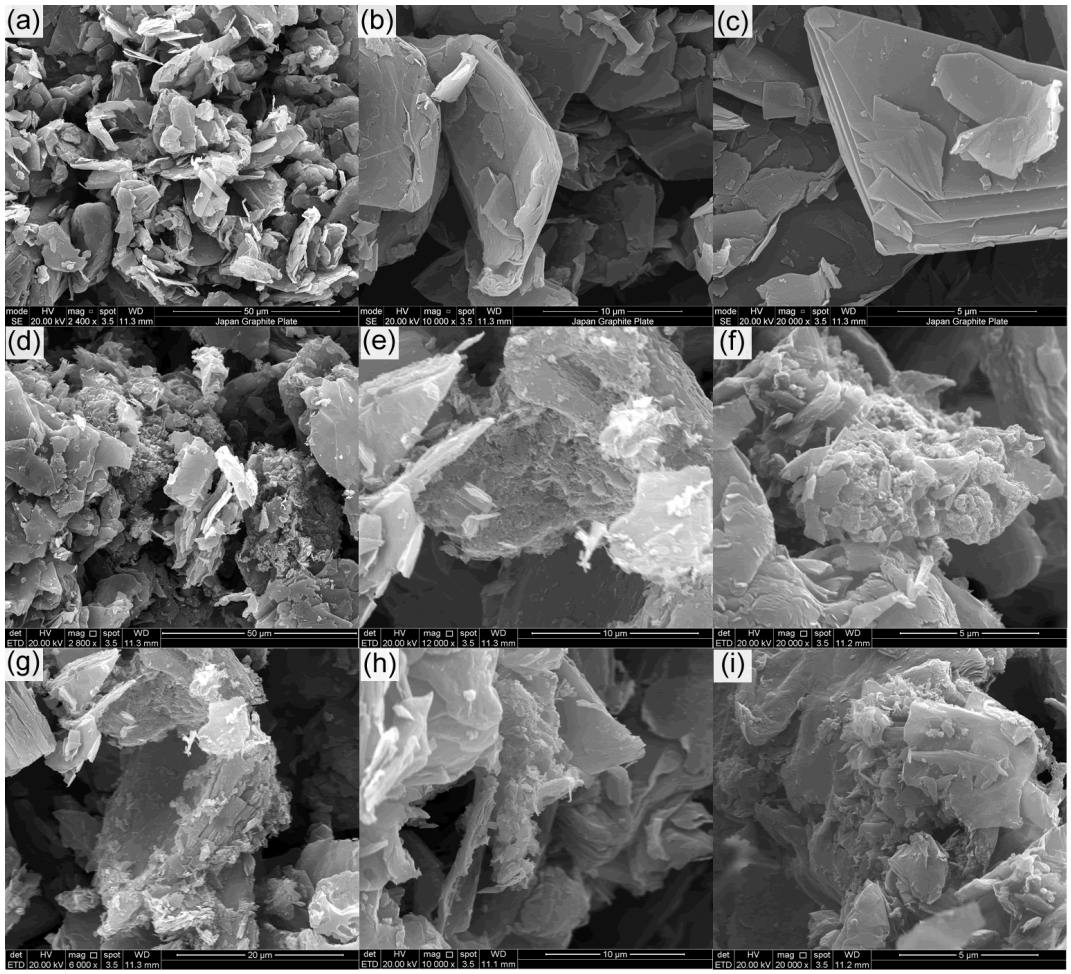

Figure 6-4. **Exfoliation and disintegration of graphite flakes.** (a-c) SEM images of the raw material graphite flakes; (d-i) SEM images of the residual graphite sediment, showing many disintegrated and exfoliated graphite edges.

The exfoliation and disintegration of MWCNTs were further confirmed by the UV/Vis and XRD analysis. The UV/Vis spectra of MWCNTs raw materials and residual MWCNTs sediment is shown in ***Figure 6-3a***. Contrasting with that of MWCNTs raw materials, the UV/Vis absorption of the residual MWCNTs sediment is much broaden, suggesting more defects formed on the tubes during the reaction. Reasonably, due to the exfoliation and disintegration of the MWCNTs, the (002) diffraction peak of residual MWCNTs sediment is much weaken than that of the MWCNTs raw materials (same quality of specimens were used in XRD analysis, see ***Figure 6-3b***). Similar exfoliation and disintegration on the GFs were also found base on the SEM, XRD and FT-IR analysis. ***Figure 6-4*** gives the SEM images of GFs before and after the reaction. The GFs raw materials have micro sizes with flake shape and sharp edges (***Figures 6-4a-c***). However, after reaction, the flake shape of the GFs was deeply destroyed. No more sharp edges were found of the residual GFs, which were highly disintegrated (***Figures 6-4d-i***). The XRD and FT-IR

examines further confirmed this exfoliation and disintegration. As shown in ***Figure 6-5a*** (XRD patterns), after reaction, the (002) (JCPDS: 41-1487) peak intensity of the residual GFs was weakened to about 2 k from 278 k of raw material, suggesting the graphitic structure of the graphite flakes was highly destroyed during the preparation. The exfoliation and disintegration of the GFs also led to the oxidization of the edges, which can be found from the FT-IR analysis (***Figure 6-5b***). In contrasting with the FT-IR spectra of GFs raw materials, the residual GFs after preparation give the oxidized vibrations at around 1500-1000 cm^{-1} (the vibrations will be discussed in detail late). All these information indicate that the MWCNTs and GFs can be effectively exfoliated and disintegrated by using current preparation. In the next sections, the created products will be discussed in detail to show that the exfoliated and disintegrated products are high yield monolayered GQDs.

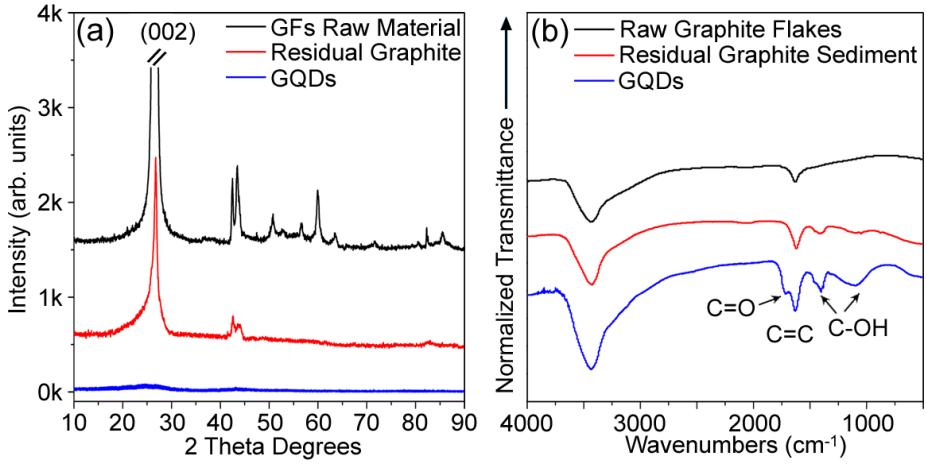

Figure 6-5. **Exfoliation and disintegration of graphite flakes.** (a) XRD patterns of GFs raw materials, residual GFs and the resultant GQDs (same quality of specimens were used for test); (b) FT-IR spectra of graphite flake raw materials, residual graphite flakes and the resultant GQDs.

6.3.2 Characterisations of the GQDs Created from MWCNTs

The resultant product (from MWCNTs) was analyzed using different techniques. No XRD diffraction peaks of the resultant product was found, suggesting possibly thin structure of the product (see ***Figure 6-3b***). The chemical composition and structure of the product was basically confirmed by FT-IR, Raman and XPS. As the result, the FT-IR spectra of the GQDs (***Figure 6-6a***) show vibrations of hydrophilic groups (C=O at around 1720 cm^{-1}, carboxyl C-OH at around 1400 cm^{-1} and hydroxyl C-OH at around 1078 cm^{-1}) and the C=C (at around 1625 cm^{-1}).[20,21] Raman spectrum of the resultant sample shows intense D (1320 cm^{-1}) and G peaks (1594 cm^{-1}) of the aromatic domains.[20,22] The resultant product mainly contain the C and O compositions, as

suggested by the XPS investigation (***Figures 6-6c&d***). C1s spectrum (***Figure 6-6d***) of the resultant sample gives four main components, arising from C=C/C-C (284.6 eV, peak 1, 84.5% molar ratio), O=C-OH (carboxyl, 288.4 eV, peak 4, 8.9% molar ratio), C=O (carbonyl, 287.3 eV, peak 3, 3.65% molar ratio), and C-OH (hydroxyl, 286.4 eV, peak 2, 2.95% molar ratio) species.[20,22] Base on XPS result and the weight of the collected product, the product yield was calculated as ~23 wt% of the total amount of starting MWCNTs (see ***Section 6.2.4*** for more details).

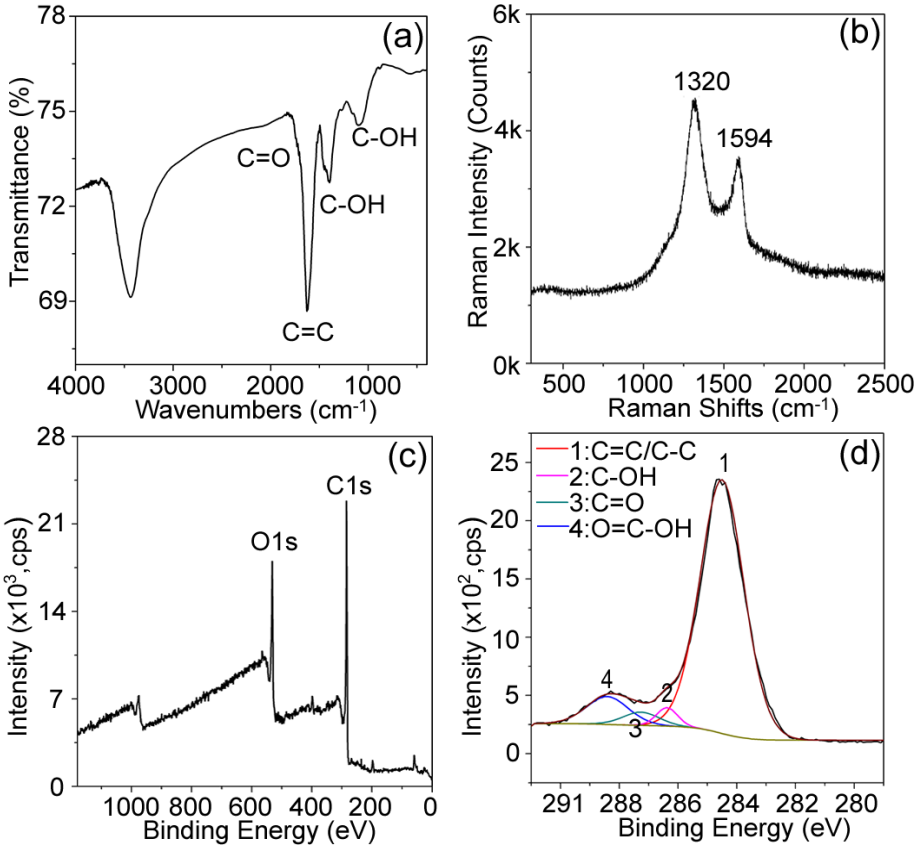

Figure 6-6. **Analysis of the resultant product from MWCNTs.** (a) FT-IR spectra; (b) Raman spectra; (c) Full XPS survey; (d) C1s XPS.

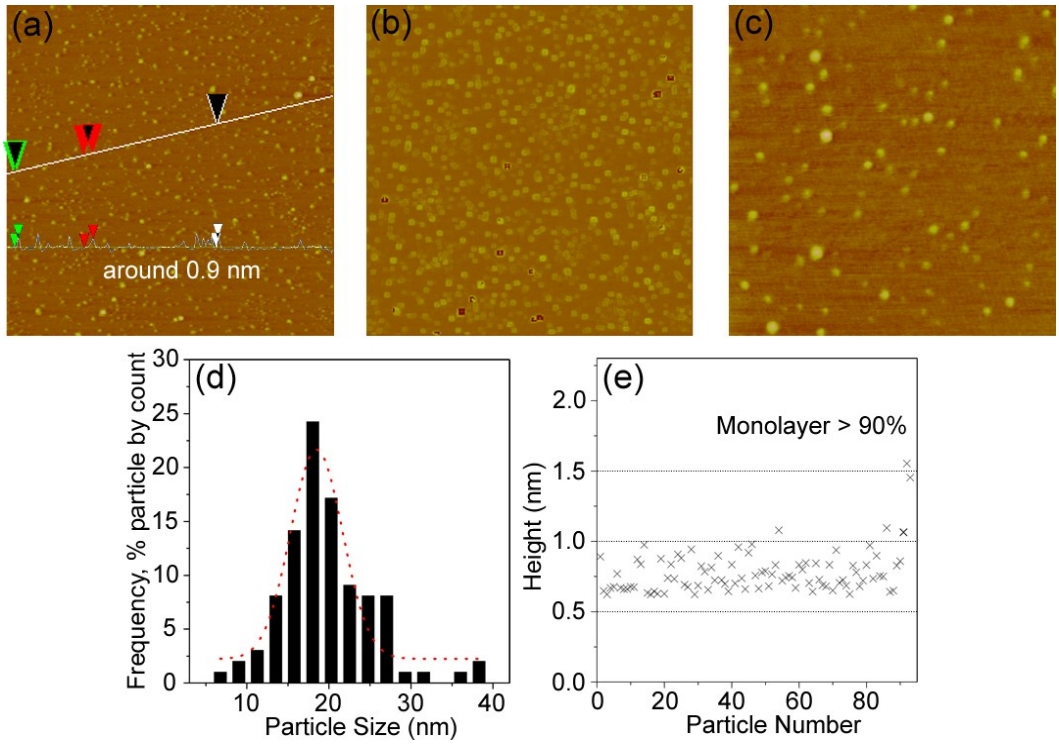

Figure 6-7. (a) AFM topography, Scale: 5 × 5 μm; (b) An edge enhanced AFM image (from image a); (c) AFM topography, Scale: 1 × 1 μm; (d) Size distribution of the resultant product (counted from image c); (e) Statistic thickness of the dots.

Figure 6-7 gives AFM images of the resultant product (from MWCNTs). The product mainly consist small dots with a size around 18.5 nm (***Figures 6-7a-d***). Shown in the ***Figure 6-7a***, the line analysis of the dots gives the thickness around 0.9 nm. Although some dots stacked together as the edge enhanced AFM image suggested (***Figure 6-7b***), statistic analysis of the thickness (***Figure 6-7e***, the analysis method is shown in ***Figure S6-1*** in the ***Supporting Information*** of this chapter) of these dots suggest that majority dots are thinner than 1 nm thus should be monolayer (> 90%, height < 1 nm: monolayer; ca. 1-1.5 nm: bi-layer, ca. 1.5-2 nm: tri-layer[23,24]). It is worthy to note that there is likely an error up to 0.2 nm with the thickness measurement (***Figure S6-1a***), which explains the thickness range of 0.6-1 nm for the monolayered GQDs. The size of the dot was further confirmed by TEM analysis (***Figure 6-8a***). ***Figures 6-8b,c&d*** are the bright field high resolution TEM (BF-HRTEM) images of the sample. A 0.24 nm lattice fringe of graphene was clearly observed on the dot (***Figure 6-8b***). The measured bond length of 0.14 nm corresponding well with that of graphene (***Figure 6-8c***). In ***Figure 6-8c***, the corresponding 2-dimensional (2D) fast Fourier transform (FFT) pattern also showing the hexagonal graphene structure. Base on the above discussed results, it is clear that the resultant products are majority monolayered oxidized GQDs. As discussed before, these GQDs should be exfoliated and disintegrated from MWCNTs. The exfoliation and

disintegration mechanism is much more clear under HRTEM observation. As shown in ***Figure 6-8d***, some multi-layered dots are captured with layer distance varies from 0.5-0.9 nm, suggesting these dots are re-stacked from GQDs and exfoliated/disintegrated from MWCNTs.

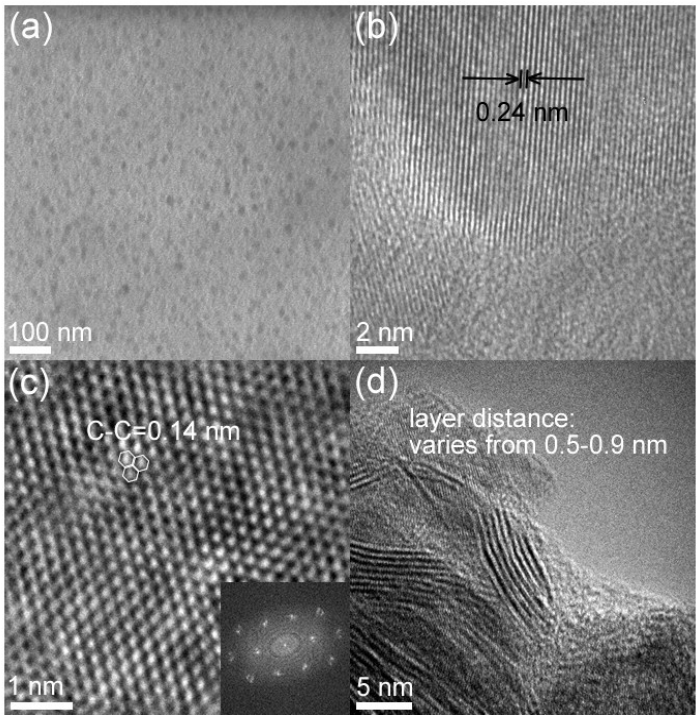

Figure 6-8. TEM images of the GQDs product created from MWCNTs (bright field, images b-d are HRTEM).

Due to the violent combustion of K-GICs on exposure to air, the resultant GQDs were gently oxidized, as suggested by the FT-IR (***Figure 6-6a***) and C1s XPS analysis (***Figures 6-6c&d***). ***Figure 6-9*** is the TGA result of the created GQDs (from MWCNTs) which show two main weight loss regions. The first weight loss prior to 155 ^{o}C can be attributed to the vaporization of the absorbed water. The deoxygenation mostly happened in the second weight loss region (155-550 ^{o}C), where around 20 wt% weight loss was found. Considering the produce of carbon oxide (dioxide and monoxide) and loss of some carbon-containing groups during the TGA, this dada is reasonable as higher than the real oxygen ration in the GQDs calculated form XPS dada (15.5% oxygen, molar ratio). The majority oxidized groups are proposed located on the GQDs edges. These oxidized sites are easy to be disintegrated during the preparation. The existence of the oxidized groups also led to hydrophily of the created GQDs. As shown in ***Figure 6-10a***, the plot of the absorbance (λ_{ex} = 260 nm) divided by the cell length, versus the concentration, fits well with the Lambert-Beer Law, indicating the good water solubility of the GQDs product. The absorbance coefficient at 260 nm was calculated as 2948.47 $L.g^{-1}.m^{-1}$. All

the UV/Vis spectra of GQDs with different concentrations show uniform feature (***Figure 6-10b***), which gives newly-opened electronic band gaps, along with blue shifted π-to-π* transition of C=C (207 nm) and n-to-π* transition of C=O (260 nm) (full details of the UV/Vis spectra will be discussed in the ***Section 6.3.3*** base on the GQDs created from GFs).

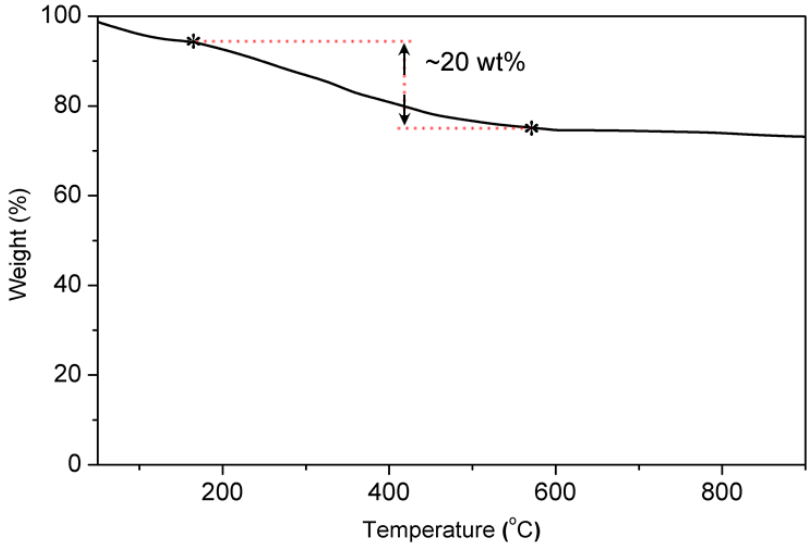

Figure 6-9. TGA of GQDs resultant from MWCNTs.

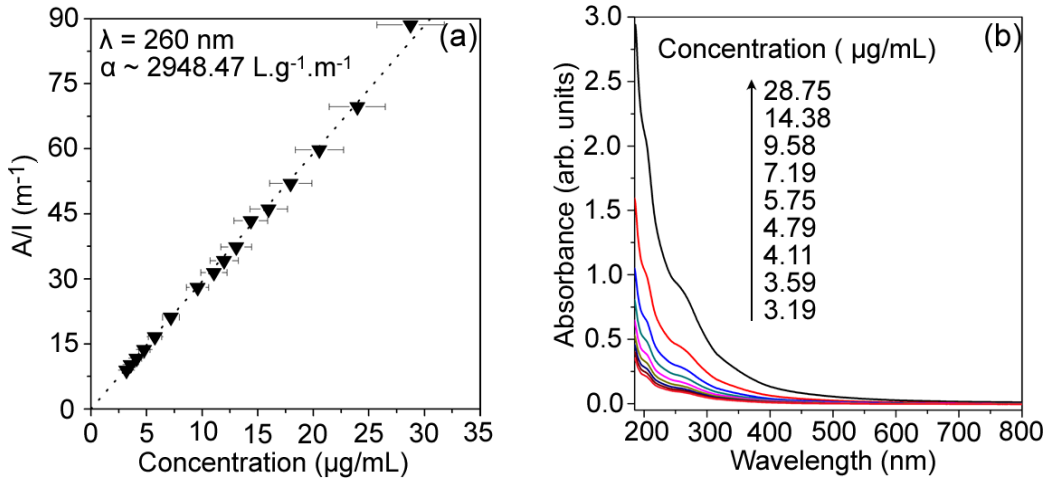

Figure 6-10. **High water solubility and absorption features which are different from those of MWCNTs.** (a) The plot of the absorbance (λ_{ex} = 260 nm) divided by the cell length, versus the concentration, fits well with the Lambert-Beer Law, indicating the good water solubility of the GQDs product; (b) All the UV/Vis absorption spectra of GQD solutions with different concentrations show three bands around 207, 260 and 310 nm.

Clearly, using this method, small (~18.5 nm) GQDs (>90% monolayered) can be effectively exfoliated and disintegrated from MWCNTs. The product yield of the GQDs (from MWCNTs) was calculated as ~23 wt% of the total amount of starting MWCNTs.

One main conclusion from this part of preparation work is that the combustion and the de-intercalation reactions (creating many defects on the graphene walls, see ***Scheme 6-1***) of the potassium intercalated MWCNTs are mainly responsible for the breaking of C-C/C=C bonds with the subsequent reaction with EtOH/H_2O under ultrasonication. However, the combustion did not seem to be a necessary step to cut GQDs, as supported by the fact that high yield GQDs (~10 wt%) also could be prepared by exfoliating/disintegrating big sized bulk GFs without relying on combustion (as described in the following ***Section 6.3.3***).

6.3.3 Characterisations of the GQDs Created from GFs

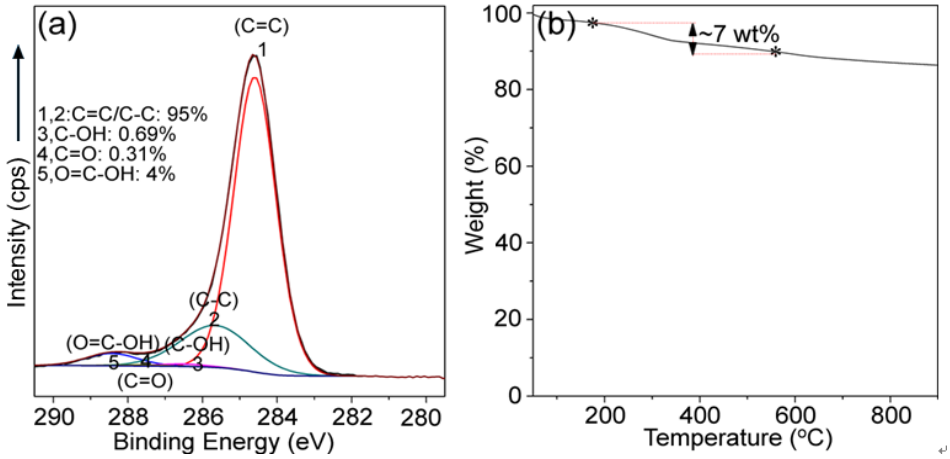

Figure 6-11. Analysis of the GQDs exfoliated and disintegrated from GFs: (a) C1s XPS spectra; (b) TGA.

The similar principle was further used to make K-intercalated GFs for creating GQDs. Interestingly, in this case, although no combustion of the intercalated compounds was observed on exposure to air, the edges of the graphite flakes were still highly exfoliated and disintegrated upon reacting with EtOH/H_2O under ultrasonication (see ***Figures 6-4 & 6-5***, discussed in ***Section 6.3.1***). The obtained yellow suspensions containing thin GQDs also showed good stability. XRD and FT-IR analysis (see ***Figure 6-5*** in ***Section 6.3.1***) of the collected GQDs are the same as that created MWCNTs, suggesting the thin structure and oxidized feature of the product. Further analysis confirmed that the products resultant from exfoliation and disintegration of GFs are monolayered GODs (see details below and ***Figure S6-2*** **to** ***Figure S6-4*** in ***Supporting Information***). Differently from those created from MWCNTs (84.5% carbon content, molar ratio), GQDs created from GFs contain high proportion of un-oxidized C=C/C-C (95% molar ratio). ***Figure 6-11*** gives the C1s XPS and TGA curve of these GQDs. In this C1s XPS, the main components arise from C=C/C-C (284.6 and 285.6 eV, peak 1 and 2, 95% molar ratio), O=C-OH (carboxyl, 288.4 eV, peak 5, 4% molar ratio), C-OH (hydroxyl, 286.4 eV,

peak 3, 0.69% molar ratio) and C=O (carbonyl, 287.3 eV, peak 4, 0.31% molar ratio) species.[20,22] During heat treatment under Ar protection, there are around 7 wt% weight loss during 155-550 °C (***Figure 6-11b***), which is close with the C1s XPS result and suggesting the GQDs (from GFs) was slightly oxidized. Starting from the C1s analysis, the GQDs yield from GFs was confirmed as ~10 wt% (see ***Section 6.2.5*** for more details).

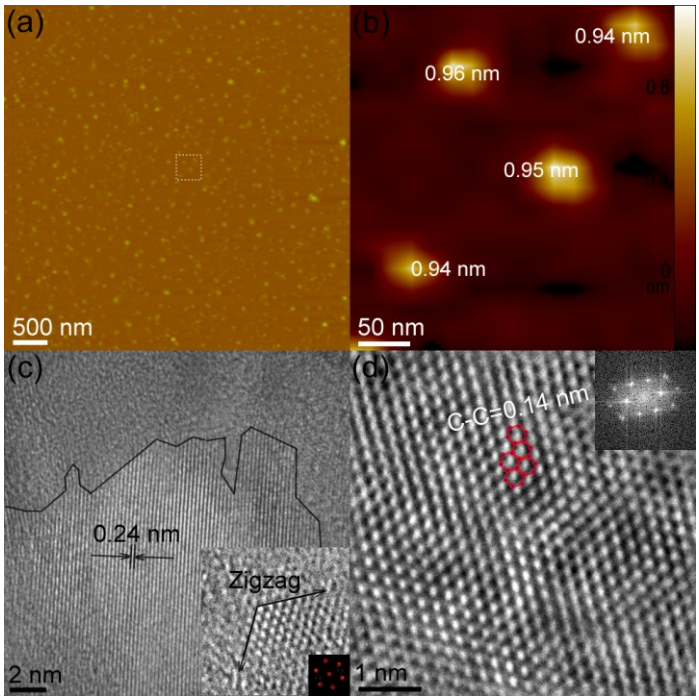

Figure 6-12. (a-b) AFM images of GQDs created from GFs, local enlarged AFM images b corresponding to the marked ones in image a; (c-d) BF-HRTEM images of GQDs created from GFs, insets of image c show zigzag edge which highly corresponding to their 2D FFT patterns.

Figures 6-12a-d show the AFM and TEM images of GQDs (from GFs). The products consist of small individual particles (***Figure 6-12a***). More Local enlarged AFM height topography images (***Figure 6-12b***) clearly show an average thickness at around 0.9 nm of the dots, which in accordance well with monolayered graphene.[23,24] This thickness is similar with that obtained from the GQDs created from MWCNTs, and suggest that the oxygen-containing groups are mostly located at the edge instead of the 2D plane of GQDs (higher thickness of the GQDs should be obtained if the oxidized groups perpendicular to the 2D place of GQDs). Meanwhile, the thickness obtained from ***Figure 6-12b*** is representative considering the very similar contrast between the selected dots and other dots. Statistical analysis on AFM images gives an average size around 20 nm (***Figure S6-3*** in ***Supporting Information***). Moreover, the majority of prepared GQDs

(>95%) are mono-layered (***Figure S6-3*** in ***Supporting Information***). Similar with the GQDs created from MWCNTs (***Figure 6-8***), the GQDs created from GFs have clearly terminated edges (***Figure 6-12c***). BF-HRTEM (***Figure 6-12c***) image of the dots also shows a lattice fringes of 0.24 nm (1120, JCPDS: 41-1487), confirming the crystal structure and high crystallinity of graphene. Because of the small size, the edge structures (*e.g.* zigzag and armchair edges) are more evident based on their fast Fourier transform (FFT) patterns (highlighted in inset of ***Figure 6-12c***, also see ***Figure S6-4*** in ***Supporting Information***). HRTEM images and their FFT patterns further confirm the hexagonal honeycomb structures and bond lengths (0.14 nm of C-C/C=C in ***Figure 6-13d***) of graphene. Therefore, it is clear that high yield GQDs can also be exfoliated and disintegrated from GFs. Further examination on these GQDs suggests that it share similar optical properties with the GQDs created from MWCNTs (details will be discussed in the next section).

6.3.4 Optical Properties of the Created GQDs

The discovered special edges and shapes of the GQDs are proposed mainly responsible for their optical property and electronic structure changes described below. Similarly to those created from MWCNTs (***Figure 6-10b***), GQDs exfoliated and disintegrated from GFs exhibit three absorption bands around 207, 260 and 310 nm in the UV/Vis spectra (***Figure 6-13a***). As far as we know, GO sheets have a π-to-π* transition of C=C bond and a n-to-π* transition of C=O bond at around 230 and 290-300 nm respectively, while typical graphene only has a single π-to-π* transition of C=C bond at 270 nm.[25,26] Therefore, the absorption peak around 207 nm (band A in ***Figure 6-13a***) is attributed to the blue shifted π-to-π* transition of C=C of oxidized aromatic structure. The absorption around 260 nm (band B in ***Figure 6-13a***) corresponds to the blue shifted n-to-π* transition of C=O bond from 290-300 nm. In the UV/Vis spectra (in ***Figure 6-13a***), bands B and C indicate newly opened band gaps arising from the triple carbene at the zigzag edges, corresponding to the transitions from the highest occupied molecular (HOMOs) to lowest unoccupied molecular orbitals (LUMOs, σ and π orbitals) of triple carbene respectively.[8]

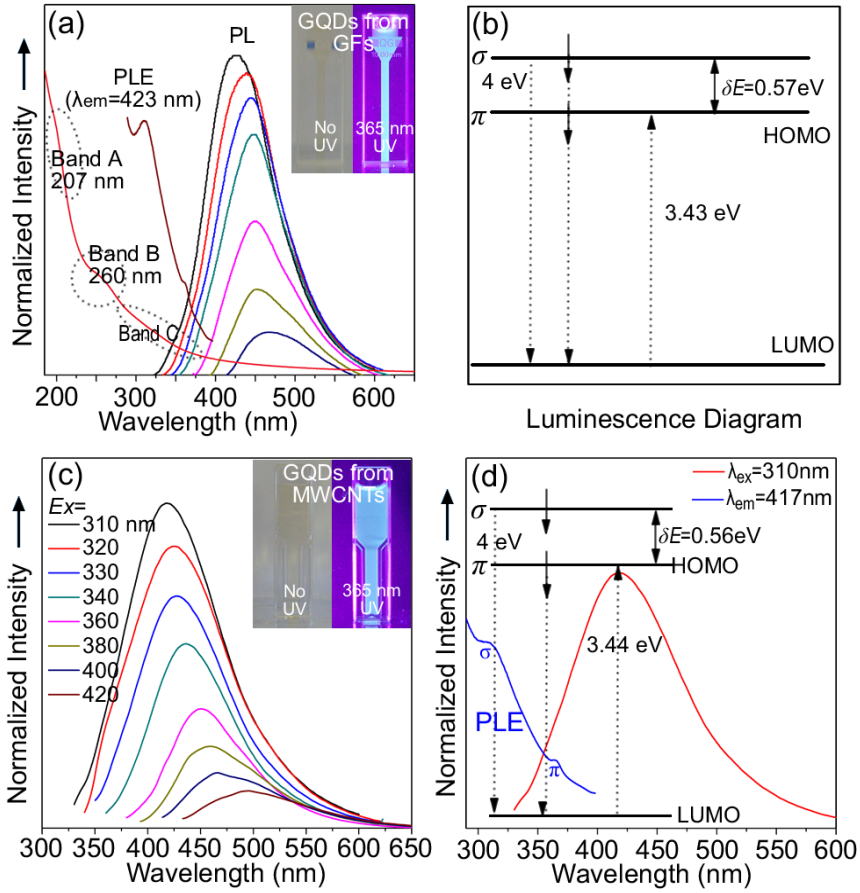

Figure 6-13. (a) UV/Vis, PLE and PL spectra (at the excitation wavelength of 310, 320, 330, 340, 360, 380, 400 nm, from left to right) of the GQDs created from GFs. The strongest photoluminescence (PL) emission occurs at 423 nm with a Stokes shift of 113 nm (1.07 eV); (b) Emission diagram (λ_{ex}=310 nm) of image a, suggesting the irradiation decay of activated electrons from the LUMO to the HOMO of the free zigzag sites with a carbine-like triplet ground state; (c) PL spectra of the GQDs created from MWCNTs under different detection wavelengths; (d) Emission diagram for GQDs created from MWCNTs. Insets in image a and c are the photographs of GQDs solvent with/without 365 nm UV illumination.

Interestingly, both GQDs created from GFs and MWCNTs have strong luminescence under UV illumination (inset of ***Figures 6-13a&c***). PL analysis indicates that the strongest emission of the GQDs (created from GFs) occurs at 423 nm with a Stokes shift of 107 nm (1.07 eV) (***Figure 6-13a***). The GQDs created from MWCNTs also gives similar luminescence. As shown in ***Figure 6-13c***, the strongest (PL) emission in this case occurs at 417 nm with a Stokes shift of 107 nm (1.03 eV). Although the quantum confinement effects are normally observed in small sized materials, the carbene structures (at the zigzag edges) described above are more likely responsible for the opening of the strong luminescence of the GQDs. As previously demonstrated by Pan *et al.* [8] triplet carbenes (described as $\sigma^1\pi^1$) have two orbitals (σ and π) which are singly occupied and commonly exist at the zigzag edges of the graphene. The electronic transitions between

these two orbitals (HOMOs) and LUMOs directly generate strong PL (inset of ***Figures 6-13b&d***). As confirmed by the PLE (λ_{em}=423 nm, ***Figure 6-13a***) spectra of the GQDs created from GFs, which show the transitions from the ground state to σ (310, ~4 eV) and π orbitals (362 nm, ~3.43 eV) (HOMOs) of the triple carbenes respectively. ***Figure 6-13b*** also illustrate this kind of emission mechanism. For triplet carbene structure, it is required that the energy gap between HOMO σ and π orbits (δE) should be below 1.5 eV.[27] Further calculation of the δE between σ and π of the GQDs (created from GFs, 0.57 eV, ***Figure 6-13b***) confirmed that the described emission mechanism is reasonable.[8] This emission mechanism is also applicable to explain the emission of the GQDs created from MWCNTs (***Figure 6-13d***).

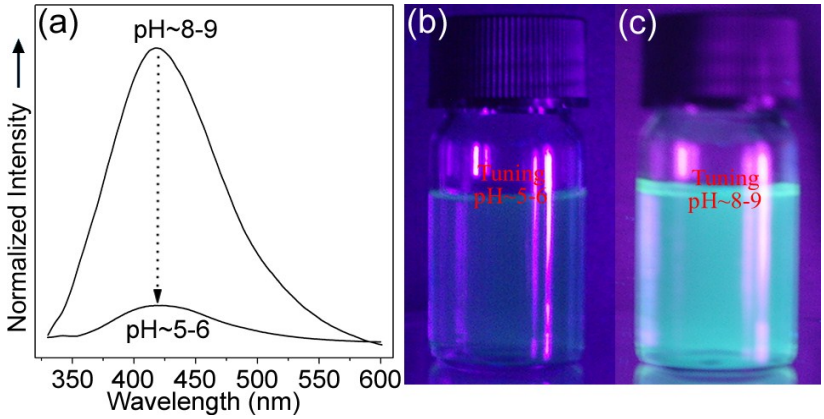

Figure 6-14. (a) The PL emission highly depends on the pH value of the media, which is reasonable as the emissive free zigzag sites has been broken under acidic condition; (b,c) Photographs of the GQDs with different pH values under 365 nm UV illumination.

For further illuminate this mechanism, as an instance, the pH value of the GQDs solution (created from MWCNTs) was tuned to around 5-6 and 8-9 respectively. PL analysis suggested that the luminescence of the GQDs highly quenched upon tuning pH to under 7 (***Figure 6-14a***). This is more evident with the photographs of the GQDs under 365 nm UV illumination (***Figure 6-14b&c***). This feature confirmed that the luminescence of the GQDs mainly induced by the zigzag carbene structures as it can be destroyed in acid media. Although both GQDs share similar optical feature, the quantum yield of the GQDS created from GFs (7.1%, see ***Table 6-1*** in ***Section 6.2.6***) is slightly higher than that created from MWCNTs (6.5%) (see ***Table 6-2*** in ***Section 6.2.6***), which is probably related to the more free zigzag edges reserved in GQDs with a lower oxidization extent. For both GQDs created from GFs and MWCNTs, the main absorption peak of the newly opened gap should centre at around 310 nm (4 eV) which is the excitation wavelength of the strongest PL emission. This opened energy level is lower than that opened in the tiny GQDs but corresponds well to the bigger size of the products here.[8] Nevertheless,

the luminescence feature of the present GQDs is similar with that of reported smaller one.[8] It's still unclear whether the luminescence is also influenced by the edge defects or surface traps.

6.3.5 Bio-imaging Application of the GQDs (Created from MWCNTs)

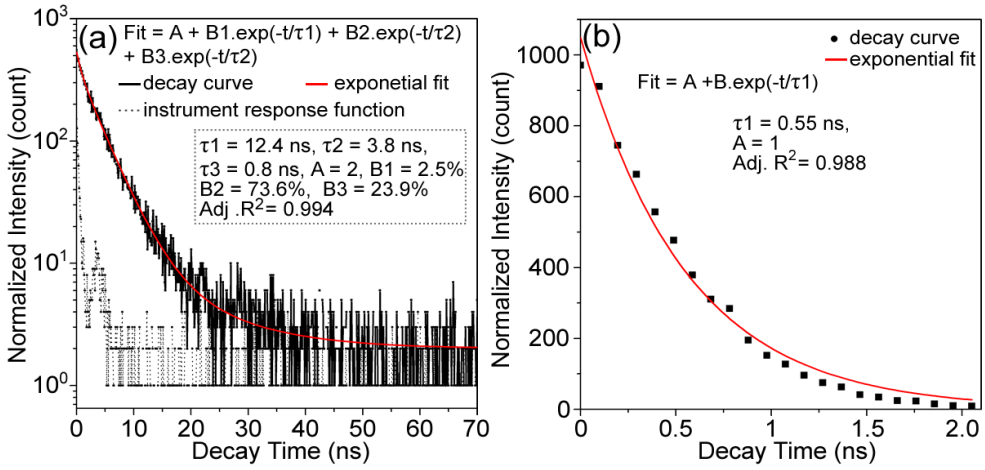

Figure 6-15. (a) TRPL decay profile of GQDs (created from MWCNTs) recorded at room temperature while monitoring the emission at 425 nm upon 320 nm excitation wavelength; (b) The single exponential function of the instrument response (before afterpulse) showing a 0.55 ns decay time, which is different from the decay time in ***Figure 6-15a*** and confirmed that all the decay time in ***Figure 6-15a*** is not the instrument response.

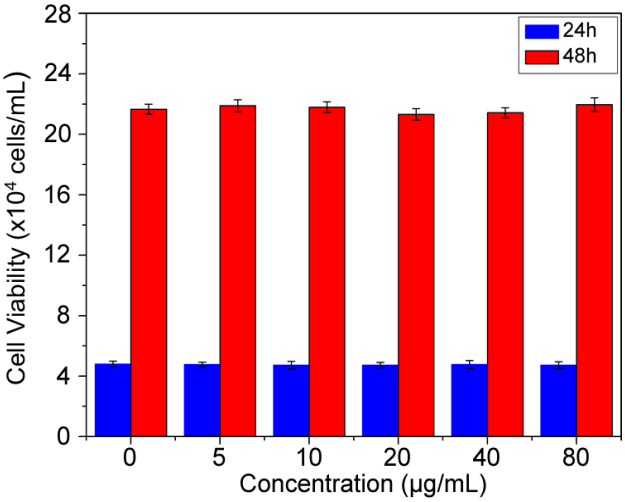

Figure 6-16. Cell viability assay with MDCKII cells treated with different concentrations of GQDs. The bars represent cell counts and the error bars represent standard errors of the mean.

The successful preparation of high yield GQDs can pay the way for many new applications of graphene, for example, bio-medical imaging. To illustrate this, the GQDs created from MWCNTs were further estimated for the cellular imaging. ***Figure 6-15a*** is

the time resolved PL (TRPL, time-correlated single photon counting technique) of the GQDs (created from MWCNTs). The lifetime of the luminescence can be fitted well with a tri-exponential function. The observed lifetimes of these main types of luminescence are 12.4 ns (2.5%), 3.8 ns (73.6%) and 0.8 ns (23.9%) respectively. The decay of 0.8 ns might due to the instrument response (0.55 ns in ***Figure 6-15b***) as it was found close to the decay from instrument response. The majority nanosecond decay suggests that the GQDs are promising candidate materials for optoelectronic and biological applications.

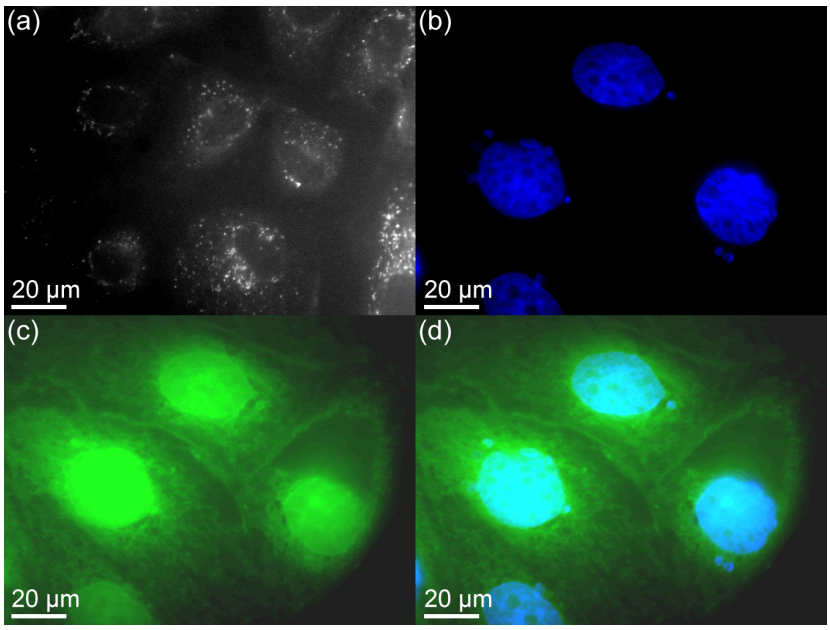

Figure 6-17. Confocal microscopy images of mammalian cells. (a) Agglomerated GQDs surrounding each nucleus (cells are stained by GQDs only); (b) Individual nucleus stained blue with DAPI; (c) GQDs with green luminescence surrounding the nuclei; (d) The overlay image of cells stained with DAPI and GQDs.

However, for biological applications (*e.g.* bioimaging, protein analysis by FRET, cell tracking, isolation of biomolecules, and gene technology), the inherent toxicity of the materials should be minimized. The cytotoxicity of GQDs (created from MWCNTs) here was evaluated using the mammalian cell line, MDCKII (Madin-Darby Canine Kidney Type II). The results (***Figure 6-16***) show that low doses of GQDs (0-80 μg/mL) are non-toxic to these cells. No obvious effect on cell number was observed at low dosage (0-80 μg/mL, ***Figure 6-16***) with prolonged exposure (24-48 h). To further illustrate the potential in bio-imaging applications, the luminescent cell imaging was performed using the GQDs. ***Figure 6-17a*** shows the image of the MDCKII cells stained with GQDs alone. The GQDs were taken up by the cells but did not penetrate the cell nuclei. ***Figures 6-17b-d*** give the images of MDCKII nucleus stained with DAPI (emission from around 400-650 nm), GQDs and the overlay image, respectively. Although the nucleus in ***Figure***

6-17c also gives green emission (from DAPI), the boundary between cells, nuclei and cytoplasm are clear. This is more clearly seen in the overlay image (***Figure 6-17d***). All these results indicate that the GQDs can be used in high contrast bio-imaging and will be well-suited for other biomedical applications.

6.4 Conclusion

Clearly, by using currently developed methods, high yield luminescent GQDs can be created from both MWCNTs and cheap GFs, which cannot be achieved using traditional routes. Both created GQDs show similar size around 20 nm and good water solubility and majority of them are monolayered (> 90%). Because of the carbene structures in the zigzag edges, prepared GQDs show interesting luminescence with high quantum yield. Although both GQDs show similar size distribution and absorption feature, the GQDs created from graphite flakes show much low oxidation extent and increased luminescent quantum yield. This successful preparation of thin oxidized GQDs and the discovery of their interesting fluorescence properties could pave the way for new applications (*e.g.* cellular application) of GQDs in a variety of fields. Next, the formation mechanism of the monolayer QDs will be further concluded in more detail. The formation of GQDs from MWCNTs is considered to rely on the bond breaking from the defects on the graphene walls, which were created by the combustion (in contact with air) and the de-intercalation of the potassium intercalated MWCNTs. The combustion could assist increasing the production yield, but it did not seem to be a necessary step, as supported by the fact that high yield GQDs (~10 wt%) also could be prepared by exfoliating/disintegrating big sized bulk flakes without relying on combustion. In other words, the rapid de-intercalation (which also generates defects on the graphene layers) of the intercalated compounds during short exposure is capable enough to disintegrate the layers under ultrasonication treatment. This is exciting because it can result in the breaking of the C=C/C-C bonds, which have a greater binding energy than in most of the other layered materials. In terms of this, a number of other layered materials could potentially be more easily exfoliated and disintegrated to form the corresponding 2D-QDs (the preparation will be further developed to prepare other monolayered QDs, see ***Chapters VII-IX***.

6.5 Supporting Information

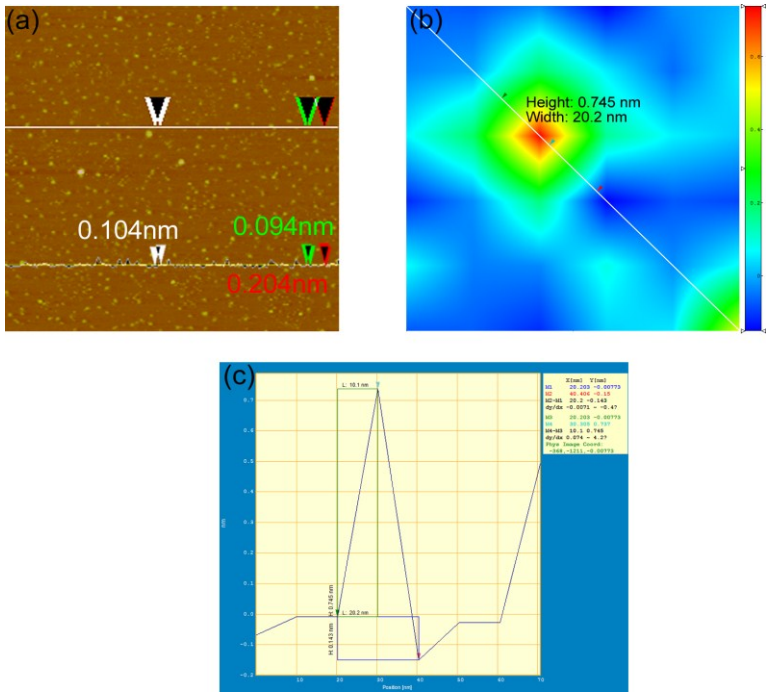

Figure S6-1. **Height error analysis and height analysis of the dot.** (a) AFM image of GQDs and height error analysis. Scale: 5 × 5 μm. The error with the thickness measurements with AFM was caused by the uneven mica substrate; (b) Height topography of one representative GQD, Scale 70 × 70 nm; (c) Height analysis of the GQD in Image a.

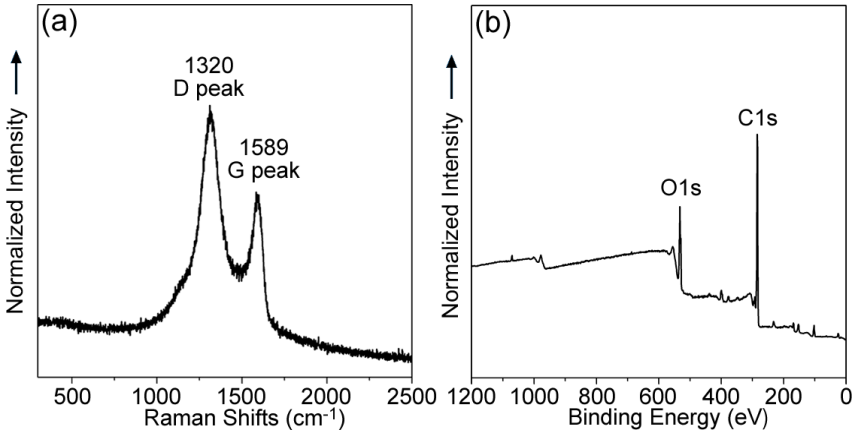

Figure S6-2. **Analysis of the GQDs resultant from exfoliating and disintegrating GFs.** (a) Raman spectrum shows D and G peaks of the GQDs at around 1320 and 1589 cm^{-1}, corresponding well with graphene; (b) XPS full profile shows C and O elements in the GQDs (O should came from the contaminations and oxygen-containing groups at the edge of GQDs).

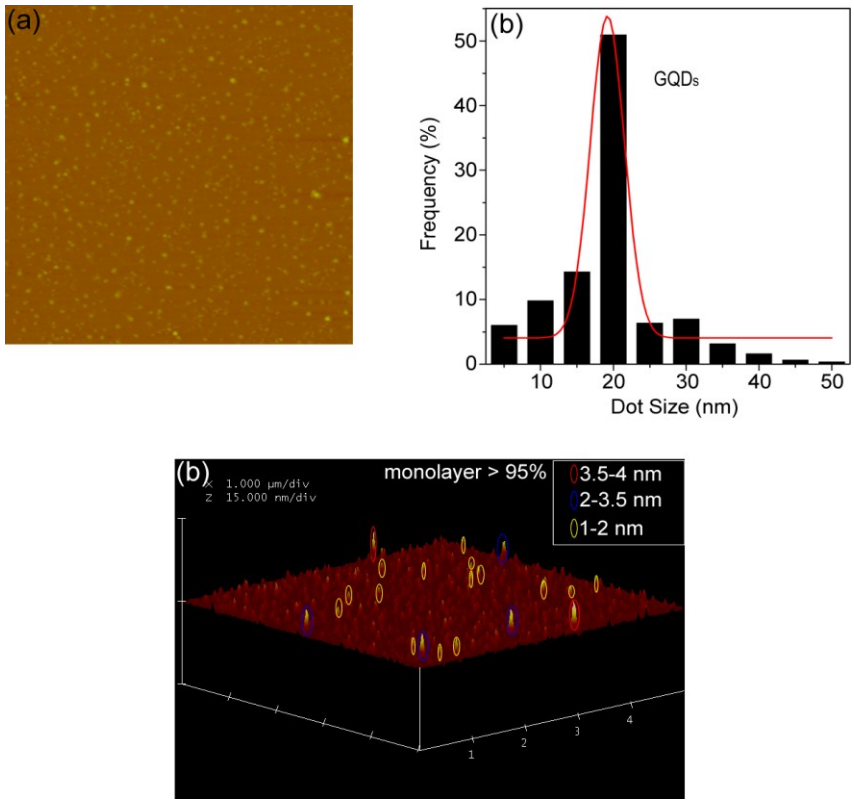

Figure S6-3. **AFM analysis of GQDs resultant from exfoliating and disintegrating GFs.** (a) AFM image for size and thickness analysis. Scale: 5 × 5 μm; (b) Size distribution; (c) Height distribution suggests more than 95% GQDs are monolayer.

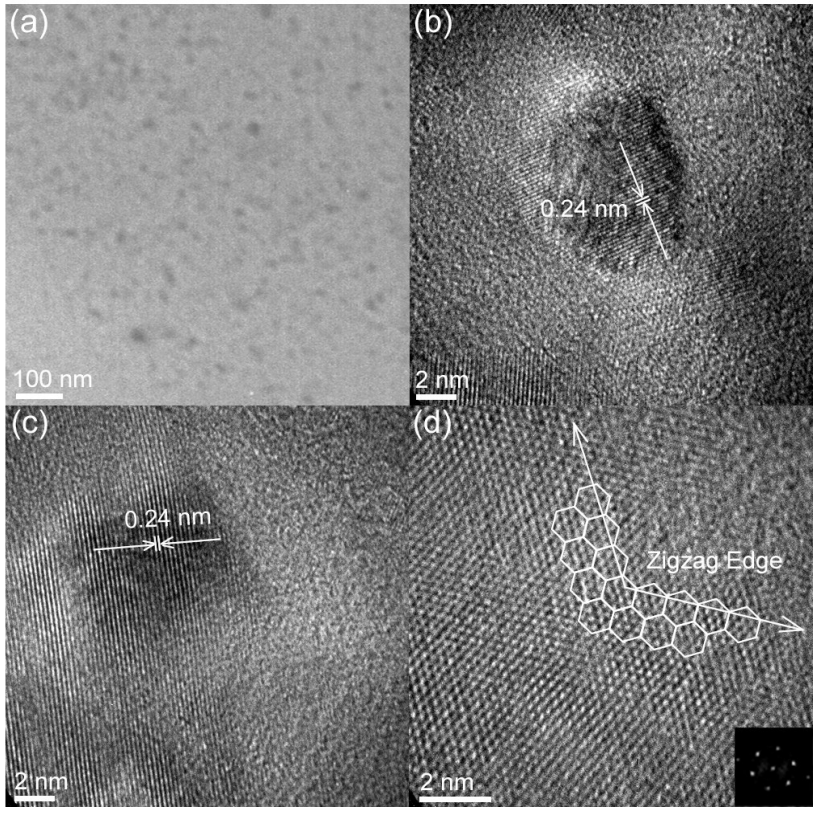

Figure S6-4. **TEM Analysis of GQDs resultant from exfoliating and disintegrating GFs.** (a) TEM image; (b) A dot showing lattice parameter of 0.24 nm, (1120) lattice fringes of graphene; (c) A lattice parameter of 0.24 nm, (1120, JCPDS: 41-1487) lattice fringes of graphene; (d) Schematic illustration showing the orientation of the graphene and zigzag edge of a dot. Inset is the corresponding FFT image.

References and Notes

[1] A. K. Geim and K. S. Novoselov, The Rise of Graphene. *Nat. Mat.* **2007**, *6*, 183-191.

[2] L. E. Brus, Quantum Crystallites and Nonlinear Optics. *Appl. Phys. A* **1991**, *53*, 465-474.

[3] A. L. Efros and M. Rosen, The Electronic Structure of Semiconductor Nanocrystals. *Annu. Rev. Mater. Sci.* **2000**, 30, 475-521.

[4] L. Li and X. Yan, Colloidal Graphene Quantum Dots. *J. Phys. Chem. Lett.* **2010**, *1*, 12572-12576.

[5] J. Lu, P. S. E. Yeo, C. K. Gan, P. Wu and K. P. Loh, Transforming C_{60} Molecules into Graphene Quantum Dots. *Nat. Nanotechnol.* **2011**, *6*, 247-252.

[6] C. Stampfer, J. Güttinger, F. Molitor, D. Graf, T. Ihn and K. Ensslin, Tunable Coulomb Blockade in Nanostructured Graphene. *Appl. Phys. Lett.* **2008**, *92*, 012102.

[7] X. Yan, X. Cui, B. Li and L. Li, Large, Solution-Processable Graphene Quantum Dots as Light Absorbers for Photovoltaics. *Nano Lett.* **2010**, *10*, 1869-1873.

[8] D. Pan, J. Zhang, Z. Li and M. Wu, Hydrothermal Route for Cutting Graphene Sheets into Blue-luminescent Graphene Guantum Dots. *Adv. Mater.* **2010**, *22*, 734-738.

[9] S. Zhu, J. Zhang, C. Qiao, S. Tang, Y. Li, W. Yuan, B. Li, L. Tian, F. Liu, R. Hu, H. Gao, H. Wei, H. Zhang, H. Sun and B. Yang, Strongly Green-Photoluminescent Graphene Quantum Dots for Bioimaging Applications. *Chem. Commun.* **2011**, *47*, 6858.

[10] Y. Li, Y. Hu, Y. Zhao, G. Shi, L. Deng, Y. Hou and L. Qu, An Electrochemical Avenue to Green-luminescent Graphene Quantum Dots as Potential Electron-acceptors for Photovoltaics. *Adv. Mater.* **2011**, *23*, 776-780.

[11] L. Li, G. Wu, G. Yang, J. Peng, J. Zhao and J.-J. Zhu, Focusing on Luminescent Graphene Quantum Dots: Current Status and Future Perspectives. *Nanoscale.* **2013**, *5*, 4015-4039.

[12] (a) Y. Dong, C. Chen, X. Zheng, L. Gao, Z. Cui, H. Yang, Y. Chi and C Li, One-step and High Yield Simultaneous Preparation of Single- and Multi-layer Graphene Quantum Dots from CX-72 Carbon Black. J. Mater. Chem. 2012, 22, 8764-8766. (b) X. Xia and Y. Zheng, Comment on "One-step and High Yield Simultaneous Preparation of Single- and Multi-layer Graphene Quantum Dots from CX-72 Carbon Black". J. *Mater. Chem.* **2012**, *22*, 21776.

[13] J. Peng, W. Gao, B. K. Gupta, Z. Liu, R. Romero-Aburto, L. Ge, L. Song, L. B. Alemany, X. Zhan, G. Gao, S. A. Vithayathil, B. A. Kaipparettu, A. A. Marti, T. Hayashi, J. Zhu and P. M. Ajayan, Graphene Quantum Dots Derived from Carbon Fibers. *Nano Lett.* **2012**, *12*, 844-849.

[14] A. J. Jacobson and L. F. Nazar, in Intercalation Chemistry. *Encyclopedia of Inorganic Chemistry*, WILEY-VCH, Weinheim, **2006**, pp. 1-37.

[15] J. N. Demas and G. A. Grosby, The Measurement of Photoluminescence Quantum Yield. A Review. *J. Phys. Chem.* **1971**, *75*, 991-1024.

[16] W. R. Dawson and M. W. Windsor, Fluorescence Yield of Aromatic Compounds. *J. Phys. Chem.* **1968**, 72, 3251-3260.

[17] G. Weber and F. W. J. Teale, Determination of the Absolute Quantum Yield of Fluorescent Solutions. *Trans. Faraday. Soc.* **1957**, *53*, 646-655.

[18] L. M. Viculis, J. J. Mack and R. B. Kaner, A Chemical Route to Carbon Nanoscrolls. *Science* **2003**, *299*, 1361.

[19] W. C. Oh, S. J. Cho and Y. S. Ko, The Stability of Potassium-Graphite Deintercalation Compounds. *Carbon* **1996**, 34, 209-215.

[20] W. Chen, L. Yan and P. R. Bangal, Chemical Reduction of Graphene Oxide to Graphene by Sulfur-Containing Compounds. *J. Phys. Chem. C* **2010**, *114*, 19885-19890.

[21] J. Li, H. Lin, Z. Yang and J. Li, A Method for the Catalytic Reduction of Graphene Oxide at Temperature Below 150 ^{o}C. *Carbon* **2011**, *49*, 3024-3030.

[22] S. Stankovich, D. A. Dikin, R. D. Piner, K. A. Kohlhaas, A. Kleinhammes, Y. Jia, Y. Wu, S. T. Nguyen and R. S. Ruoff, Synthesis of Graphene-based Nanosheets via Chemical Reduction of Exfoliated Graphite Oxide. *Carbon* **2007**, *45*, 1558-1565.

[23] K. S. Novoselov, A. K. Geim, S. V. Morozov, D. Jiang, Y. Zhang, S. V. Dubonos, I. V. Grigorieva and A. A. Firsov, Electric Field Effect in Atomically Thin Carbon Films. *Science* **2004**, *306*, 666-669.

[24] X. Li, X. Wang, L. Zhang, S. Lee and H. Dai, Chemically Derived, Ultrasmooth Graphene Nanoribbon Semiconductors. *Science* **2008**, *319*, 1229-1232.

[25] Z. Luo, Y. Lu, L. A. Somers and A. T. C. Johnson, High Yield Preparation of Macroscopic Graphene Oxide Membranes. *J. Am. Chem. Soc.* **2009**, *131*, 898-899.

[26] D. Li, M. B. Müller, S. Gilje, R. B. Kaner and G. G. Wallace, Processable Aqueous Dispersions of Graphene Nanosheets. *Nat. Nanotechnol.* **2008**, *3*, 101-105.

[27] R. Hoffmann, Preparation of Graphitic Oxide. *J. Am. Chem. Soc.* **1968**, *90*, 1475.

Chapter VII. Fabrication and Luminescence of Monolayered BN Quantum Dots

7.1 Introduction

Forming of quantum dots (QDs) can be one of the most effective ways to broaden or reveal new physical properties in a material, in particular when they are made atomically thin.[1-5] A typical example is the creation of new electronic band gap in graphene QDs (GQDs), where strong photoluminescence occurs upon reducing its size to the nanoscale (also see ***Chapter VI***).[6] Hexagonal boron nitride (hBN), meanwhile, has a layered structure[7] that is similar to graphite and can be exfoliated as monolayered BN sheets. This form of BN has rapidly become recognised as having potential for practical applications in catalysts, optoelectronic and semiconductor devices.[8-11] Theoretically, monolayered BN sheets can reproduce the unusual electronic properties of 'armchair'-edged graphene, have new electronic band gaps introduced and manipulated into a half-metal electronic configuration by controlling the edge structure and defect centres.[12-15] Further reduction of the lateral size of monolayered BN sheets should, in principle, allow the edge and defect dependent properties could become much more evident, providing a new route to controlling materials properties through QD size and quality. Thin BN sheets have been made by ultrasonication,[8] high-energy electron beam irradiation[9] and CVD[10,11] methods. However, further reduction of the lateral size of monolayered BN structures to form QDs has remained a significant challenge.

This chapter describes a method of fabricating monolayered BN QDs by exfoliating and disintegrating monolayered BN QDs from hBN flakes. Due to strong quantum confinement effects, a direct gap of 6.51 eV in the BN QDs can be achieved, which is much larger than that of pure bulk BN. Most importantly, by engineering a low proportion of edge and point defects (*e.g.* BO_2^- species, zigzag carbene edges and 1,3-B centres) into the monolayered BN QDs, blue-green luminescence with a quantum yield of 2.5% can be achieved. This may widen the opportunities for optoelectronic applications of hBN. However, this chapter also demonstrates that monolayered BN

QDs can be used as a non-toxic fluorescent label in confocal microscopy of biological cells.

7.2 Experimental Methods

7.2.1 Sample Preparation

Because hBN flakes have similar structure with that of GFs, the preparation here was similar to the preparation of GQDs from GFs (see ***Sections 6.2.3***). However, 0.1 g hBN was used to react with K as it had a similar volume to that of 0.25 g GFs, which can mix well with K (0.6 g K) and favour the intercalation reaction (more hBN is unsuitable for effective interaction). Unlike GFs, the intercalation of hBN was difficult due to stronger layer interactions (see ***Section 2.1.3*** for more introductions). Therefore, a long intercalation time (>10 h) was required for the intercalation reaction. The completion of the intercalation reaction can be determined by the colour change of the mixture (will be discussed late). After preparation, a yellow solution containing BN QDs was separated from the residual solid hBN by using a filter (with coarse filter paper) to remove hBN sediment. The remaining K ions in the solution were absorbed/removed with the cation exchange resin (fill the resin into a Millipore Millicup filter unit, with ~4 cm filling height. Long filling column will lead much loss of the BN QDs). The resultant white yellow solution was filtered (with microporous membrane) and centrifuged 3-5 times to remove any BN sheets with faint white colour. The collected BN QDs showed transparent faint yellow colour. Then the dispersed/dissolved product was heated in an oven to evaporate ethanol. To collect the solid sample, solvent was removed using a rotary evaporator and oven.

7.2.2 Calculation of the Quantum Yield of BN QDs

See ***Section 3.4*** in ***Chapter III*** for the calculation method of quantum yield.

Table 7-1. Quantum yield of BN QDs suspension (in H_2O) using anthracene as a reference.

Sample	Integrated Emission Intensity (*I*)	Absorptance at 320 nm (*A*)	Refractive Index of Solvent (η)	Quantum Yield (Φ)
Anthracene	198824	0.0365	1.36	30% (Known)[16-18]
BN QDs	48575	0.1042	1.33	~2.5%

7.3 Results and Discussions

7.3.1 The Intercalation and De-intercalation Reactions of BN

The structural similarity of hBN and graphite suggests that BN QDs could be fabricated in a manner close to that was previously demonstrated to create high yield of GQDs (also see ***Chapter VI*** and my published work[19]). As with the preparation of GQDs, the formation of thin BN QDs involved three steps: 1) the formation of potassium intercalated hBN (K-hBN, formed by intercalating K atoms between the covalently-bonded BN sheets, taking advantage of the weak interlayer van der Waals force); 2) short exposure of the K-hBN to air (de-intercalation reaction); and 3) the reaction between K-hBN and EtOH-H_2O under ultrasonic treatment. During this process, the short exposure of K-hBN to air and its reaction with EtOH-H_2O under ultrasonication drove the exfoliation and disintegration of the edges of the hBN flakes (the relevant mechanisms were discussed in ***Chapter VI***). Although the temperature (190-200 ^oC) used for the intercalation reaction here was much lower than that previously reported for the preparation of K-hBN (300 ^oC),[20] the present reaction conditions feasibly allowed intercalation of K atoms into the interlayers of hBN, with colour changes evident (***Figure 7-1***, the resultant grey colour is the same as that of the K-hBN previously prepared at 300 ^oC).[20]

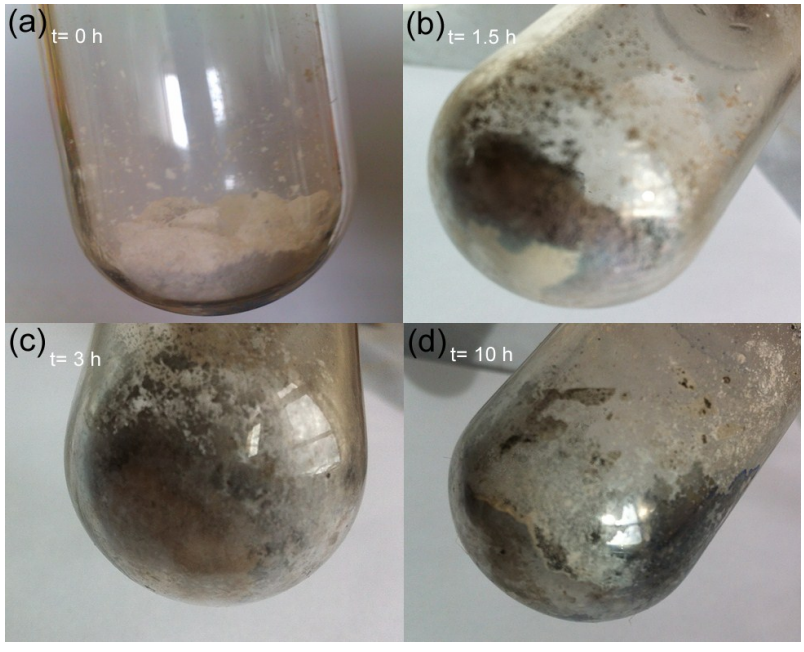

Figure 7-1. **Colour changes of the mixture during the intercalation reaction.** (a) The starting mixture of hBN and K showed white colour; (b) After 1.5 h intercalation reaction, partial mixture changed to brown colour; (c) After 3 h intercalating reaction, the mixture fully changed to brown and grey colour; (d) After 10 h intercalating reaction, the mixture changed to grey colour which is the same as the colour of intercalated hBN reported before.[20] Tube diameter: ~3 cm.

XRD, TEM and SAED confirmed that the edges of hBN flakes were effectively exfoliated and disintegrated during the reaction (***Figure 7-2*** and ***Figure 7-3***). ***Figure 7-2*** give the XRD patterns of hBN raw materials and sediment. Compared to that of the raw material hBN, the (002) peak intensity of the residual hBN sediment became much weaker (about half of the hBN raw materials), indicating that the layered structure of hBN was destroyed to certain extent during the reaction. Same changes on the BN flakes can be observed from TEM analysis (***Figure 7-3***). The hBN raw materials have good crystallinity with clear particle edges and single crystalline nature (***Figures 7-3a,d***). The SAED analyses of the hBN raw materials show simple diffraction patterns. In ***Figure 7-3b***, the SAED pattern of one hBN raw flake have second smaller diffraction spots, which possibly because of the dislocation at the edges. By contrast, TEM images of residual hBN sediment show that the BN edges were destroyed deeply (exfoliating and disintegrating) during the reaction. Corresponding SAED analysis give a lot of diffraction patterns (hexagonal rings), further confirming that the edges were effectively destroyed to form many dislocated segments. This was further evidenced by the formation of monolayered BN QDs described below (***Section 7.3.2***).

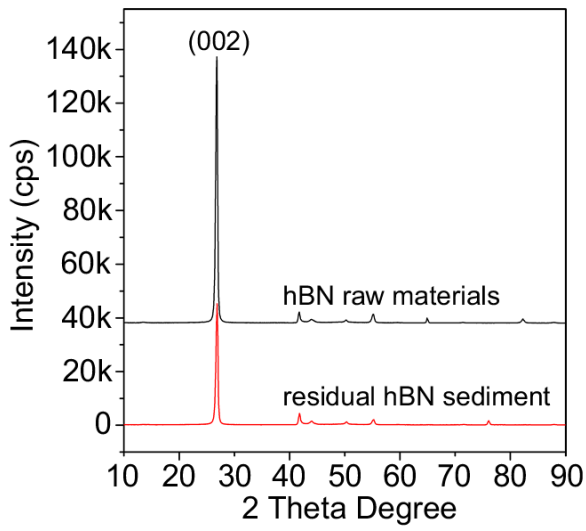

Figure 7-2. XRD patterns of the hBN raw materials and residual hBN sediment. Note: the same quality of the hBN raw materials and residual sediment were used for the XRD analysis.

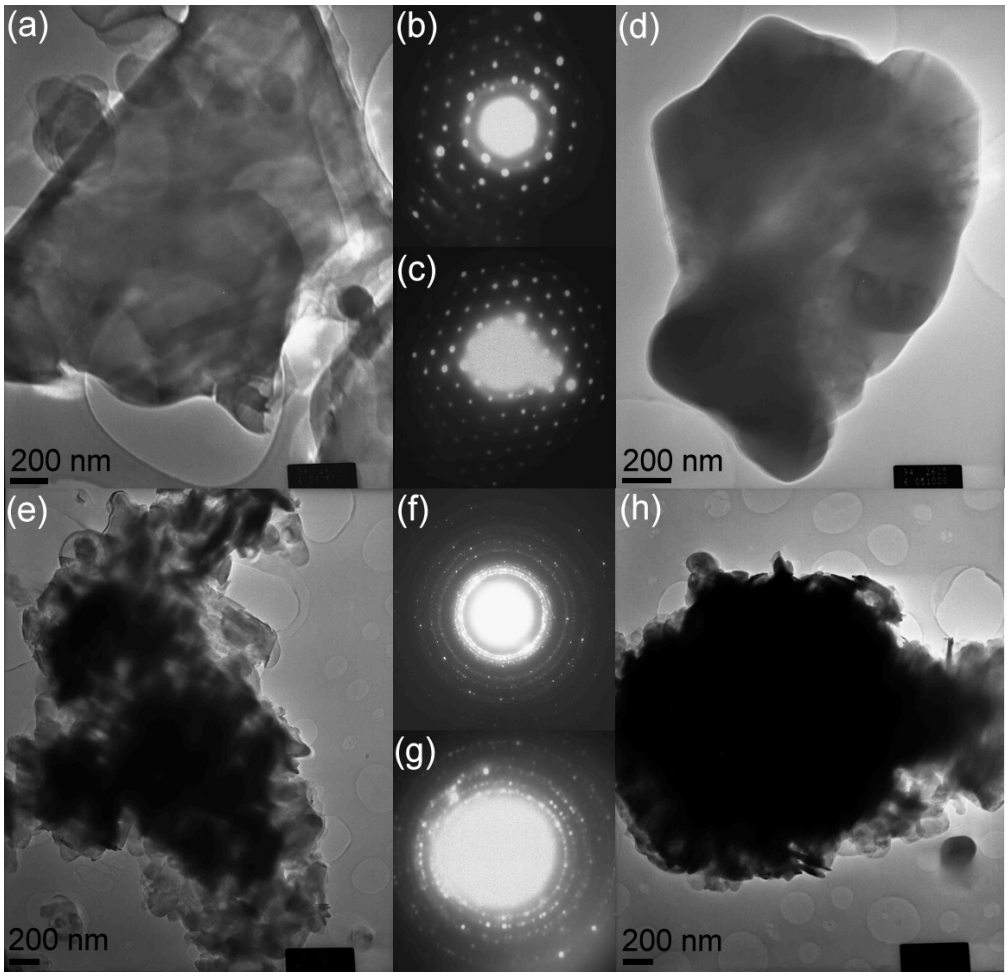

Figure 7-3. **TEM and SAED patterns. (**a-d) hBN raw materials. Image b and c corresponding to image a and d respectively; (e-h) Residual hBN sediment. Images f and g corresponding to images e and h respectively. The SAED patterns were taken on the edge of the particles.

7.3.2 Characterisations of the Created Monolayered BN QDs

After preparation and purification (filtration, cation exchange and centrifugation), the resultant solution showed a faint yellow colour and very good stability (no sediment observed after >5 months). Although no further optimization on the preparation conditions was performed in this preliminary study, a powder yield of 2.1 wt% was achieved. The Raman spectrum (E_x = 785 nm) of the resultant product (***Figure 7-4a***) shows an E_{2g} phonon mode of hBN at around 1366.5-1367 cm^{-1},[21] which is much weaker than that of raw hBN flakes under identical measurement conditions (***Figure 7-4b***). The measured HWHM of the resultant BN ranges from 11-12 cm^{-1}, slightly larger than the width from hBN raw material (10 cm^{-1}). In contrast to the Raman spectrum of raw hBN flakes (1365.6 cm^{-1}), the observed E_{2g} phonon mode of the resultant BN is

slightly upward and softened (***Figure 7-4b***), which is consistent with the reported model of the formation of thin BN decreasing the in-plane lattice constant.[22]

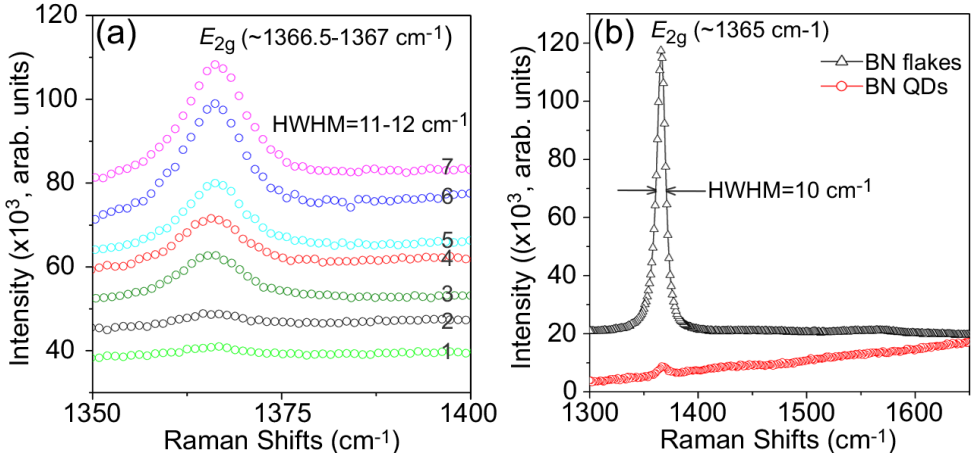

Figure 7-4. (a) Raman spectra of the sample taken on seven positions with three scan parameters (three groups: spectra 1&2, 3&4&5, 6&7). The high intensity was obtained using the accumulation measurement. For better presentation, the zero intensities of the backgrounds in both images were shifted; (b) Raman spectra of the raw BN flakes and resultant BN QDs under identical measurement conditions. Excitation was at a wavelength of 785 nm.

Although no dopant species were detectable by the Raman spectra (*e.g.* the C dopant BN at around 1587 cm^{-1}),[23] FT-IR (***Figure 7-5a***) and XPS (***Figures 7-5b-e***) of the product confirmed the sp^2 BN structure and the existence of N-B-O, O-B-O and C-N/C-B species. As shown in ***Figure 7-5a***, the FT-IR spectra give the vibrations at around 1386-1400 and 770 cm^{-1} correspond to the B-N vibrations in hBN. The splitting of vibration at around 1386-1400 may be induced by the edge oxidization of BN (electron shifted from O to N-B). The vibrations at the regions of 1500-1650 cm^{-1}, 1090-800 cm^{-1} and 750-450 cm^{-1} are attributed to the C-(BN), B-O and O-B-O vibrations respectively.[15,24-25] The B/N/C/O (mole ratio) obtained from XPS survey is around 1/1/0.35/0.21. This high carbon ratio arises mainly from contamination from the carbon film used (the BN powder was pasted on the carbon film for the analysis). In addition, no C-C=C-C structure of the product was detected by Raman test. C1s XPS (***Figure 7-5c***) of the BN QDs gives the C=C/C-C (284.6 eV) and C dopant species with different chemical environment (283.5, 286, 287.3 and 288.6 eV).[26-29] The C=C/C-C should be from the carbon film and contamination used in the analysis as discussed above. The mole ration of C dopant in the whole C element was calculated as 33.7%. Therefore, together with XPS full survey, the chemical composition of $B_xN_yC_zO_d$ was calculated as $BNC_{0.12}O_{0.21}$. The C and O dopants were most likely included during the exposure reaction of K-hBN and disintegration of BN sheets under ultrasonication treatment in EtOH/H_2O solvent

(the BN was oxidized and disintegrated to form stable edges as well as C doping). This chemical doping was further confirmed by the B1s and N1s XPS. In B1s XPS (***Figure 7-5d***), the fitted three peaks at 190.2 (peak 1), 191.4 (peak 2) and 192.8 eV (peak 3) are attributed to the sp^2 BN, oxidized BN and BN species with C dopant respectively.[26-29] Similar feature was observed from N1s XPS (***Figure 7-5e***), where the peaks at around 397.8 (peak 1), 399.1 (peak 2) and 400.4 eV (peak 3) can be attributed to the sp^2 BN, oxidized BN and BN species with C dopant respectively.[26-29]

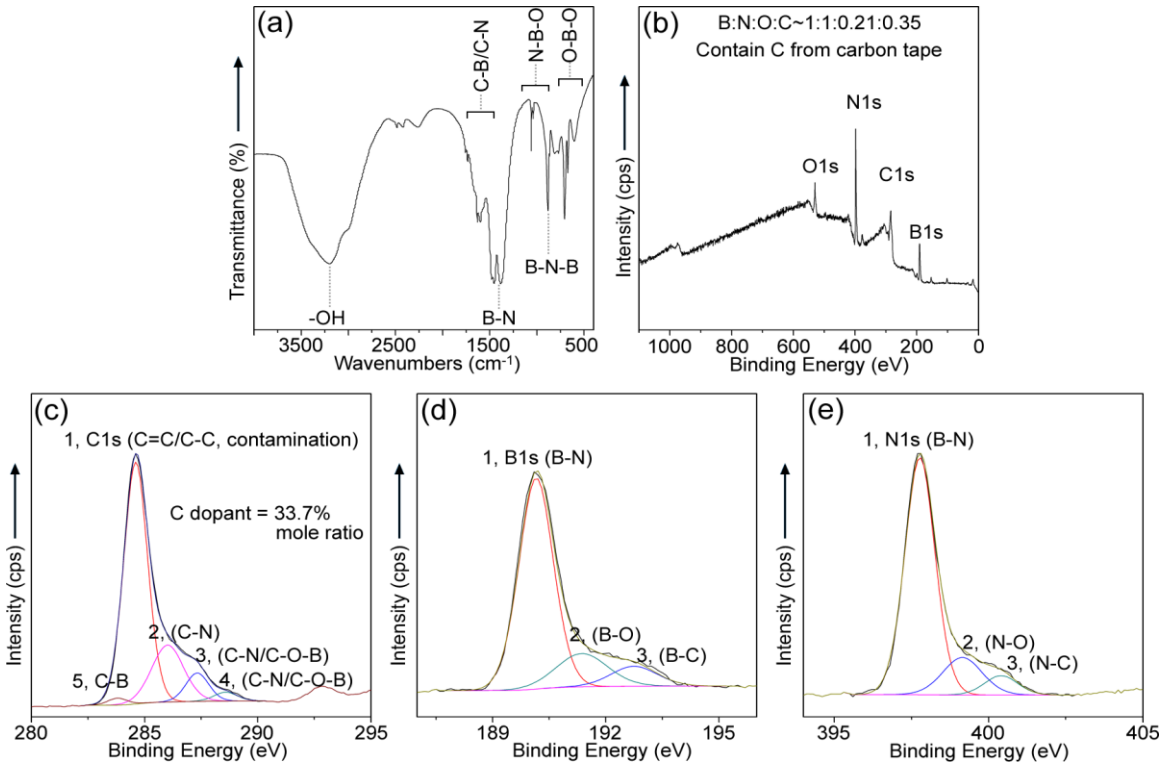

Figure 7-5. **Analysis of the as-prepared BN QDs.** (a) FT-IR spectra; (b) XPS survey; (c) C1s XPS; (d) B1s XPS; (e) N1s XPS.

The created product could be well dissolved/dispersed in H_2O and EtOH. As indicated by ***Figure 7-6a***, the plots of the A/I (A: UV/Vis absorbance; I: cell length, 10^{-2} m, H_2O solvent) versus the concentration (μg/mL) of the sample, fit the Lambert-Beer law well, indicating good water solubility/dispersion of the created product. The absorption coefficients of α_{200} (at 200 nm) and α_{260} (at 260 nm) are calculated to be 8374 and 3420 $L.g^{-1}m^{-1}$ respectively. UV/Vis spectra of higher concentration solutions show clear absorption at around 220-350 nm, which can be attributed to the existence of the defects. All the UV/Vis spectra suggest the existence of an absorption band with a peak below 190 nm (***Figure 7-6b***, also see ***Figure 7-7a***), which is significantly lower than that of hBN raw materials (***Figure 7-7b***) and that (peak at 203.5 nm) of the multi-layered hBN nanosheets previously reported (<30 layers, lateral size < 200 nm).[30]

With decreasing concentration, the peak shifted from around 189 to 186 nm (***Figure 7-7a***), indicating that higher concentrations lead to the slight agglomeration of the particles in solution. Additionally, an optical band gap of 6.51 eV also can be estimated from the UV/Vis spectra of the diluted sample (3.66 μg/mL, ***Figure 7-7c***). All these results suggest that the lateral size of the resultant BN product should be much smaller than 200 nm due to the observed strong quantum confinement effect, if the created BN are also thin enough.

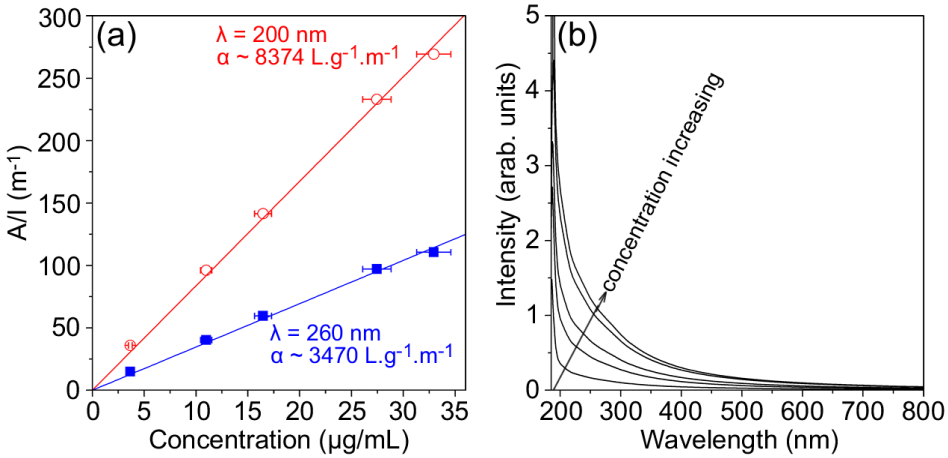

Figure 7-6. (a) Plots of absorbance (λex = 200 and 260 nm) normalized to cell length, versus the concentration of BN product in water solution. The errors arise from uncertainty in the weighing and diluting processes; (b) UV/Vis absorption spectra of the BN product solution.

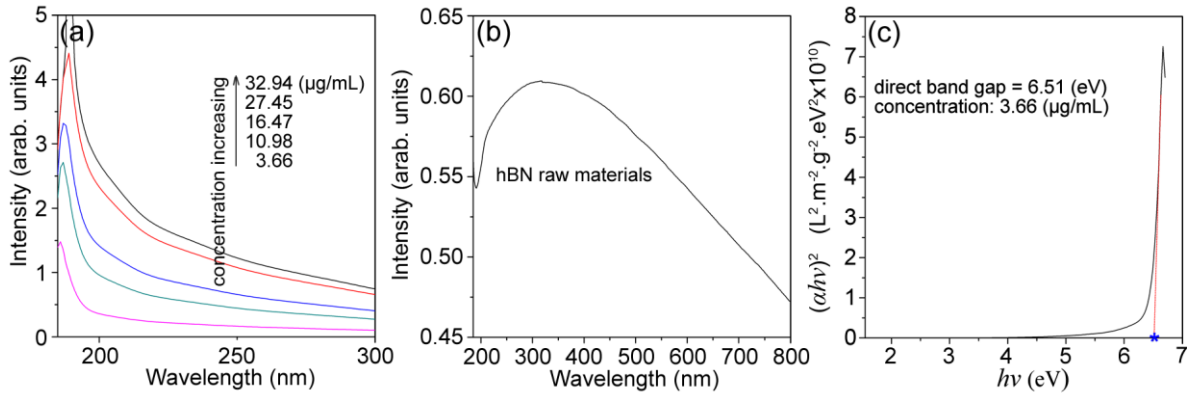

Figure 7-7. (a) Local enlarged UV/Vis spectra of BN product with different concentrations; (b) UV/Vis spectra of hBN raw materials; (c) Estimation of the optical band gap using the equation $(\alpha h\nu)^n = A(h\nu - E_g)$,[31] where A is a constant, α is the absorption coefficient (can be calculated from series UV/Vis absorption spectra in image a, E_g is the band gap and n equals 2 for a direct transition. E_g could be obtained by extrapolating the linear region of plots of $(\alpha h\nu)^2$ versus energy ($h\nu$).

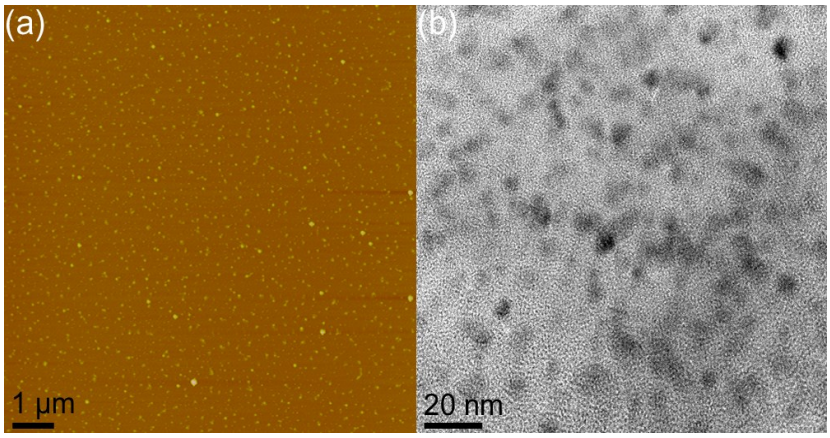

Figure 7-8. (a) AFM topography image of BN QDs dispersed/distributed on a mica substrate; (b) TEM images of the BN dots.

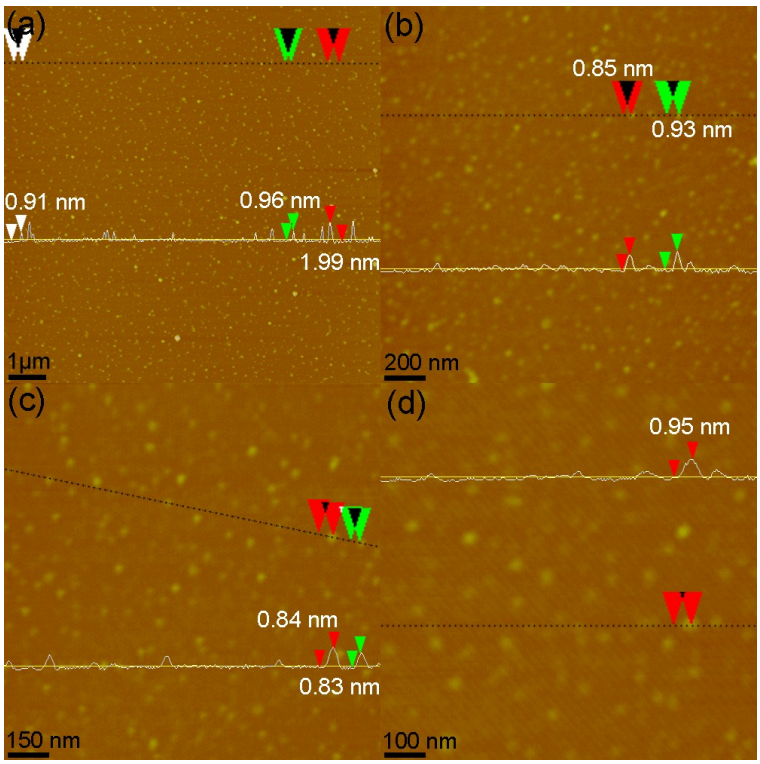

Figure 7-9. **AFM height analysis.** (a) The line analysis image, corresponding to ***Figure 7-8a***; (b-d) AFM line analysis on different dots gives an average thickness of 0.9 nm, corresponding well with the thickness of monolayered BN under AFM measurement. Note: for the thickness analysis, lines were plotted cross the centre of the selected dots to minimize the measurement errors.

This is further confirmed by AFM and TEM. As shown in ***Figure 7-8a*** (AFM), BN dots are no wider than 50 nm. Statistical analysis (***Figure S7-1*** in ***Supporting Information*** of this chapter) of three 2 x 2 μm regions in ***Figure 7-8a*** selected at random gives an average QD size around 10 nm, corresponding well with that from TEM analysis (***Figure***

7-8b). Although some dots appeared to be stacked together under AFM, the measured thicknesses were still quite thin (***Figure 7-9a***, and ***Figure S7-2*** in ***Supporting Information***). AFM height analysis on a diluted sample (to avoid stacking) suggests that the average thickness of the majority of dots (at least > 95% on the measured AFM images) was approximately 0.9 nm, corresponding to monolayered BN (***Figures 7-9b-d***).[30] ***Figures 7-10a-c*** are bright field high resolution TEM (BF-HRTEM) images of the thin BN QDs. With these images, clear terminated edges (***Figure 7-10a***), the lattice fringe of 0.22 nm (100, ***Figure 7-10a***) and the bond length of B-N (0.14 nm, ***Figure 7-10c***) in hexagonal honeycomb BN structures (***Figures 7-10b & c***) are revealed (see ***Figure S7-3*** in ***Supporting Information*** for more TEM images). TEM analysis also shows that stacked QDs have interlayer separations between 0.5 to 0.88 nm (***Figure 7-10d***). This is much larger than that of the hBN (002) lattice spacing of 0.33 nm and strongly suggests that the exfoliation and disintegration of hBN flakes produces created monolayered BN QDs (occasionally, these monolayered BN QDs stacked together as shown in ***Figure 7-10d***, which is different with multilayered BN). The stacking simply results from the monolayered QDs overlaying on the carbon film.

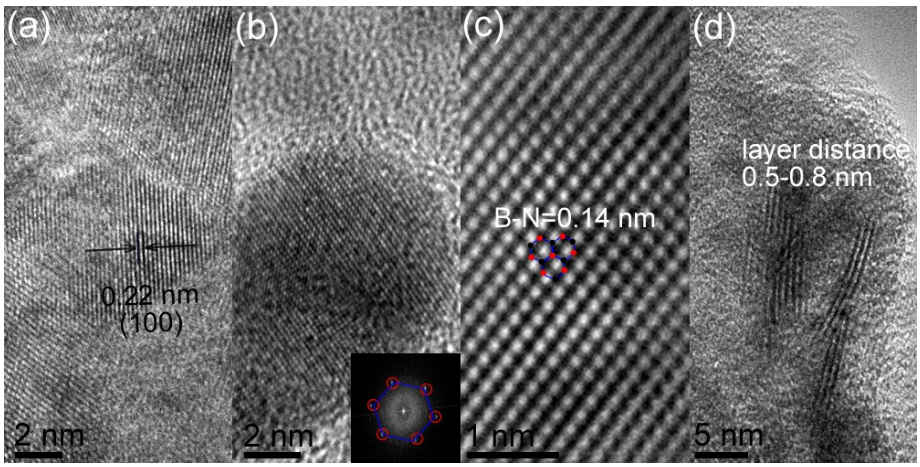

Figure 7-10. HRTEM images of the BN dots. Inset in image b is the FFT pattern of the crystal, showing the hexagonal structure. Image c is the simulated HRTEM image from the inverse FFT of ***Figure S7-3a*** in ***Supporting Information***. Image d showing stacked monolayered QDs.

7.3.4 Luminescent Properties of the Created BN QDs

The as-prepared BN QDs exhibited strong PL, emitting blue-green light under UV (365 nm) illumination (***Figure 7-11a*** inset). ***Figure 7-11a*** gives the broad PL and PL-excitation (PLE) spectra of solutions of as-prepared and pre-purification BN QDs (see ***Figure 7-11b*** for series of PL spectra, which reveal that the emission also covers the green light region, from 325-625 nm). The strongest emission of the purified QDs

occurs at around 425 nm with a Stokes shift of 105 nm (0.96 eV). This is blue shifted compared with the PL of the un-purified BN QDs (PL_2 in ***Figure 7-11a*** with the strongest peak emission at around 465 nm, E_x = 380 nm) owing to the removal of larger thin BN nanosheets during the purification process (see ***Figure S7-4*** in ***Supporting Information*** for more details). The PL spectra also give a very weak peak at around 360.5 nm, appearing as a shoulder to the main PL peak. This minor peak was observed with either water or EtOH as the solvent. By using anthracene as a fluorescent standard (***Table 7-1*** in ***Section 7.2.2***), the luminescent quantum yield of the purified BN QDs was determined as 2.5% (see ***Table 7-1*** in ***Section 7.2.2***), which is comparable to that of GQDs in neutral-pH media.[6] PLE spectra (with detection wavelength of 425 nm, ***Figures 7-11a&c***) of the sample show a main peak at ~320 nm (3.87 eV) and three weak excitation peaks at around 260 (4.77 eV), 370 (3.35 eV) and 398 nm (3.12 eV).

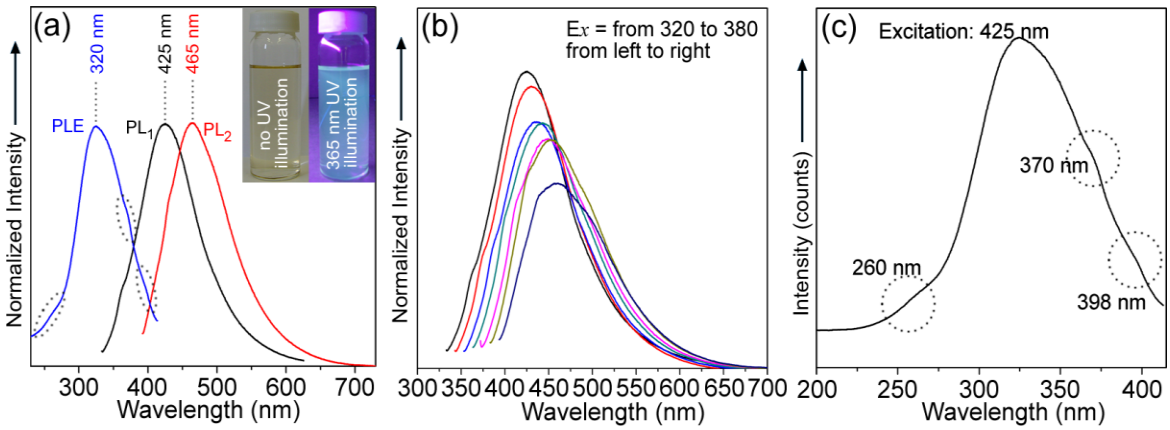

Figure 7-11. (a) PLE and PL_1 spectra of resultant BN QDs, and PL_2 spectra of un-purified BN QDs (before K^+ removal). Insets are the photographs of resultant BN QDs with and without UV illumination.; (b) PL spectra of the thin BN QDs at the excitation wavelengths of 320, 330, 340, 350, 360, 370, 380 nm, from left to right; c) PLE spectra of the resultant BN QDs with detective wavelength of 425 nm, showing a main peak at around 320 nm and three weak peaks at around 260, 370 and 398 nm.

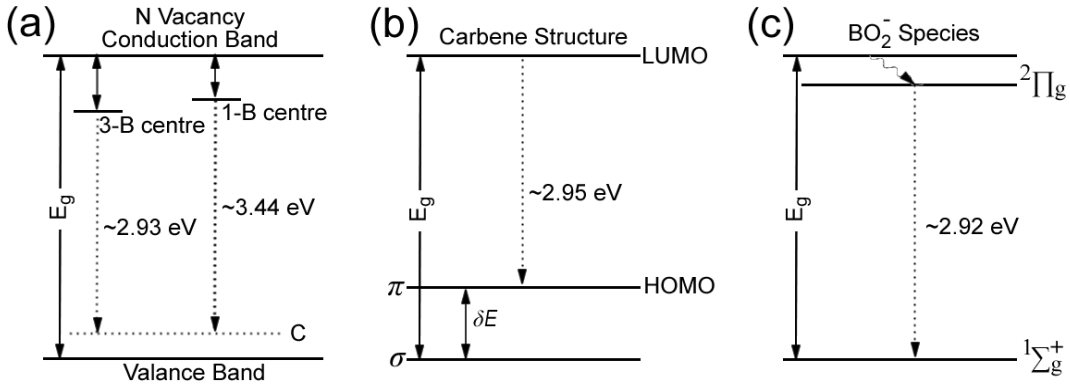

Figure 7-12. Luminescence diagrams of the resultant BN QDs.

This strong emission has never previously been observed from pure hBN. It is believed that the emission in present BN samples is induced by three types of effective luminescent centres: carbon-replaced N vacancy point defects (3-B and 1-B centres)[32,33] carbene structure at zigzag edges[6] and BO_x^- (x = 1 and 2) species.[15] The 1,3-B centres consist of unpaired electrons trapped in the vicinity of ^{11}B nuclei. The luminescence is generated directly by the electron transition between 1,3-B centres and lower carbon level (***Figure 7-12a***, some N atoms were replaced by C to form 1,3-B centres). The carbene structure at BN zigzag edges also supports a luminescent transition (from LUMO to HOMO, ***Figure 7-12b***), as found in GQDs.[6] As for BO_2^-, it is a closed-shell species with a linear ground state ($^1\Sigma_g^+$, characterized by a degenerate π_g orbital) and a first excited state (the ground state of $^2\Pi_g$).[34-36] The transition from $^2\Pi_g \rightarrow {}^1\Sigma_g^+$ observed using PL is essentially a single peak emission (***Figure 7-12c***).[37] BO^- is also a closed-shell species with a ground state $^1\Sigma_g^+$ and first excited state $^2\Sigma_g^+$.[37] BO^- should have three well-resolved, equally-spaced emission lines because its HOMO (3σ) is essentially a B 2s lone pair with slight BO antibonding.[15,37] The absence of these three well-resolved emission lines suggests that the emission from BO^- species here should be much weaker than that from the others.

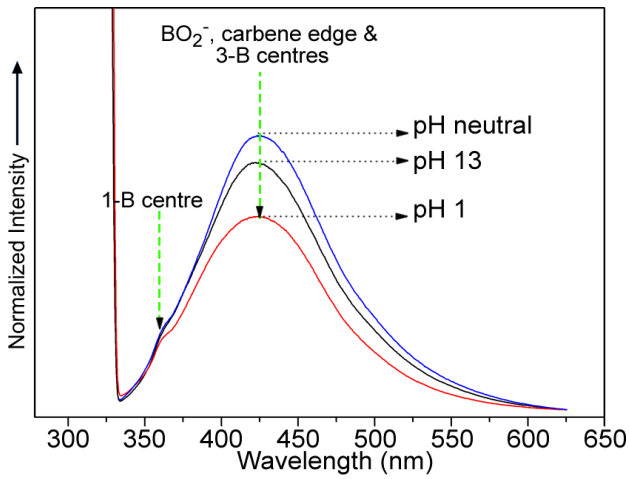

Figure 7-13. PL spectra of the BN QDs with pH change.

It is, however, difficult to separate the specific luminescence contributions from 1,3-B centres (emission at around 3-3.4 eV),[32-33] carbene zigzag edges (emission at around 2.9 eV[6]) and BO_2^- (emission at around 2.7-3 eV) from the broad emission peak observed in ***Figure 7-11a***. Increasing the pH of the BN QDs suspension to 13 will enhance the contribution of the zigzag edges[6] and reduce that from the 1,3 B centres, whilst decreasing the pH will have the opposite effect (***Figure 7-13***, the presence of electron-attracting species (OH^-) destroyed the electrons trapping of 1,3 B centres). At

pH = 13, the observed BN QD PL peak weakened (by 9.7%) and shifted from 425 nm to 421 nm (***Figure 7-13***). The PL intensity decreased further (additional peak intensity reduction of 20%) and shifted to 423 nm upon changing the pH from 13 to 1. These observations suggest that the PL of BN QDs is dominated by emission from BO_2^- species, and also indicate that the emissions of BO_2^-, zigzag carbene edge and 3-B centres should be at around 425 nm (2.92 eV), 421 nm (2.95 eV) and 423 nm (2.93 eV) respectively (***Figure 7-12***). Because the 1-B centre is closer to the conduction band than the 3-B centre,[32] the weak emission at around 360.5 nm (3.44 eV) should be attributed to the 1-B centre. These attributions and energy levels are close to the reported theoretical predictions and experimental findings (emissions from 1 and 3-B centre at around 3.4 and 3 eV respectively,[32,33] emission from zigzag carbene structure at around 2.9 eV[6] and the emission from BO_2^- species at around 2.7-3 eV[15]). The three weak peaks in PLE spectra (268 nm, 397 nm and 408 nm) probably arise from different coordination environments (*e.g.* -OH, $-NH_2$, $-N^{3-}$ ligands), though it is still not clear what the precise effects are.[15]

7.3.5 Bio-imaging Application of the Monolayered BN QDs

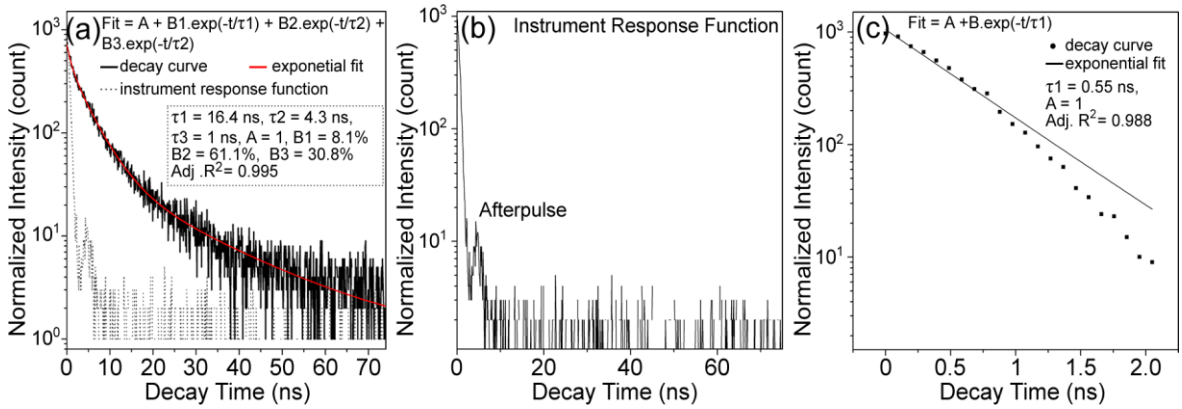

Figure 7-14. TRPL decay profile of BN QDs recorded at room temperature while monitoring the emission at 425 nm upon 320 nm excitation wavelength. The inset shows the lifetime data and the parameter generated by the exponential fitting. (a) The instrument response function; (b) The single exponential function of the instrument response (before afterpulse) showing a 0.55 ns decay time, which is different from the decay time in image a and confirmed that all the decay time in image a is not the instrument response.

The discovery of luminescence broadens the potential applications of BN, for example, bio-medical imaging. Therefore, the luminescence decay of the BN QDs is further studied. As shown in TRPL (TRPL, ***Figure 7-14a***, time-correlated single photon counting technique), the lifetime of the luminescence can be fitted well with a tri-exponential function, suggesting that the decay process is dominated by the

contributions from the three main emissive centres discussed above. The observed lifetimes of these main types of luminescence are all in nanoseconds (16.4 ns, 8.1%; 4.3 ns, 61.1%; 1 ns, 30.8%, the decay from instrument response is 0.55 ns, see ***Figures 7-14b & c***), suggesting that BN QDs are promising candidate materials for optoelectronic and biological applications. However, for biological applications (*e.g.* bioimaging, protein analysis, cell tracking, isolation of biomolecules, and gene technology), the inherent toxicity of the materials should be minimized. The cytotoxicity of BN QDs was evaluated here using the mammalian cell line, MDCKII (Madin-Darby Canine Kidney Type II). The results show that low doses of BN QDs (0-40 μg/mL) are non-toxic to these cells. No obvious effect on cell number was observed at low dosage (0-40 μg/mL, ***Figure 7-15***) with prolonged exposure (24-48 h).

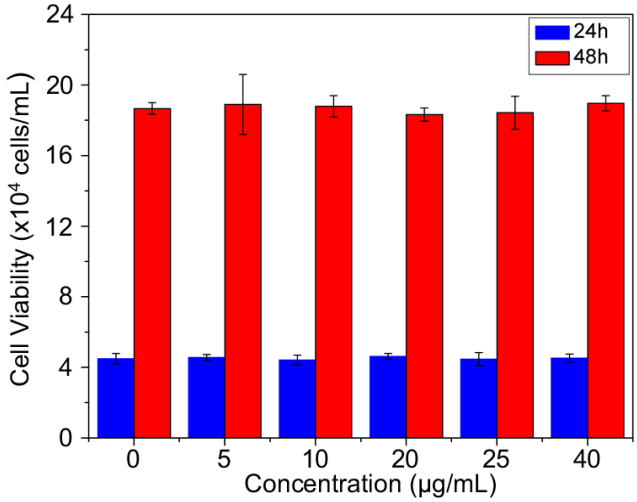

Figure 7-15. Cell viability assay with MDCKII cells treated with different concentrations of BN QDs. The bars represent cell counts and the error bars represent standard errors of the mean.

To further illustrate the potential in bio-imaging applications, the luminescent cell imaging was performed using the monolayered BN QDs. ***Figure 7-16a*** shows the image of the MDCKII cells stained with BN QDs alone. The QDs were taken up by the cells but did not penetrate the cell nuclei. ***Figures 7-16b-d*** give the images of MDCKII nucleus stained with DAPI (diamidino-2-phenylindole, emission from around 400-650 nm), BN QDs (emission from 325-625 nm) and the overlay image, respectively. Although the nucleus in ***Figure 7-16c*** also gives green emission (from DAPI), the boundary between cells, nuclei and cytoplasm are clear. This is more clearly seen in the overlay image (***Figure 7-16d***). All these results indicate that BN QDs can be used in high contrast bio-imaging and will be well-suited for other biomedical applications. To further improve

cellular imaging, the quantum yield of the BN QDs could be enhanced by using appropriate technologies (*e.g.* further size separation).

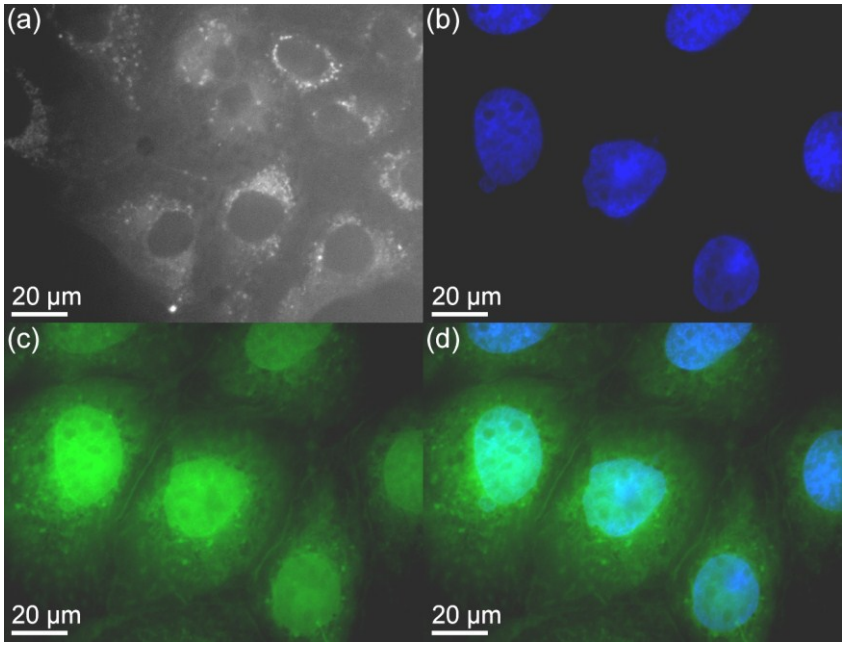

Figure 7-16. Confocal microscopy images of mammalian cells. (a) Agglomerated BN QDs surrounding each nucleus (cells are stained by BN QDs only); (b) Individual nucleus stained blue with DAPI; (c) BN QDs with green luminescence surrounding the nuclei; (d) The overlay image of cells stained with DAPI and BN QDs.

7.4 Conclusion

In conclusion, this chapter described a method to create atomically-thin BN QDs from bulk hBN flakes. The majority of the created QDs are monolayered with a lateral size around 10 nm. Due to the introduction of oxidized defect centres (*e.g.* BO_2^-, carbene zigzag edge, C replaced N vacancy point), the BN QDs exhibit reasonable blue-green luminescence. The strongest emission of the BN QDs occurs at 425 nm with nanosecond-order luminescent decay, which is well suited for optoelectronic and biological application requirements. Furthermore, with the decrease in thickness and size, strong quantum confinement was also observed. The optical direct band gap of the BN QDs was estimated to be around 6.51 eV. This successful preparation of thin oxidized BN QDs and the discovery of their interesting fluorescence properties could pave the way for new applications of BN in a variety of fields.

7.5 Supporting Information

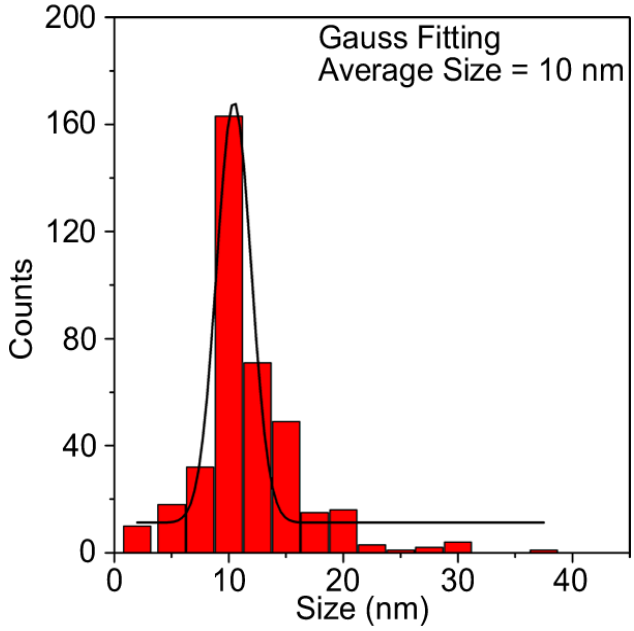

Figure S7-1. **Size distribution of the BN QDs.** The BN for the analysis was random selected from the local area in ***Figure 7-8a***.

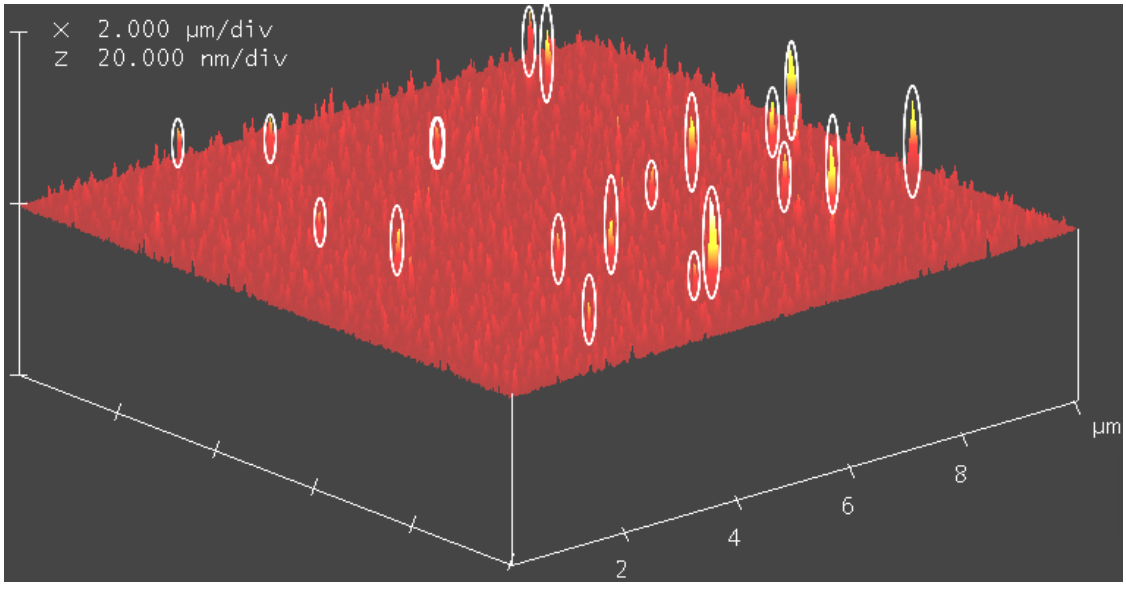

Figure S7-2. Three-dimensional (3D) AFM image of the BN QDs corresponding to ***Figure 7-8a***. The marked dots are higher than 1.5 nm. Most dots are thinner than 1.5 nm, suggesting the majority BN QDs are monolayered.[30]

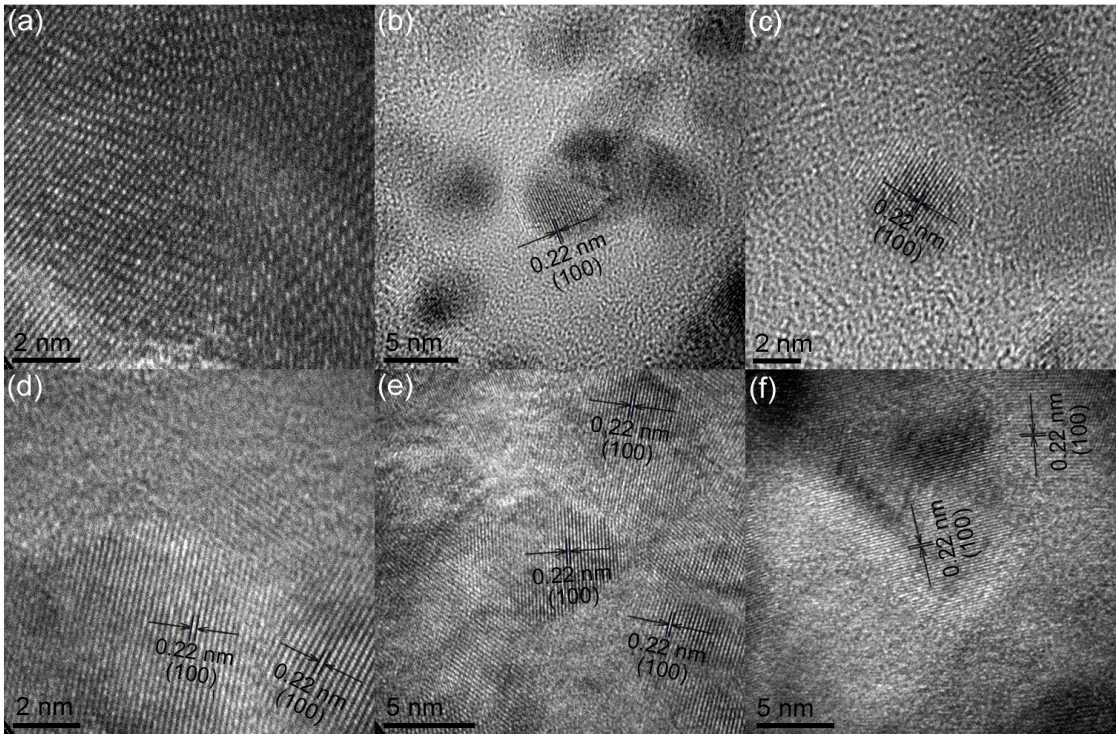

Figure S7-3. **HRTEM images of the BN QDs.** (a) A simulated HRTEM image from the reversed FFT of local image a shown in the ***Figure 7-10c***; (b-f) More than one QDs are shown in these images. The lattice and boundary between the QDs are clear in images d-f.

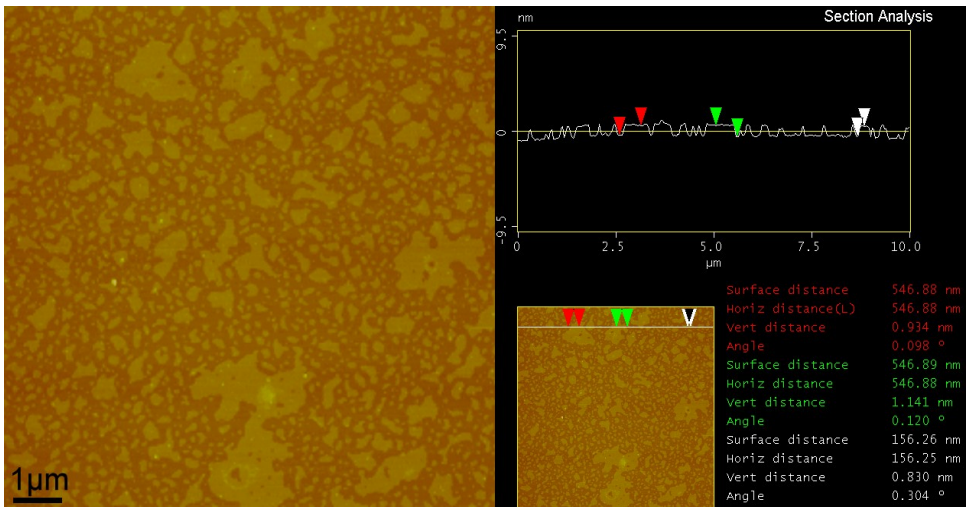

Figure S7-4. **AFM image and height line analysis of the thin BN sheets with bigger size.** For collecting BN sheets with bigger size, the sample (after K^+ removal) was just centrifuged for many times to concentrate and separate aimed product (no filtering process was conducted). BN sheets with big size will be suspended on the top of the centrifuge tube with faint white colour. It was found that this separation obviously led to the blue shift of the PL spectra. Besides, no obvious influence of the solvents (H_2O and EtOH) on the PL position was found. Therefore, the blue shift of the PL spectra after purification was considered as the removal of BN sheet with bigger size.

References and Notes

[1] X. G. Peng, L. Manna, W. Yang, J. Wickham, E. Scher, A. Kadavanich and A. P. Alivisatos, Shape Control of CdSe Nanocrystals. *Nature* **2000**, *404*, 59-61.

[2] L. Manna, D. J. Milliron, A. Meisel, E. C. Scher and A. P. Alivisatos, Controlled Growth of Tetrapod-Branched Inorganic Nanocrystals. *Nat. Mat.* **2003**, *2*, 382-385.

[3] Y. Yin and A. P. Alivisatos, Colloidal Nanocrystal Synthesis and the Organic-Inorganic Interface. *Nature* **2005**, *437*, 664-670.

[4] L. E. Brus, Quantum Crystallites and Nonlinear Optics. *Appl. Phys. A* **1991**, *53*, 465-474.

[5] S. Ithurria, M. D. Tessier, B. Mahler, R. P. S. M. Lobo, B. Dubertret and Al. L. Efros, Colloidal Nanoplatelets with Two-Dimensional Electronic Structure. *Nature Mater.* **2011**, *10*, 936-941.

[6] D. Pan, J. Zhang, Z. Li and M. Wu, Hydrothermal Route for Cutting Graphene Sheets into Blue-Luminescent Graphene Quantum Dots. *Adv. Mater.* **2010**, *22*, 734-738.

[7] R. T. Paine and C. K. Narula, Synthetic Routes to Boron Nitride. *Chem. Rev.* **1990**, *90*, 73-91.

[8] C. Zhi, Y. Bando, C. Tang, H. Kuwahara and D. Golberg, Largescale Fabrication of Boron Nitride Nanosheets and Their Utilization in Polymeric Composites with Improved Thermal and Mechanical Properties. *Adv. Mater.* **2009**, *21*, 2889-2893.

[9] C. Jin, F. Lin, K. Suenaga and S. Iijima, Fabrication of a Freestanding Boron Nitride Single Layer and Its Defect Assignments. *Phys. Rev. Lett.* **2009**, *102*, 195505.

[10] L. Song, L. Ci, H. Lu, P. B. Sorokin, C. Jin, J. Ni, A. G. Kvashnin, D. G. Kvashnin, J. Lou, B. I. Yakobson and P. M. Ajayan, Large Scale Growth and Characterization of Atomic Hexagonal Boron Nitride Layers. *Nano Lett.* **2010**, *10*, 3209-3215.

[11] Y. Shi, C. Hamsen, X. Jia, K. K. Kim, A. Reina, M. Hofmann, A. L. Hsu, K. Zhang, H. Li, Z.-Y. Juang, M. S. Dresselhaus, L.-J. Li and J. Kong, Synthesis of Few-Layer Hexagonal Boron Nitride Thin Film by Chemical Vapor Deposition. *Nano Lett.* **2010**, *10*, 4134-4139.

[12] M. Terrones, J.-C. Charlier, A. Gloter, E. Cruz-Silva, E. Terrés, Y. B. Li, A. Vinu, Z. Zanolli, J. M. Dominguez, H. Terrones, Y. Bando and D. Golberg, Experimental and Theoretical Studies Suggesting the Possibility of Metallic Boron Nitride Edges in Porous Nanourchins. *Nano Lett.* **2008**, *8*, 1026-1032.

[13] B. Huang, H. Lee, B.-L. Gu, F. Liu and W. Duan, Edge Stability of BN Sheets and Its Application for Designing Hybrid BNC Structures. *Nano Research* **2012**, *5*, 62-72.

[14] L A. Lopez-Bezanilla, J. Huang, H. Terrones and B. G. Sumpter, Boron Nitride Nanoribbons Became Metallic. *Nano Lett.* **2011**, *11*, 3267-3273.

[15] C. Tang, Y. Bando, C. Zhi and D. Golberg, Boron-Oxygen Luminescence Centres in Boron-Nitrogen Systems. *Chem. Commun.* **2007**, 4599-4601.

[16] J. N. Demas and G. A. Grosby, The Measurement of Photoluminescence Quantum Yield. A Review. *J. Phys. Chem.* **1971**, *75*, 991-1024.

[17] W. R. Dawson and M. W. Windsor, Fluorescence Yield of Aromatic Compounds. *J. Phys. Chem.* **1968**, *72*, 3251-3260.

[18] G. Weber and F. W. J. Teale, Determination of the Absolute Quantum Yield of Fluorescent Solutions. *Trans. Faraday. Soc.* **1957**, *53*, 646-655.

[19] L. Lin and S. Zhang, Creating High Yield Water Soluble Luminescent Graphene Quantum Dots *via* Exfoliating and Disintegrating Carbon Nanotubes and Graphite Flakes. *Chem. Commun.* **2012**, *48*, 10177-10179.

[20] A. G. Freeman and J. P. Larkindale, Evidence for the Formation of Boron Nitride-Alkali Metal Intercalation Compounds. *Inorg. Nucl. Chem. Lett.* **1969**, *5*, 937-939.

[21] R. V. Gorbachev, I. Riaz, R. R. Nair, R. Jalil, L. Britnell, B. D. Belle, E. W. Hill, K. S. Novoselov, K. Watanabe, T. Taniguchi, A. K. Geim and P. Blake, Hunting for Monolayer Boron Nitride: Optical and Raman Signatures. *Small* **2011**, *7*, 465-468.

[22] R. Arenal, A. C. Ferrari, S. Reich, L. Wirtz, J.-Y. Mevellec, S. Lefrant, A. Rubio and A. Loiseau, A. Raman Spectroscopy of Single-Wall Boron Nitride Nanotubes. *Nano Lett.* **2006**, *6*, 1812-1816.

[23] C. Zhi, X. Bai and E. Wang, Raman Characterization of Boron Carbonitride Nanotubes. *App. Phys. Lett.* **2002**, 80, 3590-3592.

[24] G. D. Khattak and A. Mekki, Structure and Electrical Properties of SrO-Borovanadate. *J. Phys. Chem. Sol.* **2009**, *70*, 1330-1336.

[25] J. R. Holst and E. G. Gillan, From Triazines to Heptazines: Deciphering the Local Structure of Amorphous Nitrogen-Rich Carbon Nitride Materials. *J. Am. Chem. Soc.* **2008**, *130*, 7373-7379.

[26] M. A. Mannan, M. Nagano, K. Shigezumi, T. Kida, N. Hirao and Y. Baba, Characterization of Boron Carbonitride (BCN) Thin Films Deposited by Radiofrequency and Microwave Plasma Enhanced Chemical Vapor Deposition. *Am. J. Applied Sci.* **2007**, *5*, 736-741.

[27] C. D. Wagner, W. M. Riggs, L. E. Davis, J. F. Moulder and G. E. Muilenberg (Eds.), *Handbook of X-ray Photoelectron Spectroscopy*, Perkin-Elmer Corporation, Physical Electronics Division, Eden Prairie, Minnesota, **1979**.

[28] S. Dong, W. Han, Y. Luo, T. Zhao and C. Xu, Synthesis and Thermal Behavior of New Precursors for B-C-N Ceramics. *J. Mater. Sci. Techol.* **2010**, *26*, 228-233.

[29] M. A. Mannan, M. Nagano, K. Shigezumi, T. Kida, N. Hirao and Y. Baba, Characterization of Boron Carbonitride (BCN) Thin Films Deposited by Radiofrequency and Microwave Plasma Enhanced Chemical Vapor Deposition. *Am. J. Appl. Sci.* **2007**, *5*, 736-741.

[30] Y. Lin, T. V. Williams, T. -B. Xu, W. Cao, H. E. Elsayed-Ali and J. W. Connell, Aqueous Dispersions of Few-Layered and Monolayered Hexagonal Boron Nitride Nanosheets from Sonication-aAssisted Hydrolysis: Critical Role of Water. *J. Phys. Chem. C* **2011**, *115*, 2679-2685.

[31] J. I. Pankove, *Optical Processes in Semiconductors*, Prentice-Hall, New Jersey, **1971**.

[32] A. Katzir, J. T. Suss, A. Zunger and A. Halperin, A. Point defects in hexagonal boron nitride. I. EPR, Thermoluminescence, and Thermally-Stimulated-Current Measurements. *Phys. Rev. B* **1975**, *11*, 2370-2377.

[33] A. Zunger and A. Katzir, Point Defects in Hexagonal Boron Nitride. II. theoretical studies. *Phys. Rev. B* **1975**, *11*, 2378-2390.

[34] J. V. Ortiz, Electron Propagator Theory of BO_2 and BO_2^- Electronic Structure. *J. Chem. Phys.* **1993**, *99*, 6727-6731.

[35] V. G. Zakrzewski and A. I. J. Boldyrev, The Upper Ionization Potentials of F-, LiF2-, BeF3-, BO2-, AlO2-, and NO3- Ions Calculated by Green's Function Method. *Chem. Phys.* **1990**, *93*, 657-660.

[36] H. Zhai, L. Wang, S. Li and L. Wang, Vibrationally Resolved Photoelectron Spectroscopy of BO^- and BO_2^-: a Joint Experimental and Theoretical Study. *J. Phys. Chem. A* **2007**, *111*, 1030-1135.

[37] J. Agreiter, M. Lorenz, A. M. Smith and V. E. Bondybey, Neon Matrix Spectra and Isotopically Dependent Fluorescence Quantum Yields of BO_2. *Chem. Phys.* **1997**, *224*, 301-313.

Chapter VIII. Fabrication of Luminescent Monolayered Tungsten Disulphide Quantum Dots with Giant Spin-Valley Coupling

8.1 Introduction

Tungsten disulphide (WS_2) is a typical layered transition-metal dichalcogenide (LTMD) with fundamental two-dimensional (2D) building blocks (strongly bonded S-W-S layers) weakly bonded to each other by van der Waals forces.[1] This highly anisotropic bonding of WS_2 is responsible for strongly anisotropic electrical and mechanical properties suitable for use in solid state lubricants,[2] catalytic reactions,[3] solar cells[4] and field-effect transistors (FETs).[5] New interesting properties and applications of WS_2 have been discovered on the basis of the formation of monolayered WS_2 sheets.[6] For example, WS_2 changes from an indirect to a direct band gap semiconductor with strong luminescence when converted from multilayers to monolayered sheets.[7-8] By reducing the lateral size of monolayered sheets, unique physical and chemical properties could be expected as WS_2 can be significantly affected by the edge structure and atomic defects in small nanostructures,[9] as well as quantum confinement effects emerging. Possible effects of WS_2 monolayer miniaturization include enhanced luminescent efficiency and giant spin-orbit coupling (as will be confirmed in this chapter) of relevance to optoelectronic and spintronic devices.

Although the exfoliation of monolayered WS_2 sheets from their bulk multilayers is well established (*e.g.* liquid exfoliation of monolayered WS_2 sheets),[6] effective preparation of monolayered WS_2 QDs are greatly underdeveloped and their properties not well understood. This chapter describes the effective exfoliation and disintegration of bulk WS_2 flakes to form, with high yield, monolayered WS_2 QDs of lateral size around 8-15 nm. The monolayered WS_2 QDs show a direct band gap nature, similar to monolayered sheets, which activate strong fluorescence. However, the direct gap (~3.16 eV) of the monolayered WS_2 QDs is much larger than that of monolayered WS_2 sheet (direct gap of ~2.1 eV),[8] which leads the strong luminescence (quantum yield of ~4.0%) to be at shorter (green-blue) wavelengths than with the sheets. Unlike monolayered WS_2 sheets,

the WS_2 QDs also show evidently improved giant spin-valley coupling, making them highly valuable for semiconductor-based spintronics. The spin-valley quantum states may allow future quantum entanglement of the QDs to enable quantum computation. However, due to the strong fluorescence, this chapter also demonstrates that monolayered WS_2 QDs can be used as a non-toxic fluorescent label in confocal microscopy of biological cells.

8.2 Experimental Methods

8.2.1 Sample Preparation

The preparation was similar to the preparation of GQDs from GFs (see ***Sections 6.2.3***). The addition of WS_2 was 1 g, aiming to well mix the WS_2 and K (~0.6 g) in the Pyrex tube. Although the intercalation of WS_2 was more effective and the yield was much higher than that of GQDs, the intercalation reaction was controlled as 170-180 ^oC and held for >2 h. Serve intercalation and less addition of WS_2 led to the damage of WS_2 structure (can be determined by simple check of the luminescence: use UV lamp to illuminate the created QDs suspension) and the production of more K_2S, which should be avoided. Experiments showed that the 2 h (or slightly longer than 2 h) intercalation was suitable to create stable WS_2 QDs. After preparation, a yellow solution containing WS_2 QDs was separated from the residual solid WS_2 by using filter (with coarse filter paper) to remove WS_2 sediment. Then the collected suspension was heated in an oven to evaporate ethanol. The remaining K ions in the solution were absorbed/removed with the cation exchange resin (fill the resin into a Millipore Millicup filter unit, with ~5 cm filling height) and dialysis tubing respectively.

8.2.2 Calculation of the Quantum Yield of WS_2 QDs

See ***Section 3.4*** in ***Chapter III*** for the calculation method of quantum yield.

Table 8-1. Quantum yield of WS_2 QDs suspension (in H_2O) using anthracene as a reference.

Sample	Integrated Emission Intensity (I)	Absorptance at 360 nm (A)	Refractive Index of Solvent (η)	Quantum Yield (Φ)
Anthracene	286101	0.0875	1.36	30% (Known)[1-3]
WS_2 QDs	75033	0.1642	1.33	~4.0%

8.3 Results and Discussion

8.3.1 WS_2 Flake Exfoliation and Disintegration

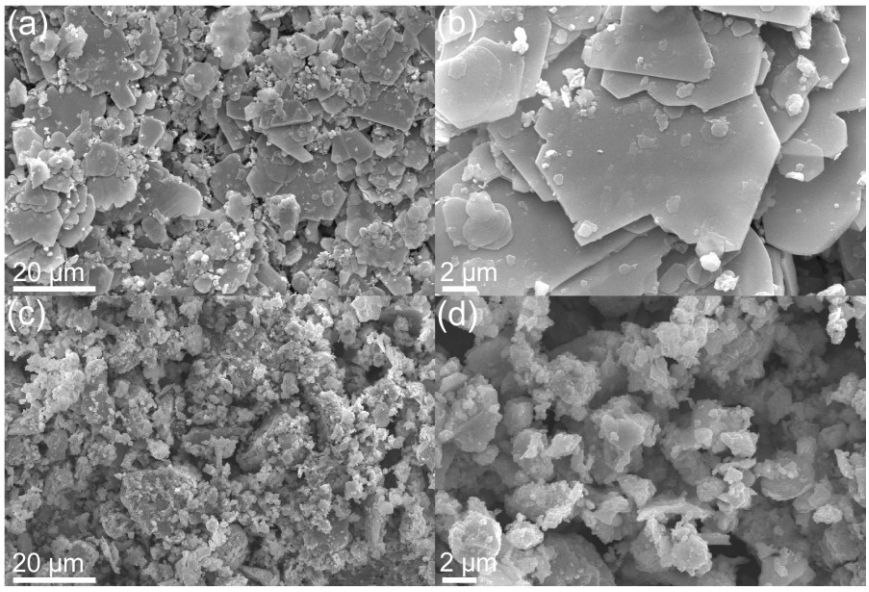

Figure 8-1. (a-b) SEM images of raw WS_2 flakes; (c-d) SEM images of the WS_2 sediment after preparation.

Since WS_2 has similar layered structure to that of graphite, the monolayered WS_2 QDs are exfoliated and disintegrated in the same manner used to cut graphene QDs from graphite (***Chapter VI***, also see my published work[10]). This includes the following steps (also see ***Section 8.2.2*** for more details): 1) formation of potassium intercalated WS_2 (K-WS_2, intercalation reaction) by intercalating K atoms between the covalently-bonded WS_2 sheets, taking advantage of the weak interlayer Van der Waals force; 2) short exposure of K-WS_2 to air (de-intercalation reaction) and 3) reaction between K-WS_2 and EtOH-H_2O under ultrasonication treatment. The large layer-layer distance (d=6.18 Å, JCPDS: 84-1389, much larger than the *d* space of graphite) and weak Van der Waals force between WS_2 layers readily allows the intercalation reaction to take place. The intercalation leads to the expansion of the layer-layer distance, which is useful for effective exfoliation and disintegration of the sheets when the K-WS_2 was exposed to air and reacted with EtOH/H_2O under ultrasonication. Although the starting (grey) and final (dark) intercalated WS_2 are not obviously different in colour, SEM and XRD observations (***Figure S8-1*** in the ***Supporting Information*** in this chapter) of the starting and residual WS_2 sediment strongly supported the exfoliation and disintegration of WS_2 flakes. As suggested by the SEM images and XRD patterns, the raw WS_2 materials have clear flake shape (***Figures 8-1a & b***) and are highly crystalline (***Figure S8-1***, clear diffraction pattern and strong (002) diffraction peak). By contrast, during the preparation, the WS_2 size was remarkably reduced and their edge was highly disintegrated (***Figures 8-1c & d***). XRD analysis further suggested that the layered

structure of the WS_2 flakes was severely damaged (much weaker diffraction peak; ***Figure S8-1***) due to the exfoliation and disintegration.

8.3.2 Characterisation of Prepared WS_2 QDs

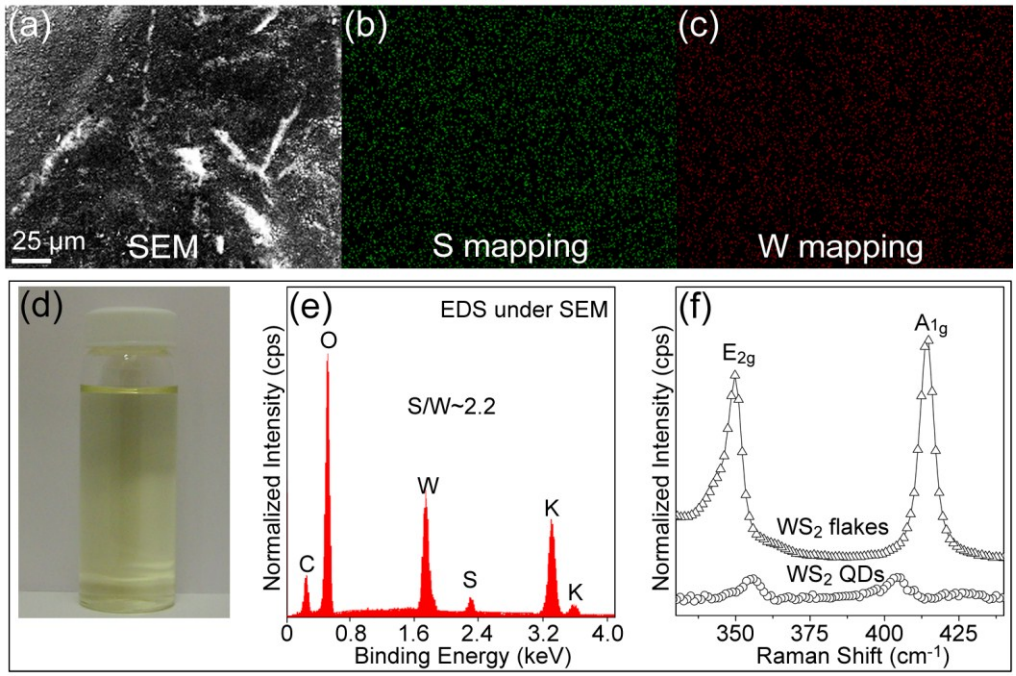

Figure 8-2. Characterisation of the exfoliated and disintegrated WS_2 product in suspension (prior to K^+ removal). (a) SEM image and (b,c) EDS element mapping of the dried suspension; (d) Photo of the suspension; (e) EDS analysis of the dried suspension under SEM observation; (f) Raman analysis of the dried suspensions.

After preparation, the collected suspension (containing K^+) showed a yellow colour (***Figure 8-2d***) which was stable over many months without any colour or UV/Vis (ultraviolet-visible) absorption changes. However, the exfoliated and disintegrated WS_2 was not stable once the K^+ in the suspension was removed using cation exchange resin (faint yellow solid S was found after a few days settling). Therefore the created suspension (containing K^+) was dried for further analyses of XRD, EDS, XPS and Raman techniques. The fabricated WS_2 was also purified using dialysis tubing for other examinations and applications. The dried suspension (prior to K^+ removal) did not show any XRD peaks (***Figure S8-1***) from (002) diffraction of the multilayered WS_2, which suggests that the exfoliated and disintegrated products are thin structures. SEM and EDS element mappings (***Figure 8-2a-c***) confirm that the dried suspension contains W and S. Nevertheless, the measured S/W molar ratio of ~2.2 (***Figure 8-2e***, in some cases on different regions, the ratios are different but not higher than 2.5) is higher than the stoichiometric ratio of WS_2, suggesting that another S phase also existed in the dried

suspension (before K removal). In the EDS spectra (***Figure 8-2e***), the C, O and K most likely arise from the chemicals involved in the preparation (K, EtOH and H_2O). ***Figure 8-2f*** is the Raman spectra of the dried suspension (before K removal) and WS_2 raw materials. The WS_2 raw materials show two intensive peaks around 350 and 414 cm^{-1}, corresponding to the E^1_{2g} and A_{1g} phonon modes of 2H-WS_2.[1,7] By contrast, these peaks of the dried suspension are much weaker and shift to 356 cm^{-1} and 405 cm^{-1}, respectively, possibly due to the very thin structure of the WS_2 product and absence of layer-layer interactions.[1,7]

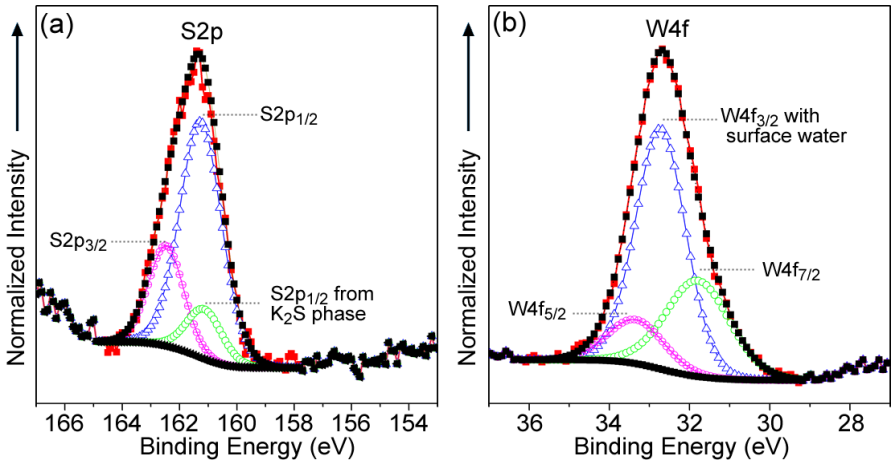

Figure 8-3. (a) S2p XPS of dried suspension (before K removal); (b) W4f XPS of dried suspension (before K removal).

The chemical composition of the exfoliated and disintegrated product was further confirmed with XPS indicated that the dried suspension contained both 2H-WS_2 and K_2S phases. As shown in ***Figure 8-3***, the S2p and W4f XPS show peaks at around 161.4 and 32.7 eV, respectively, consistent with those reported for 2H-WS_2.[11-13] Deconvolution of the S2p and W4f into its components suggests that the $S2p_{3/2}$ (162.5 eV), $S2p_{1/2}$ (161.3 eV), W4f5/2 (33.4 eV) and $W4f_{7/2}$ (31.9 eV) peaks of present 2H-WS_2 are shifted to lower binding energies (shift of ~0.5 eV) compared to bulk 2H-WS_2.[11-13] This may be due to the contact between K^+ and OH^- with the WS_2 surface. In both spectra, $S2p_{1/2}$ (around 15% molar ratio of all the S) from K_2S phase at around 161.2 eV[14] and $W4f_{3/2}$ of defected 2H-WS_2 bonded with surface OH^- groups at around 32.8 eV were also found.[15] The absence of the binding peaks of tungsten oxide (W4f7/2 = 35.7 eV, W^{6+}) and tungsten hydroxide ($W4f_{7/2}$ = 36.1 eV; W^{6+})[11,12] suggests that the edges of 2H-WS_2 are S-terminated. The chemical composition of the dialyzed suspension (K^+ removed) was further analyzed using EDS under TEM observation. As shown in ***Figure 8-4a***, which was taken from the agglomerated WS_2 nanoclusters shown in ***Figure 8-4b***, the EDS of the dialyzed WS_2 only give W and S signals from the nanostructures (the Cu and

C are from the support grid; no O or K was found). The S/W ratio of these purified nanoclusters was around 2, which is highly consistent with the stoichiometric ratio of WS_2. It suggests that the S of the K_2S phase in the dried suspension prior to purification is more likely to be derived from WS_2 sediment rather than the exfoliated and disintegrated WS_2 product. Together with EDS analysis on different regions of the dried suspension (S/W molar ratio not higher than 2.5), by weighing the WS_2 raw material and collected sediment (mass reduced by over 45 wt%), it can be concluded that over 36 wt% WS_2 was reduced to small WS_2 dots (the morphology and size will be confirmed below).

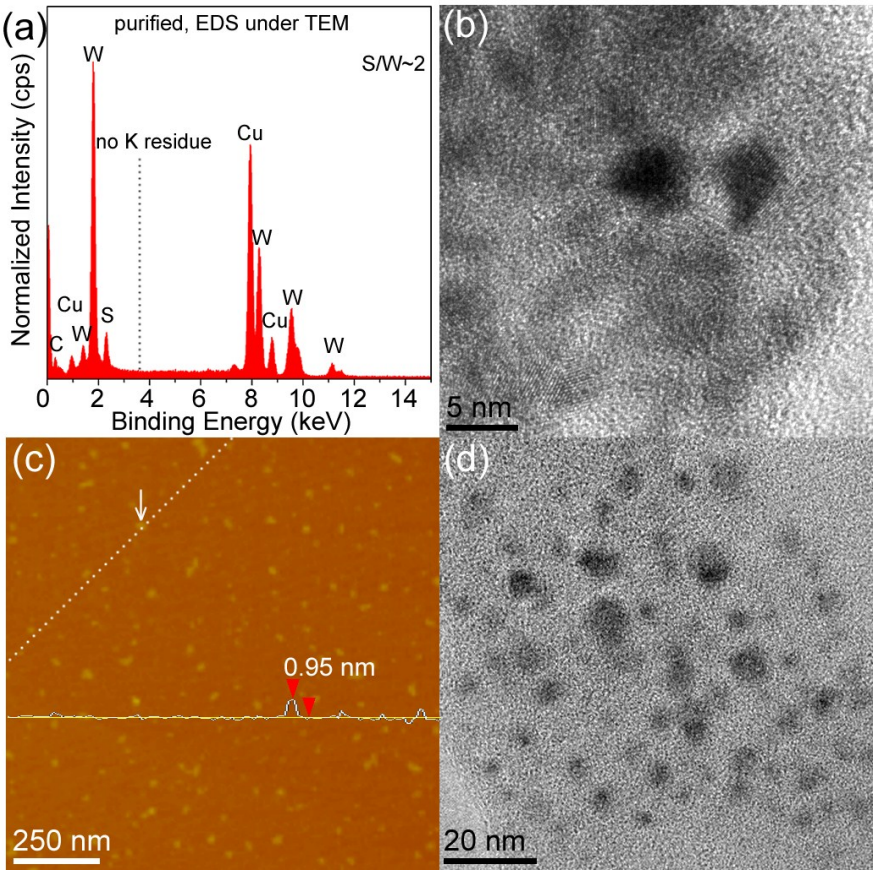

Figure 8-4. (a) EDS analysis taken from the region shown in (b) TEM of dialyzed WS_2 nanoclusters; (c) AFM topography image; (d) BFTEM of the dialyzed WS_2 QDs.

The above results suggest that the exfoliated and disintegrated WS_2 possibly has quite small size and thin structure. To further confirm this, AFM and bright-field TEM (BFTEM) analysis were performed on the purified WS_2 product (using dialysis tubing). AFM (***Figure 8-4c***) and TEM (***Figure 8-4d***) observations of purified WS_2 dots both gave an average size of 8-15 nm. AFM line analysis of some dots suggests that the QDs are thin to around 0.9 nm (***Figure S8-2***). The line profile in ***Figure 8-4c*** gives an example,

showing the thickness of 0.95 nm of the arrow indexed dot, corresponding well with that of monolayered WS_2.[7] The WS_2 dots under AFM observations should have similar thickness (reflected by their similar contrasts), which is also confirmed by a three-dimensional view of the AFM image (***Figure S8-3***). As revealed by HRTEM analysis (***Figure 8-5***), these monolayered WS_2 dots have good crystallinity. HRTEM analysis in ***Figure 8-5*** also gives different information about the QDs. With these images, clear terminated edges (*e.g.* ***Figure 8-5a***, zigzag edges determined by the FFT pattern), the bond length of W-S (~0.24 nm of 2H-WS_2,[16] ***Figure 8-5b***), the lattice fringe of (102) with ~0.24 nm (JCPDS: 84-1389) (***Figures 8-5c&d***) and hexagonal lattice structures (***Figures 8-5a***) are revealed. Some products of WS_2 flake exfoliation and disintegration were oriented side-on to the substrate, allowing direct observations of their thickness. In ***Figure 8-5e***, both tri-layered WS_2 with layer distances of ~0.62 nm (lattice fringe of 002, JCPDS: 84-1389) and stacked monolayered WS_2 QDs with layer distances >1 nm are discovered.

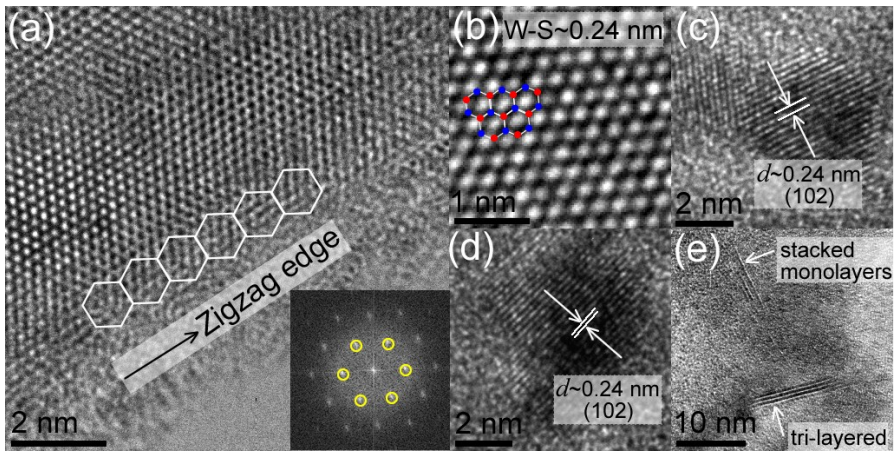

Figure 8-5. HRTEM images show different information of the WS_2 QDs. Inset in image c is the FFT pattern of the crystal, showing the hexagonal structure.

8.3.3 Optical Properties of Monolayered WS_2 QDs

On the basis of the above characterisations, it is clear that high yield monolayered WS_2 QDs have been exfoliated and disintegrated from bulk WS_2 flakes. Previous studies suggested that the thickness reduction of some LTMDs (*e.g.* WS_2, MoS_2) to that of monolayers resulted in a change from an indirect to a direct semiconductor.[17-19] The formation of monolayered WS_2 QDs may also lead to a similar change and interesting optical properties. Therefore, further investigation on the optical properties of the prepared monolayered WS_2 QDs was performed. Shown in ***Figure 8-6a*** are the UV/Vis absorption spectra of the WS_2 QDs prior to purification (contains K^+) and purified using either ion exchange or dialysis, all exhibiting clear absorption peaks at around 277 and

393 nm. In the UV/Vis spectrum of pre-purified WS_2 QDs, an intense absorption peak at around 230 nm was also found, which can be attributed to the absorption from KS^-.[20] Although the K^+ in the WS_2 QDs suspension can be effectively removed using ion exchange resin, this purification normally led to the instability of WS_2 QDs as faint yellow sediment (solid S) was seen after some days of settling. This can be understood as being due to the reaction between terminating S atoms and local strong acid centres of cation exchange resin. This will leave W atoms exposed, which are easily oxidized in water solution. However, by contrast, dialyzed WS_2 QDs are stable and give similar absorption peaks, suggesting the K^+ can also be effectively removed without destroying the QD surfaces using dialysis tubing. ***Figure 8-6b*** shows the UV/Vis spectra of dialyzed WS_2 QDs at different concentrations, in which two strong absorption peaks at around 393 (3.16 eV), 277 nm (4.48 eV), and one weak absorption peak at around 333 (3.73 eV) were found. In WS_2 nanoclusters (4-7 nm), only the strong absorptions peaks at around 364 (3.41 eV) and 295 nm (4.20 eV) were found (the weak peak between the two strong absorption peaks had disappeared).[21] The authors investigated correlating these peaks with the excitonic absorption peaks A and B of WS_2 but concluded assignment was incorrect.[21] At least, the peak at the shortest wavelength cannot be attributed as excitonic absorption peak of WS_2 as no emission was found with excitation wavelength of 277 nm (4.48 eV).

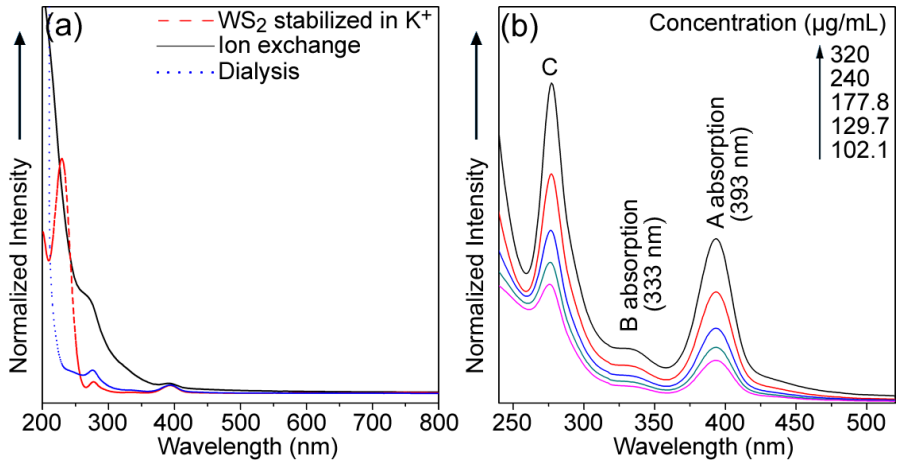

Figure 8-6. (a) UV/Vis spectra of WS_2 QDs stabilized in K^+ and WS_2 QDs purified using different methods. For better presentation, the zero intensities of the spectra were shifted; (b) UV/Vis spectra of WS_2 QDs purified using dialysis tubing.

In monolayered WS_2 sheets, three absorption peaks (from long to short wavelengths) were found and attributed to excitonic absorption peaks A, B and optical transitions between the density of states peaks in the valence and conduction bands.[22] Therefore, the absorption peaks of 393 (3.16 eV) and 333 (3.73 eV) in present UV/Vis spectra are

most likely to be the excitonic absorption peaks A and B, respectively, of monolayered WS_2 QDs. The 277 nm (4.48 eV) absorption peak of the UV/Vis spectra should be attributed to the optical transitions between the density of states peaks in the valence and conduction bands.[22] The A and B absorption peaks here (***Figure 8-6b***) are at noticeably shorter wavelengths than is the case with monolayered WS_2 sheets (625 and 550 nm).[22] The concentration dependent absorbance at 393 nm (***Figure S8-4***) follows the Beer-Lambert law (suggesting good water solubility of dialyzed WS_2 QDs) and yields an absorption coefficient α_{393} = 9225 $L.g^{-1}m^{-1}$. This is much higher than for A peak absorption with monolayered WS_2 sheets (2756 $L.g^{-1}m^{-1}$).[6]

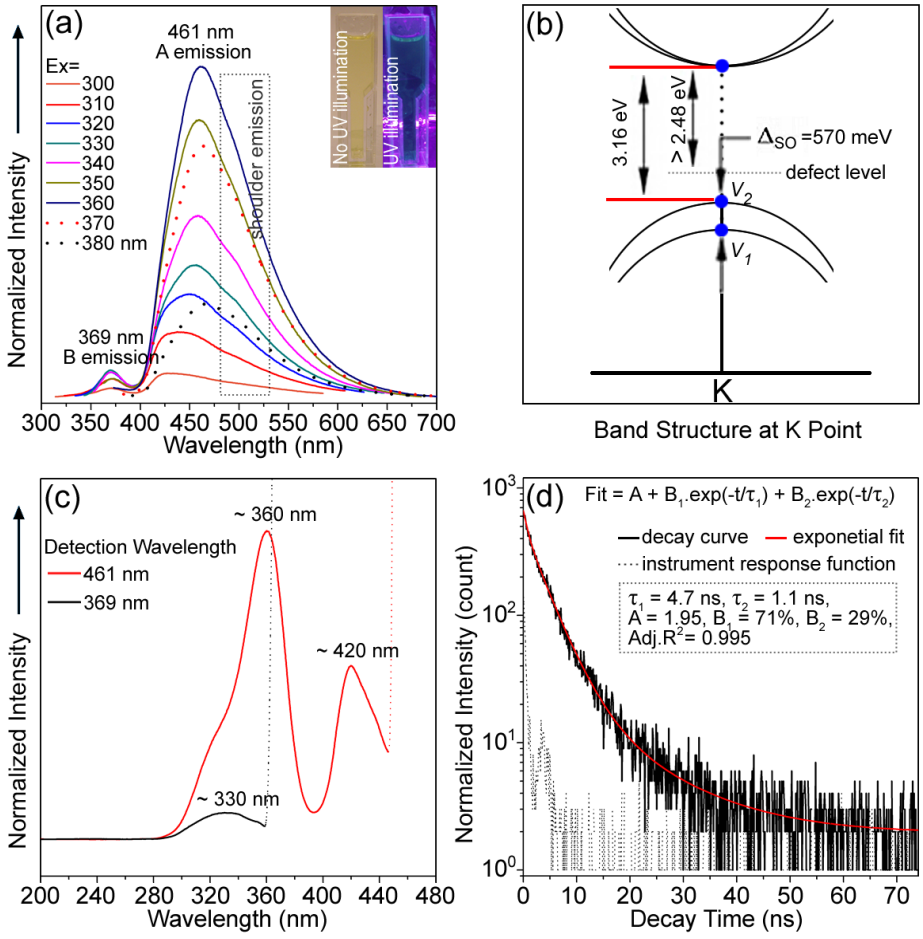

Figure 8-7. (a) PL spectra of dialyzed WS_2 QDs with various excitation wavelengths. Inset shows photographs of the QDs with and without UV (365 nm) illumination; (b) diagram of the band structure of purified WS2 QDs close to the K point; (c) PL excitation spectra of WS2 QDs with 369 nm and 461 nm detection wavelengths; (d) TRPL decay profile of WS2 QDs recorded at room temperature while monitoring the emission at 461 nm upon 360 nm excitation wavelength.

The strong absorption by WS_2 QDs of relatively near-UV/blue light suggests they might be capable of efficient blue or green emission. To confirm this, the room temperature PL

of the dialyzed WS_2 QDs was measured under various excitation wavelengths (***Figure 8-7a***). A brief visual inspection of the QDs under UV (365 nm) illumination shows significant PL emission (***Figure 8-7a*** inset). Spectral measurements of PL show the strongest emission of the WS_2 QDs occurs at ~461 nm (~2.69 eV) with an excitation wavelength of 360 nm (~3.44 eV). By using anthracene as a fluorescent standard, the luminescent quantum yield was determined as ~4.0% (***Table 8-1*** in ***Section 8.2.4***). This is greater than that of bulk WS_2, which exhibits only negligible luminescence due to its indirect band gap, and of monolayered TMDC (*e.g.* MoS_2) sheets, which remains low at about 0.4% despite their direct band gap nature.[18] Monolayered WS_2 sheets show similarly low PL quantum yields although the reasons for this are still unclear.[22] The higher PL quantum yield observed with the monolayered WS_2 QDs may yet serve to open the way for the use of TMDCs in optical applications (*e.g.* optoelectronic and bio-imaging applications).[19]

Previous studies have found that bulk WS_2 changes to a direct gap semiconductor upon assuming monolayer thicknesses.[17,19,22,24] The increased luminescence of monolayered WS_2 QDs should depend directly on this band structure change (as described in the following, a new defect level may also contribute to the main emission at around 461 nm). However, the blue-shift of the QD PL (as well as the UV/Vis spectra) compared with that of monolayered sheets (emission at 630 nm with excitonic absorption peak A at around 625 nm)[22] may also indicate strong quantum confinement. Layered metal dichalcogenides should exhibit large quantum confinement effects.[21-24[Upon the reduction of thickness, quantum confinement effect has led to the blue shift of excitonic absorption peak A from 713 nm (1.74 eV) from bulk WS_2 to 653 nm (1.9 eV) from monolayered WS_2 sheets.[22-24] As reported for layered metal dichalcogenides, the energy shifts produced by lateral size reduction is over an order of magnitude larger than those due to thickness reduction.[25] Therefore, the large energy of excitonic absorption peak A (393 nm, compared with monolayered sheets) from the monolayered WS_2 QDs is reasonable and similar to that found from WS_2 nanoclusters (4-7 nm).[21] In the PL spectra, a small emission peak at ~369 nm (3.36 eV) and a very weak shoulder emission at ~500 nm (2.48 eV) are also found and the later might be due to a new defect level introduced in the WS_2 QDs. To understand the small emission peak at 369 nm (3.36 eV), it is necessary to consider that due to the broken inversion symmetry in monolayered WS_2, the d-orbitals of metal W atoms have strong spin-orbit coupling (a direct consequence of the giant spin-valley coupling).[24] This leads to spin splitting of the valence band, showing the largest effect at the K point of the Brillouin

zone (split with an energy gap of ~0.4 eV in monolayered WS_2 sheets).[24,26,27] This band structure is illustrated schematically in ***Figure 8-7b***. The strength of this spin-valley coupling can be indicated by the energy difference ($\triangle_{SO}$) between excitonic absorption peaks A and B in the UV/Vis spectra (***Figure 8-6b***, also shown as the gap between V_1 and V_2 points in ***Figure 8-7b***). Based on the UV/Vis spectra in ***Figure 8-6b***, the energy ($\triangle_{SO}$) between V_2 (excitonic absorption peak A at 393 nm/3.16 eV) and V_1 (excitonic absorption peak B at 333 nm/3.73 eV) is 570 meV (near IR region, ~2175 nm). This is much greater than that of monolayered WS_2 sheets (around 400 meV),[22,24] suggesting that the spin-orbit splittings of monolayered WS_2 can be manipulated by lateral size control of the QDs. Although this giant spin-valley coupling was suggested by UV/Vis spectra,[6,22,24] the direct proof from PL is not always clear in monolayered WS_2 sheets.[7,22,24] In the monolayered WS_2 QDs prepared here, due to the giant spin-valley coupling, a new emission (B emission at around 369 nm, ***Figure 8-7a***) from the transition between conduction band minimum and V_1 point is also discovered. Upon increasing the excitation wavelength (E*x*) from 300-380 nm, the strength of the B-peak PL emission (***Figure 8-7a***) increases first before decreases again, with a maximum at E*x* ~ 330 nm. This result corresponds well with the UV/Vis result as the maximum excitonic absorption peak B was found at around 333 nm (***Figure 8-6b***). Further PL excitation (PLE) of the monolayered WS_2 QDs, using a detection wavelength of 369 nm (B emission position in ***Figure 8-7a***), only gave a broad peak around 330 nm (***Figure 8-7c***), corresponding well with UV/Vis and PL results and suggesting that the B emission (~369 nm) results from a transition between the conduction band minimum and the V_1 point (see ***Figure 8-7b***). However, for the A emission (***Figure 8-7a***), a new defect level also contributed to the emission. The strength of the A-peak PL emission (***Figure 8-7a***) increased with increasing the excitation wavelength (E*x*) from 300 to 360 nm, close to the band edge of V_2 point (393 nm). The highest emission was found at E*x* = 360 nm instead of the maximum excitonic absorption peak A at ~393 nm. To clarify this further, PLE of the monolayered WS_2 QDs using a detection wavelength of 461 nm (A emission position in ***Figure 8-7a***) was further studied. It was found that the PLE consisted of three peaks, including a shoulder peak at 330 nm and two strong peaks at 360 and 420 nm respectively. This suggests that the A emission (~461 nm) results from three contributory excitation processes: 1) excitation from the V_2 point to the conduction band minimum (360 nm excitation in PLE spectra, ***Figure 8-7c***); 2) excitation from the V_1 point to the conduction band minimum (330 nm excitation in PLE spectra, ***Figure 8-7c***); and 3) the last transition around 420 nm (***Figure 8-7c***) which might be the transition to the conduction band minimum from a new defect level above the valence

band (***Figure 8-7b***). The contribution of the latter two transitions above results in the excitation wavelength for maximum A emission becoming shifted from 393 to 360 nm. TRPL (***Figure 8-7d***, time-correlated single photon counting technique) provided more details of these transition processes. In the TRPL curve, the lifetime of the luminescence at 461 nm can be fitted well with a bi-exponential function, suggesting that the decay is dominated by two of the processes discussed above (the decays of the emissions from processes 1 & 2 are the same). The observed lifetimes of the main types of luminescence are all in nanoseconds, with 71% of 4.7 ns and 29% of 1.1 ns (the decay from instrument response is 0.55 ns, see ***Figure S8-5*** for more information). Base on above analysis, it can be conclude that the multiple PL emissions are the result of giant spin-orbit coupling of the monolayered WS_2 QDs, and the shift of the highest A emission is due to the additional emission contributions originate from V_1 point and a new defect level.

8.3.4 Bio-Imaging with Monolayered WS_2 QDs

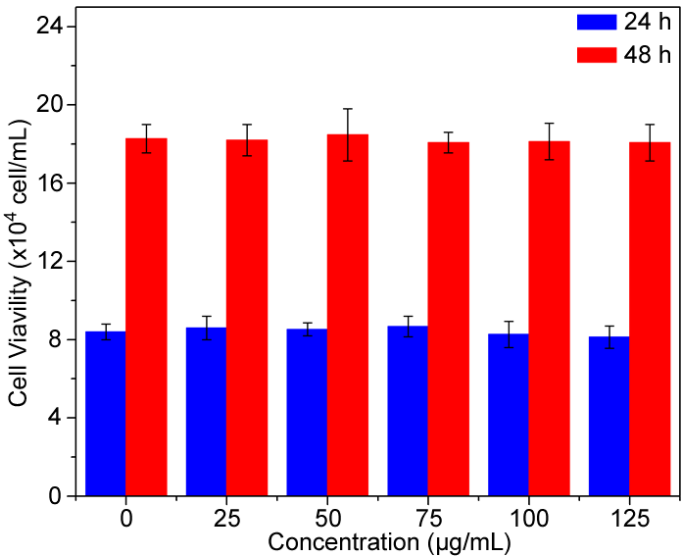

Figure 8-8. Cell viability assay with MDCKII cells treated with different concentrations of WS_2 QDs. The bars represent cell counts and the error bars represent standard errors of the mean.

The discovery of giant spin-valley coupling and modest luminescence broadens the potential applications of WS_2. For example, the nanosecond lifetime of the luminescence suggests that WS_2 QDs are potential candidate materials for optoelectronic and biological applications. However, for biological applications (*e.g.* bioimaging, cell tracking, isolation of biomolecules, and gene technology), any possible K_2S in the WS_2 suspensions should be removed (*e.g.* using dialysis here) to avoid cell toxicity. Here, the cytotoxicity of purified WS_2 QDs is further estimated using the mammalian cell line

MDCKII (madin-darby canine kidney type II). As shown in ***Figure 8-8***, low doses of WS_2 QDs (0-125 μg/mL) were non-toxic to these cells and no obvious effect on cell number was observed at these dosages (0-125 μg/mL) with prolonged exposure times (24-48 h).

To illustrate the potential in bio-imaging applications, cellular imaging was performed using monolayered WS_2 QDs as fluorescent labels. In the MDCKII cells stained with WS_2 QDs alone, the QDs were taken up by the cells but did not penetrate the cell nuclei (***Figure 8-9a***). ***Figures 8-9b-c*** give the images of MDCKII nucleus stained with DAPI (emission from around 400-650 nm) and WS_2 QDs (emission from ~350-650 nm). By selecting appropriate fluorescence filters, cell nuclei can be shown as blue (***Figure 8-9b***) or green (***Figure 8-9c***) respectively. In ***Figure 8-9c***, the cytoplasm was only stained by WS_2 QDs and appears green. Although the nuclei in ***Figure 8-9c*** also give green emission from DAPI (diamidino-2-phenylindole), the boundary between cells, nuclei and cytoplasm are clear. This is more clearly seen in the overlay image of ***Figure 8-9b*** and ***Figure 8-9c*** (***Figure 8-9d***) and suggests that WS_2 QDs can be used in high contrast bio-imaging and will be well-suited for other biomedical applications.

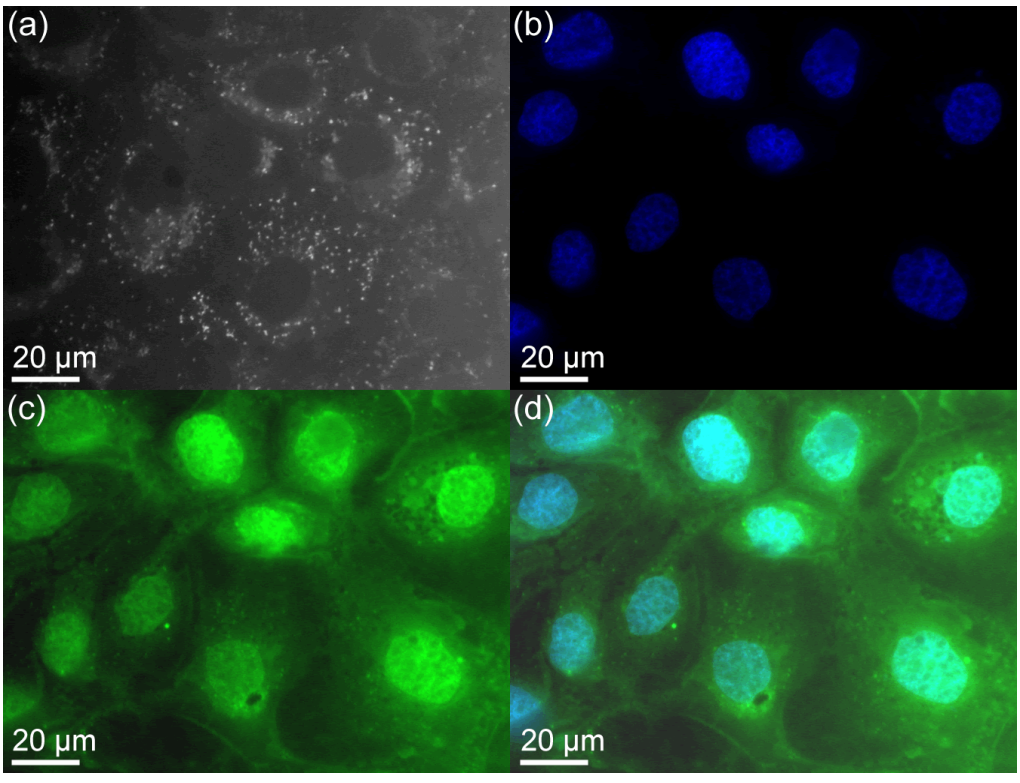

Figure 8-9. (a) Agglomerated WS_2 QDs surrounding each nucleus (cells are stained by WS_2 QDs only); (b) Individual nucleus stained with DAPI; (c) Cell nucleus and cytoplasm were stained with DAPI and WS_2 QDs respectively; (d) The overlay image of ***Figure 8-9b*** and ***Figure 8-9c***.

8.4 Conclusion

In conclusion, this chapter presented the successful preparation of monolayered WS_2 QDs from bulk WS_2 flakes. The majority of the QDs are monolayered with a lateral size around 8-15 nm. Like the monolayered WS_2 sheets, the monolayered WS_2 QDs also exhibit direct semiconductor nature which is different with bulk multilayered WS_2 (indirect semiconductor) and activated strong luminescence at room temperature. The luminescence of the monolayered WS_2 QDs was found at the region of green-blue light (centred at 461 nm with multiple emission peaks) with a quantum yield of ~4% which is much improved from that of monolayered sheets. The strong luminescence and multiple emissions are considered to be the result of the direct excitonic transitions at K point and giant spin-valley coupling respectively. As was noted, a new defect level also contributes the emission, which led to the shift of the highest main emission position. Unlike monolayered WS_2 sheets, the created monolayered WS_2 QDs have stronger spin-orbit coupling and much blue shifted emission, suggesting the spin-orbit splitting and luminescence of monolayered WS_2 can be effectively manipulated by lateral size control, which make them highly valuable for the applications in semiconductor based spintronics and optoelectronic devices. Further evaluations suggested that monolayered WS_2 QDs can be well used for biological application.

8.5 Supporting Information

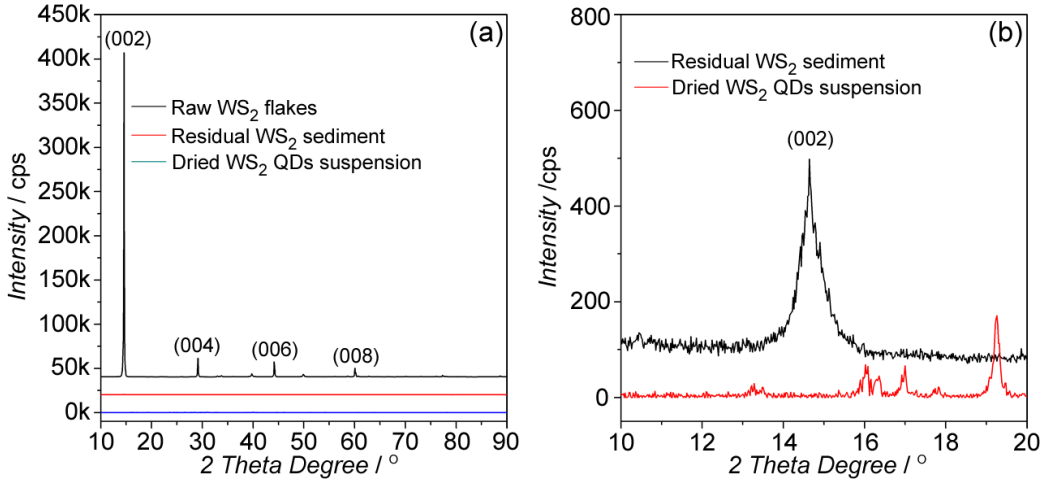

Figure S8-1. (a) XRD patterns of WS_2 flakes raw material, residual WS_2 sediment after preparation and dried suspension which contains WS_2 QDs; (b) Local enlarged XRD patterns of residual WS_2 sediment and dried suspension which contains WS_2 QDs. For better presentation, the zero intensities of the patterns were shifted. The diffraction peaks were indexed base on JCPDS: 84-1389. Disappearance of the (002) diffraction peak in dried suspension which contains WS_2 QDs suggest thin structure of the QDs. Due to destroy of

layered structure (exfoliation and disintegration), the (002) diffraction of residual WS_2 sediment are much weakened from that of WS_2 raw materials. In the XRD pattern of dried suspension, the other diffraction peaks should from the diffractions of K salt.

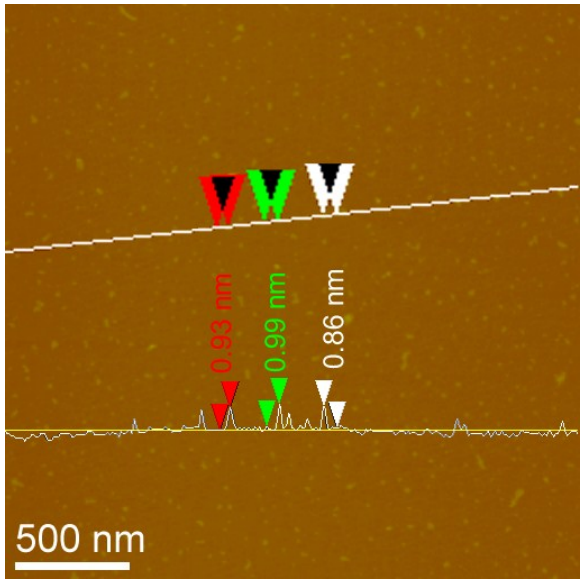

Figure S8-2*.** AFM image of WS_2 QDs. The line was plotted to across the dots' centres (three marked) to minimize measurement errors. This thickness was also proved by three-dimensional AFM image (Figure S8-3***).

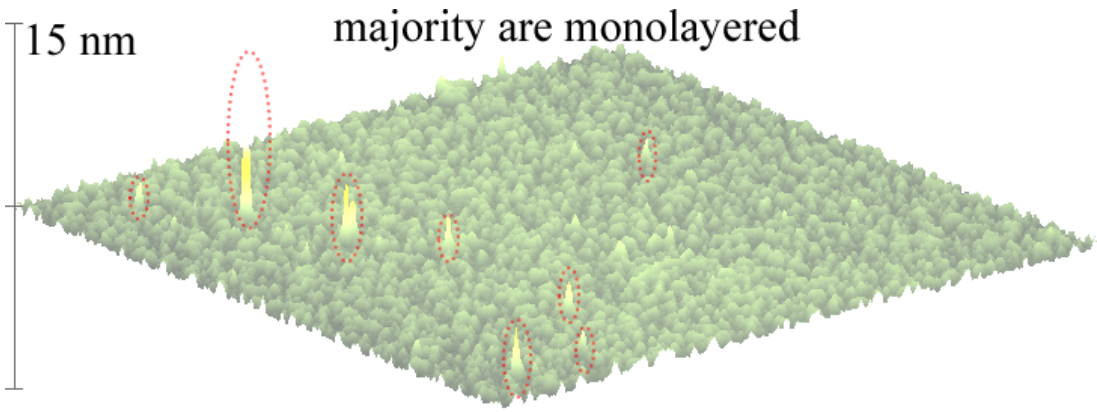

Figure S8-3*.** Three-dimensional view of the AFM image in ***Figure S8-2. The majority dots under AFM observation have same thickness (monolayered).

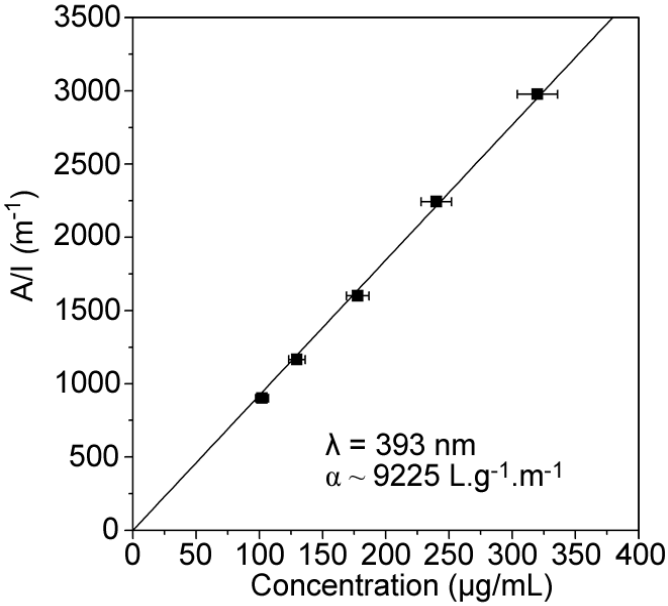

Figure S8-4. Plots of absorbance (λ_{ex} = 393 nm) normalized to cell length, versus the concentration of dialyzed WS_2 QDs product in water solution. The errors arise from uncertainty in the weighing and diluting processes.

References and Notes

[1] A. Molina-Sánchez and L.Wirtz, Phonons in Single-Layer and Few-Layer MoS_2 and WS_2. *Phys. Rev. B* **2011**, *84*, 155413.

[2] L. Rapoport, N. Fleischer and R.Tenne, Fullerene-Like WS_2 Nanoparticles: Superior Lubricants for Harsh Conditions. *Adv. Mater.* **2003**, *15*, 651-655.

[3] D. Merki and X.Hu, Recent Developments of Molybdenum and Tungsten Sulfides as Hydrogen Evolution Catalysts. *Energy Environ. Sci.* **2011**, *4*, 3878-3888.

[4] M. Wu, Y. Wang, X. Lin, N. Yu, L. Wang, L. Wang, A. Hagfeldt and T. Ma, Economical and Effective Sulfide Catalysts for Dye-Sensitized Solar Cells as Counter Electrodes. *Phys. Chem. Chem. Phys.* **2011**, *13*, 19298-19301.

[5] W. S. Hwang, M. Remskar, R. Yan, V. Protasenko, K. Tahy, S. D. Chae, P. Zhao, A. Konar, H. Xing, A. Seabaugh and D. Jena, Transistors with Chemically Synthesized Layered Semiconductor WS_2 Exhibiting 10^5 Room Temperature Modulation and Ambipolar Behavior. *Appl. Phys. Lett.* **2012**, *101*, 013107.

[6] J. N. Coleman, M. Lotya1, A. O'Neill1, S. D. Bergin, P. J. King, U. Khan, K. Young, A. Gaucher, S. De, R. J. Smith, I. V. Shvets, S. K. Arora, G. Stanton, H.-Y. Kim, K. Lee, G. T. Kim, G. S. Duesberg, T. Hallam, J. J. Boland, J. Wang, J. F. Donegan, J. C. Grunlan, G. Moriarty, A. Shmeliov, R. J. Nicholls, J. M. Perkins, E. M. Grieveson, K, Theuwissen, D. W. McComb, P. D. Nellist and V. Nicolosi, Two-Dimensional Nanosheets Produced by Liquid Exfoliation of Layered Materials. *Science* **2011**, *331*, 568-571.

[7] H. R. Gutiérrez, N. Perea-López, A. L. Elías, A. Berkdemir, B. Wang, R. Lv, F. López-Urías, V. H. Crespi, H. Terrones and M. Terrones, Extraordinary Room-Temperature Photoluminescence in Triangular WS_2 Monolayers. *Nano Lett.* **2013**, *8*, 3447-3454.

[8] H. Jiang, Electronic Band Structures of Molybdenum and Tungsten Dichalcogenides by the GW Approach. *J. Phys. Chem. C* **2012**, *116*, 7664-7671.

[9] Z. Liu, K. Suenaga, Z. Wang, Z. Shi, E. Okunishi and S. Iijima. Identification of Active Atomic Defects in A Monolayered Tungsten Disulphide Nanoribbon. *Nat. Commun.* **2011**, *2*, 213.

[10] L. Lin and S. Zhang, Creating High Yield Water Soluble Luminescent Graphene Quantum Dots *via* Exfoliating and Disintegrating Carbon Nanotubes and Graphite Flakes. *Chem. Commun.* **2012**, *48*, 10177-10179.

[11] I. Martin-Litas, P. Vinatier, A. Levasseur, J. C. Dupin, D. Gonbeau and F. Weill, Characterisation of r.f. Sputtered Tungsten Disulfide and Oxysulfide Thin Films. *Thin Solid Films* **2002**, *4156*, 1-9.

[12] H. Martinez, A. Benayad, D. Gonbeau, P. Vinatier, B. Pecquenard and A. Levasseur, Influence of the Cation Nature of High Sulfur Content Oxysulfide Thin Films MO_yS_z (M=W, Ti) Studied by XPS. *Appl. Surf. Sci.* **2004**, *236*, 377-386.

[13] K. Dartigeas, D. Gonbeau and G. Pfister-Guillouzo, Core and Valence Spectra of TaS_2 and WS_2. Experimental and Theoretical Studies. *J. Chem. Soc., Faraday Trans*. **1996**, *92*, 4561-4566.

[14] X. Yu, F. Liu, Z. Wang and Y. Chen, Auger Parameters for Sulfur-Containing Compounds Using A Mixed Aluminum-Silver Excitation Source. *J. Electron. Spectrosc. Relat. Phenom.* **1990**, *50*, 159-166.

[15] A. P. Shpak, A. M. Korduban, L. M. Kulikov, T. V. Krvshchuk, N. B. Konig and V. O. Kandvba, XPS Studies of The Surface of Nanocrystalline Tungsten Disulfide. *J. Electron. Spectrosc. Relat. Phenom.* **2010**, *181*, 234-238.

[16] R. A. Gordon, D. Yang, E. D. Crozier, D. T. Jiang and R. F. Frindt, Structures of Exfoliated Single Layers of WS_2, MoS_2, and $MoSe_2$ in Aqueous Suspension. *Phys. Rev. B* **2002**, *65*, 125407.

[17] A. Ramasubramaniam, Large Excitonic Effects in Monolayers of Molybdenum and Tungsten Dichalcogenides. *Phys. Rev. B* **2012**, *86*, 115409.

[18] K. F. Mak, C. Lee, J. Hone, J. Shan and T. F. Heinz, Atomically Thin MoS_2: A New Direct-Gap Semiconductor. *Phys. Rev. Lett.* **2010**, *105*, 136805.

[19] Q. H. Wang, K. Kalantar-Zadeh, A. Kis, J. N. Coleman and M. S. Strano, Electronics and Optoelectronics of Two-Dimensional Transition Metal Dichalcogenides. *Nat. Nanotechnol.* **2012**, *7*, 699-712.

[20] H. G. Karge and J. Raskó, Hydrogen Sulfide Adsorption on Faujasite-Type Zeolites with Systematically Varied Si-Al Ratios. *J. Colloid Interface Sci.* **1978**, *64*, 522-532.

[21] J. M. Huang, R. A. Laitinen and D. F. Kelley, Spectroscopy and Tapping Dynamics in WS_2 Nanoclusters. *Phys. Rev. B* **2000**, *62*, 10995-11005.

[22] W. Zhao, Z. Ghorannevis, L. Chu, M. Toh, C. Kloc, P.-H. Tan and G. Eda, Evolution of Electronic Structure in Atomically Thin Sheets of WS_2 and WSe_2. *ACS Nano* **2013**, *7*, 791-797.

[23] K. K. Kam and B. A. Parkinson, Detailed Photocurrent Spectroscopy of The Semiconducting Group VIB Transition Metal Dichalcogenides. *J. Phys. Chem.* **1982**, *86*, 463-467.

[24] H. Zeng, G.-B. Liu, J. Dai, Y. Yan, B. Zhu, R. He, L. Xie, S. Xu, X. Chen, W. Yao, and X. Cui, Optical Signature of Symmetry Variations and Spin-Valley Coupling in Atomically Thin Tungsten Dichalcogenides. *Scientific Reports* **2013**, *3*, 1608.

[25] J. P. Wilcoxon, P. P. Newcomer and G. A. Samara. Synthesis and Optical Properties of MoS_2 and Isomorphous Nanoclusters in The Quantum Confinement Regime. *J. Appl. Phys.* **1997**, *81*, 7934-7944.

[26] D. Xiao, G.-B. Liu, W. Feng, X. Xu and W. Yao, Coupled Spin and Valley Physics in Monolayers of MoS_2 and Other Group-VI Dichalcogenides. *Phy. Rev. Lett.* **2012**, *108*, 196802.

[27] Z. Y. Zhu, Y. C. Cheng and U. Schwingenschlögl, Giant Spin-Orbit-Induced Spin Splitting in Two-Dimensional Transition-Metal. *Phys. Rev. B* **2011**, *84*, 153402.

Chapter IX. Luminescent Monolayered Molybdenum Disulphide Quantum Dots with Giant Spin-Orbit Coupling

9.1 Introduction

Preparation of inorganic quantum dots (QDs) is a rapidly developing research area, attracting significant interests from various communities.[1-2] By developing new and novel preparation techniques, better size control of a nanostructured material can be achieved and some new size-dependent properties discovered and explored.[1-4] For example, the formation of graphene QDs from graphite activates strong photoluminescence (PL) due to a dramatically increased edge structure ratio.[5] Like graphite, molybdenum disulfide (MoS_2) is also a widely known layered material, serving as a solid state lubricant and catalyst (*e.g.* for hydrodesulfurization and hydrogen generation).[6-8] Bulk MoS_2 is an indirect gap material with negligible luminescence.[6] Many interesting changes in its electronic, magnetic and optical properties are expected when MoS_2 is "tailored" to monolayered QDs. For instance, monolayered MoS_2 sheet is a direct semiconductor with strong luminescence, and can be ferromagnetic/metallic or nonmagnetic/semiconducting depending on its edge profile.[6,9-11] These, and other so far unpredicted, changes could, in principle, be made more evident by decreasing the lateral size of the sheets to form monolayered MoS_2 QDs and increase the significance of edge effects. Similar observations were found on hexagonal boron nitride (hBN) (see ***Chapter VII***) and monolayered tungsten disulfide (WS_2) QDs (see ***Chapter VIII***). Size dependent effects will allow materials properties to be manipulated and enhanced for various applications (*e.g.* energy harvesting, photocatalysis, bioimaging and single-electron-transistors).

Although the formation of monolayered MoS_2 sheets has been achieved,[12] the preparation and properties of monolayered MoS_2 QDs are not well developed and lack understanding. Very recently, Štengl *et al.* suggested that monolayered MoS_2 sheets can be further disintegrated to form MoS_2 nanodots (lateral sizes of 4-70 nm were produced) using a similar approach to that used in the preparation of graphene QDs.[13] However, like the solvothermal cutting of graphene QDs from graphene oxide sheets,[14] poor

disintegration efficiency of MoS_2 led to broad luminescence (the product required stabilizing in ethylene glycol to sustain the luminescence) of the product that was similar to that of MoS_2 sheets.[13] This also inhibits the possible use of MoS_2 in applications such as bio-imaging (high purity and strong luminescence are normally required) and optoelectronic devices (needs pure, consistent materials). Reducing bulk MoS_2 to thin and small QDs effectively and efficiently with stable structural, optical and electronic properties has become a technical challenge. This chapter describes the direct exfoliation and disintegration of bulk MoS_2 flakes to form high yield (31 wt%) monolayered QDs with lateral sizes from 8-20 nm. Like monolayered MoS_2 sheets, the monolayered MoS_2 QDs are direct semiconductors, which leads to strong luminescence. However, due to strong quantum confinement effects, the luminescence of the monolayered MoS_2 QDs was found at shorter (green-blue, centred at ~ 471 nm) wavelengths than with the monolayered sheets (centred at ~780 nm[6]). The luminescence of the monolayered MoS_2 QDs with a quantum yield of 7.9% is much stronger than that of monolayered sheets, which has a quantum yield of around 0.4%.[6] The monolayered MoS_2 QDs also show giant spin-orbit coupling (SOC) with a split energy gap of 530 meV, far greater than is the case for monolayered sheets with a split energy gap of 130 meV.[10-12] These optical and electronic effects may be useful in imaging and semiconductor-based spintronics. This chapter also demonstrates that monolayered MoS_2 QDs can be used as a non-toxic fluorescent label in confocal microscopy of biological cells. However, the spin-valley quantum states of the monolayered QDs may also allow quantum entanglement to enable quantum computation.

9.2 Experimental Methods

9.2.1 Sample Preparation

As a transition-metal dichalcogenide (LTMD), MoS_2 has similar crystal structure to that of WS_2. Therefore, the preparation was performed using a similar manner with that of monolayered WS_2 QDs (see ***Section 8.2.1***). A higher reaction (180-190 ^oC) and longer intercalation time (held for >4 h) were used here to improve the yield. Comparisons suggest that the intercalation of MoS_2 was harder than WS_2. However, further improvement of the reaction condition (longer reaction time and higher reaction temperature) also led to the damage of the WS_2 structure (which can be determined by simple check of the luminescence: use UV lamp to illuminate the created QDs suspension) and the produce of more K_2S. After preparation, a yellow solution containing MoS_2 QDs was separated from the residual solid MoS2 by using filter (with

coarse filter paper) to remove MoS_2 sediment. Then the collected suspension was heated in an oven to evaporate ethanol. The remaining K ions in the solution were absorbed/removed with the cation exchange resin (fill the resin into a Millipore Millicup filter unit, with ~5 cm filling height) and dialysis tubing respectively.

9.2.2 Calculation of the Quantum Yield of WS_2 QDs

See ***Section 3.4*** in ***Chapter III*** for the calculation method of quantum yield.

Table 9-1. Quantum yield of MoS_2 QDs suspension (in H_2O) using Rhodamine B as a reference.

Sample	Integrated Emission Intensity (*I*)	Absorptance at 360 nm (*A*)	Refractive Index of Solvent (η)	Quantum Yield (Φ)
Rhodamine B	43622	0.0076	1.36	~70% (Known)[15-17]
MoS_2 QDs	31484	0.0467	1.33	~7.9%

9.3 Results and Discussion

9.3.1 MoS_2 Flake Exfoliation and Disintegration

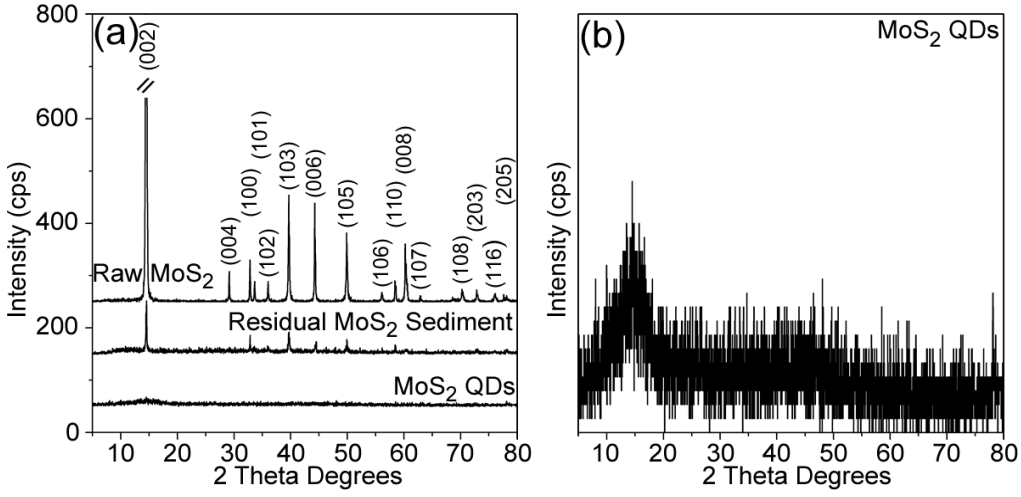

Figure 9-1. (a) XRD patterns of MoS_2 raw material, residual MoS_2 sediment and purified MoS_2 QDs; (b) XRD pattern of purified MoS_2 QDs. The zero intensities of the backgrounds in (a) have been offset for clarity. Diffractions are indexed with JCPDS: 87-2416.

Previous studies (see ***Chapters VI-VII***) have showed that layered materials (*e.g.* graphite and hexagonal boron nitride (hBN)) can be effectively and efficiently degraded to monolayered QDs using an intercalation and quick deintercalation approach with the assistance of ultrasonication. The layered structure of MoS_2 (with fundamental two-dimensional S-Mo-S building blocks weakly bonded to each other by van der Waals

forces)[18] allows the preparation of monolayered MoS_2 QDs in a similar manner. During preparation, the intercalation of MoS_2 leads to the expansion of the interlayer space, readily allowing the exfoliation and disintegration of the S-Mo-S sheets to proceed when the K-MoS_2 was exposed to air and reacted with EtOH/H_2O under ultrasonication. Although the starting (grey) and final (dark) K-MoS_2 are not obviously different in colour, XRD and SEM investigations of the starting and residual MoS_2 sediment suggested that current reaction conditions are capable to intercalate K into MoS_2 interlayers, which allowed the following effective exfoliation and disintegration of MoS_2 (***Scheme 9-1***). The MoS_2 raw materials (flakes) were of high crystallinity, indicated by the intense XRD peaks (***Figure 9-1a***). However, XRD of MoS_2 sediment was much weaker (***Figure 9-1a***). For example, the (002) diffraction of MoS_2 raw materials has an intensity of 3400 cps, suggesting ordered layered structure. By contrast, this intensity of residual MoS_2 sediment was ~100 cps using identical scan parameters. This is only possible if the layered structure of the MoS_2 flakes was destroyed (exfoliated and disintegrated) during the preparation procedure. The exfoliation and disintegration are further proved by SEM observations. As shown in ***Figures 9-2a&b***, the MoS_2 raw materials have clear flake shape and evident edges. In contrast, the residual MoS_2 sediment particles are smaller in size and have more indistinct edges (***Figures 9-2c&d***).

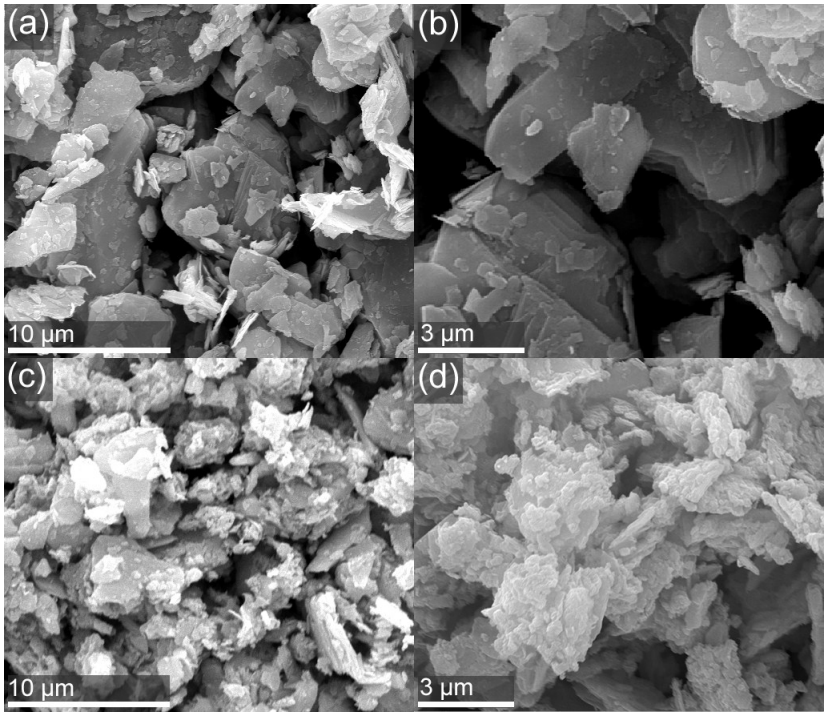

Figure 9-2. SEM images of (a,b) MoS_2 raw material and (c, d) residual MoS_2 sediment.

9.3.2 Characterisation of Prepared MoS_2 QDs

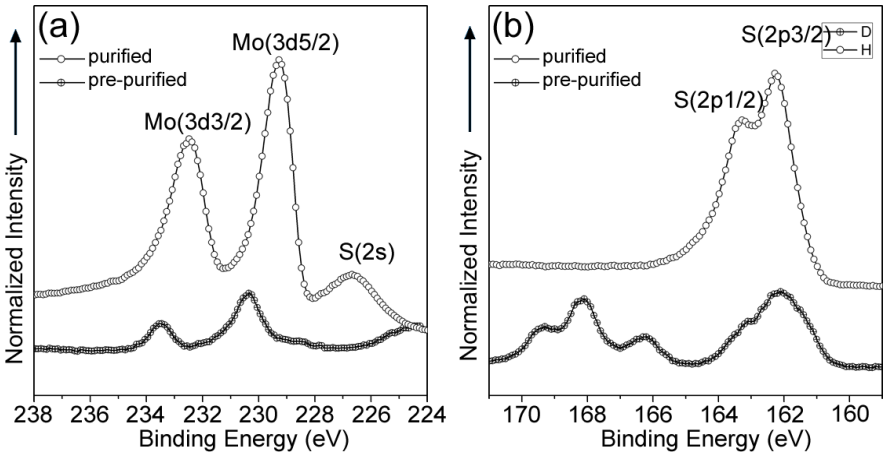

***Figure 9-3*.** (a) Mo(3d) and (b) S(2p) XPS of purified and pre-purified products. The baseline intensities of all traces have been offset for clarity.

After preparation, a transparent yellow suspension can be collected by using simple centrifugation and filtering (***Figure S9-1***). XPS confirmed the existence of Mo and S elements (together with K, C, O) in this dried suspension (***Figure S9-2***), though their intensities were highly suppressed by the K and C impurities (from K metal and EtOH). Dialysis resulted in the removal of the impurities (K and C) and clear XPS binding energy peaks of Mo and S from the dialyzed sample (K, O and C peaks are very weak (***Figure S9-2***). Based on XPS of the purified product (***Figure S9-2***), the mole ratio of S/Mo was calculated to be ~2.0, corresponding well with the stoichiometry of MoS_2. The Mo(3d) and S(2p) peaks XPS of the dried suspension (pre-purification) and purified product are clearly very different from each other (***Figure 9-3***). The Mo($3d_{3/2}$) and Mo($3d_{5/2}$) XPS peaks of the pre-purified product (containing K^+) are not well separated from each other and shifted to higher binding energies (~0.5 eV) than is expected, which might be due to K^+ and OH^- ions interacting with the MoS_2 surface, and the existence of S (K_2S), K and C impurities. However, the Mo(3d) XPS peak from the purified product shows the split peaks at 229.3 and 232.5 eV, corresponding well with the reported Mo^{4+}($3d_{5/2}$) and Mo^{4+}($3d_{3/2}$) components of 2H-MoS_2, respectively (***Figure 9-3a***).[11,19] No prominent Mo^{6+}($3d_{5/2}$) peak was found from either MoS_2 samples (before and after purification) at around 236 eV, suggesting oxidation of Mo is minimal.[11,19] The lower binding energy peak, of purified MoS_2 at around 226.7 eV, can be attributed to the S(2s) of MoS_2.[11,19] ***Figure 9-3b*** shows the S(2p) region of XPS spectra of pre-purified and purified MoS_2 products. The pre-purified product gives two peaks at around 166.3 and 167-170 eV (probably due to the existence of other S sources such as K_2S), along with the detected broad S(2p) of 2H-MoS_2 at around 161-164 eV.[11,19] Nevertheless, once the impurities were removed, the XPS spectra only

contained the peaks at 162.3 and 163.3 eV in this region, corresponding well with $S(2p_{3/2})$ and $S(2p_{1/2})$ of 2H-MoS_2. In addition, the absence of an observable peak between 168 and 170 eV indicates that the S atoms in purified product also remained unoxidized.[11,19] The purity of the dialyzed sample allowed the yield to be calculated as > 31 wt% of the exfoliated/disintegrated product.

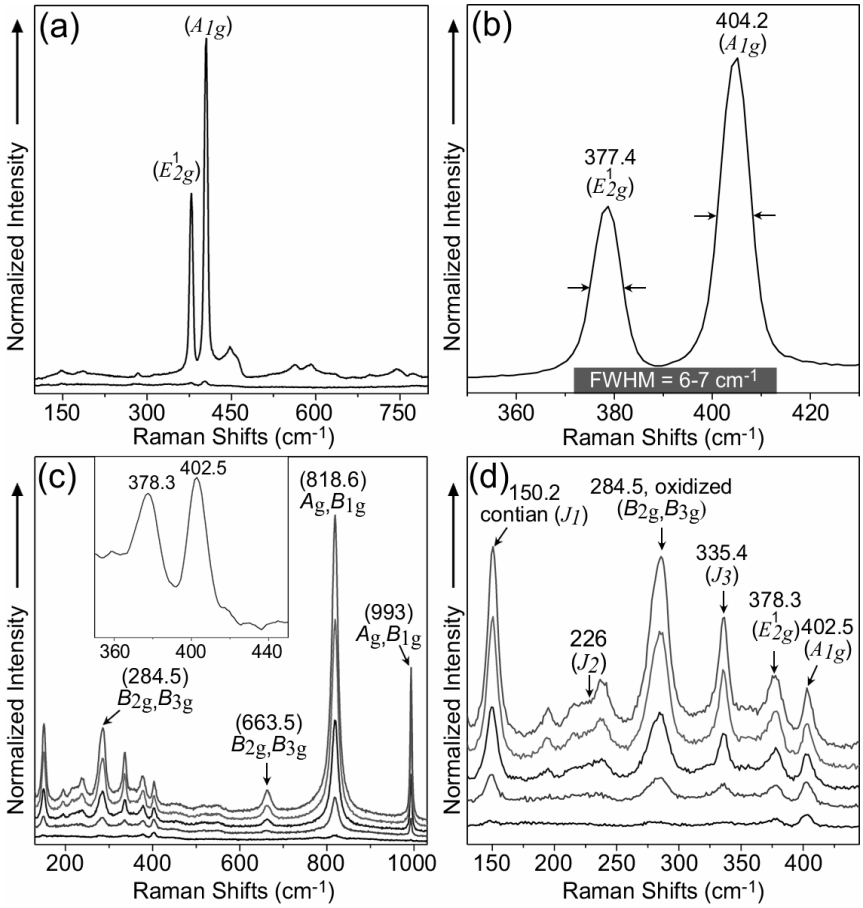

Figure 9-4. Raman analysis of: (a) MoS_2 raw materials (upper trace) and purified MoS_2 product (lower trace) using identical measurement conditions; (b) MoS_2 raw materials (zoomed view); (c) and (d) purified MoS_2 product (zoomed views) with successively higher intensities obtained using different periods of accumulation measurement. The baseline intensities of some traces were shifted for clarity.

Raman investigations (***Figure 9-4***) further confirmed the 2H-MoS_2 structure of the purified MoS_2 product. The E_{2g} and A_{1g} modes that are characteristic of 2H-MoS_2 structure were detected from bulk MoS_2 flakes at 377.4 and 404.2 cm^{-1}, respectively (***Figures 9-4a-b***). These modes were much weaker from the MoS_2 product (***Figure 9-4a***) and detected at 378.3 and 402.5 cm^{-1}, respectively (***Figure 9-4c***). These are slightly shifted (higher energy for E_{2g} and lower energy for A_{1g}) from that of bulk MoS_2 flakes, suggesting a thinner structure to the as-prepared MoS_2 product.[20] The FWHM values of

these peaks from the MoS_2 product (11-12 cm^{-1}, ***Figure 9-4c*** inset) are also greater than that from bulk MoS_2 flakes (6-7 cm^{-1}, ***Figure 9-4b***), which is considered to be a result of phonon confinement, and suggests small lateral sizes of the created MoS_2 product.[21] Increasing the Raman signal intensity to resolve fine structure of Raman resonance usually requires the excitation beam power or irradiation time to be increased. However, observation of Raman peaks at 284.5, 663.5, 818.6 and 993 cm^{-1} suggests that the prepared MoS_2 structures oxidized while under Raman measurement. These peaks arise from: a doublet composed of wagging modes of terminal oxygen atoms (B_{2g}, B_{3g}); asymmetric stretching of the Mo-O-Mo bridge along the *c* axis (B_{2g}, B_{3g}); symmetric stretch of the terminal oxygen atoms (A_g, B_{1g}); and asymmetric stretch of the terminal oxygen atoms (A_g, B_{1g}), respectively.[22] The peaks also assumed greater prominence relative to the E_{2g} and A_{1g} modes of 2H-MoS_2 with increased irradiation time (***Figures 9-4 c&d***), indicating a gradual oxidization of MoS_2 while under beam irradiation. This interpretation is also supported by XPS spectra having showed no oxidized Mo phase in the purified MoS_2 product. Further analysis of the Raman spectra suggested that the MoS_2 product were most likely to be as thin as single layer. As seen from the local enlarged Raman spectra of the MoS_2 product (***Figure 9-4d***), in addition to the detected E_{2g} and A_{1g} modes of 2H-MoS_2, three other peaks at 150.2 (J_1), 226 (J_2) and 335.4 cm^{-1} (J_3) appeared, which were absent in the case of bulk MoS_2 flakes and other reported monolayered MoS_2 sheets.[11,12] Appearance of these peaks most likely resulted from the formation of a superlattice in the basal planes of single layers of MoS_2 (note that the peak at 150 cm^{-1} might also contain a (A_g, B_{1g}) band originating from the translation of the rigid chains of MoO_3,[22] generated during the beam irradiation).[23] This thin structure can also be learned from XRD analysis as the diffraction pattern only gives very weak and broad diffraction peak at around 14.5° (the lower trace in ***Figure 9-1a***, and ***Figure 9-1b***).

AFM and TEM analysis were performed on the purified MoS_2 product to investigate further their possible thin and small structure. The AFM images (***Figures 9-5a-b***) show the samples to be composed of small dots with average sizes of 8-20 nm, which is similar with that of TEM observations (***Figures 9-5c***, also show small size of the product). AFM line analysis of some dots (***Figure 9-5b***) gives thicknesses of around 0.9 nm, corresponding well with that of monolayered MoS_2.[11] The majority of MoS_2 dots under AFM observations had a similar thickness, as indicated by their similar image contrast. ***Figure 9-5d*** shows some stacked QDs with clear ordering lying on the edge of a film and suggesting that these QDs are crystallized. This is confirmed by high

resolution TEM (HRTEM) analysis (***Figure 9-6***), which shows these monolayered MoS_2 dots have high crystallinity. HRTEM analysis (***Figure 9-6***) also indicates a (100) spacing of 0.27 nm (***Figure 9-6a***) and (104) spacing of ~0.2 nm (***Figure 9-6b***) (JCPDS: 87-2416), clear terminated edges (*e.g.* ***Figure 9-6b***, and ***Figure 9-6d*** which shows zigzag edges determined by the FFT pattern), the bond length of Mo-S (~0.24 nm of 2H-MoS_2;[24] ***Figure 9-6c***), and hexagonal crystal structures (***Figure 9-6c*** and ***Figure 9-6d*** inset).

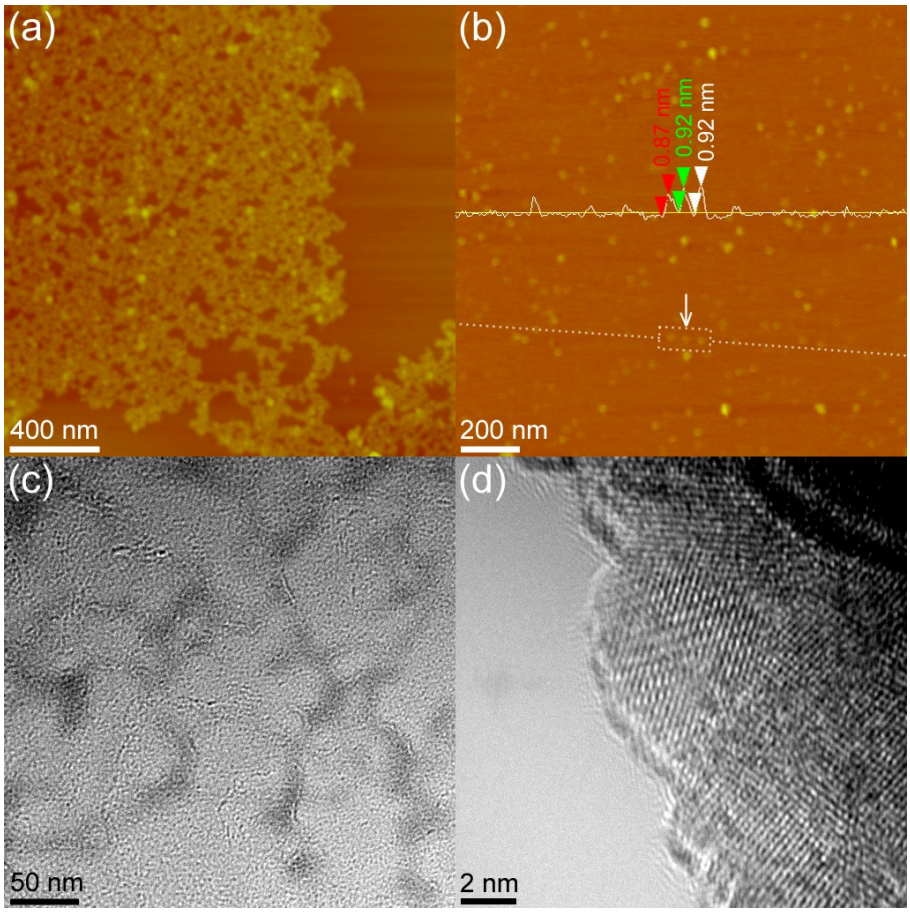

Figure 9-5. (a, b) Atomic force (c, d) and transmission electron micrographs of purified MoS_2 quantum dots.

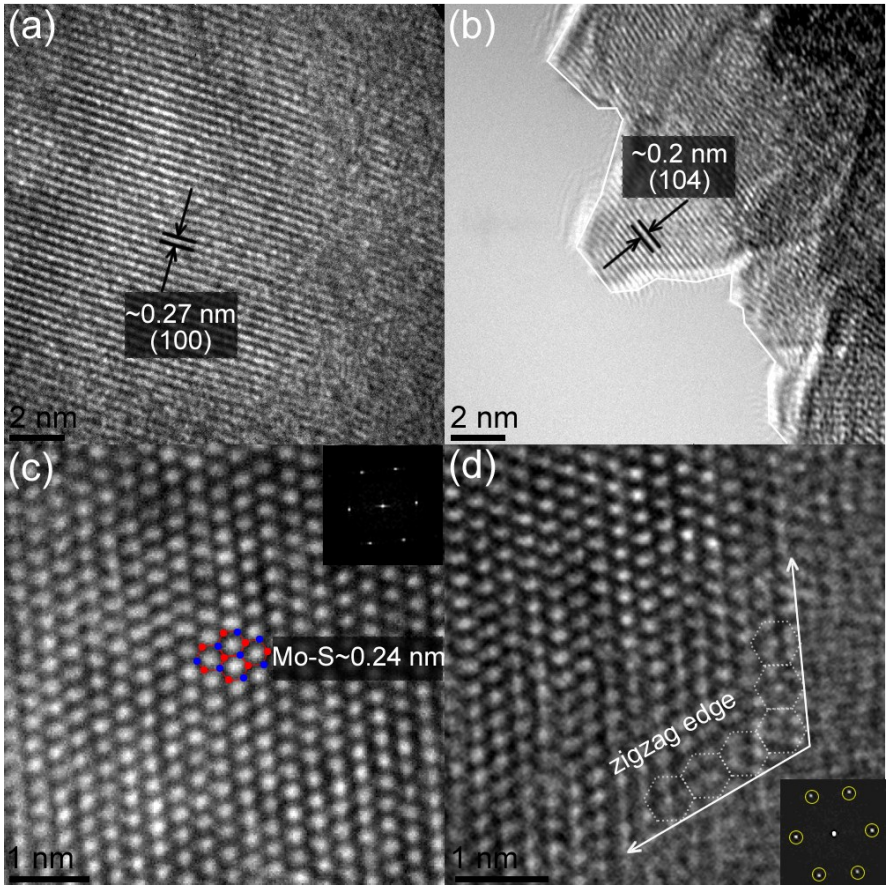

Figure 9-6. HRTEM images and diffraction patterns of various MoS_2 quantum dots, with determined structural parameters indicated

9.3.3 Optical Properties of Monolayered MoS_2 QDs

On the basis of the above characterisations, it is clear that high yield monolayered MoS_2 QDs with high crystallinity have been exfoliated and disintegrated from bulk MoS_2 flakes. Like monolayered sheets (direct semiconductor) which is different with bulk flakes (indirect semiconductor),[6,10,11] the formation of monolayered MoS_2 QDs may also lead to a similar change of band structure and interesting optical properties. The optical properties of the prepared monolayered MoS_2 QDs are further investigated ***Figure 9-7a*** shows the UV/Vis absorption spectra of the MoS_2 QDs prior to purification (contains K^+) and purified using either ion exchange or dialysis. The UV/Vis spectrum of pre-purified MoS_2 QDs (contains K^+) gives an intense absorption peak at around 230 nm, which evidently weaken upon the purification using either resin exchange and dialysis and therefore can be attributed to the absorption from S^{2-} (*e.g.* K_2S produced in the preparation).[26] Although the K^+ in the MoS_2 QDs suspension can be effectively removed using ion exchange resin, it is found that this purification normally led to the instability of MoS_2 QDs. In the UV/Vis spectrum of fresh ion exchanged MoS_2 QDs

(***Figure 9-6a***), the band structure is unclear as it only shows one broad absorption bands around 220-500 nm. This can be understood as being due to the reaction between MoS_2 QDs and local strong acid centres of cation exchange resin, leading to the destroy of structure (MoS_2 QDs also changed to black without any luminescence). However, by contrast, dialyzed MoS_2 QDs are stable as no UV/Vis absorption changes with months (> 6 months) settling, which gives absorption bands at the regions of 420-530 (peak 1) and 354-420 nm (peak 2) (see inset of ***Figure 9-7a***). These absorptions are more evident to be around 470 nm (2.64 eV) and 390 (3.18 eV) once the dialyzed MoS_2 QDs are concentrated further ***(Figure 9-7b***). All these absorption peaks discovered on the dialyzed MoS_2 QDs are at noticeably shorter wavelengths than is the case with monolayered MoS_2 sheets (*e.g.* the excitation A blue shifted with an energy of ~0.79 eV). In monolayered MoS_2 sheets, three absorption peaks (from long to short wavelengths) were found and attributed to excitonic absorption peaks A (670 nm/1.85 eV), B (627 nm/1.98 eV) and C (D) (around 420 nm/2.95 eV).[10-12] Therefore, the absorption peaks (470 nm, 390 nm) can be correlated with the excitonic absorption peaks A, B (at K point of) of the Brillouin zone, which will be further confirmed by our photoluminescence (PL) and PL excitation (PLE) analysis. This assignment is close to that found on MoS_2 nanoclusters with small sizes (~ 4 nm diameter).[27] In the UV/Vis spectra, there is another two weak absorptions at around 290-320 nm (***Figure 9-7b***), which can be correlated with new defect levels.

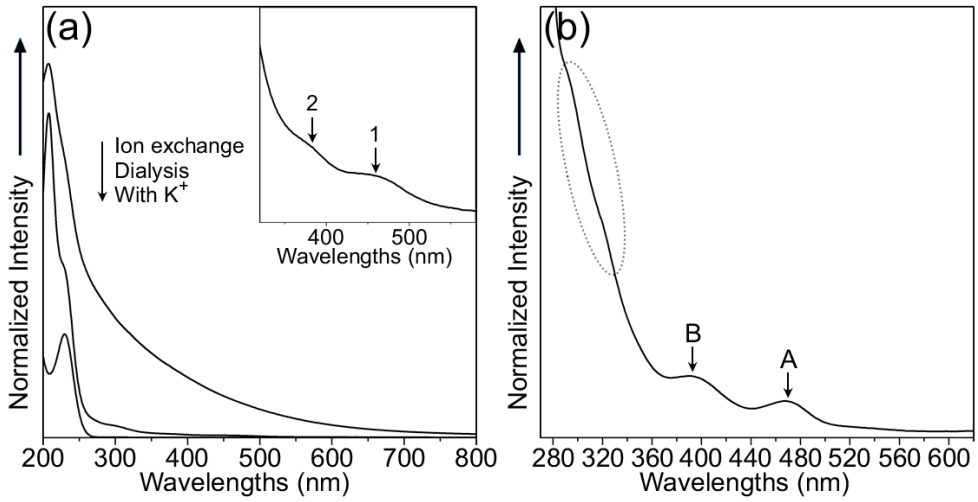

Figure 9-7. (a) UV/Vis spectra of MoS_2 QDs pre-purification and MoS_2 QDS purified using different methods. For clarify, the absorption intensity of the MoS_2 QDs pre-purification was highly reduced. Inset is the local enlarged UV/Vis spectrum of the dialyzed MoS_2 QDs (b) UV/Vis spectra of the concentrated dialyzed MoS_2 QDs.

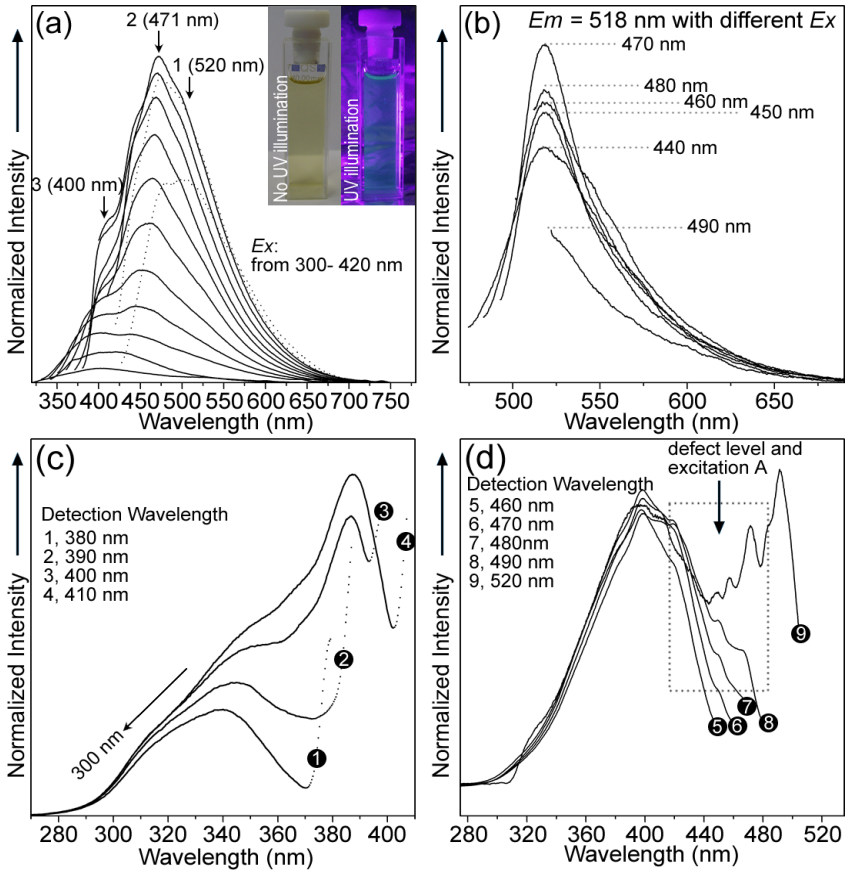

Figure 9-8. (a) PL spectra of dialyzed MoS_2 QDs with excitation wavelength from 300-420 nm (interval of 10 nm). Two dotted lines show the PL spectra with excitation wavelengths of 410 and 420 nm. Inset shows photographs of dialyzed MoS_2 QDs in suspension with and without UV illumination; (b) PL spectra of dialyzed MoS_2 QDs with excitation wavelength from 440-490 nm (interval of 10 nm); (c, d) PLE spectra with different detection wavelengths, as indicated.

The large blue shift of the excitation peaks observed above suggests that the monolayered MoS_2 QDs might show different photoemission behaviour to the monolayered sheets. The strong luminescent nature of MoS_2 QDs is indicated by dialyzed species showing blue-green emission at room temperature that can be observed by eye under UV (365 nm) illumination (***Figure 9-8a*** inset). Spectral measurements of PL shows the strongest emission of the MoS_2 QDs occurs at ~471 nm (~2.63 eV, emission peak 2 in ***Figure 9-8a***) with an excitation wavelength of 400 nm (~3.1 eV). By using Rhodamine B as a fluorescent standard, the luminescent quantum yield was determined as ~7.9% (see ***Table 9-1*** in ***Section 9.2.2***), which is much greater than that of bulk MoS_2 (only negligible luminescence due to its indirect band gap). This luminescence is also greater than that found on monolayered WS_2 QDs (quantum yield of ~4%)[28] and monolayered MoS_2 sheets (remains low at about 0.4% despite their direct band gap nature, the reasons for which remain unclear).[6] The high PL quantum

yield observed here may yet serve to open the way for the use of monolayered MoS_2 QDs in optical applications (*e.g.* optoelectronic and bio-imaging applications).

As previously discovered, MoS_2 changes from an indirect to a direct semiconductor upon assuming monolayer thickness.[6] This change is most likely chiefly responsible for the strong luminescence observed from the monolayered MoS_2 QDs here. However, the PL emission of the monolayered MoS_2 QDs with emission around 471 nm (2.63 eV) is blue shifted and broader compared with monolayered sheets (main emission at around 1.9 eV) due to quantum confinement effects and size distributions. In the PL spectra, two small emission shoulder peaks (one below 400 nm wavelength, one above 500 nm) are also observed. By using excitation wavelengths from 450-490 nm, the long wavelength emission peak was identified at around 518 nm with excitation wavelength of 470 nm (***Figure 9-8b***), which is consistent with the excitation absorption peak A centred at around 470 nm (***Figure 9-7a***). The maximum intensity of the 518 nm peak (***Figure 9-8b***) is only a quarter that of the main emission at around 471 nm (emission peak 2 in ***Figure 9-8a***). Further PLE analysis suggests that the emissions 1 and 2 are mainly the result of A and B excitations (***Figure 9-7b***), respectively (defect levels also contribute to the emission, which will be clarified later). With detection wavelengths of 380 and 390 nm, only the PLE peak at around 340 nm was found (***Figure 9-8c***). The PLE peaks at higher wavelengths (excitation absorption peak B) are possibly too close to the detection wavelength. Nevertheless, a PLE peak (excitation absorption peak B) was found at around 380-390 nm excitation wavelengths with detection wavelengths of 400 and 410 nm, suggesting that the shoulder emission peak 3 in ***Figure 9-8a*** originates from both excitation absorption B (see ***Figure 9-7b***) and a defect level over 300 nm (< 4.1 eV). Further PLE analysis, with detection wavelengths of 460-490 nm, suggested that the main emission 2 in ***Figure 9-8a*** is mainly related with excitation absorption B (see ***Figure 9-7b***) and new absorptions at around 440-480 nm. Precise assignment of these new absorptions is difficult, although they possibly originate from excitation peak A and defects (defects were also observed on MoS_2 nanoclusters[27]). Due to the contribution to the maximum emission 2 (~471 nm in ***Figure 9-8a***) from both excitation peak A and defect levels, it is reasonable to find that the emission 2 reached a maximum with an excitation wavelength of 400 nm rather than the 390 nm of the excitation absorption peak B (see ***Figure 9-7b***).

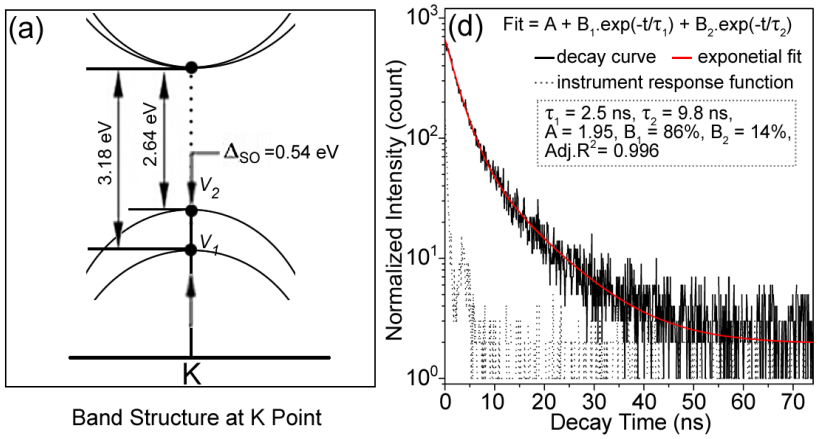

Figure 9-9. (a) Band structure diagram of the monolayered MoS_2 QDs at K point; (b) TRPL decay profile of MoS_2 QDs recorded at room temperature while monitoring the emission at 471 nm upon 400 nm excitation wavelength.

To check the origin of emission 1 (the small shoulder emission), the PLE spectra with a detection wavelength of 520 nm is further analyzed (***Figure 9-8a***). Besides peaks at around 490 nm and 440-460 nm (which might be from defects), PLE peaks at around 470 nm and 390 nm were observed, which correspond well with excitation absorptions A and B, respectively. However, it is interesting to find that the excitation peak B at around 390 nm also contributed to emission peak 1 (~520 nm, this peak was initially found to be contributed by the excitation peak A at ~470 nm, see ***Figure 9-8b***). To understand this feature, the band structure diagram at K point of monolayered MoS_2 QDs is provided in ***Figure 9-9a***. Due to the broken inversion symmetry in MoS_2 monolayers, the strong spin-orbit coupling (SOC) from the d-orbitals of Mo results in a valance band spin splitting, which is largest at the K point of the Brillouin zone (split with an energy gap of ~0.13 eV in monolayered MoS_2 sheets[10-12]). The strength of the SOC can be indicated by the energy difference (Δ_{SO}) between excitonic absorption peaks A and B in the UV/Vis spectra (***Figure 9-7b***, also shown as the gap between V_1 and V_2 points in ***Figure 9-9a***). In the monolayered MoS_2 QDs, due to the split valance band, the transitions between either the V_1 or V_2 points and the conduction band (spectrum 9 in ***Figure 9-8d***) are shown. Excitation from the V_1 point (390 nm, 3.18 eV) leads to emissions both at 520 nm (spectrum 9 in ***Figure 9-8d***, transition from conduction band minimum to V_2 point) and 471 nm (***Figure 9-8a***, main emission peak 2). Excitation from the V_2 point (470 nm, 2.64 eV) leads only to emission at around 520 nm (***Figure 9-8b***, transition from conduction band minimum to V_2 point). These features correspond well with the band structure and the SOC feature of monolayered MoS_2 QDs. On this basis, the energy gap between the split energy levels at the K point (V_1 and V_2) can be calculated as 540 meV (***Figure 9-9a***), which is much larger than that of monolayered

MoS_2 sheets (130 meV).[10-12] It is worth postulating that this large SOC of MoS_2 monolayers might be tunable by lateral size control, although this needs to be tested in future experiments. Based on the above analysis, it can also conclude that the main emission (emission 2 at around 471 nm, ***Figure 9-8a***) was mainly caused by the excitation transition from the V_1 point of the monolayered MoS_2 QDs. Nevertheless, new defect levels (see ***Figures 9-8c&d***) also contributed to the emission. To specify these contributions, time resolved PL (TRPL, ***Figure 9-9b***, time-correlated single photon counting technique) was performed on the MoS_2 QDs by monitoring the emission at 471 nm after 400 nm wavelength excitation. The lifetime of the luminescence can be fitted well with a bi-exponential function (the result from tri-exponential function is nearly the same), giving lifetimes of 2.5 ns (86% component of the full emission) and 9.8 ns (14% component of full emission). This suggests that excitation from the V_1 point contributed nearly 90% of the main emission centred at around 471 nm.

9.3.4 Bio-Imaging with Monolayered WS_2 QDs

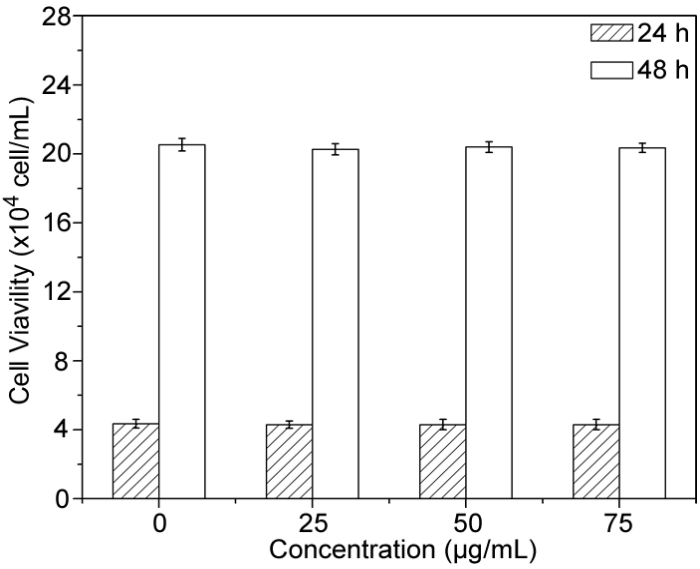

Figure 9-10. Cell viability assay with MDCKII cells treated with different concentrations of MoS_2 QDs. The bars represent cell counts and the error bars represent standard errors of the mean.

The discovery of strong luminescence and the observed nanosecond lifetime of the emission broadens the potential applications of MoS_2 and, in particular, suggests MoS_2 QDs may be interesting candidates for optical applications. For use in biological techniques (*e.g.* bioimaging, isolation of biomolecules, protein analysis, and cell tracking), cell labels should have minimal toxicity. The cytotoxicity of purified MoS_2 QDs is evaluated using the mammalian cell line MDCKII (madin-darby canine kidney type II). As shown in ***Figure 9-10***, low doses of MoS_2 QDs (0-75 μg/mL) were non-toxic to these

cells and no obvious effect on cell number was observed at these dosages (0-75 μg/mL) with prolonged exposure times (24-48 h).

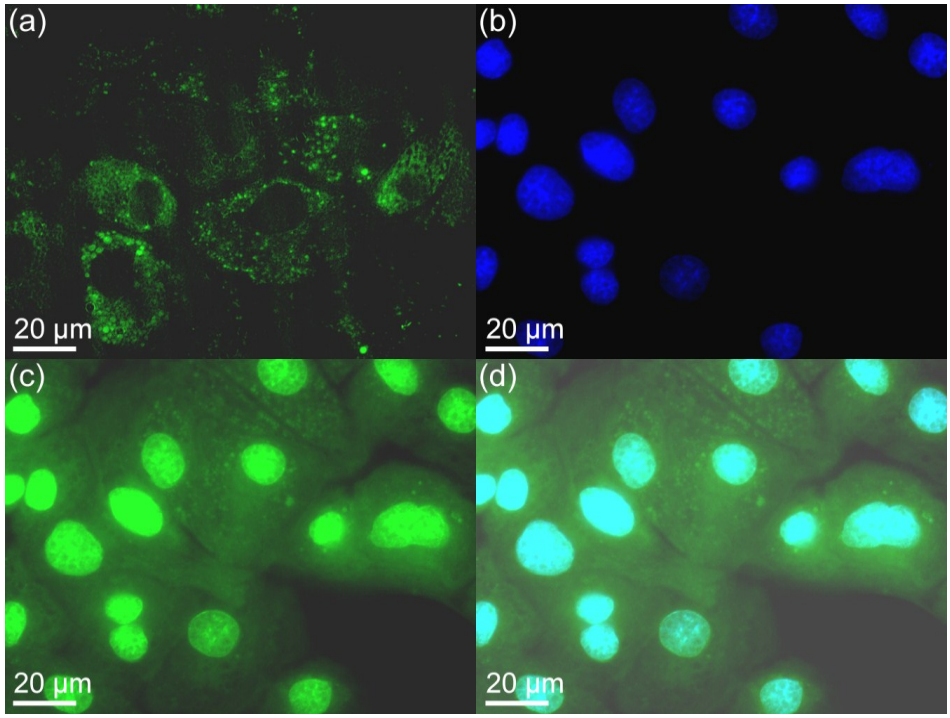

Figure 9-11. (a) Agglomerated MoS_2 QDs surrounding each nucleus (cells are stained by MoS_2 QDs only); (b) Individual nucleus stained blue with DAPI; (c) MoS_2 QDs with green luminescence surrounding the nuclei; (d) The overlay image of cells stained with DAPI and MoS_2 QDs.

To illustrate the potential in bio-imaging application, imaging of the MDCKII cells was performed in fluorescein isothyocyanate (FITC) mode using the purified monolayered MoS_2 QDs as fluorescent tags. As suggested by ***Figure 9-11a*** (the MDCKII cell stained with MoS_2 QDs alone), the MoS_2 QDs were taken up by the cells but did not penetrate the cell nuclei. ***Figures 9-11b-c*** give the images of MDCKII nucleus stained with DAPI (diamidino-2-phenylindole, emission from around 400-650 nm) and MoS_2 QDs (emission from ~350-650 nm). By selecting appropriate fluorescence filters, cell nuclei can be shown as blue (***Figure 9-11b***) or green (***Figure 9-11c***). In ***Figure 9-11c***, the cytoplasm was only stained by MoS_2 QDs and appears green. Although the nuclei in ***Figure 9-11c*** also give green emission from DAPI, the boundary between cells, nuclei and cytoplasm are clear. This is more evidently seen in the overlay image of ***Figure 9-11b*** and ***Figure 9-11c*** (***Figure 9-11d***) and suggests that MoS_2 QDs can be used in high contrast bio-imaging and will be well-suited for other biomedical applications.

9.4 Conclusion

In conclusion, stable monolayered MoS_2 QDs have been successfully created from bulk MoS_2 flakes with high yield (31 wt%). The majority of the QDs are monolayered with a lateral size around 8-20 nm. Like the monolayered MoS_2 sheets, the monolayered MoS_2 QDs also exhibit direct semiconductor nature, unlike bulk multilayered MoS_2 (indirect semiconductor), and strong luminescence at room temperature. However, the monolayered MoS_2 QDs have blue shifted excitation absorption and emission peaks compared with monolayered sheets. The main emission of the monolayered MoS_2 QDs was found in the green-blue spectral region, centred at 471 nm with a quantum yield of ~ 7.9%, which is much improved from that of monolayered sheets (~ 0.4%). This emission was mainly (~ 90%) contributed by the excitation from the V_1 point to the conduction band. A large spin-orbit coupling split of 540 meV was found in monolayered MoS_2 QDs (compared with 130 meV in monolayered sheets). In future it may be possible to tune this split with the lateral size of the monolayered QDs, making them potentially valuable for applications such as semiconductor based spintronics and optoelectronic devices. In this chapter, the use of monolayered MoS_2 QDs as a non-toxic fluorescent label for biological cell imaging is also demonstrated.

9.5 Supporting Information

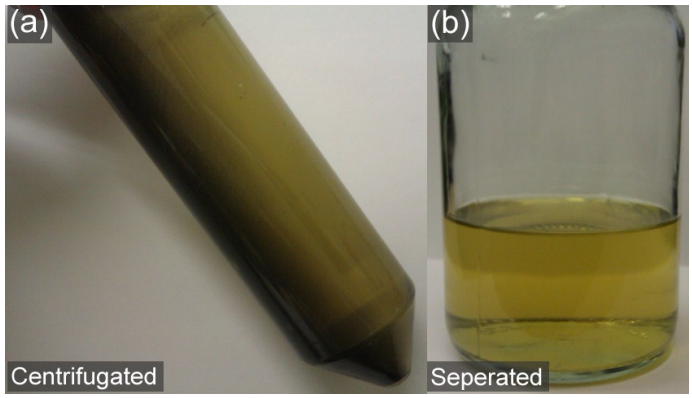

Figure S9-1. Photographs of the product after sonication treatment: centrifuged suspension (a) and separated MoS_2 suspension (b).

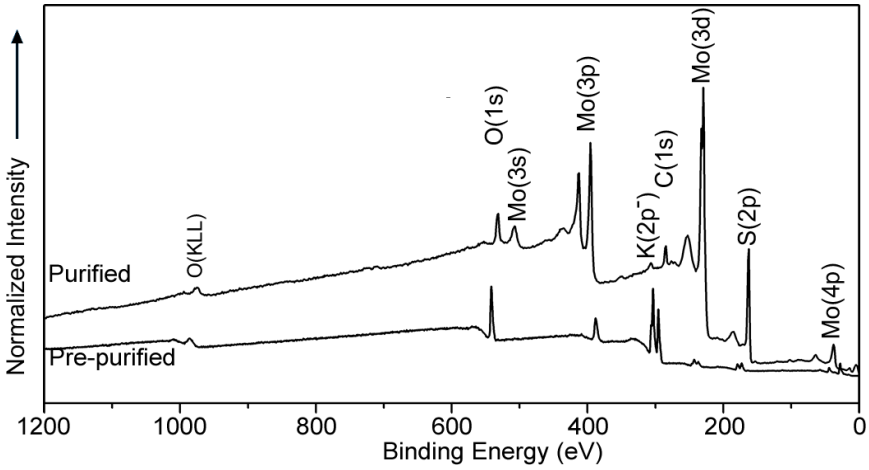

Figure S9-2. XPS of the purified and pre-purified products.

References and Notes

[1] L. E. Brus, Quantum Crystallites and Nonlinear Optics, *Appl. Phys. A* **1991**, *53*, 465-474.

[2] A. L. Efros, M. Rosen, The Electronic Structure of Semiconductor Nanocrystals. *Annu. Rev. Mater. Sci.* **2000**, *30,* 475-521.

[3] L. Manna, D. J. Milliron, A. Meisel, E. C. Scher and A. P. Alivisatos, Controlled Growth of Tetrapod-Branched Inorganic Nanocrystals. *Nature Mater.* **2003**, *2*, 382-385.

[4] Y. Yin, and A. P. Alivisatos, Colloidal Nanocrystal Synthesis and the Organic–Inorganic Interface. *Nature* **2005**, *437*, 664-670.

[5] J. Peng, W. Gao, B. K. Gupta, Z. Liu, R. Romero-Aburto, L. Ge, L. Song, L. B. Alemany, X. Zhan, G. Gao, S. A. Vithayathil, B. A. Kaipparettu, A. A. Marti, T. Hayashi, J. Zhu and P. M. Ajayan, Graphene Quantum Dots Derived from Carbon Fibers. *Nano Lett.* **2012**, *12*, 844-849.

[6] K. F. Mak, C. Lee, J. Hone, J. Shan and T. F. Heinz, Atomically Thin MoS_2: A New Direct-Gap Semiconductor. *Phys. Rev. Lett.* **2010**, *105*, 136805.

[7] J. V. Laurutsen, M. Nyberg, J. K. NØrskov, B. S. Clausen, H. TopsØc, E. Lægsgaard and F. Besenbacher, Hydrodesulfurization Reaction Pathways on MoS_2 Nanoclusters Revealed by Scanning Tunneling Microscopy. *J. Catal.* **2004**, *224*, 94-106.

[8] H. Vrubel, D. Merki and X. Hu, Hydrogen Evolution Catalyzed by MoS_3 and MoS_2 Particles. *Energy Environ. Sci.* **2012**, *5*, 6136-6144.

[9] A. R. Botello-Méndez, F. López-Urías, M. Terrones and H. Terrones, Metallic and Ferromagnetic Edges in Molybdenum Disulfide Nanoribbons. *Nanotechnology* **2009**, *20*, 325703.

[10] A. Splendiani, L. Sun, Y. Zhang, T. Li, J. Kim, C.-Y. Chim, G. Galli and F. Wang, Emerging Photoluminescence in Monolayer MoS_2. *Nano Lett.* **2010**, *10*, 1271-1275.

[11] G. Eda, H. Yamaguchi, D. Voiry, T. Fujita, M. Chen, M. Chhowalla, Photoluminescence from Chemically Exfoliated MoS_2. *Nano Lett.* **2011**, *11*, 5111-5116.

[12] J. N. Coleman, M. Lotya1, A. O'Neill1, S. D. Bergin, P. J. King, U. Khan, K. Young, A. Gaucher, S. De, R. J. Smith, I. V. Shvets, S. K. Arora, G. Stanton, H.-Y. Kim, K. Lee, G. T. Kim, G. S. Duesberg, T. Hallam, J. J. Boland, J. Wang, J. F. Donegan, J. C. Grunlan, G. Moriarty, A. Shmeliov, R. J. Nicholls, J. M. Perkins, E. M. Grieveson, K, Theuwissen, D. W. McComb, P. D. Nellist and V. Nicolosi, Two-Dimensional Nanosheets Produced by Liquid Exfoliation of Layered Materials. *Science* **2011**, *331*, 568-571.

[13] V. Štengl and J. Henych, Strongly Luminescent Monolayered MoS_2 Prepared by Effective Ultrasound Exfoliation. *Nanoscale* **2013**, *5*, 3387-3394.

[14] D. Pan, J. Zhang, Z. Li and M. Wu, Hydrothermal Route for Cutting Graphene Sheets into Blue-luminescent Graphene Guantum Dots. *Adv. Mater.* **2010**, *22*, 734-738.

[15] C. A. Parker and W. T. Rees, Correction of Fluorescence Spectra and Measurement of Fluorescence Quantum Efficiency. *Analyst* **1960**, *85*, 587-600.

[16] J. N. Demas and G. A. Crosby, Measurement of Photoluminescence Quantum Yields. Review. *J. Phys. Chem.* **1971**, *75*, 991-1024.

[17] A. N. Fletcher, Quinine Sulfate as a Fulorescence Quantum Yield Standard. *Photochem. Photobio.* **1969**, *9*, 439-444.

[18] A. F. Wells, *Structural Inorganic Chemistry* (3rd Ed.). **1984**, Oxford: Clarendon Press.

[19] C. A. Papageorgopoulos and W. Jaegermann, Li Intercalation Across and Along the Van der Waals Surfaces of MoS_2 (0001). *Surf. Sci.* **1995**, *338*, 83-93.

[20] A. Molina-Sánchez and L. Wirtz, Phonos in Single-Layer and Few-Layer MoS_2 and WS_2. *Phys. Rev. B* **2011**, *84*, 155413.

[21] G. L. Frey, R. Tenne, M. J. Matthews, M. S. Dresselhaus and G. Dresselhaus, Raman and Resonance Raman Investigation of MoS_2 Nanoparticles. *Phys. Rev. B* **1999**, *60*, 2883-2892.

[22] B. C. Windom, W. G. Sawyer and D. W. Hahn, A Raman Spectroscopic Study of MoS_2 and MoO_3: Applications to Tribological Systems *Tribol. Lett.* **2011**, *42*, 301-310.

[23] D. Yang, S. J. Sandoval, W. M. R. Divigalpitiya, J. C. Irwin and R. F. Frindt, Structure of Single-Molecular-Layer MoS_2. *Phys. Rev. B* **1991**, *43*, 12053-12056.

[24] H. S. S. Ramakrishna Matte, A. Gomathi, A. K. Manna, D. J. Late, R. Datta, S. K. Pati and C. N. R. Rao, MoS_2 and WS_2 Analogues of Graphene. *Angew. Chem. Int. Ed.* **2010**, *49*, 4059-4062.

[26] H. G. Karge and J. Raskó, Hydrogen Sulfide Adsorption on Faujasite-Type Zeolites With Systematically Varied Si-Al Ratios. *J. Colloid Interface Sci.* **1978**, *64*, 522-532.

[27] J. P. Wilcoxon, P. P. Newcomer and G. A. Samara, Synthesis and Optical Properties of MoS_2 and Isomorphous Nanoclusters in the Quantum Confinement Regime. *J. Appl. Phys.* **1997**, *81*, 7934-7944.

[28] L. Lin, Y. Xu, S. Zhang, I. M. Ross, A. C. M. Ong and D. A. Allwood, Fabrication of Luminescent Monolayered Tungsten Dichalcogenides Quantum Dots with Giant Spin-Valley Coupling. *ACS Nano **2013**, 7,* 8214-8223.

Chapter X. Conclusions and Future Work

10.1 Conclusions

The conclusions of the thesis are summarized below:

1) An effective solvothermal deoxidation technique has been developed to prepare chemically reduced graphene oxide (rGO), using solid S as a reducing agent and NMP or DMF as a surfactant. The rGO product showed high electronic conductivity (15200~16700 S/m) and comparable dispersibility to that of functionalized rGO/graphene. For deep deoxidation of GO, the addition of a surfactant (*e.g.* NMP and DMF) is essential to alleviate π-π stacking and self-assembly between the rGO. On the basis of this addition, reducing effects of H_2S and H_2SO_3 generated from the reaction between S and H_2O, combined with the thermal deoxygenation of GO at 110 ^oC, are believed to be responsible for the full deoxidation of GO.
2) The solvothermal deoxidation of GO proceeds in two stages: 1) partial deoxidation that depends on the solvent polarity and 2) further deoxidation to fully restore sp^2 structure of graphene. The second stage is strongly dependent upon solvent surface energy, which is consistent with controlling (and preventing) the agglomeration of partially reduced GO (p-rGO) agglomeration. GO cannot be fully deoxidized in a hydrothermal reaction simply by adding strong reducing agents (*e.g.* Fe^{2+}, S and hydrazine) since this doesn't overcome the p-rGO sheet amalgamation due to their high surface enthalpy. In the solvothermal deoxidation of GO, the solvent surface energy should be considered a primary factor in maintaining a good dispersal of p-rGO, which can then go on to be fully deoxidized. The ideal solvent surface energy of the solvothermal deoxidation at 100 °C should around 85.6 mJ/m^2 (between 84.7-87.6 mJ/m^2), which can be achieved with heated NMP (<188 °C) and DMF (55-147 °C) solvents alone. Binary solvents such as NMP-H_2O and DMF-H_2O also achieved this by tuning of the solvent ratios. In a solvothermal reaction, the polarity of the solvent remains important as it allows dissolution of the GO and reducing agent. However, it is not as influential as the solvent surface energy on achieving deeply deoxidized GO.
3) High yields (~23 wt% and 10 wt%) of GQDs can be obtained by cutting multi-layered carbon nanotubes (MWCNTs) and graphite flakes (GFs) respectively using an exfoliation and disintegration method (quick de-intercalation of potassium

intercalated graphite materials, which then react with $EtOH/H_2O$ under ultrasonication). The formation of GQDs from MWCNTs is considered to rely on the bond breaking from the defects on the graphene walls, which were created by the combustion and the de-intercalation of the potassium intercalated MWCNTs. The combustion could assist increasing the production yield, but it did not seem to be a necessary step in producing GQDs. The rapid de-intercalation (which also generates defects on the graphene layers) of the intercalated compounds during short exposure is capable enough to disintegrate the layers under ultrasonication treatment. GQDs created from either route showed a similar size of around 20 nm and good water solubility and the majority (>90%) were monolayered. Because of the carbene structures in the zigzag edges, prepared GQDs show interesting luminescence with high quantum yield (7.1% and 6.5% for the GQDs created from GFs and MWCNTs, respectively). The created GQDs can be used as a non-toxic fluorescent label in confocal microscopy of biological cells.

4) Using the intercalation method (quick de-intercalation of the potassium intercalated boron nitride/BN materials, which then react with $EtOH/H_2O$ under ultrasonication), atomically-thin BN QDs were fabricated from hexagonal BN (hBN) flakes with a yield of 2.1 wt%. The majority of the created BN QDs are monolayered with a lateral size around 10 nm. Due to the introduction of oxidized defect centres (*e.g.* BO_2^-, carbene zigzag edge, C replaced N vacancy point) during the fabrication, the BN QDs exhibit blue-green luminescence (centred at 425 nm with quantum yield of 2.5 %). With the decrease in thickness and size, strong quantum confinement was observed. The optical direct band gap of the BN QDs was estimated to be around 6.51 eV. Furthermore, monolayered BN QDs can be used as a non-toxic fluorescent label in confocal microscopy of biological cells.
5) High yield (>36 wt%) monolayered tungsten disulphide (WS_2) QDs (lateral size around 8-15 nm) have been successfully fabricated from bulk WS_2 flakes. The monolayered WS_2 QDs exhibit direct semiconductor nature which is different with bulk multilayered WS_2 (indirect semiconductor) and activated strong luminescence at room temperature. The luminescence of the monolayered WS_2 QDs was found at the region of green-blue light (centred at 461 nm with multiple emission peaks) with a quantum yield of ~4 % which is much improved from that of monolayered sheets (~0.4 %). The strong luminescence and multiple emissions are considered to be the result of the direct excitonic transitions at K point and giant spin-orbit coupling (SOC) respectively. Nevertheless, a new defect level also contributes the emission, which led to the shift of the highest main emission position. Unlike

monolayered WS_2 sheets (with a SOC of 400 meV), the created monolayered WS_2 QDs have stronger SOC (570 meV) and much blue shifted emission, suggesting that the spin-orbit splitting and luminescence of monolayered WS_2 can be effectively manipulated by lateral size control. Furthermore, these fabricated monolayered WS_2 QDs can be used in biological imaging applications.

6) Stable monolayered MoS_2 QDs (lateral size around 8-20 nm) have been exfoliated and disintegrated from bulk MoS_2 flakes with high yield (31 wt%). Like the monolayered MoS_2 sheets, the monolayered MoS_2 QDs also exhibit direct semiconductor nature which is different with bulk multilayered MoS_2 (indirect semiconductor) and activated strong luminescence at room temperature. However, unlike monolayered MoS_2 sheets, the created monolayered MoS_2 QDs have much blue shifted excitation absorptions and emission. The main emission of the monolayered MoS_2 QDs was found at the region of green-blue light, centred at 471 nm with a quantum yield of ~ 7.9 % which is much improved from that of monolayered sheets (~ 0.4 %). This emission was mainly (~ 90%) contributed by the excitation from V_1 point to the conduction band. Besides, a giant SOC (with a split energy gap of 540 meV which is much larger than 130 meV of monolayered sheets) was found on the created MoS_2 QDs, suggesting that the SOC of monolayered MoS_2 can also be effectively manipulated by lateral size control. Additionally, these fabricated monolayered MoS_2 QDs can be well used for cellular imaging.
7) The preparation of monolayered QDs from layered materials were highly dependent on the intercalation reaction which was related to the raw materials. From BN flakes (190-200 ^oC, >10 h) to GFs (190-200 ^oC, >4 h), MWCNTs (190-200 ^oC, >3 h), MoS_2 flakes (180-190 ^oC, >4 h) and WS_2 flakes (170-180 ^oC, >2 h), the react condition for the intercalation was alleviated gradually. Correspondingly, the yield of the products decreased from WS_2 QDs (~36 wt%) to MoS_2 QDs (~31 wt%), GQDs (from MWCNTs, ~23 wt%), GQDs (from GFs, ~10 wt%) and BN QDs (2.1 wt%).
8) The QDs of graphene, BN, WS_2 and MoS_2 are all suitable for cellular imaging. At the low dosages (0-80 μg/mL for GQDs; 0-40 μg/mL for BN QDs; 0-125 μg/mL for WS_2 QDs; 0-75 μg/mL for MoS_2 QDs), all these QDs are non-toxic for bio-imaging with exposure time of 48 h. Experimental results showed that the monolayered MoS_2 QDs are the best label for cellular imaging with the highest quantum yield (~7.9 %, pH~7). The WS_2 and BN QDs have lower quantum yields (~4.0 % and ~2.5 % respectively, pH~7). Although GQDs have high quantum yields (~6.5-7.1 %, pH~8-9), the emission evidently weakened under acid condition (or netural condition, pH~7), which affected the application in bio-imaging. By contrast, the luminescence

of BN QDs was stable under different pH values (emission slightly changed). Further estimations should involve the cytotoxicity evaluation of different QDs with improved concentrations and prolonged exposure time.

10.2 Future Works

Graphene has already found application in the fields of catalysis, biological sensors, supercapacitors, batteries and structural composites.[1-8] Many potential industrial applications require the large scale and cheap preparation of graphene. The solvothermal approach to deoxidizing GO could be a route that meets these industrial requirements. The yields are very high (near 100 % in principle; the preparation can be scaled up to prepare rGO with kilograms), the deoxidation is complete or near-complete and the solution chemistry method should be well suited to scale up. Further development here would required demonstration of larger volumes of reaction and investigation of the use of the graphene product in specific applications. One simple possibility would be the use of the graphene as a stiffener in structural composites. It is as yet unclear how the mechanical properties of the composites will be influenced by the size, thickness and extent of deoxidation of the solvothermal deoxidized GO.

Graphene is also considered as a potentially transformative electronic material. However, the use of chemically reduced GO (rGO) for these applications would require some technical advances. This method of preparation often leads to some of the aromatic features of the graphene product being broken, which reduces its electrical conductivity significantly. It has been found that some carbon source (*e.g.* CH_4 or CO) can be used to repair/grow the graphene using CVD method.[9] Therefore, in principle, the damage of rGO can be repaired by reacting at high temperatures the chemically formed rGO with a carbon source (*e.g.* CH_4 or CO). However, a previous study indicates that severe scrolling, graphitization and agglomeration of the graphene sheets is unavoidable at high temperatures.[10] It may be possible to use the principles established in ***Chapter V*** to overcome these technical problems by tuning the solvent surface energy close to that of rGO in the presence of a carbon source. This can be achieved by adding a molten salt appropriate for the high temperature reaction. For example, molten KCl+NaI (15 mol% NaI) has a surface energy around 80 mJ/m^2 at 800 ^oC[11]. Systematic investigations of this proposal will yield an answer to its effectiveness.

As for the layered transition-metal disulfides (LTMDs; *e.g.* WS_2 and MoS_2 nanoparticles) involved in this thesis, which have already found application as catalysts.[12-15] A recent

study suggests that small MoS_2 molecular units could serve as a good metal-free catalyst for hydrogen generation.[16] The fabrication of monolayered WS_2 and MoS_2 QDs demonstrated in this thesis could be an effective strategy for creating materials for hydrogen generation. The QDs have very high edge-to-volume ratios, giving a high density of catalytically active metal sites. Nevertheless, systematical investigations on the application of these monolayered QDs for water splitting are required.

Research on monolayered BN and transition-metal dichalcogenides (TMDs) is progressing rapidly. The monolayered BN can be a competitor to graphene as thermal conductor. Unlike GQDs, the large direct gap of the monolayered BN QDs (6.51 eV) can be potentially used as deep UV light emitter, although this needs further estimation.[17] As for the LTMDs, it was now well established that thickness reduction of some LTMDs (*e.g.* WS_2, MoS_2) to monolayers causes the emergence of some remarkable optical and transport properties (*e.g.* monolayers changed to be direct semiconductor from indirect multilayer semiconductors) and suggests potential applications for nanodevices (*e.g.* field effect transistors).[18] Furthermore, due to the broken inversion symmetry in the monolayered LTMDs (*e.g.* WS_2, MoS_2, $MoSe_2$, WTe_2), the d-orbits of heavy metal (W/Mo) atoms give strong spin-orbit coupling (SOC).[18,19] This leads to spin splitting of the valance band, showing the largest effect at the K point of the Brillouin zone.[18,19] The SOC makes these monolayers intriguing materials that hold much promise for spintronics.[19] The studies in this thesis show that the layered materials can be exfoliated and disintegrated to monolayered QDs. QDs of hexagonal BN and the disulfides WS_2 and MoS_2 are demonstrated but it should be possible to extend the fabrication method to a wide range of other monolayered systems (*e.g.* $MoSe_2$, WTe_2). New and interesting properties of the QDs are expected which could result in their use in current applications or even the development of new applications.

One possible area of application of these QDs (TMDs) is in semiconductor spintronics devices. These offer advantages over traditional electronics by taking advantage of spin coherence to combine operations that usually require separate components. One approach in semiconductor spintronics is the use of electrical fields to promote spin-orbit interactions in order to create spin polarization. This requires complex device fabrication and high fabrication costs. However, the giant SOC effects seen in many of the direct semiconductor QDs here (see ***Chapters VIII-IX***) may offer an alternative cheap solution. The SOC leads to the formation of spin-dependent 'valleys' in the energy-momentum curves that describe the available electron wave functions within a

material. The energy states associated with these valleys form the basis for manipulation of spin and valley degrees of freedom, and can effectively be described by a new quantum number.[19] The SOC is stronger in QD systems than in monolayered sheets studied elsewhere,[20-22] making study of valley states in QDs especially attractive.

It will be interesting to investigate how strongly these effects can be tuned by controlling the lateral size of QDs. Examining and understanding the electronic structure and spin nature (*e.g.* spin states on different valleys) of individual QDs will be fundamentally important in moving towards applications in electronics and spintronics (*e.g.* transistors from individual QD system). A future study of either individual QD or size-separated QDs could, therefore, prove very fruitful. It will also be necessary to establish effective methods of manipulating the QD spin states in different valleys. This may involve investigating electronic, magnetic and optical methods of stimulating valley-based transitions.

Control of valley states may then offer a novel route to manipulating quantum systems and possibly even enable entanglement for quantum computation. This would be an exciting departure for the semiconductor QD materials considered here. Quantum computation is likely to be among the next generation of rapidly maturing technologies and it may prove that the distinctive electronic and spin character of valley state QDs can contribute to this development.

References and Notes

[1] N. G. Shang, P. Papakonstantinou, M. McMullan, M. Chu, A. Stamboulis, A. Potenza, S. S. Dhesi and H. Marchetto, Graphene Nanoflake Films with Sharp Edge Planes. *Adv. Funct. Mater.* **2008**, *18*, 3506-3514.

[2] L. H.Tang, Y. Wang, Y. M. Li, H. B. Feng, J. Lu and J. H. Li, Preparation, Structure, and Electrochemical Properties of Reduced Graphene Sheet Films. *Adv. Funct. Mater.* **2009**, *19*, 2782-2789.

[3] M. Zhou, Y. M. Zhai and S. Dong, Electrochemical Sensing and Biosensing Platform Based on Chemically Reduced Graphene Oxide. *J. Anal. Chem.* **2009**, *81*, 5603-5613.

[4] D.Wang, D. Choi, J. Li, Z. Yang, Z. Nie, R. Kou, D. Hu, C. Wang, L. V. Saraf, J. Zhang, I. A. Aksay and J. Liu, Self-Assembled TiO_2–Graphene Hybrid Nanostructures for Enhanced Li-Ion Insertion. *ACS Nano* **2009**, *3*, 907-914.

[5] S. M. Paek, E. J. Yoo and I. Honma, Enhanced Cyclic Performance and Lithium Storage Capacity of SnO_2/Graphene Nanoporous Electrodes with Three-Dimensionally Delaminated Flexible Structure. *Nano Lett.* **2009**, *9*, 72-75.

[6] C. Xu, X. Wang and J. W. Zhu, Graphene-Metal Particle Nanocomposites. *J. Phys. Chem. C* **2008**, *112*, 19841-19845.

[7] R. Kou, Y. Y. Shao, D. H. Wang, M. H. Engelhard, J. H. Kwak, J. Wang, V. V. Viswanathan, C. M. Wang, Y. H. Lin, Y. Wang, I. A. Aksay and J. Liu, Enhanced Activity and Stability of Pt Catalysts on Functionalized Graphene Sheets for Electrocatalytic Oxygen Reduction. *Electrochem. Commun.* **2009**, *11*, 954-957.

[8] L. Wang, Y. Li, Z. Han, L. Chen, B. Qian, X. Jiang, J. Pinto and G. Yang, Composite Structure and Properties of Mn_3O_4/Graphene Oxide and Mn_3O_4/Graphene. *J. Mater. Chem. A* **2013**, *1*, 8385-8397.

[9] C. Mattevi, H. Kim, M. Chhowalla, A Review of Chemical Vapour Deposition of Graphene on Copper. *J. Mater. Chem.* **2011**, *21*, 3324-3334.

[10] T. Tojo, K. Fujisawa, H. Muramatsu, T. Hayashi, Y. A. Kim, M. Endo, M. Terronesce and M. S. Dresselhaus, Controlled Interlayer Spacing of Scrolled Reduced Graphene Nanotubes by Thermal Annealing. *RSC Adv.* **2013**, *3*, 4161-4166.

[11] J. D. Pandey and U. Gupta, Surface Tension of Binary Molten Salt Mixtures. *J. Phys. Chem.* **1982**, *86*, 5234-5237.

[12] D. Merki and X.Hu, Recent Developments of Molybdenum and Tungsten Sulfides as Hydrogen Evolution Catalysts. *Energy Environ. Sci.* **2011**, *4*, 3878-3888.

[13] M. Wu, Y. Wang, X. Lin, N. Yu, L. Wang, L. Wang, A. Hagfeldt and T. Ma, Economical and Effective Sulfide Catalysts for Dye-Sensitized Solar Cells as Counter Electrodes. *Phys. Chem. Chem. Phys.* **2011**, *13*, 19298-19301.

[14] J. V. Laurutsen, M. Nyberg, J. K. NØrskov, B. S. Clausen, H. TopsØc, E. Lægsgaard and F. Besenbacher, Hydrodesulfurization Reaction Pathways on MoS_2 Nanoclusters Revealed by Scanning Tunneling Microscopy. *J. Catal.* **2004**, *224*, 94-106.

[15] H. Vrubel, D. Merki and X. Hu, Hydrogen Evolution Catalyzed by MoS_3 and MoS_2 Particles. *Energy Environ. Sci.* **2012**, *5*, 6136-6144.

[16] H. I. Karunadasa, E. Montalvo, Y. Sun, M. Majda, J. R. Long and C. J. Chang, A Molecular MoS_2 Edge Site Mimic for Catalytic Hydrogen Generation. *Science* **2012**, *335*, 698-702.

[17] L. Song, L. Ci, H. Lu, P. B. Sorokin, C. Jin, J. Ni, A. G. Kvashnin, D. G. Kvashnin, J. Lou, B. I. Yakobson and P. M. Ajayan, Large Scale Growth and Characterization of Atomic Hexagonal Boron Nitride Layers. *Nano Lett.* **2010**, *10*, 3209-3215.

[18] H. Zeng, G.-B. Liu, J. Dai, Y. Yan, B. Zhu, R. He, L. Xie, S. Xu, X. Chen, W. Yao, and X. Cui, Optical Signature of Symmetry Variations and Spin-Valley Coupling in Atomically Thin Tungsten Dichalcogenides. *Scientific Reports* **2013**, *3*, 1608.

[19] D. Xiao, G. Liu, W. Feng, X. Xu, and W. Yao, Coupled Spin and Valley Physics in Monolayers of MoS_2 and Other Group-VI Dichalcogenides. *Phys. Rev. Lett.* **2012**, *108*, 196802.

[20] H. Zeng, J. Dai, W. Yao, D. Xiao and X. Cui, Valley Polarization in MoS_2 Monolayers by Optical Pumping. *Nat. Nanotechnol.* **2012**, *7*, 490-493.

[21] T. Cao, G. Wang, W. Han, H. Ye, C. Zhu, J. Shi, Q. Niu, P. Tan, E. Wang, B. Liu and J. Feng, Valley-Selective Circular Dichroism of Monolayer Molybdenum Disulphide. *Nat. Commun.* **2012**, *3*, 887.

[22] J. Klinovaja and D. Loss, Spintronics in MoS_2 Monolayer Quantum Wires. *Phys. Rev. B* **2013**, *8*8, 075404.